Dissertation
zur Erlangung des akademischen Grades
Doktor der Ingenieurwissenschaften (Dr.-Ing.)

der Technischen Fakultät
der Christian-Albrechts-Universität zu Kiel

Readout Methods for Magnetoelectric Sensors

Kiel, 6/2018

Author:
Sebastian D. Salzer

1st Referee: Prof. Dr.-Ing. Reinhard Knöchel
2nd Referee: Prof. Dr.-Ing. Eckhard Quandt
3rd Referee: Prof. Dr.-Ing. Dr.-Ing.habil. Robert Weigel

Date of the oral examination: 28th June, 2018

Abstract

The detection of weak magnetic fields has the potential to provide additional, non-redundant information in scientific fields such as medical diagnostics, geomagnetic investigations, data storage, amongst others. Many substances feature a low permeability and magnetic fields can penetrate them nearly unhindered which yields the possibility to detect signals that originate from within a volume without contact. Thin-film magnetoelectric sensors are mm-sized magnetometers that transform magnetic fields into a measurable polarisation via a mechanical coupling of a magnetostrictive and a piezoelectric layer. They do not need to be cooled and their high dynamic range allows them to be operated in unshielded environments. The output signal of the cantilever-shaped sensors is enhanced at their resonance frequency which can be exploited to increase the signal-to-noise ratio. This dissertation treats the signal processing for thin-film magnetoelectric sensors from a system point of view. Four main readout methods are investigated, modelled, and evaluated with the aim to lower the limit of detection: The direct detection, magnetic frequency conversion, electric frequency conversion, and a completely novel method utilising the sensor as a microwave resonator. With the focus on the signal-to-noise ratio, the noise sources of the measurement systems are discussed in depth and the dominant noise sources identified. The ultimate noise limit is given by the thermal-mechanical noise of the sensors. Acoustic environmental interference can be reduced with a tuning fork assembly that discriminates magnetic and mechanical excitation of two cantilevers clamped face-to-face. In order to measure magnetic fields at small frequencies in the range of biomagnetic signals, frequency conversion approaches that utilise the nonlinear characteristic of the magnetostrictive material are employed to convert the signals into the resonance frequency of the cantilever. The magnetic frequency conversion introduces additional noise sources into the system, in particular magnetic noise from the magnetostrictive layer and noise from the pump signal, which are both investigated in detail. By modifying the excitation network and a close cooperation with the fabricators of the sensors, the limit of detection is lowered significantly. Another concept for frequency conversion utilises an electrical conversion that has the advantage of requiring far less power. Its functionality is proven and first sensors are evaluated with the prospect of replacing the magnetic frequency conversion. A novel approach for the readout utilises the sensor as part of a microwave resonator that is detuned by magnetic fields. After the system noise sources have been reduced by signal processing measures, the thermal-mechanical noise proved to be the dominating noise contribution. Thus, the method reaches the same limit of detection as compared to direct detection. However, no piezoelectric layer is required which significantly simplifies the fabrication process and also alleviates the system of the thermal-electrical and charge amplifier noise. The best limit of detection for thin-film magnetoelectric sensors at 10 Hz is $50\,\mathrm{pT}/\sqrt{\mathrm{Hz}}$ achieved with the magnetic frequency conversion leading the way towards measurements of biomagnetic signals.

Kurzzusammenfassung

Die Detektion von schwachen magnetischen Feldern hat das Potential in Forschungsfeldern wie der medizinischen Diagnostik, geomagnetischen Untersuchungen, Datenspeicherung, usw. zusätzliche, nicht redundante Informationen verfügbar zu machen. Viele Stoffe haben eine geringe Permeabilität und sind daher für Magnetfelder nahezu uneingeschränkt durchlässig. Dadurch entsteht die Möglichkeit tieferliegende Signale kontaktlos zu detektieren. Dünnfilm magnetoelektrische Sensoren sind millimeter große Magnetometer, welche magnetische Felder über die mechanische Kopplung eines magnetostriktiven und eines piezoelektrischen Materials in eine messbare Polarisation transformieren. Die Sensoren brauchen nicht gekühlt werden und weisen einen hohen Dynamikbereich auf, wodurch sie in ungeschirmten Umgebungen betrieben werden können. In der mechanischen Resonanzfrequenz der balkenförmigen Sensoren wird deren Ausgangssignal erhöht, wodurch das Signal-zu-Rausch Verhältnis verbessert wird. In dieser Dissertation wird die Signalverarbeitung von diesen Sensoren aus Systemsicht behandelt. Mit dem Ziel das Detektionslimit zu senken werden vier Ausleseverfahren untersucht, modelliert und bewertet: Die direkte Detektion, die magnetische Frequenzumsetzung, die elektrische Frequenzumsetzung und ein komplett neues Verfahren, in dem der Biegebalken als Mikrowellen Resonator verwendet wird. Mit dem Fokus auf dem Signal-zu-Rausch Verhältnis werden die einzelnen Rauschquellen der Messsysteme diskutiert und die jeweils dominanten Rauschquellen ermittelt. Das grundlegende Rauschlimit ist das thermisch-mechanische Rauschen des Sensors. Akustische Umweltstörungen können mit einer Stimmgabelanordnung bestehend aus zwei Einzelsensoren unterdrückt werden, welche magnetische und mechanische Einkopplungen bauartbedingt unterscheiden kann. Um magnetische Felder bei kleinen Frequenzen im Bereich biomagnetischer Signale zu messen, wird die Nichtlinearität der magnetostriktiven Schicht ausgenutzt um die Signale in die mechanische Resonanz des Biegebalkens umzusetzen. Durch das Verfahren der magnetischen Frequenzumsetzung treten zusätzliche Rauschquellen auf, insbesondere magnetisches Rauschen der magnetostriktiven Schicht und Rauschen des Anregungssignals. Mittels Modifkationenen an der Ansteuerungselektronik und enger Zusammenarbeit mit den Sensorherstellern konnte das Detektionslimit signifikant gesenkt werden. Ein alternatives Konzept zur Frequenzumsetzung verwendet statt eines magnetischen ein beinahe leistungsloses elektrisches Pumpsignal. Die Methode wird erfolgreich angewendet und könnte mit neuen Sensoren in Zukunft möglicherweise die magnetische Frequenzumsetzung ersetzen. Ein neuer Ansatz zum Auslesen integriert den Sensor in einen Mikrowellenresonator, der durch ein magnetisches Feld verstimmt wird. Nach der Eliminierung von verschiedenen Systemrauschquellen erwies sich ebenfalls das thermisch-mechanische Rauschen als dominante Rauschquelle. Daher erreicht die Methode das gleiche Detektionslimit wie die direkte Detektion, kommt im Gegensatz dazu aber ohne piezoelektrische Schicht aus. Dies erleichtert den Herstellungsprozess und sorgt gleichzeitig dafür, dass thermisch-elektrisches und Ladungsverstärkerrauschen weg-

fallen. Als bestes Detektionslimit für dünnfilm magnetoelektrische Sensoren bei 10 Hz wird $50\,\mathrm{pT}/\sqrt{\mathrm{Hz}}$ gemessen.

Declaration

Hereby I declare, that I have produced the doctoral thesis

Readout Methods for Magnetoelectric Sensors

independently and without improper external assistance and that I have identified all word-for-word quotations of other authors, as well as comments based closely on other authors' ideas, and I have listed the relevant sources. Furthermore, this thesis has not been, partially or completely, submitted to any other university or institute in the context of an examination procedure. I declare that, the following work has been written in compliance with the rules of good scientific practice of the German Research Foundation.

Kiel, Monday 23rd July, 2018
Sebastian D. Salzer (Signature) .....

Acknowledgement

This dissertation is a product of my work at the group of Microwave Engineering at the Institute of Electrical Engineering and Information Engineering of the Christian-Albrechts-Universität zu Kiel in the course of the project PAK 902 "Magnetoelektrische Sensoren für die Medizin" and the inter-disciplinary Collaborative Research Center 1261 "From Composite Materials to Biomagnetic Diagnostics".
I would like to thank my supervisor Prof. Dr.-Ing. Reinhardt Knöchel for his ongoing support, fruitful discussions, and his down-to-earth way of explanation. Also, I would like to express my gratitude to Dr. Dirk Meyners for helping me in particular with the physical backgrounds, to Prof. Dr.-Ing. Michael Höft for the opportunity to write a doctoral thesis while working at his chair, and to Prof. Dr.-Ing. Eckhard Quandt for assessing this thesis.
Furthermore, I would like to thank the members of my chair and my colleagues from the research group for a pleasant work climate, scientific cooperation, sensor supply, and simply a good time:
Volker Röbisch, Patrick Hayes, Erdem Yarar, Phillip Durdaut, Matic Klug, Robert Jahns, Onur Urs, Alexander Teplyuk, Jens Reermann, Lennart Nissen, Leonhard Buck, Frank Daschner, Wolfgang Taute, Melanie Bork, André Piorra, Jeffrey McCord, Gerhard Schmidt, Benjamin Spetzler, Sebastian Zabel, Lars Thormählen, Iulian Teliban, Kai Körber, Hendrick Brüns, Jascha Lukas Gugat, Alwin Reinhardt, Daniel Miek, and my scientific assistants and thesis graduates.
My sincere thanks to my family, in particular my mother Elke and my father Bernd (who made me do this), og til min skatta Marlene.
And to Grønland.

Contents

1 Introduction

In this dissertation, readout schemes for magnetoelectric sensors utilised as highly sensitive magnetometers are discussed from a system point of view. In order to measure weak signals and to access new application areas, the signal-to-noise ratio needs to be improved. The first chapter provides the motivation for this discourse and introduces into the subject. After a short general review on magnetoelectric sensors, the structure of the dissertation is outlined.

1.1 Motivation

The ongoing progress in medical diagnostics is the foundation for the treatment of certain diseases that prior were not even known to be the cause of a patient's discomfort. Misdiagnosis caused by sheer lack of knowledge leads to false therapy recommendations and may cause irreversible damage or even be lethal. A vivid example is the improvement of automatic implantable cardioverter-defibrillators (ICD). These devices continuously monitor the heart via transcardiac electrodes and scan its waveforms for arrhythmias. In case of ventricular fibrillation, the heart can be reset with a short pulse directly to the heart. According to [Mir85], around 1980 a new version of the ICD was clinically tested that is able to additionally detect ventricular tachycardia by improved signal processing within the device. Upon occurrence, short pulses synchronised with the heart rate are delivered to the heart with a method called *overpacing*, intentionally decreasing the pulse back to normal. The average mortality rate in discussed clinical studies was significantly decreased from about 10 % for the conventional ICD to 2 % with the new version!
The measurement of magnetic instead of electric fields may yield particular advantages for medical diagnosis. In contrast to the electrical conductivity, the relative permeability of human tissue is $\mu_r \approx 1$ [FCD09]. Thus, magnetic fields penetrate human tissue more or less unhindered. The origin of a measured quantity may lie

Car in 50 m distance	1-10 nT
Current-carrying wire	0.001 T
Earth's magnetic field	$6 \cdot 10^{-5}$ T DC
Small bar magnet	0.01–0.1 T DC
Electromagnet with an iron core	≤ 2 T
Superconducting magnet	5–20 T

Table 1.1: Exemplary magnetic flux densities in the environment on earth according to [Pop04; AN07]. The current wire value is for a current of 100 A, at the distance of 2 cm from the wire axis.

well below the surface and can still be detected practically unaltered. Moreover, magnetic fields can be measured contactless. It is to be expected that magnetic signals contain information that cannot be observed with electrical measurements on the surface.

In [Moh+17], the retrospective impact of magnetoencephalography (MEG) data based diagnosis on the treatment of epilepsy is discussed. Before a surgery where a confined area of brain tissue is to be removed, many different diagnosis and localisation tools such as intercranial EEG (icEEG, invasive method directly on the brain) or MEG are applied. In the clinical study, the MEG data is not exploited prior to the surgery due to various reasons. Unfortunately, in retrospective it is concluded that the data from the MEG would have changed decisions about the resection areas and drastically improved the outcome of the surgery. It is concluded that MEG may not only have had a significant effect on the surgical outcome, but may also reduce cost and complications of the operation.

However, magnetic signals from biomagnetic sources are commonly very weak, especially in comparison to environmental interferences.

Tab. 1.1 gives an overview of average magnetic flux densities in the environment on earth. The span from very weak flux densities to those of the environment can be quite large. For example, magnetic signals from the human brain are more than four decades weaker than urban noise (cf. Fig. 1.1). Thus, the requirements for the dynamic range and interference and noise suppression are extensive.

Fig. 1.1 depicts typical amplitude densities for a small selection of desired signals. Measurements of biomagnetic signals require a sensor that works well in a low-frequency regime. Biomagnetic signals are typically in the frequency range between 0.1 and 100 Hz [BML01].

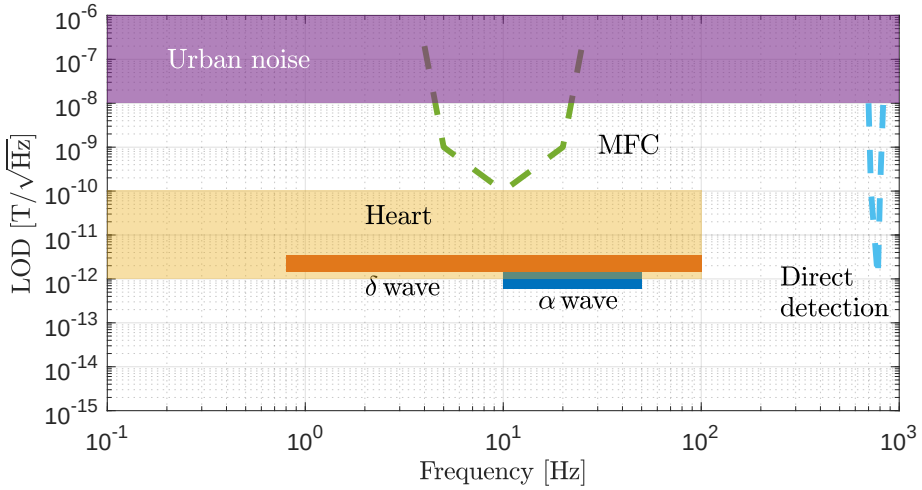

Figure 1.1: Overview of amplitude densities of desired signals, urban noise, and limits of detection schemes with magnetoelectric (ME) sensors [CB06].

This discourse is part of three research projects funded by the German Research Foundation (Deutsche Forschungsgesellschaft, DFG): The CRC 855, the grant PAK 902, and the CRC 1261. While the first two projects have already expired, the third project continues until the year 2020. The CRC 1261 is an inter-disciplinary project with the aim to develop and apply magnetoelectric (ME) sensors for medical diagnosis, e.g. in MEG and magnetocardiography (MCG). The direct magnetoelectric effect (cf. Sec. 2.1) leads to a measurable polarisation as a function of an applied magnetic field which enables ME sensors to measure weak magnetic signals. In comparison to other magnetic sensors (see App. B), ME sensors do not necessarily require cooling, have a high dynamic range and feature a mechanical resonance frequency (cf. Sec. 2.2).

The focus of this dissertation is the interface between sensor fabrication and application. To describe the sensors from a system point of view, their characteristics are investigated and integrated into signal models which allow the identification of their limits. In the course of the sensor development a close collaboration between the fabrication and system engineering is necessary. For the measurement of weak magnetic fields, the ME sensors need to be integrated in a measurement environment that induces no additional limits to the system. The signal-to-noise ratio (SNR) can be enhanced by means of signal processing and by the implementation of various measurement schemes. In order to approach an application in real diagnosis of patients, the sensors have to be able to operate in non-laboratory environments and be

robust against external interferences. Aside from the SNR, other parameters such as bandwidth, frequency, measurement time, spatial and time resolution, dynamic range, etc. need to be taken into consideration. A customary parameter that summarises many of the above requirements is the limit of detection (LoD) which noise density at the working point where signal of interest cannot be distinguished from the noise floor anymore (SNR=1).
In the beginning of this work in 2014, it was not possible to measure biomagnetic signals with the direct detection scheme (cf. Sec. 2.4), although LoDs of $1\,\mathrm{pT}/\sqrt{\mathrm{Hz}}$ were achieved with thin-film ME sensors for test signals applied at their resonance frequency [Jah+13]. The sensors can be tuned to lower frequencies by scaling their dimensions up which results also in a decreased bandwidth and higher susceptibility to acoustic and vibration noise. Moreover, the origin of the limiting noise for direct detection at the resonance frequency was unknown. *Magnetic frequency conversion* (MFC) is a readout method to convert low-frequency signals into the mechanical resonance of the sensors. The LoDs for a 1 Hz signal measured with MFC were around $1\,\mathrm{nT}/\sqrt{\mathrm{Hz}}$ [Jah+12; Jah13]. For this detection scheme, the dominant noise source was supposedly Barkhausen noise in the magnetostrictive layer.
First measurements of signals from a human heart show the potential of ME sensors for biomagnetic sensing [Ree+17]. By triggering the R-wave (the highest peak in a standard electrocardiogram (ECG)), the heart signal can be averaged which increases the SNR by the number of averages (for amplitudes with the square root of the number of averages). This is due to the correlation of the peaks in the signal. Due to the insufficient LoD of the investigated ME sensor, a large number of averages is required to achieve an adequate SNR.
Therefore, the readout methods and the noise sources need to be further investigated to decrease the LoD in order to measure biomagnetic signals.

1.2 Conventions

Throughout this discourse, some conventions are presumed. The LoD improves as it gets smaller, since a low limit means that weak signals can be measured. It is given in the unit of a density, i.e. $\mathrm{T}/\sqrt{\mathrm{Hz}}$. That implies that sometimes referenced values are converted into an amplitude density. Frequency dependence is written both with angular frequency ω in rad/s and frequency f in Hz. They are related by $\omega = 2\pi f$. The terms *magnetic flux density* and *magnetic field* are used interchangeably, as in

magnetic flux field. The unit for the magnetic flux density used in this work is Tesla (T), according to the SI unit system and [Mic14]. Especially in material sciences, the CGS system units are commonly used: Gauß (Gs) for magnetic flux density and Oersted (Oe) for magnetic fields. The conversion from Oe to T is given by

$$\mu_0 \cdot 1\,\mathrm{Oe}\cdot = 1\,\mathrm{Gs} = 10^{-4}\,\mathrm{T}. \tag{1.1}$$

The utilised sensors are categorised into general layer designs (cf. Fig. 2.3). Additional sensor fabrication information is only provided if deemed necessary for the investigation because the sensors are not the focus of this discourse. The terms *pump signal* and *carrier* are used interchangeably. For materials, the common chemical abbreviations from the periodic table are used. Amplitudes are indicated with lower case letters with a hat. However, most signals are described by their root mean square (RMS) value written with capital letters. Further specific mathematical notations are provided in the glossary at the end of the document.

1.3 Structure of the Dissertation

The dissertation is divided into three main chapters. In the first chapter, the magnetoelectric effect is introduced which is the basis for all following contents. The reader is introduced to the characteristics of magnetoelectric thin-film sensors and important parameters. As a basis for the following chapters, the direct detection operation mode is explained and the noise behaviour of the sensors is investigated. Furthermore, two general methods for signal enhancement and noise suppression are discussed. In the second chapter, magnetoelectric sensors operated with frequency conversion approaches are introduced. In order to understand the conversion processes, the magnetic behaviour of the magnetostrictive layers is reviewed from a system point of view. The MFC is discussed in terms of the occurring physical processes, the signal, noise, LoD, and limits. The chapter also contains an investigation of the operation with the related electric frequency conversion which avoids practical shortcomings of the MFC. The fourth chapter treats an alternative readout scheme utilising a magnetoelectric sensor as a resonating structure in the GHz range. The dissertation is concluded with a summary, conclusions, and a brief discussion about possible future work.

For convenience, a list of abbreviations, used notations, and symbols is provided after the main contents. A list of figures is followed by the bibliography which is divided into general publications and publications with involvement of the author. In the appendix, additional derivations, explanations, and data is provided.

2 | Magnetoelectric Sensors

ME sensors can be used to detect magnetic fields by making use of the magnetostrictive and the piezoelectric effect. The fields to be measured may be as small as some pT at frequencies from DC up to several kHz. This makes the measurement of biomagnetic sources, such as heart stimulation signals and other weak signals possible. Throughout this dissertation, measurements and simulations are conducted with ME sensors aiming for the detection of biomagnetic signals. This chapter introduces thin-film ME sensors, their working principle, operation, characteristic parameters, and investigations related to the direct detection with the sensors. A short review about other magnetic field sensors and their performances is given in the appendix (App. B).

2.1 Magnetoelectric Effect

The magnetoelectric effect can be categorised into the direct and the indirect magnetoelectric effect [Fie05; Nan+08]. The direct effect is a linear magnetoelectric behaviour of a single-phase compound, which features intrinsic magnetostriction and piezoelectricity. It is orders of magnitude smaller than the indirect effect of multiple-phase composites [Zha+09]. The indirect effect is nonlinear by nature, but linearised with a working point set by a magnetic bias for weak AC magnetic fields to be measured. In the following, the magnetoelectric effect only refers to the indirect effect. As mentioned before, magnetoelectric sensors are based on two effects: magnetostriction and piezoelectricity. A magnetostrictive material changes its length and/or volume as a function of applied magnetic field. Piezoelectric materials generate a polarisation, if they are subject to a directed mechanical deformation [CC82]. If the magnetostrictive material is mechanically coupled to the piezoelectric material, an applied magnetic field leads to a polarisation. The polarisation and thus the magnetisation can then be measured with an appropriate readout device.

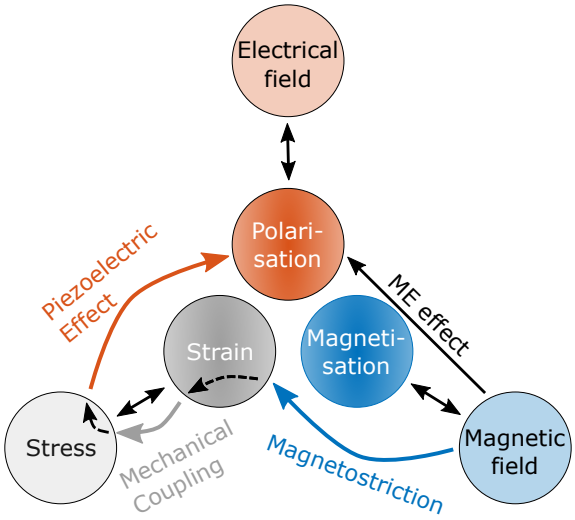

Figure 2.1: Visualisation of the involved effects of magnetoelectric sensors for the sensing of magnetic fields. The indirect (composite) magnetoelectric effect is indicated by curved arrows via the magnetostrictive effect, mechanical coupling and the piezoelectric effect [SF05].

This product property is displayed in Fig. 2.1. The effects can be used in different directions, e.g. from an electric field to a magnetisation. This is called the inverse (or likewise converse) ME effect and will be of particular interest in Sec. 3.2. The product behaviour of the composite allows, to a certain degree, for individual design and optimisation of the single constituents.

2.2 Thin-film Magnetoelectric Sensors

Two structural types of magnetoelectric sensors need to be distinguished [Pio14]: Composites from volume materials, which are mainly laminated together, and thin-film composites. The laminated (bulk) sensors exhibit large magnetoelectric effects [Ma+11]. For magnetoelectric sensors the Joule magnetostriction [CG09] given by

$$\lambda\big(M(H)\big) = \frac{\Delta l}{l}, \tag{2.1}$$

with the magnetostriction λ, the magnetisation M, the magnetic field H, the change in length Δl, and the length l, is the dominant magnetostrictive effect. It is a function of the magnetisation M which is a function of the magnetic field H (cf. Sec. 3.1.1). Since the magnetostriction does not scale with the length, the change in

length increases for longer sensors. The ratio between substrate thickness and functional layer thickness is crucial for the ME effect. A higher deflection amplitude produces more mechanical stress and polarisation in the piezoelectric layer. Due to the L-L operation mode (longitudinal magnetisation - longitudinal polarisation, if symmetrical also called push-pull [Nan+08]) of the sensors, the mechanical coupling leads to a charge generation over the complete length of the sensors. At low frequencies, centimeter-sized laminated sensors are state of the art in terms of LoD. Petrie et al. and Wang et al. presented sensors with a LoD of $4\,\mathrm{pT}/\sqrt{\mathrm{Hz}}$ and $10\,\mathrm{pT}/\sqrt{\mathrm{Hz}}$ at 1 Hz, respectively [Pet+12], [Wan+11]. The lamination of piezoelectric and magnetostrictive materials for bulk sensors can lead to an irregular and fragile adhesion that deteriorates the coupling, and thus, is limiting the magnetoelectric effect. The trend for miniaturisation and higher spacial resolution requires smaller structures, which leads to thin-film composites. The term *thin-film* refers to magnetoelectric sensors with a substrate, on which the functional layers are deposited and structured with microelectromechanical system (MEMS) techniques [Zha+09]. Film deposition techniques result in a better adhesion and make lamination superfluous. In the following, the term *magnetoelectric sensors* refers to thin-film magnetoelectric sensors. All measured and investigated sensors are from batches of multiple generations of sensor fabrication in the time range from approximately 2010 until 2017. The fabrication in the Kiel Nanolaboratory was conducted by numerous scientists from the Institute of Material Science of the University Kiel.

The sensors are manufactured most commonly by applying a magnetostrictive and a piezoelectric layer, as well as seed, isolation, and electrode layers, onto a silicon wafer. The structuring is done with standard optical lithography as well as wet and dry etching techniques. The deposition can be realised by e.g. sputtering. From the wafer, the cantilever shaped sensors are cut and glued onto a rigid support mount [Zha+09; Gre+10].

Fig. 2.2 shows a schematic drawing of a typical ME sensor. Several kinds of thin-film magnetoelectric sensors are used in this work.

A selection is given in Fig. 2.3, which shows exemplary layouts of the sensors. Other measured sensor types are MEMS sensors, e.g. with a beam length of $l_{\mathrm{cant}} \approx 3\,\mathrm{mm}$. In general, these have smaller dimensions as the sensors in Figs. 2.3 and 2.4, aim at further miniaturisation and integration, and are designed to pronounce different effects such as for example the ΔE_{d}-effect [Goj+11]. This work focusses on the variants shown in Fig. 2.3, in particular the *Multilayer* layout, and its layer

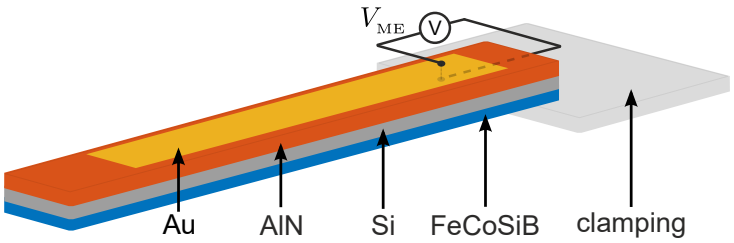

Figure 2.2: Schematic of an exemplary ME sensor. The magnetostrictive material is iron cobalt boron silicon (FeCoSiB), the substrate material is silicon, the piezoelectric material is aluminium nitride (AlN), and the electrode material is gold (Au), all indicated with arrows in the figure. The clamping is made of a specific glass-reinforced epoxy laminate called FR-4, a typical material for printed circuit boards (PCB). The circled V represents a voltage measurement device that can measure the magnetoelectric voltage V_{ME}.

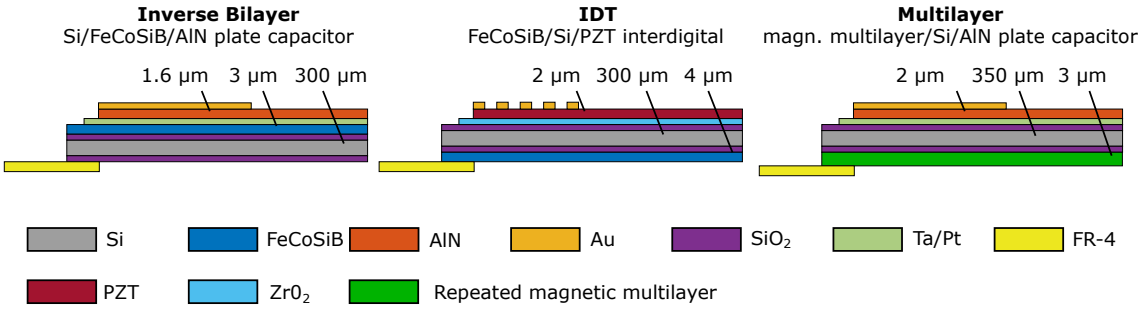

Figure 2.3: Selection of different magnetoelectric sensor designs from [Yar+16a; Pio+13; Sal+17a] respectively. These, and several other layer configurations and designs, are used with varying thickness's in the following investigations. The FR-4 is the material, on which the sensor is mounted. The name in bold serves to distinguish the designs. Au is usually deposited with an adhesion layer of chromium (Cr).

variations. The *Inverse Bilayer* type introduced a new fabrication method with iron cobalt boron silicon (FeCoSiB) in between the substrate and the piezoelectric layer. With the *IDT* (interdigital transducer, IDT) design, lead zirconate titanate (PZT) can be utilised as the piezoelectric layer. The Multilayer type can lead to a reduction of magnetic noise contributions during operation.

The magnetostriction λ of the ferromagnetic FeCoSiB as a function of the applied magnetic field B is nonlinear as shown in Fig. 2.5. It is hysteretic and saturates for high magnetic fields. While the stress of aluminium nitride (AlN) behaves linearly with the applied electric field E, the stress of the ferroelectric PZT features a nonlinear (butterfly) curve with hysteresis and saturation for high fields. The associated

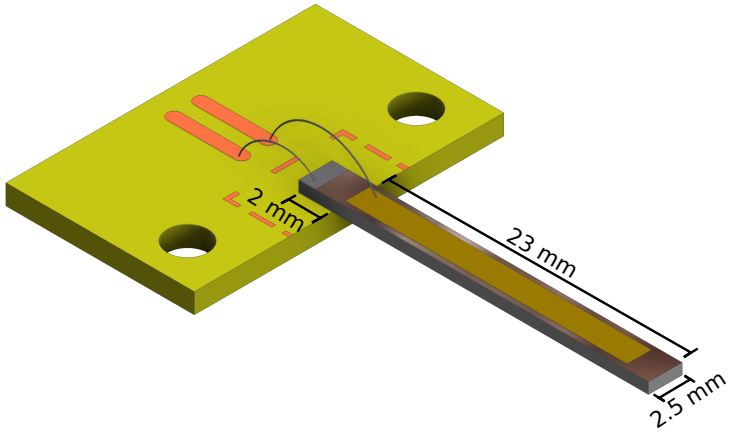

Figure 2.4: 3d model of an exemplary magnetoelectric thin-film sensor glued to a PCB made of FR-4. The electrodes are connected with bond-wires to copper pads. The drill holes are for the mounting to a sensor holder.

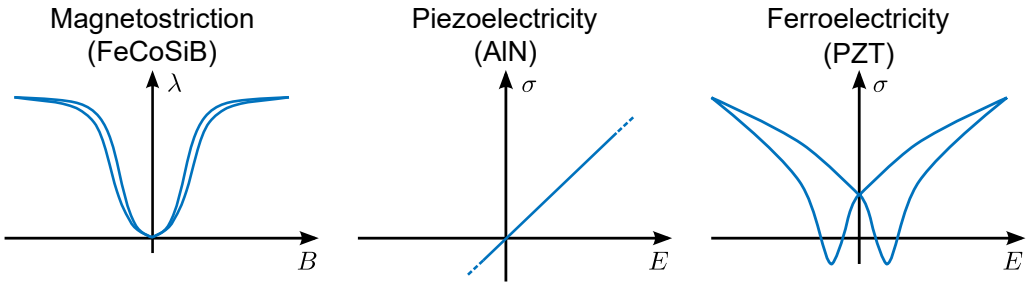

Figure 2.5: Schematic magnetostriction and stress (σ) curves of FeCoSiB, AlN, and unpoled PZT.

dominant piezoelectric coefficients from the tensors are d_{31} and d_{33}, respectively, for the investigated sensors. The coefficient is a measure of the piezoelectric effect strength in a specific direction. The first index indicates the direction of the excitation or mechanical deformation. The second index is the direction of polarisation change. Since the d_{33} coefficient for PZT has both the excitation and polarisation parallel to the long axis of the cantilever, IDT electrodes as depicted in Fig. 2.3 are used for PZT to maximise the voltage output.

The sensors are cut and mounted as unilaterally clamped cantilevers. They feature several resonances associated with resonance frequencies, also called modes. The resonance frequencies of order ν can be calculated by [LL03]

$$f_\nu = \left(\frac{\beta_\nu^2}{\sqrt{12}}\right) \frac{t_{\mathrm{cant}}}{2\pi\, l_{\mathrm{cant}}^2} \sqrt{\frac{E_{\mathrm{d,cant}}}{\rho_{\mathrm{cant}}}}, \tag{2.2}$$

Parameter	Value	Parameter	Value
$E_{\mathrm{d,cant}} \approx E_{\mathrm{d,Si}}$	169 GPa	f_2	5436 Hz
$\rho_{\mathrm{cant}} \approx \rho_{\mathrm{Si}}$	2.239 g/cm^3	$R_{\mathrm{m}}(f_1)$	358 kΩ
l_{cant}	23 mm	$L_{\mathrm{m}}(f_1)$	8 kH
t_{cant}	365 µm	$C_{\mathrm{m}}(f_1)$	56 fF
f_1	867 Hz	$C_{\mathrm{ME}}(f_1)$	500 pF

Table 2.1: Parameters of a typical cantilever as shown in Fig. 2.4 [Zab+16].

with the thickness t_{cant}, length l_{cant}, elastic modulus $E_{\mathrm{d,cant}}$ of the cantilever, the material density of the cantilever ρ_{cant}, and a factor β_ν. The equation stems from the Euler-Bernoulli Beam theory [Bal07]. For the first two bending modes is $\beta_1 = 1.875$ and $\beta_2 = 4.694$.

Table 2.1 gives some typical values for the sensor design in Fig. 2.4. For the mechanical parameters, silicon (Si) is considered to contribute the dominant part. As a good approximation, the bulk parameters of Si can be used for the calculation and seed, isolation, electrode and functional layers are neglected. The output signal of the cantilever experiences an increase in resonance, which can be described by the magnitude frequency response of the model of a damped mechanical oscillator [Gab93]:

$$G_{\mathrm{mech}}(f) = \frac{1}{\sqrt{\left(1 - (\frac{f}{f_{\mathrm{res}}}^2)\right)^2 + \left(\frac{f}{f_{\mathrm{res}}\,Q}\right)^2}}, \tag{2.3}$$

with the resonance frequency f_{res} and the quality factor Q (Q-factor). Eq. (2.3) is depicted in Fig. 2.6 for different values of the Q-factor. According to [Ger13], magnetoelectric sensors can be described more precisely by a Fano resonance for specific sensor designs. The shape of the transfer function differs from a damped mechanical oscillator outside of the resonance frequency, as can be seen in a measurement later in Fig. 2.11. For the direct detection and the frequency conversion techniques, the simpler description by a damped mechanical oscillator is sufficient because they operate at the mechanical resonance frequency.

The quality factor is generally defined by

$$Q = 2\pi \frac{\text{energy stored}}{\text{energy dissipated per cycle}}, \tag{2.4}$$

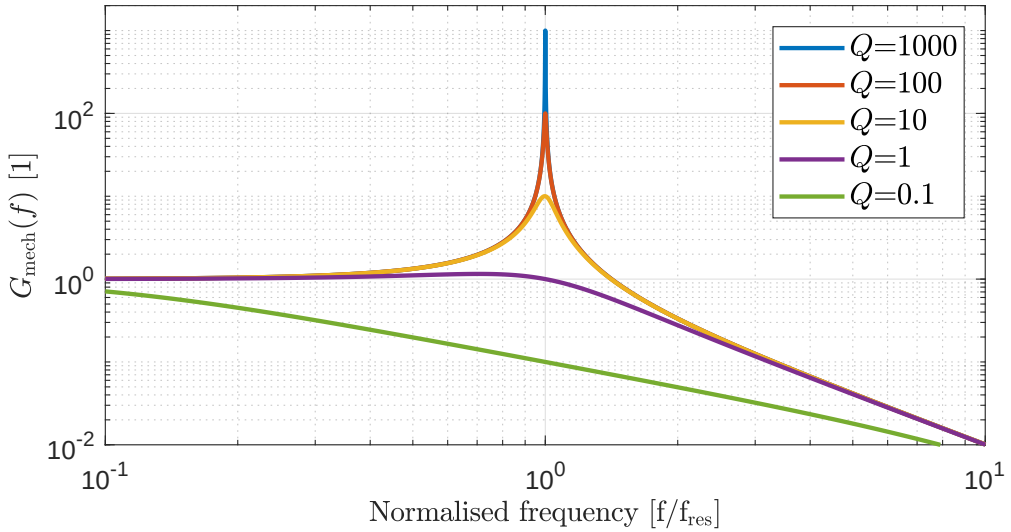

Figure 2.6: Normalized amplitude frequency response of a damped mechanical oscillator for various Q-factors [Gab93; BEO10]. The frequency axis is normalised to f_{res}.

proportional to the inverse of the damping of a resonator and for a single tuned resonance given by

$$Q = \frac{f_{\mathrm{res}}}{\Delta f}, \tag{2.5}$$

with the 3-dB bandwidth Δf. It determines the settling time of the ME sensor with

$$Q = \pi \cdot f_{\mathrm{res}} \cdot \tau_{\mathrm{ME}}, \tag{2.6}$$

and the time constant τ_{ME}. At low resonance frequencies, the sensor needs more time to settle. The Q-factor Q can be calculated from all involved loss mechanisms by

$$Q = \left(\frac{1}{Q_1} + \frac{1}{Q_2} + \ldots + \frac{1}{Q_i} \right)^{-1}, \tag{2.7}$$

described by i different Q-factors in the system. According to [Kir17], the most important loss mechanisms stem from clamping, the viscous environment, and volume/surface effects, [HEA03; Lüb+11; Yas+00] respectively. The air damping can effectively be eliminated by vacuum encapsulation [Kir+13].

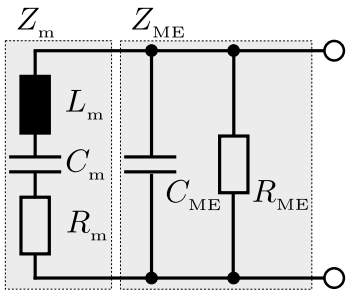

Figure 2.7: Equivalent circuit diagram (ECD) of a thin-film magnetoelectric sensor according to [IE88]. The grey backgrounds summarise individual elements with the impedances Z_{m} and Z_{ME}.

The sensor and its capacitive terminal behaviour can be described with the equivalent circuit diagram (ECD) in Fig. 2.7. The electrical loss of the piezoelectric layer is modelled by R_{ME}, whereas the sensor capacitance is given by C_{ME}. Its (mechanical) resonant behaviour is represented by a series resonant circuit with the equivalent inductance L_{m}, capacitance C_{m}, and resistance R_{m}. The impedances Z_{m} and Z_{ME} can be calculated by

$$Z_{\mathrm{m}} = R_{\mathrm{m}} + j\omega L_{\mathrm{m}} + \frac{1}{j\omega C_{\mathrm{m}}} \tag{2.8}$$

and

$$Z_{\mathrm{ME}} = \frac{1}{\frac{1}{R_{\mathrm{ME}}} + j\omega C_{\mathrm{ME}}}. \tag{2.9}$$

According to [Jah13], the resistance of the ME sensor R_{ME} is given by

$$R_{\mathrm{ME}} = \frac{1}{\omega\, C_{\mathrm{ME}} \tan\delta_{\mathrm{ME}}} \tag{2.10}$$

and the capacitance by

$$C_{\mathrm{ME}} = \frac{\varepsilon_0 \varepsilon_{\mathrm{r}} A_{\mathrm{elec}}}{t_{\mathrm{piezo}}}, \tag{2.11}$$

with the vacuum permittivity ε_0, the relative permittivity ε_{r} of C_{ME}, the cross-sectional area of the electrode A_{elec}, and the distance between the electrode plates t_{piezo} which equals the thickness of the piezoelectric layer.
Typical values are given in Tab. 2.1.

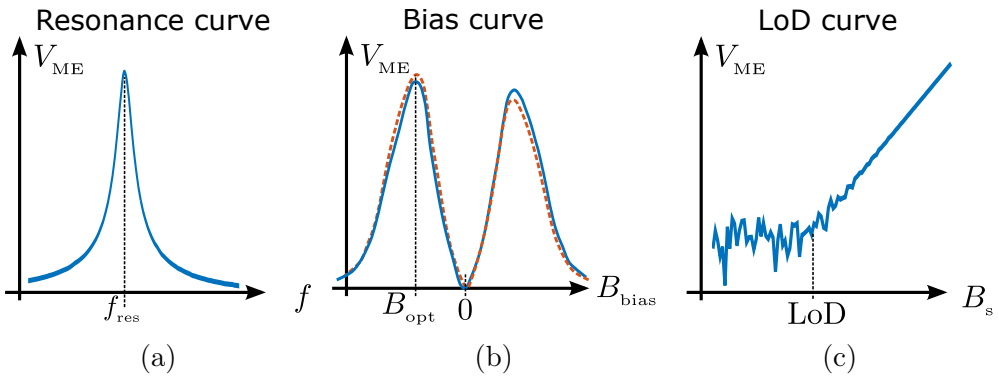

Figure 2.8: (a) Schematic resonance curve of the output voltage of a magnetoelectric sensor for a specific bias field B_{bias} and signal B_s versus frequency. (b) Schematic of the output voltage of a magnetoelectric sensor for a specific signal frequency f_s and a fixed signal B_s versus the magnetic bias field. The solid line comes from negative magnetic saturation, whereas the dashed line comes from positive saturation. (c) Schematic LoD curve of the output voltage of a magnetoelectric sensor for a specific signal frequency f_s and bias field B_{bias} versus the signal B_s. V_{ME} is the output voltage of the sensor.

A polarisation change caused by an applied magnetic field can be detected as a magnetoelectric voltage V_{ME} at the electrodes of the cantilever.
Fig. 2.8 shows three characteristic curves of magnetoelectric sensors: they are named *Resonance curve*, *Bias curve*, and *LoD curve*. The maximum of the resonance curve in Fig. 2.8a indicates the mechanical resonance frequency. The Q-factor and the bandwidth are also obtained from this measurement (see Eq. (2.5)). This curve is a function of the applied bias field B_{bias} and signal to be measured $B_s(t)$, while the frequency is swept around f_{res}. The bias field curve shows V_{ME} as a function of the applied bias field for a fixed frequency f_s and signal B_s (RMS value). The bias field is directed parallel to the long axis of the cantilever. To obtain the largest output signal V_{ME}, the bias is set to the working point B_{opt}. The curve is closely related to the hysteresis loop of the magnetic material and will be further discussed in Sec. 3.1.1. Its shape allows to draw conclusions about the magnetic behaviour of the magnetostrictive layer because it is proportional to the derivative of the magnetostriction curve. The used magnetic materials are designed to be soft magnetic, and show minor hysteretic behaviour (see Fig. 2.8b). The LoD can be read from the LoD curve (see Fig. 2.8c), measured with the optimal bias field B_{opt} at the resonance frequency f_{res}. The magnetic field, at which the signal cannot be distinguished from the system noise floor any more, is considered the LoD. The unit

Table 2.2: Parameters used for the description of the sensor performance.

Parameter	Unit	Meaning
LoD	$\mathrm{T}/\sqrt{\mathrm{Hz}}$	noise floor in operating point
Resolution	T	smallest detectable signal
Sensitivity S	V/T	output signal per input signal

of the LoD for magnetic sensors in this work is $\mathrm{T}/\sqrt{\mathrm{Hz}}$. Another commonly used related parameter is the resolution which has the unit T. Both units are related by the equivalent noise bandwidth (ENBW) [MC93]. This will be further explained in Sec. 2.5.2. Another parameter that results from Fig. 2.8c is the sensitivity in V/T. The sensitivity indicates how much output signal per input signal is generated. In the literature e.g. in [Fie05], it is customary to use the ME coefficient α_{ME} instead of the sensitivity, which is defined by

$$\alpha_{\mathrm{ME}} = \frac{\partial E}{\partial \sigma} \cdot \frac{\partial \sigma}{\partial \lambda} \cdot \frac{\partial \lambda}{\partial H} = \frac{V_{\mathrm{ME}}}{t_{\mathrm{piezo}} \cdot H} \quad \left[\frac{\mathrm{kV}}{\mathrm{cmOe}}\right], \tag{2.12}$$

with the electric field E, the mechanical stress σ, the magnetostriction λ, the magnetic field H, the ME voltage V_{ME}, and the unit in square brackets. It additionally takes into account the piezoelectric layer with its thickness t_{piezo}. The magnetic field strength is given in CGS units (Oersted).
In the following, the sensitivity S will be given by

$$S = \frac{V_{\mathrm{ME}}}{B_{\mathrm{s}}}, \tag{2.13}$$

with B_{s} in T (SI-units). In some publications, the sensitivity is confused with the LoD or the resolution.
Tab. 2.2 summarises these definitions.

2.3 State of the Art

To detect very weak signals with a capacitive sensor such as a magnetoelectric sensor, its output quantity needs to be amplified and processed before the results can be further analysed. Because the noise contributions of the components in the signal chain must not degrade the SNR of the sensor, a system based noise analysis is necessary. In order to do so, it is customary to describe all involved elements in

equivalent signal and noise circuits that allow to determine the total output SNR and the interrelation between the individual contributions. The signal is often described with a transfer function that mathematically models the sensor behaviour [Fra04]. Such an approach requires profound knowledge about the physical backgrounds often involving nonlinear effects and dynamic characteristics that may also depend on the excitation. The noise behaviour can be modelled with a set of standard noise sources adapted to the sensor system at hand [Bel85; MC93] which give insight into the acceptable noise contributions for components of the readout system. State of the art for low noise readout amplifiers are commercially available operational amplifiers that are adapted to the sensor characteristic by a surrounding network of passive components [Gro+16]. Their voltage noise is in the $\mathrm{nV}/\sqrt{\mathrm{Hz}}$ range which can be inserted into the noise model to determine whether a less noisy component is required. To further reduce the amplifier noise often discrete transistor input stages that may reduce the noise floor are employed [NPS91; Lev08] and additional matching networks are inserted [LLB92]. Sensitive measurements are commonly conducted in shielded environments to exclude external interferences. According to the IEEE standard for sensor performance parameter definitions [Mic14], important parameters to be determined by measurement and simulation are the sensitivity, the LoD, and the noise behaviour, amongst others.

For the detection of weak magnetic signals with magnetoelectric sensors, the enhanced bending amplitude at the mechanical resonance frequency can be exploited. Models and readout methods exploiting this resonance are reviewed in [Fie05] and [Nan+08] for bulk magnetoelectric sensors. For the investigated thin-film sensors, a measurement setup and a noise model were presented in [Jah11; Jah+11] which also include shielding measures. A wide range of methods to improve the SNR is available to the system engineer. To increase the gain of receivers for example, regenerative circuits [Arm22] can be used that reinforce the desired signal with the help of a positive feedback. The concept has already been used to improve the signal strength from radio stations after the invention of the Audion and the regenerative receiver [Arm15]. Another example is the parallel measurement of one source with two sensors and averaging of the output signals to increase the SNR. Whereas signal power increases with the square of the number of averages, noise only increases with the number of averages [MC93]. A method to detect low-frequency signals of several Hz was presented in [JKQ11; JKQ12; Gil+11; Pet+11; Jah+12; Jah13; Fet+13] using a magnetic pump signal. By exploiting the nonlinearity of the magnetic ma-

terial the sensor behaves like a frequency mixer (e.g. comparable to a mixer diode) relocating the signal frequency.
The above methods have in common that the charge generation in the piezoelectric layer caused by magnetic field induced deformation of the cantilever is utilised for the readout. In order to determine basic sensor parameters and introduce into the electric sensor behaviour, the direct detection readout method can be utilised which is reviewed in the following section.

2.4 Direct Detection

Direct detection is a standard operation mode for the characterisation of thin-film magnetoelectric sensors.

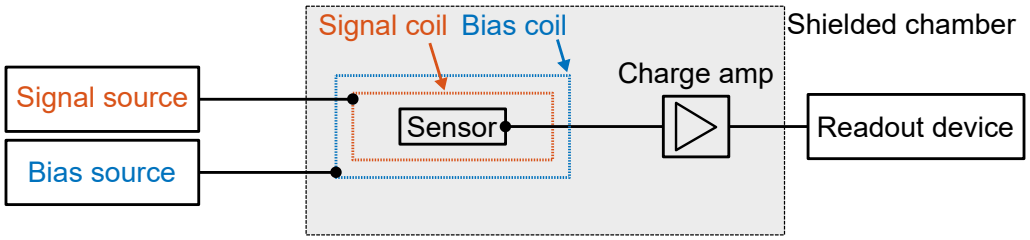

Figure 2.9: Schematic of setup for sensor characterisation by direct detection. Devices inside the shielding chamber are indicated with a grey background.

The signal to be measured B_s is applied via a signal coil as depicted in Fig. 2.9. The signal current is supplied by a Keithley 6221 low noise current source (Keithley 6221, [KE08]). To maximise the output signal, an additional magnetic bias field is applied via a bias coil. The optimal magnetic bias field, where the output voltage V_{ME} is at its maximum, depends on the frequency of the applied signal f_s. A Kepco BOP 20-10ML power source (Kepco, [KE11]) supplies the current required to achieve the bias field.
The sensor output is amplified by a home-made charge amplifier (see Fig. 2.10). The equivalent *voltage* gain of the charge amplifier G_{CA} is given by

$$G_{CA} = \frac{|Z_f|}{|Z_{ME}|}, \tag{2.14}$$

with the impedance of the feedback Z_f and the sensor impedance Z_{ME}. Two batteries supply the charge amplifier with $\pm 12\,\mathrm{V}$ to avoid spurious signals from e.g. a switched-mode power supply. The sensor, the coils, and the charge amplifier are

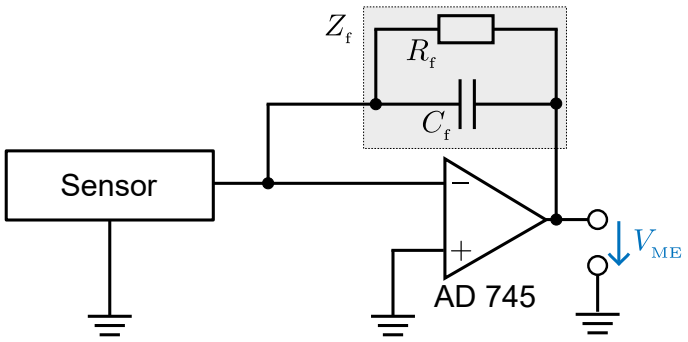

Figure 2.10: Charge amplifier to read out the sensor. The operational amplifier is a AD 745 low noise amplifier [AD02]. The feedback resistance is $R_f = 5\,\mathrm{G\Omega}$, and the feedback capacitance is $C_f = 10\,\mathrm{pF}$, unless specified otherwise.

placed inside a shielded box. The output of the charge amplifier is fed into a read-out receiver, e.g. a Stanford Research lock-in amplifier SR830 (SR830, [SR11]), and digitised. The output signal is processed directly at the frequency of the applied signal f_s.

The LoD versus signal frequency f_s is depicted in Fig. 2.11 for a typical inverse bilayer sensor. For low frequencies from 1 Hz to 100 Hz, the LoD is orders of magnitude higher as compared to the LoD with the signal applied at the resonance frequency $f_s = f_{res}$. Therefore, it is advantageous to operate magnetoelectric sensors at their mechanical resonance frequency. The resonance frequency of a thin-film magnetoelectric sensor depends, amongst others, on the geometric dimensions of the sensor Eq. (2.2). It is inversely proportional to the size of the sensor. Sensors with a resonance frequency below 100 Hz are very large and hence often not practical. An applied magnetic field can shift the resonance frequency by several of Hz. This is called the ΔE_d-effect [Goj+11]. Usually, this effect can be neglected for direct detection for the investigated thin-film sensors with $f_{res} < 2\,\mathrm{kHz}$, mostly due to the high thickness ratio of approximately 350/4 between substrate and magnetostrictive material. The shape of the resonance curve in Fig. 2.11 can be described by a Fano resonance, as mentioned before. Fano resonances feature an antiresonance which can be seen at about 408 Hz for this sensor.

In conclusion, direct detection is not suitable for the measurement of small low frequency signals below 100 Hz. Either the signal frequency is below the resonance and the sensor's LoD is not low enough to detect small signals (c.f. Fig. 2.11), or the sensor is designed to have its f_{res} at the signal frequency, and is therefore impractically large. The lower the detection frequency is chosen, the more dominant

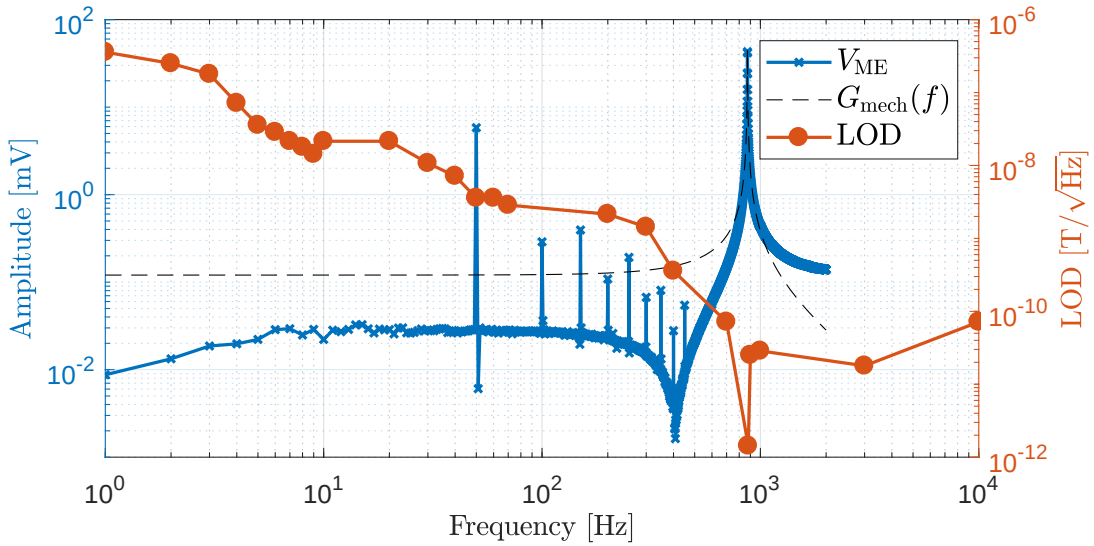

Figure 2.11: Measured LoDs and ME voltage for various frequencies of an inverse bilayer sensor investigated in [Yar+16a]. The applied bias is $B_{opt} = -0.2\,\mathrm{mT}$. The resonance frequency of the sensor is $f_{res} = 872\,\mathrm{Hz}$, where the LoD reaches its minimum of approximately $1.6\,\mathrm{pT}/\sqrt{\mathrm{Hz}}$. The ME voltage reaches its maximum at f_{res}. The peaks at $f = 50\,\mathrm{Hz}$ and its harmonics stem from the mains voltage in the laboratory. The dashed line represents a fit of the frequency response with Eq. (2.3).

are 1/f noise components which degrade the SNR. Bulk laminated ME sensors reach LoDs as small as $5\,\mathrm{pT}/\sqrt{\mathrm{Hz}}$ [Wan+11] in resonance because their active layers have significantly larger volumes (factor 500-8000). For the measurement of low frequency signals, frequency conversion techniques can be utilised (see Sec. 3). However, the LoD in resonance and the ME coefficient provide important benchmarks for the evaluation of the sensor performance and comparison.

The signal strength can be described well with the ME coefficient. But, a low LoD requires not only a high signal amplitude but also low noise in order to achieve a high SNR. In resonance, the dominant noise source is the thermal-mechanical noise [Dur+17c] (see Subsec. 2.5.5).

2.5 Noise

For very sensitive sensors it is essential to understand the individual noise contributions within the system. They can be categorised into internal and external sources. The latter are, for example, airborne or vibrational noise, 50 Hz mains voltage, mo-

bile phone transmission, 16.7 Hz train voltage, environmental magnetic noise, etc. These noise sources are not included in the noise models. Because the measurement setup is sufficiently shielded against electrical, magnetic, vibrational, and airborne coupling from external sources, they can be neglected.

2.5.1 Shielding

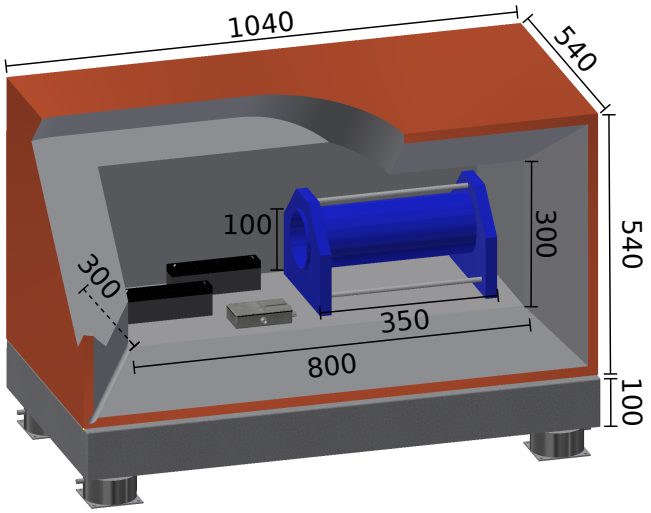

Figure 2.12: Schematic of shielding box with dimensions in mm [Jah13]. The box is placed on top of a heavy cuboid-formed stone plate, which is decoupled from structure-borne noise by four vibration isolators. The inside can be reached via a swinging flap. Inside are two 12 V batteries, a home-made amplifier and a magnetic shielding cylinder.

The utilised shielding box [Jah11] is schematically depicted in Fig. 2.12. The box is made of wood and covered with a copper fleece (*EMC Kupfer-Polyester Vlies Cu-ZFT-NW*) to shield electric fields. The fleece is connected to the common ground of the system. On the inside, acoustic absorber material (*Sonatech Baso Plan G100 SK*) dampens airborne noise. Magnetic fields are rejected by a magnetic shielding cylinder (*Aaronia Null-Gauss-Kammer ZG1*), consisting of 10 layers of µ-metal. The magnetic noise floor inside the cylinder in the low frequency regime is approximately $150\,\mathrm{fT}/\sqrt{\mathrm{Hz}}$ from 10 Hz to 1 kHz (c.f. purple trace in Fig. B.1 in the appendix), which is lower than the noise floor of all magnetoelectric sensors measured in this work. The box is placed on top of a heavy cuboid-formed stone plate, which is situated on a vibration isolator (*Qioptiq Schwingungsisolator S150*) to reduce vibrational coupling.

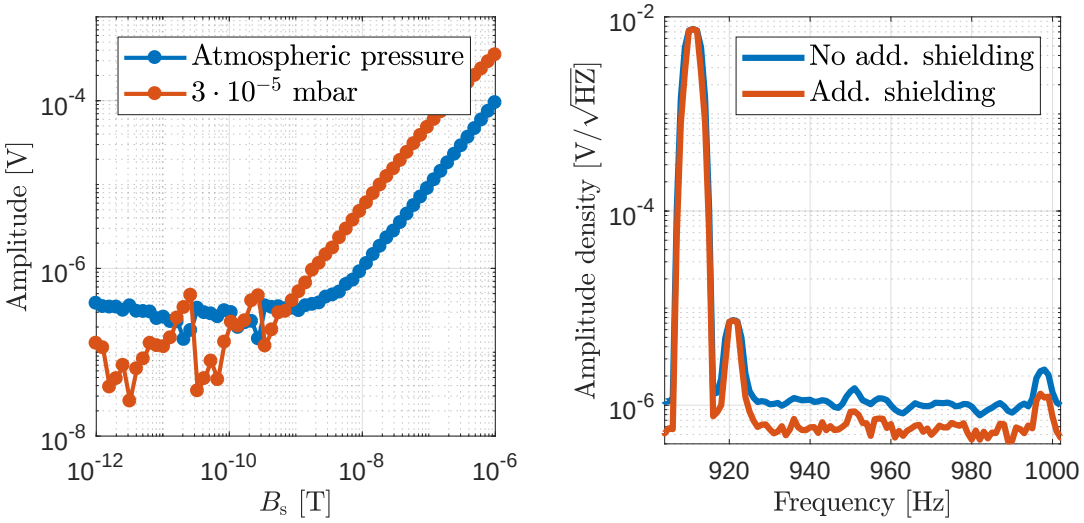

(a) (b)

Figure 2.13: Representative measurements of shielding problems of (a) LoD curves [Kir+13] with a zigzag signal behaviour in the white noise region that stems from insufficient shielding of the sensor against electric fields and (b) spectral densities where the noise floor and spurious signals increase, while the sensor signals remain constant.

However, the shielding against electric fields of the existing setup is not sufficient, which can be seen by artefacts in LoD measurements or increased noise floors in spectral measurements (see Fig. 2.13). In Fig. 2.13b for example a noise model would not fit the measurements, because the higher noise floor is due to grounding issues and device settings. The problem is solved by placing the sensor in an additional grounded aluminium cylinder to shield against electric fields inside the wooden box.
In the following, the box depicted in Fig. 2.12 is referred to as the shielding box.

2.5.2 Noise Units

Noise power of white noise is proportional to the system bandwidth. Therefore, noise voltage is commonly given per square root hertz in order to ensure comparability. It is then called a linear spectral density (LSD) or noise voltage spectral density (NVSD).
The LoD determines whether a signal can be distinguished from the noise floor (SNR=1) or not. Therefore, it has the same unit as the noise. In the literature,

two methods to determine the LoD of magnetoelectric sensors can be found: measurement of the quadratic mean using a lock-in amplifier or measurement of the noise floor. Lock-in amplifiers can detect small signals in noisy environments. The frequency and phase of the wanted signal are fed into the lock-in as reference. This enables the device to convert the measured signal to DC, where a low-pass filter then suppresses all other frequency components. The low-pass filter is characterised by the time constant τ and the low-pass filter order which also determine the ENBW. The LoD is often measured with lock-in amplifiers, e.g. with a Stanford Research SR830 lock-in amplifier with a time constant of $\tau = 1\,\mathrm{s}$ and a filter slope of $24\,\mathrm{dB/oct}$ [Jah11; Lag+12; Jia+12; Jah+13; Kir+13; Pio+13; Sal+16]. This results in an ENBW of $5/(64\,\tau) = 78\,\mathrm{mHz}$, according to the data sheet of the SR830 [SR11]. The output of the lock-in is a RMS value ($\mathrm{Resolution}_{\mathrm{SR830}}$) and not a LSD. In order to convert to a LSD, the results need to be divided by the square root of the ENBW

$$\mathrm{LoD} = \frac{\mathrm{Resolution}_{\mathrm{SR830}}}{\sqrt{\mathrm{ENBW}_{\mathrm{SR830}}}}. \tag{2.15}$$

In publications that state the resolution with units per square root hertz, the LoDs are a factor ≈ 3.6 too small for the above reasons. For the correct units refer to Tab. 2.2. In this work, the LoD is given in $\mathrm{T}/\sqrt{\mathrm{Hz}}$.
In general, the linear spectrum can be calculated from the LSD by multiplication with the square root of the ENBW

$$\mathrm{LS} = \mathrm{LSD} \cdot \sqrt{\mathrm{ENBW}}. \tag{2.16}$$

In Eq. (2.15), the LoD is a LS or a resolution.

2.5.3 Sensor Noise Sources

The magnetoelectric sensor has several internal noise sources. All dissipative elements contribute noise to the system as described by the fluctuation-dissipation theorem [CW51].
Fig. 2.14 shows the noise ECD of a magnetoelectric sensor. A fundamental noise source in electrical systems is the thermal (also called Johnson or Nyquist) noise [Joh28; Nyq28]. Every resistor yields a measurable thermal-electrical noise. The complex impedance $Z(\omega)$ with its real part $R(\omega)$ is given by

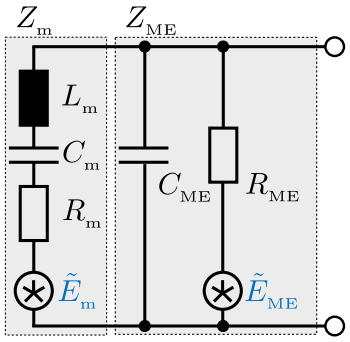

Figure 2.14: Noise ECD of of a magnetoelectric sensor. The voltage noise sources $\tilde{E}_{\mathrm{m}}$ and $\tilde{E}_{\mathrm{ME}}$ are marked with stars within a circle and blue labels.

$$
\begin{aligned}
Z(\omega) =& \frac{R}{1 + j\omega RC_{\mathrm{p}}} \\
=& \frac{R(1 - j\omega RC_{\mathrm{p}})}{(1 + j\omega RC_{\mathrm{p}})(1 - j\omega RC_{\mathrm{p}})}) \\
=& \underbrace{\frac{R}{1 + (\omega RC_{\mathrm{p}})^2}}_{R(\omega)} - j\frac{R^2\omega C_{\mathrm{p}}}{1 + (\omega RC_{\mathrm{p}})^2} \\
=& R(\omega) + jX(\omega),
\end{aligned}
\tag{2.17}
$$

with a resistance R in parallel with a capacitance C_{p}. The real part of the impedance $R(\omega)$ is a function of the frequency. All resistors have a capacitor in parallel with a non-null capacitance. Also, they have a dielectric constant $\varepsilon_{\mathrm{r}} \neq 0$ and a conductivity $\kappa \neq 0$ between their terminals. The dielectric relaxation time τ_{D} is

$$
\tau_{\mathrm{D}} = \frac{\varepsilon}{\kappa} = R \cdot C_{\mathrm{int}}, \tag{2.18}
$$

with the permittivity $\varepsilon = \varepsilon_{\mathrm{r}}\varepsilon_0$ and the intrinsic capacitance $C_{\mathrm{int}} \neq 0$ [MH03]. In vacuum, the permittivity is $\varepsilon = \varepsilon_{\mathrm{r}}\varepsilon_0 = 1 \cdot \varepsilon_0$, whereas in other materials the relative permittivity is $\varepsilon_{\mathrm{r}} \neq 1$. The capacitance C_{p} mainly consists of the stray capacitance and the intrinsic capacitance. The mean square voltage noise of a resistance is given by (see e.g. [MC93])

$$
< \hat{v}_{\mathrm{n}}^2(t) >= \frac{k_{\mathrm{B}}T}{C_{\mathrm{p}}}, \tag{2.19}
$$

with $< \ldots >$ denoting the mean value and the Boltzmann constant k_{B}.

The linear spectral noise density $\tilde{E}_{\mathrm{R}}$ of a resistor can be calculated by [Nyq28]

$$\tilde{E}_{\mathrm{R}} = \sqrt{4k_{\mathrm{B}}TR}, \tag{2.20}$$

with the temperature of the resistance T and its resistance R. The tilde indicates a spectral density. It is referred to a bandwidth of $\Delta f = 1\,\mathrm{Hz}$. From Johnson's [Joh28] and Nyquist's publications, it can be deduced that Eq. (2.20) is an approximation and would contain the real resistance $R(\omega)$ deduced above in order to describe $\tilde{E}_{\mathrm{R}}$ without loss of generality. In the following, only the pure resistance R will be taken into account in accordance with the commonly accepted engineering theory.
The piezoelectric layer and the equivalent resistance for the mechanical loss exhibit noise according to Eq. (2.20). With Eq. (2.10), the voltage noise density of the piezoelectric loss is given by

$$\tilde{E}_{\mathrm{ME}} = \sqrt{4k_{\mathrm{B}}TR_{\mathrm{ME}}}. \tag{2.21}$$

For mechanical resonators, the ultimate noise limit is the thermal-mechanical noise [MNK10]. It is preferable to minimise the size of sensors for further integration. However, the smaller movable parts of a sensor are, the more susceptible are they to mechanical noise originating from molecular agitation [Gab93]. If thermal-mechanical noise can be visualised with the random movement due to the impact of very small particles or atoms, this is intuitively comprehensible because a smaller sensor size decreases the aspect ratio. According to [Rie+97], thermal-mechanical noise becomes more pronounced the smaller the dimensions of a cantilever beam are.
In [Dur+17c], the thermal-mechanical noise for thin-film magnetoelectric sensors is investigated. A dissipative MEMS can be described by the differential equation for a damped mechanical oscillator

$$m\frac{d^2z}{dt^2} + R_{\mathrm{mech}}\frac{dz}{dt} + kz = f_{\mathrm{f}}(t), \tag{2.22}$$

with the mass m, the spring constant k, the mechanical resistance R_{mech}, the displacement z, and the fluctuating force f_{f}.
The movement of the sensor is damped by the surrounding medium, as well as by internal dissipation on the surface and in the volume [Dju00]. Exchange of energy must be bidirectional according to the fluctuation-dissipation theorem. For measurements of magnetic fields, the path from fluctuation of the viscose environment and dissipation within the structure of the sensor is of interest because it results in

a measurable noise voltage at the output of the sensor. In analogy to the spectral noise density of a resistor in Eq. (2.20), the linear spectral density of the fluctuating force $\tilde{F}$ is given by

$$\tilde{F} = \sqrt{4k_{\mathrm{B}}TR_{\mathrm{mech}}}. \tag{2.23}$$

The mechanical resistance R_{mech} and the spring constant of a rectangular beam k [Wal+96] can be calculated by

$$R_{\mathrm{mech}} = \frac{k}{2\pi f_{\mathrm{res}} \cdot Q}. \tag{2.24}$$

and

$$k = \frac{E_{\mathrm{d,cant}} w_{\mathrm{cant}}}{4} \left(\frac{t_{\mathrm{cant}}}{l_{\mathrm{cant}}}\right)^3, \tag{2.25}$$

with the elastic modulus $E_{\mathrm{d,cant}}$, the width w_{cant}, the thickness t_{cant}, and the length l_{cant} of a cantilever. The frequency response of a damped mechanical oscillator introduced in Sec. 2.2 shapes the white spectrum of $\tilde{F}$ according to Eq. (2.3). This leads to the linear deflection noise density [Gab93]

$$\tilde{D}(f) = k^{-1}\tilde{F}G_{\mathrm{mech}}(f). \tag{2.26}$$

In the mechanical resonance, Eq. (2.26) becomes

$$\tilde{D}(f_{\mathrm{res}}) = \sqrt{\frac{4k_{\mathrm{B}}TQ}{2\pi f_{\mathrm{res}} k}}. \tag{2.27}$$

For magnetoelectric sensors, the deflection noise can be transformed to an equivalent electric noise because a deflection produces a voltage at the terminals of the sensor. The conversion is in agreement with measurements [Dur+17c].
The displacement noise before the mechanical resonator is proportional to the inverse of the square root of the quality factor

$$\frac{\tilde{D}(f)}{G_{\mathrm{mech}}} \propto \frac{1}{\sqrt{Q}}. \tag{2.28}$$

For an electrical equivalent circuit of the displacement noise, the ECD in Fig. 2.7 contains the equivalent quantities R_{m}, L_{m}, and C_{m} of the mechanical part (index $_{\mathrm{m}}$) [Dur+17c].

These parameters can be obtained by the measurement of the sensor impedance versus frequency. The impedance measured (index $_{\text{meas}}$) at the terminals of the sensor is given by [Jah13; Sal+17b]

$$\begin{aligned} Z_{\text{meas}} &= Z_{\text{m}} \parallel Z_{\text{ME}} \\ &= R_{\text{meas}} + j\, X_{\text{meas}} \\ &= \frac{1}{\omega C_{\text{meas}} \tan\delta_{\text{meas}}} - j\frac{1}{\omega C_{\text{meas}}}, \end{aligned} \tag{2.29}$$

with the loss tangent $\tan\delta$ and $\parallel$ denoting a parallel circuit.
At $f = f_{\text{res}}$, the reactive components compensate each other and the measured capacitance stems only from the piezoelectric layer (index $_{\text{ME}}$)

$$C_{\text{ME}} = C_{\text{meas}}(f_{\text{res}}), \tag{2.30}$$

Far above the resonance frequency ($f \gg f_{\text{res}}$), the loss from the piezoelectric layer is dominant

$$\tan\delta_{\text{ME}} = \tan\delta_{\text{meas}}(f \gg f_{\text{res}}). \tag{2.31}$$

The mechanical loss can then be obtained by subtracting the piezoelectric loss from the measured loss at f_{res}

$$\tan\delta_{\text{m}} = \tan\delta_{\text{meas}} - \tan\delta_{\text{ME}}. \tag{2.32}$$

The parameters of the equivalent circuit can be calculated by

$$R_{\text{m}} = \frac{1}{2\pi\, f_{\text{res}}\, C_{\text{ME}} \tan\delta_{\text{meas}}(f_{\text{res}})}, \tag{2.33}$$

$$C_{\text{m}} = \frac{C_{\text{ME}} \tan\delta_{\text{meas}}(f_{\text{res}}) \left[f_{\text{up}}^2 - f_{\text{res}}^2\right]}{f_{\text{res}}^2} \tag{2.34}$$

with the frequency f_{u} of the upper extreme value of C_{meas} and

$$L_{\text{m}} = \frac{1}{(2\pi)^2 C_{\text{ME}} \tan\delta_{\text{meas}}(f_{\text{res}}) \left[f_{\text{up}}^2 - f_{\text{res}}^2\right]}. \tag{2.35}$$

The resulting voltage noise density from the mechanical loss is given by

$$\tilde{E}_{\mathrm{m}} = \sqrt{4k_{\mathrm{B}}TR_{\mathrm{m}}} \tag{2.36}$$

2.5.4 Signal Processing Noise

The involved circuits for the signal processing such as amplifiers contribute noise. Being a two port, the noise of an amplifier can be modelled with two equivalent noise sources, e.g. a voltage noise source in series and a current noise source in parallel at its input [MC93].

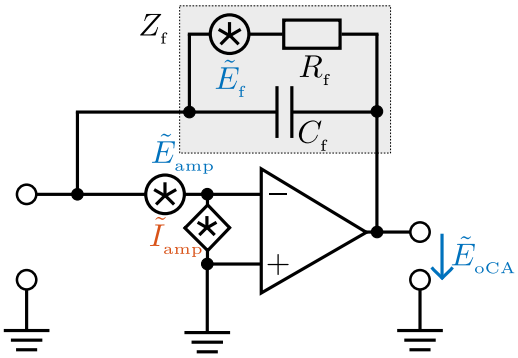

Figure 2.15: Noise ECD of the charge amplifier. The feedback impedance contributes a noise source $\tilde{E}_{\mathrm{f}}$. Current noise sources are marked with a star in a diamond and red labels. The total noise voltage density of the charge amplifier at its output is $\tilde{E}_{\mathrm{oCA}}$.

Fig. 2.15 depicts the noise ECD of a charge amplifier used for readout. The noise voltage of the feedback impedance is

$$\tilde{E}_{\mathrm{f}} = \sqrt{4k_{\mathrm{B}}TR_{\mathrm{f}}}. \tag{2.37}$$

The values for the voltage and current noise sources can be approximately deduced from the datasheet of the operational amplifier with limited accuracy. However, the values are often only given for specific frequencies or operational modes. For the charge amplifier setup, they can be measured by altering the capacitance on the input in such a way, that either the voltage noise or the current noise becomes dominant. For the AD745, the measured noise densities are $\tilde{E}_{\mathrm{amp}} = 3\,\mathrm{nV}/\sqrt{\mathrm{Hz}}$ and $\tilde{I}_{\mathrm{amp}} = 6.5\,\mathrm{fA}/\sqrt{\mathrm{Hz}}$, respectively.

Other noise sources contributed by the signal processing are circuit quantisation noise of an analogue-to-digital converter (ADC), noise from lossy connecting cables, noise from batteries, and noise from the signal and bias sources. Quantisation noise from an ADC $\tilde{E}_{\mathrm{oQuant}}$ at the output of the charge amplifier (index $_{\mathrm{o}}$) of course depends on the type of converter and its operating point. An important parameter for the quantisation noise is the dynamic range (DR). It determines the range between the strongest and weakest signal. The available quantisation bits are distributed over the dynamic range. In the presence of a very strong signal, a weak signal can only be quantised with a limited number of bits. Most readout devices feature an internal adaptive amplifier that ensures a full scale input signal to the ADC. Quantisation noise can be measured at a reference channel with the same settings as the signal channel but having a short-circuit at its input.

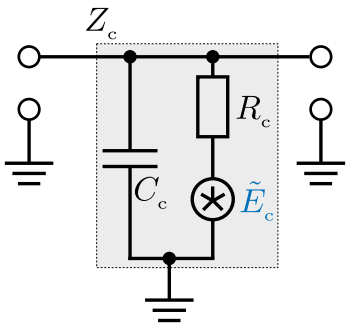

Figure 2.16: Noise ECD of a coaxial cable.

Noise from the connecting cables can be modelled as the noise from a parallel circuit of a resistor R_{c} and capacitor C_{c}. An ECD for a cable is depicted in Fig. 2.16. The equivalent voltage noise of the cable $\tilde{E}_{\mathrm{c}}$ is then

$$\tilde{E}_{\mathrm{c}} = \sqrt{4k_{\mathrm{B}}TR_{\mathrm{c}}}. \tag{2.38}$$

Because the dielectric of the cable is often polythene with a $\tan\delta < 0.0005$ and a typical capacitance of $100\,\mathrm{pF/m}$, $\tilde{E}_{\mathrm{c}}$ is relatively small and can often be neglected. Possible noise from the signal source and bias source can be described as a voltage noise sources at the coil (see Fig. 2.9). However, these sources are only present during characterisation and are not dominant. For sensitive measurements, the bias field is supplied by batteries whose noise contribution is negligible.

2.5.5 System Noise

An important figure of merit is the signal to noise ratio at the output of the sensor system, including the sensor plus the signal processing electronic circuit. All individual noise contributions can be translated to the output using a transfer function. The noise sources investigated in this work are treated as if they were not correlated, since they originate from different physical sources. The total system noise $\tilde{E}_{\mathrm{total}}$ can be calculated by adding the power of i contributing noise sources (cf. e.g. [MC93])

$$\tilde{E}_{\mathrm{total}} = \sqrt{(\tilde{E}_{1})^2 + (\tilde{E}_{2})^2 + \ldots + (\tilde{E}_{\mathrm{i}})^2}. \tag{2.39}$$

Using the equivalent circuit of the signal processing chain, transfer functions for all noise sources are calculated. The impedances of the cable and the feedback network are given by

$$Z_{\mathrm{i}} = \frac{1}{\frac{1}{R_{\mathrm{i}}} + j\omega C_{\mathrm{i}}}, \quad i \in \{\mathrm{c,f}\}. \tag{2.40}$$

The parallel circuit formed by the resonant branch, the piezoelectric layer, and the cable is given by

$$Z_{\mathrm{mMEc}} = Z_{\mathrm{m}} \parallel Z_{\mathrm{ME}} \parallel Z_{\mathrm{c}}. \tag{2.41}$$

With (2.9) and (2.8), the individual equivalent noise contributions at the output of the charge amplifier are:

$$\tilde{E}_{\mathrm{oampV}} = \left| 1 + \frac{Z_{\mathrm{f}}}{Z_{\mathrm{mMEc}}} \right| \cdot \tilde{E}_{\mathrm{amp}} \tag{2.42}$$

$$\tilde{E}_{\mathrm{oampI}} = |Z_{\mathrm{f}}| \cdot \tilde{I}_{\mathrm{amp}} \tag{2.43}$$

$$\tilde{E}_{\mathrm{of}} = \frac{1}{\sqrt{1 + (\omega C_{\mathrm{f}} R_{\mathrm{f}})^2}} \cdot \sqrt{4k_{\mathrm{B}} T R_{\mathrm{f}}} \tag{2.44}$$

$$\tilde{E}_{\mathrm{oME}} = \frac{|Z_{\mathrm{ME}}|}{R_{\mathrm{ME}}} \cdot G_{\mathrm{CA}} \cdot \sqrt{4k_{\mathrm{B}} T R_{\mathrm{ME}}} \tag{2.45}$$

$$\tilde{E}_{\mathrm{oc}} = \frac{|Z_{\mathrm{ME}}|}{R_{\mathrm{c}}} \cdot G_{\mathrm{CA}} \cdot \sqrt{4k_{\mathrm{B}} T R_{\mathrm{c}}} \tag{2.46}$$

$$\tilde{E}_{\mathrm{om}} = \frac{|Z_{\mathrm{f}}|}{|Z_{\mathrm{m}}|} \cdot \sqrt{4k_{\mathrm{B}}TR_{\mathrm{m}}} \tag{2.47}$$

where $\tilde{E}_{\mathrm{oampV}}$ means the output referred (index $_{\mathrm{o}}$) voltage noise of the amplifier, $\tilde{E}_{\mathrm{oampI}}$ is the current noise of the amplifier, $\tilde{E}_{\mathrm{of}}$ is the noise from the feedback resistance, $\tilde{E}_{\mathrm{oME}}$ that of the piezoelectric layer of the sensor, $\tilde{E}_{\mathrm{oc}}$ the contribution of the cable to the amplifier, and $\tilde{E}_{\mathrm{om}}$ the noise contribution from the loss of the mechanical resonator. A derivation of the formulas is given in Sec. A in the appendix. The total output noise is then determined as

$$\tilde{E}_{\mathrm{o}} = \sqrt{\tilde{E}^2_{\mathrm{oEn}} + \tilde{E}^2_{\mathrm{oIn}} + \tilde{E}^2_{\mathrm{of}} + \tilde{E}^2_{\mathrm{oME}} + \tilde{E}^2_{\mathrm{oc}} + \tilde{E}^2_{\mathrm{om}} + \tilde{E}^2_{\mathrm{oQuant}}}. \tag{2.48}$$

It is common to reassign this noise density to an equivalent noise source at the input of the charge amplifier which is obtained by dividing the equivalent output noise by the gain G_{CA}.

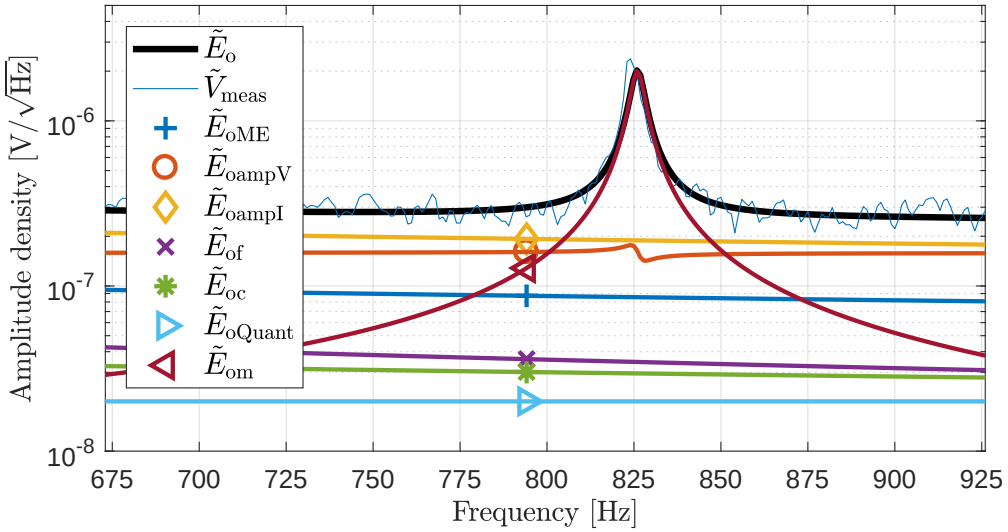

Figure 2.17: Exemplary noise calculation for direct detection near the resonance frequency. The reference measurement is conducted without any excitation.

In Fig. 2.17 the result of the presented noise model is shown for a typical multilayer sensor followed by an AD745 charge amplifier. The calculated total output noise fits the measurement quite well. At the resonance frequency, the thermal-mechanical noise dominates the system. It limits the LoD for direct detection. Towards lower

frequencies, the current noise $\tilde{I}_{\mathrm{amp}}$ dominates (not visible in Fig. 2.17), whereas towards higher frequencies, excluding the region around the resonance frequency, the voltage noise of the amplifier $\tilde{E}_{\mathrm{amp}}$ yields the highest contribution. Noise from the cable, the feedback network, and the readout device can be neglected.
With this noise model, individual noise contributions can be calculated and dominant sources can be identified. Thermal-mechanical noise is identified as the dominant internal noise source for direct detection.
In resonance, the thermal mechanical noise at the output is given by

$$\tilde{E}_{\mathrm{om}}(f_{\mathrm{res}}) = \frac{\frac{1}{\sqrt{\frac{1}{R_{\mathrm{f}}}^2+(\omega C_{\mathrm{f}})^2}}}{\sqrt{\frac{1}{2\pi\, C_{\mathrm{ME}} \tan\delta_{\mathrm{meas}}(f_{\mathrm{res}})}}} \cdot \sqrt{4k_{\mathrm{B}}T}. \tag{2.49}$$

because the reactive components of the mechanical equivalent circuit cancel out at resonance [Sal+17b]. According to Eq. (2.49), a reduction of the sensor capacitance $C_{\mathrm{ME}} = C_{\mathrm{meas}}(f_{\mathrm{res}})$ and its loss tangent $\tan\delta_{\mathrm{meas}}(f_{\mathrm{res}})$ reduces the thermal-mechanical noise at the output of the measurement system using a charge amplifier. The sensor capacitance depends on the electrode design and the loss tangent mainly on the chosen material, mechanical clamping, and viscous environment. The impact of thermal-mechanical noise on the SNR can be reduced by vacuum encapsulation [Kir+13] due to the higher Q-factor. Fig. 2.13a exemplarily shows the increased sensitivity due to vacuum operation.
The SNR in resonance for dominant thermal-mechanical noise is given by

$$\mathrm{SNR}(f_{\mathrm{res}}) = \frac{S(f \ll f_{\mathrm{res}}) \cdot G_{\mathrm{mech}}(f_{\mathrm{res}}) \cdot B_{\mathrm{s}} \cdot G_{\mathrm{CA}}(f_{\mathrm{res}})}{\tilde{E}_{\mathrm{om}}(f_{\mathrm{res}})\sqrt{\Delta f}}. \tag{2.50}$$

Eq. (2.50) can be rewritten as (derivation in Sec. A in the appendix)

$$\mathrm{SNR}_{\mathrm{tm}}(f_{\mathrm{res}}) = \frac{S(f \ll f_{\mathrm{res}}) \cdot B_{\mathrm{s}}}{\sqrt{4k_{\mathrm{B}}T}\sqrt{\Delta f}} \sqrt{\frac{2\pi\, f_{\mathrm{res}}^5\, C_{\mathrm{ME}}(1+\tan\delta_{\mathrm{ME}}^2)}{\tan\delta_{\mathrm{meas}}(f_{\mathrm{res}})\left[f_{\mathrm{up}}^2 - f_{\mathrm{res}}^2\right]^2}}. \tag{2.51}$$

An increase of the sensor capacitance C_{ME} and sensor loss tangent $\tan\delta_{\mathrm{ME}}$ increases the $\mathrm{SNR}_{\mathrm{tm}}$ and lowers the LoD for the case of dominant thermal-mechanical noise. The loss in resonance $\tan\delta_{\mathrm{meas}}(f_{\mathrm{res}})$ should be as low as possible for a low LoD.
A reduction of the mechanical loss or increase of the mechanical quality factor can be achieved by several approaches, which are: an adapted resonator geometry and

Parameter	First mode	Second mode
Resonance frequencies	$f_{\mathrm{res},1} = 859\,\mathrm{Hz}$	$f_{\mathrm{res},2} = 5297\,\mathrm{Hz}$
Quality factor	467	122
Sensitivity	$314\,\mathrm{V/T}$	$7.4\,\mathrm{V/T}$
LoD	$51\,\mathrm{pT}/\sqrt{\mathrm{Hz}}$	$896\,\mathrm{pT}/\sqrt{\mathrm{Hz}}$

Table 2.3: Properties of the investigated multilayer sensor. The sensor capacitance is 578 pF and the top electrode is 7 mm long. The layout and fabrication is similar to that of the sensor described in Tab. 3.5 in Subsec. 3.1.7.

mechanical clamping for each respective resonant mode e.g. to exploit the stress distribution better, vacuum encapsulation, prevention of eddy currents e.g. by appropriate layering, thinner substrates, etc.

Another alternative to reduce the thermal-mechanical noise is to operate the sensor at higher frequencies. For a standard multilayer sensor, the resonance frequency $f_{\mathrm{res},2}$ of the second mode is approximately by a factor 6.2 higher than the first mechanical resonance frequency $f_{\mathrm{res},1}$. For the investigated sensor, the second resonance has a higher bandwidth, a lower quality factor, and less sensitivity.

Tab. 2.3 summarises the characteristics of an exemplary measured multilayer sensor. The respective resonance and noise measurements are depicted in Fig. B.2 in the appendix. For noise measurement at $f_{\mathrm{res},2}$, the AD745 charge amplifier is replaced by a special low-noise amplifier having a junction gate field-effect transistor (JFET) pre-stage [Dur+17b] that has lower wideband noise at higher frequencies. At $f_{\mathrm{res},2}$, the noise due to thermal-mechanical noise is a factor 5 less at the output of the charge amplifier as compared to $f_{\mathrm{res},1}$. With a decreased dominant noise contribution, the LoD is expected to decrease for the second resonance frequency. Unfortunately, the sensitivity decreases even more resulting in a worse LoD for $f_{\mathrm{res},2}$. Nevertheless, there are certain advantages at higher resonant frequencies: Higher bandwidth, lower thermal-mechanical noise, less susceptibility for acoustic interferences. In order to increase the sensitivity, the sensor electrodes need to be arranged according to the stress distributions of the respective bending modes [Zab+16].

The preceding sections introduced the ME effect, thin-film ME sensors, and their application in a direct detection scheme as well as the involved noise sources. In case of dominant thermal-mechanical noise, the SNR is closely related to the Q-factor. Therefore, it is attempted to enhance the Q-factor by using a closed loop detection circuit in the next section.

2.6 Closed Loop Detection

For direct detection, the thermal-mechanical noise is the limiting noise source. From Eq. (2.28) it is known that the thermal-mechanical noise scales with the square root of the Q-factor, whereas the signal scales linearly with it. An increase in Q should consequently enhance the SNR.
The sensor can be described as a resonant circuit with dissipative processes. Its transfer function is given by Eq. (2.3). In resonance, Eq. (2.3) simplifies to Q.

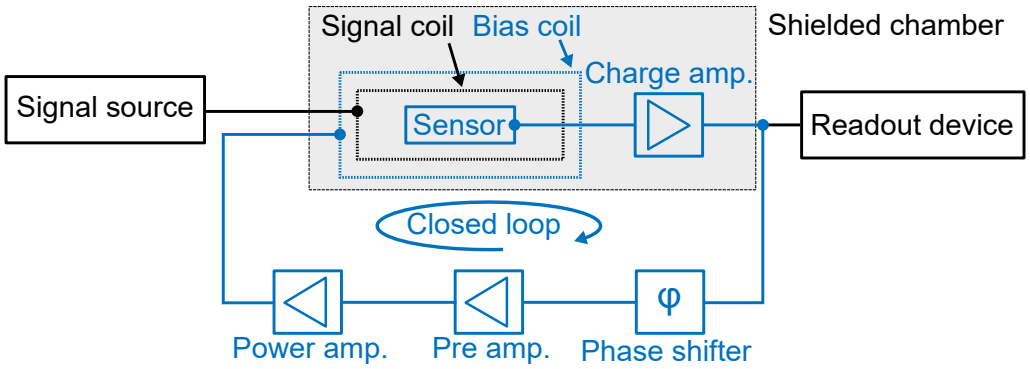

Figure 2.18: Schematic of the closed loop setup for Q-factor enhancement. The path of the closed loop is marked with blue. Devices inside the shielding chamber are indicated by the grey background.

The Q-factor can be increased by operating the magnetoelectric sensor in a closed loop acting as a regenerative circuit as depicted in Fig. 2.18. This circuit can be described by a positive-feedback structure (see e.g. [SS04]). It has been used for the reception of amplitude modulated signals in radios. To form a closed loop, the signal voltage behind the charge amplifier is fed back into the chain of a phase shifter, a pre amplifier, a power amplifier, and eventually fed back in phase into the signal path in front of the sensor via the bias coil of the measurement system. The phase shifter is required to compensate for the phase shift the signal suffers from the sensor and the charge amplifier. In order to obtain positive feedback, the phase has to be set to an integral multiple of 2π referred to the phase of the signal. Via the pre-amplifier, the loop gain is set. Mathematically this can be described by a positive-feedback loop with the transfer function

$$A_{\mathrm{f}}(s) = \frac{A(s)}{1 + A(s)\,\gamma(s)} \tag{2.52}$$

where the feedback-gain is A_f, the gain of the two-port is A, the feedback factor is γ, and s means the complex angular frequency.

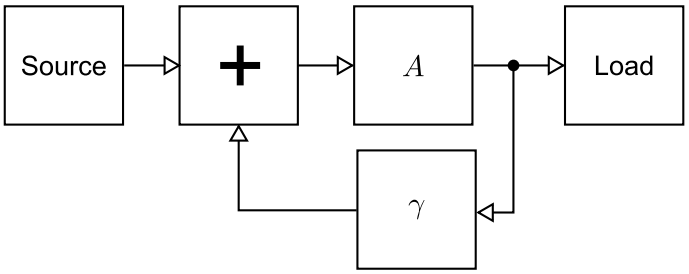

Figure 2.19: Schematic of a positive-feedback loop.

Fig. 2.19 shows a block diagram of the positive-feedback loop which corresponds to the schematic of Fig. 2.18. The quantity $A \cdot \gamma$ is called the loop gain. If the denominator becomes zero at a specific frequency, the oscillation criterion is met and the circuit starts to oscillate. If the loop gain exceeds minus one, the oscillations will grow until it is limited by e.g. the charge amplifier and the loop gain drops again to minus one. In the present case, the loop gain must be kept just to somewhat less than minus one in order to prevent self-oscillation of the loop and to obtain a high Q-factor.

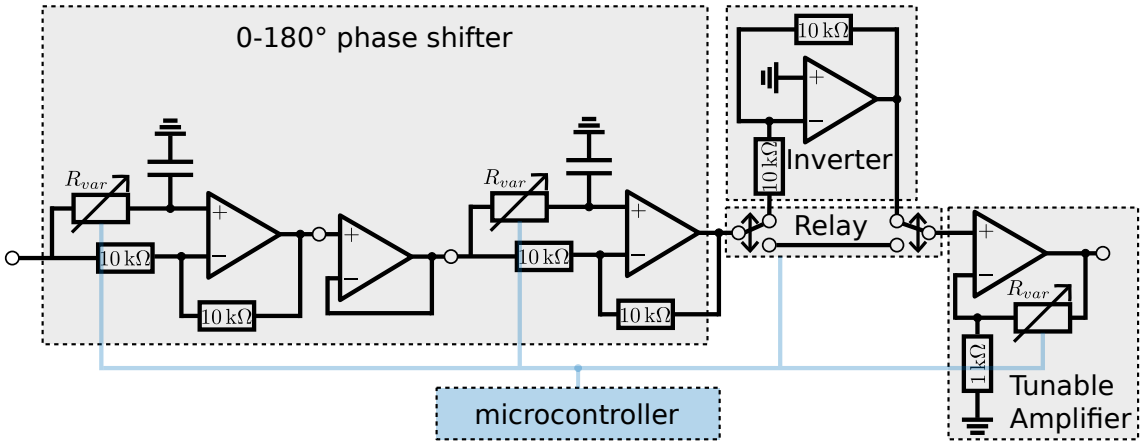

Figure 2.20: Phase shifter circuit.

The phase shifter is designed as a concatenation of analogue, active all-pass filters controlled by a microcontroller (see Fig. 2.20). Each all-pass filter shifts the phase to a maximum of 90° degrees by varying the resistor R_{var}. The concatenation of two of those filters then results in a shifting range of $0-180°$ degrees. The following inverter finally allows 360° degrees of phase shift and is optionally inserted into the signal

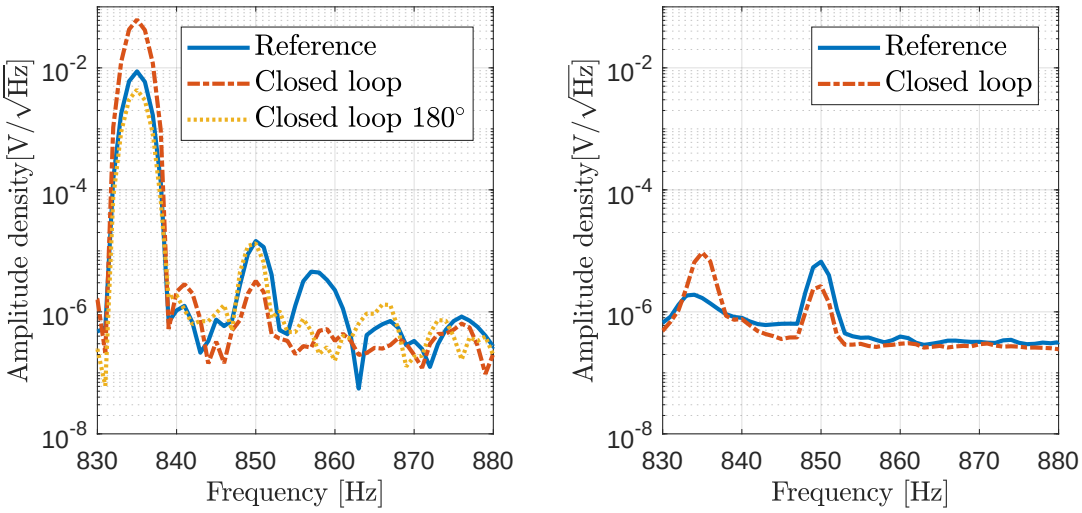

Figure 2.21: Results of the closed loop setup. (a) Amplitude densities for standard direct detection (reference), closed loop operation with optimal phase setting, and closed loop operation with 180° phase relative to the signal phase. The applied signal $B_s = 100\,\mathrm{nT}$ is applied in the mechanical resonance of the sensor $f_{res} = 835\,\mathrm{Hz}$. The bias is set to $B_{opt} = 0.94\,\mathrm{mT}$. (b) Amplitude densities for standard direct detection (reference) and closed loop operation without excitation or working point settings. The measurement is averaged 100 times to reduce the variance.

path by a relay switch. The phase shift characteristic is not linear, i.e. small shifts are more precise. The last stage is a tuneable amplifier to provide pre-amplification. The power amplifier converts the output voltage into a current to drive the bias coil. The phase angle and amplification factor are determined by an iterative algorithm that alters the single stages consecutively maximising the signal in resonance. The algorithm continues until either a specified number of repetitions is reached or the amplitude increase is below a set threshold. With the loop closed and phase and amplification settings determined automatically, the signal at resonance increases by a factor of ≈ 6 (see Fig. 2.21a) as compared to a standard direct detection (reference). The utilised sensor is a standard multilayer sensor. If the phase is inverted, the signal at f_{res} decreases as a result of destructive interference. The noise in resonance increases by a factor of ≈ 5.5 (c.f. Fig. 2.21b).
The Q-factor can be determined from the resonance curve as explained in Sec. 2.2. In Fig. 2.22, the resonance curves for the three settings of Fig. 2.21a are depicted. The Q-factor of the closed loop increases by a factor of 6 and decreases for the closed

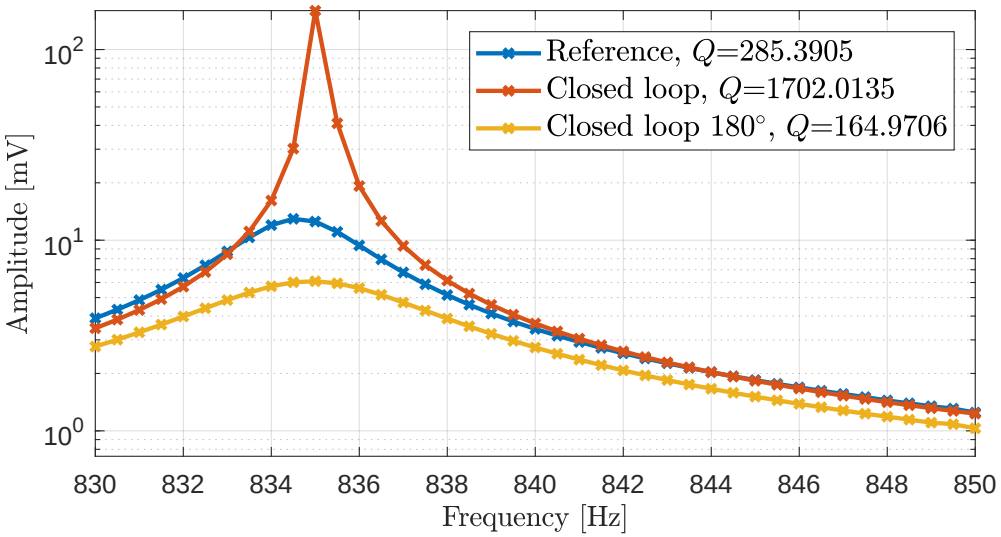

Figure 2.22: Resonance curves for the three cases from Fig. 2.21a. The Q-factor of the curves is given in the legend.

loop with 180° phase shift. This nearly complies with the change in signal strength in Fig. 2.21a and confirms that the signal scales with Q. The noise should scale with the square root of Q if it was thermal-mechanical noise. Therefore, additional noise must be due to the circuitry in the feedback loop.

In conclusion, the Q-factor and the signal B_s can be increased with positive feedback. However, the SNR cannot be significantly improved with the current setup because the noise also increases with Q at virtually the same rate.

As a side effect and hitherto not applied approach, the closed loop can also be used to measure low-frequency signals. If the phase and gain settings of the setup in Fig. 2.18 are set in order to induce self-oscillation of the loop, the resonator begins to oscillate in its resonance frequency without further excitation. It can then act as a self-oscillating mixer. According to Eq. (2.52), the loop gain must be equal or exceed minus one. The amplitude growth can be intentionally constrained with a limiter circuit, which can be realised through the insertion of a amplitude dependent resistor such as a Schottky diode. Application of a low-frequency signal B_s, e.g. at $f_s = 10\,\mathrm{Hz}$, then leads to sidebands that are linearly dependent on B_s.

Fig. 2.23 shows measured spectral densities for two scenarios. The sidebands are located at the same frequency offset from the resonance frequency and their amplitudes are equal. The solid line depicts uncontrolled self-oscillation and application of a desired signal with $B_s = 10\,\mu\mathrm{T}$. Due to the self-oscillation, the noise floor is increased

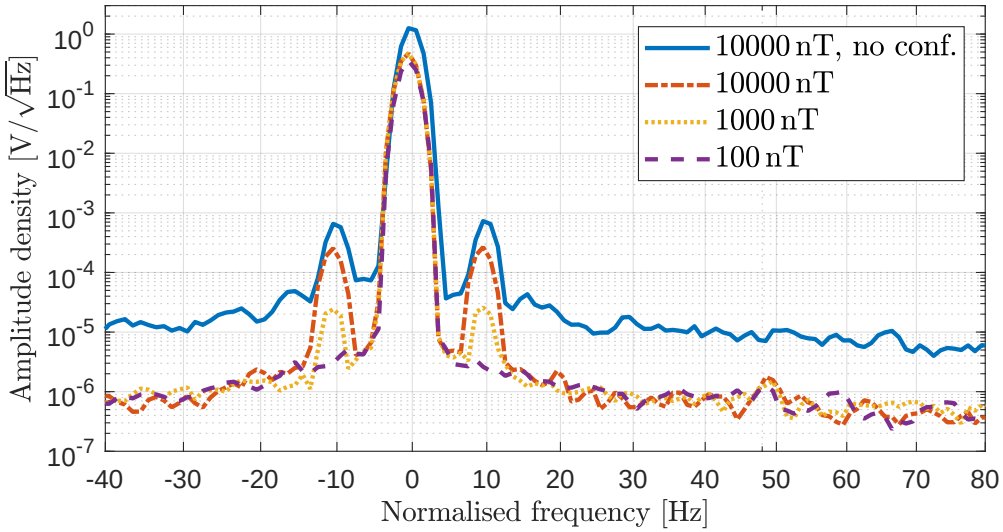

Figure 2.23: Spectral densities of 10 Hz measurement with a self-oscillating ME sensor. For the solid trace the maximum oscillation amplitude is not confined (no conf.). For the other measurements, the amplitude is constrained with a limiter circuit. The frequency axis is normalised to the resonance frequency $f_{\mathrm{res}} = 852\,\mathrm{Hz}$ of the utilised standard multilayer cantilever.

considerably from approximately $400\,\mathrm{nT}/\sqrt{\mathrm{Hz}}$ up to $40\,\mu\mathrm{T}/\sqrt{\mathrm{Hz}}$ at $f_{\mathrm{res}} + 10\,\mathrm{Hz}$. If the maximum amplitude is confined, the noise floor increases less and smaller desired signals can be measured. In Fig. 2.23, the self-oscillation is confined such that the oscillation just does not cease. The sideband amplitude is lowered by the confinement as well, but the SNR is still increased as compared to the non-oscillating case. However, even if there was no noise increase and the noise floor was determined by the thermal-mechanical noise or the voltage noise of the amplifier, respectively, the smallest detectable signal would be 10 nT, assuming linear behaviour. This is also due to the missing resonance enhancement of the sidebands intrinsic to this method. Therefore, this approach is not further pursued.

2.7 Tuning Fork

The investigated sensors are very susceptible to air- and structure-borne noise because their resonance frequency lies in the low-frequency region around $f \approx 1\,\mathrm{kHz}$. At practical applications, it is not always possible to conduct measurements in well shielded environments.

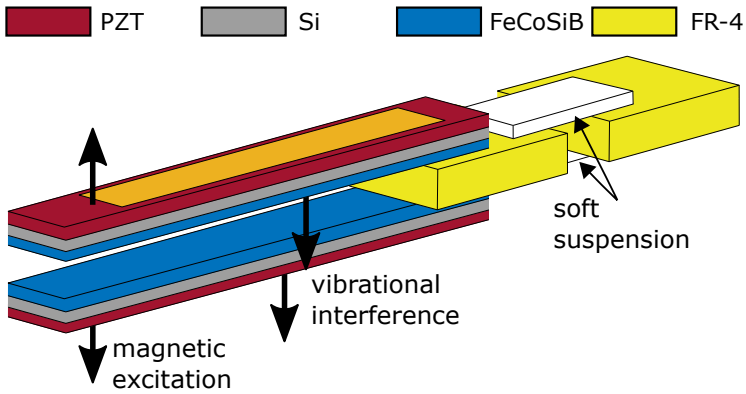

Figure 2.24: Two cantilevers in tuning fork assembly. Magnetic excitations move the cantilevers in opposite directions, whereas, vibrational interference predominantly bends the cantilevers in the same direction (indicated with arrows). The FR-4 substrates are suspended with two adhesive strips of foam [Sal+16].

However, these interferences can be strongly reduced by attaching two similar cantilevers to a PCB in a tuning fork-like structure as depicted in Fig. 2.24 [JRK13; Sal+16]. Both sensors are clamped rigidly to a FR-4 substrate with instant glue. The magnetostrictive layers are directed face to face. This leads to a bending in opposite directions under a magnetic excitation. The voltages at the terminals of the sensors are then 180° out of phase (differential-mode). Provided that both cantilevers are identical and clamped completely symmetrically, the two stresses induced by the individual beams cancel out completely with a net force of zero at the clamping point. Under vibrational interference, a bending predominantly in the same direction occurs and produces an in-phase signal (common-mode). Due to the fact that the two FR-4 substrates are coupled with a soft adhesive foam, this movement is additionally attenuated.
The output signal is a mixture of the two modes. By taking the difference and the sum of the two sensor signals, the common-mode and the differential-mode signals can be separated. The output signal Y of a differential operational amplifier is given by

$$Y = G_{\text{diff}}(A_{\text{TF}} - B_{\text{TF}}) + G_{\text{comm}}\frac{1}{2}(A_{\text{TF}} + B_{\text{TF}}) \overset{G_{\text{comm}} \ll G_{\text{diff}}}{\approx} G_{\text{diff}}(A_{\text{TF}} - B_{\text{TF}}) \quad (2.53)$$

with the filtered signal A_{TF} from the tuning fork amplifier at the positive input of the differential amplifier, the filtered signal B_{TF} at the negative input, the dif-

ferential gain G_{diff} and the common-mode gain G_{comm}. The common-mode gain of instrumentation amplifier is generally about 80 dB less than the differential gain (common-mode-rejection-ratio, CMMR).

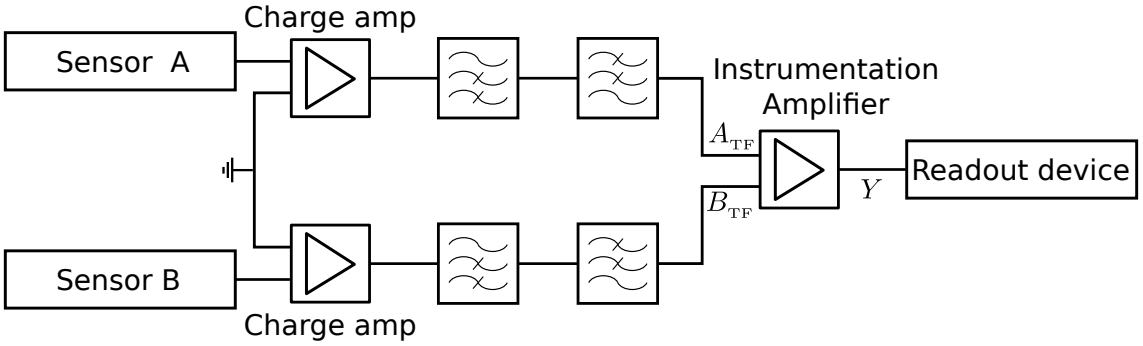

Figure 2.25: Analogue signal processing of the output signals of the tuning fork. The signals are preamplified with identical charge amplifiers, filtered, and then fed into an instrumentation amplifier.

Eq. (2.53) is realised with an analogue signal processing stage as depicted in Fig. 2.25. In addition to the suppression of vibrational interference, the circuit features a signal averaging. While the signal amplitudes from sensor A and Sensor B add coherently, the noise power is added according to Eq. (2.39). Consequently, the SNR is increased by 3 dB. Whether the sum or the difference yields the magnetic signal depends on the connections made between the sensor and the readout electronics.
A prerequisite for the optimal suppression is the symmetry of the assembly. The sensors need to have the same magnetoelectric and mechanic behaviour. Thus, their resonance frequency, sensitivity, and capacitance should be as similar as possible.
For the experiment, two PZT cantilevers of similar characteristics are clamped to a substrate in a tuning fork setup. Both sensors have the same layer composition (see [Pio+13]). An IDT structure is applied by lithography and sputter-deposition as a mechanic-electric transducer. It has 15 µm spacing, 1.4 mm effective width, a total IDT width of 1.8 mm, a total length of 10 mm, an electrode finger width of 15 µm, and a thickness of 5 nm Cr and 100 nm Au. The cantilever dimensions are 25 mm length and 2 mm width.
The tuning fork is enclosed in a specifically designed polyvinyl chloride (PVC) cylindrical tube. A self-wound coil is wrapped around it, to provide the bias field B_{opt} to achieve the highest sensitivity. The bias is supplied by 6 V batteries, thus its noise contribution can be neglected. A copper foil covers the assembly to shield from electrical fields. Both cantilevers have a capacitance of about $C = 820\,\text{pF}$, have

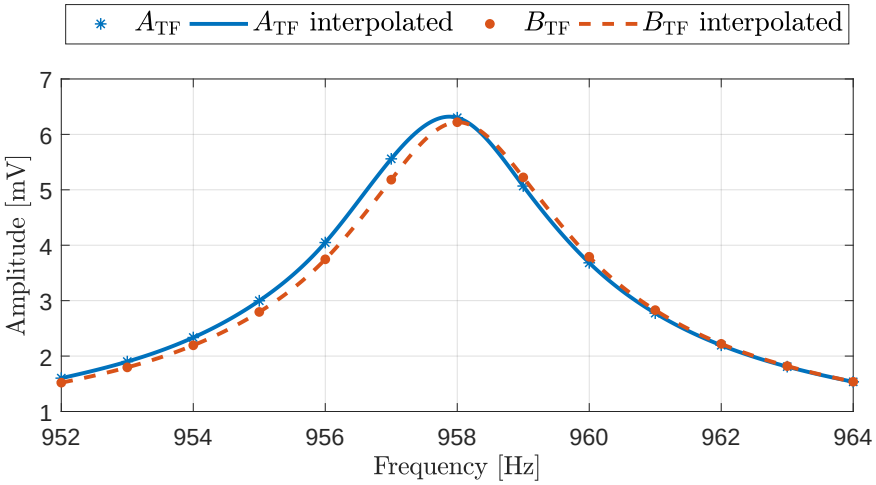

Figure 2.26: Resonance frequencies of two IDT sensors assembled in tuning fork configuration. The amplitude is given at the input of the charge amplifier ($G_c = 82$).

nearly the same resonance frequency of $f \approx 958\,\mathrm{Hz}$, and Q-factors of $Q = 309$ and $Q = 312$, respectively (see Fig. 2.26).

The similarity in resonance frequency can be explained by phenomenon of synchronisation (self-locking). According to [Bir56], synchronisation was first observed by the Dutch scientist Christiaan Huygens and reported in a letter to the Royal Society in 1665. Two pendulum clocks, both mounted on a wooden frame, attained an anti-phase state after a certain number of swinging cycles, no matter its initial state. Huygens concluded that the coupling was due to the common frame and its mutual movement. The coupling strength is a function of the relative masses in the system [Ben+02]. A requirement for the synchronisation is a sufficiently close match between the natural frequencies of the oscillators. In [ABG06], synchronisation is investigated for two organ pipes placed next to each other on a common bar. A 4 Hz plateau is found where the coupled frequency difference is zero depending on the difference of the uncoupled frequencies and the organ pipe structure. For the investigated tuning forks made of magnetoelectric sensors, the individual sensors stem from the same batch and have similar characteristics. They are arranged with a home-made positioning device. All combined sensors show self-locking for applied sinusoidal magnetic signals indicating that their uncoupled resonance frequencies are close enough. The sensors of the tuning fork are coupled via the FR-4 substrate as depicted in Fig. 2.24. For the measurements, the sensor is placed inside the shielding box explained in Subsec. 2.5.2.

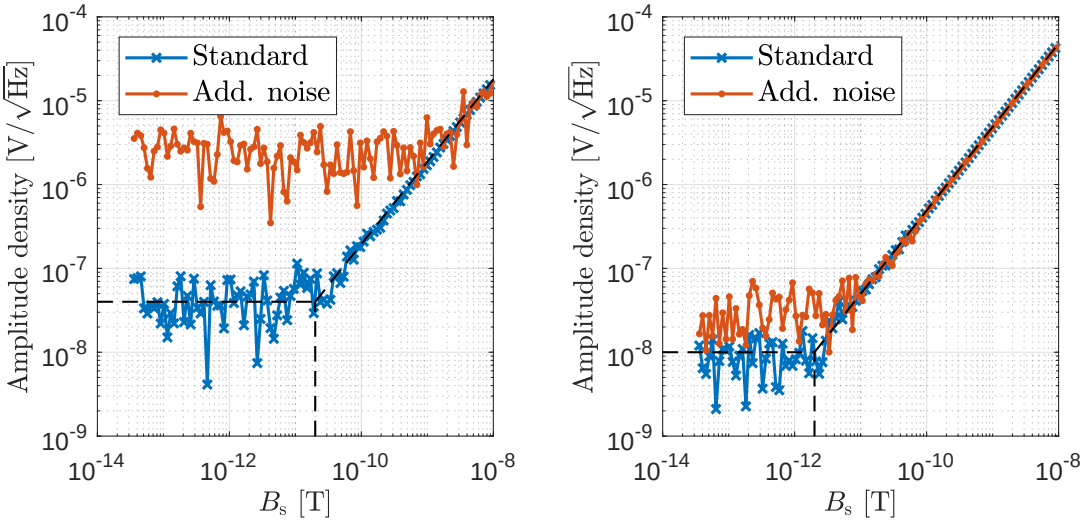

Figure 2.27: LoDs in resonance of (a) a single sensor (reference) and (b) a tuning fork setup, with and without additional white acoustic noise. The sensors are excited at their respective resonance frequencies with $B_s = 100\,\mathrm{nT}$ under optimal bias. The dashed lines indicate the crossing point of the linear sensor response and the mean of the noise floor.

In Fig. 2.27, the LoD measurements of a single ME sensor with similar characteristics and the LoD of the differential signal Y of the tuning fork are displayed. The LoD of the tuning fork is approximately $2\,\mathrm{pT}/\sqrt{\mathrm{Hz}}$. The single sensors of the tuning fork have LoDs of approximately $4\,\mathrm{pT}/\sqrt{\mathrm{Hz}}$ (not depicted). This agrees with the theoretical decrease in LoD with the square root of number of averages. The LoD of a single reference sensor from the same batch and of similar characteristics is approximately $20\,\mathrm{pT}/\sqrt{\mathrm{Hz}}$ and its sensitivity is slightly lower as compared to the tuning fork sensors.

To demonstrate the suppression of acoustic noise, additional acoustic noise is introduced into the system by a piezoelectric loudspeaker. The acoustic interference raises the noise floors of the sensors. The increase is more pronounced for the single sensor (approximately 20 dB) because the tuning fork (approximately 6 dB) suppresses acoustical interferences.

The tuning fork can be assembled from any two similar sensors to suppress air- and structure-borne noise.

Fig. 2.28 shows an improved version of the tuning fork. The suspension stabilises the frame within the chassis, while the correct orientation of the tuning fork is ensured

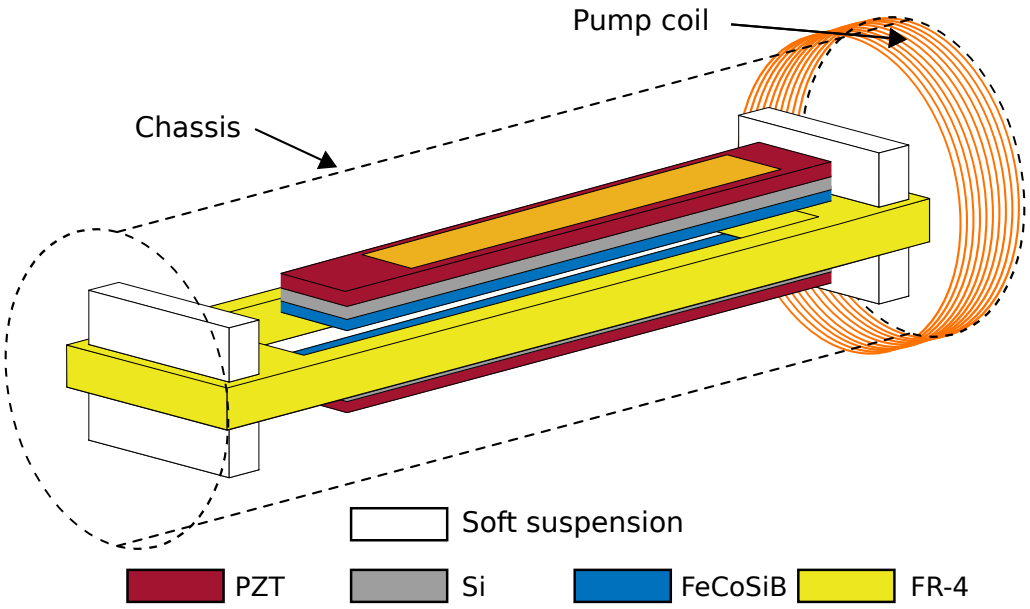

Figure 2.28: Tuning fork assembly mounted on a frame. The frame is supported directly on the inside of the closed coil chassis via soft suspensions. The coil is wound around the chassis along the whole length of the chassis.

by the symmetrical design. The soft suspension additionally dampens common-mode signals while being invisible to differential-mode signals. With the help of an additional positioning mount that fits the frame, the sensors can be attached precisely and symmetrical to the substrate.

Fig. 2.29 shows the individual time signals of both sensors A and B of another tuning fork depicted in Fig. 2.28 with $f_{\mathrm{res}} = 1076\,\mathrm{Hz}$. As mentioned before, the connections at the sensor determine whether the sum or the difference yields the wanted signal. On this tuning fork, the second sensor is connected vice versa and is consequently shifted by a half period ($-B_{\mathrm{TF}}$). For this sensor, the magnetic signals are nearly in phase and have similar amplitudes (see Fig. 2.29a). The sum and difference for this measurements are conducted digitally after the signals A_{TF} and B_{TF} are digitised with an ADC before the differential amplifier. In accordance with Eq. (2.53), the differential signal obtained by the sum $A_{\mathrm{TF}} - B_{\mathrm{TF}}$ is doubled and the common-mode signal $A_{\mathrm{TF}} + B_{\mathrm{TF}}$ is suppressed by 28 dB. In Fig. 2.29b, an additional acoustical sinusoidal noise signal with $f = 500\,\mathrm{Hz}$ is superimposed with a *Sonitron SPS-29-T00* piezoelectric loudspeaker driven by a signal generator with 10 V amplitude. The loudspeaker is placed behind the tuning fork such that both cantilevers have the same direct distance to the loudspeaker. This leads to a distortion of both

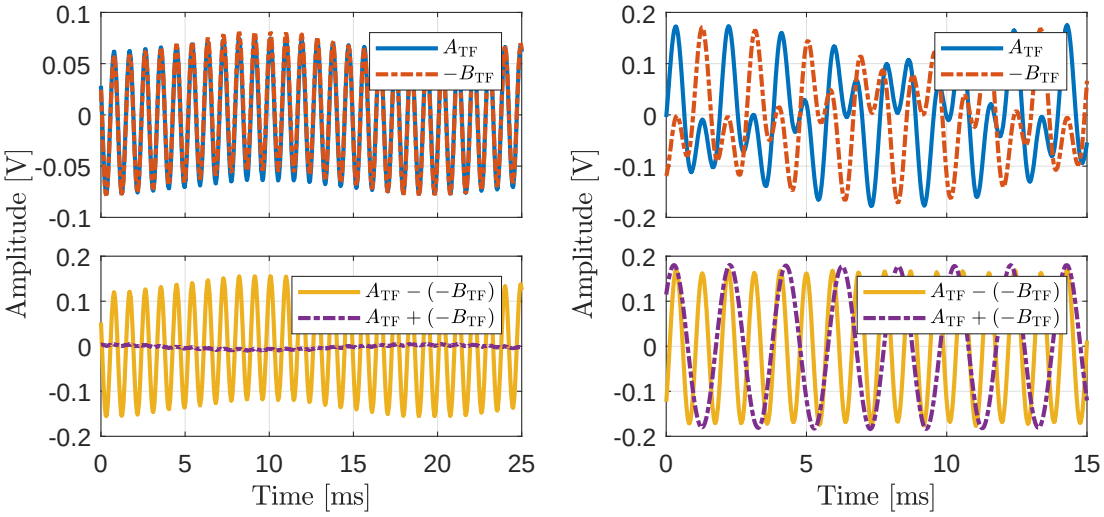

Figure 2.29: Time signals of the two individual sensors A and B of a tuning fork as depicted in Fig. 2.28, their signal difference A-B, and their signal sum A+B (a) without additional acoustic noise but with visible 50 Hz mains voltage in both output signals and (b) with an additional sinusoidal acoustic noise signal applied with the frequency $f = 500\,\mathrm{Hz}$. A test signal with $f_s = f_{res} = 1074\,\mathrm{Hz}$ and $B_s = 100\,\mathrm{nT}$ is applied in both cases. To reach the maximum output voltage a bias field of $B_{bias} = 3.1\,\mu\mathrm{T}$ is generated via the bias coil. The difference and sum of the signals are processed digitally for this sensor.

sensor signals. In the differential signal, the noise signal is strongly suppressed and the dominant output signal is the wanted signal with $f = 1076\,\mathrm{Hz}$. Likewise, the noise signal can be obtained with the common-mode signal which suppresses the magnetic signal.

The remaining phase shift may originate from deviation in the positioning of the loudspeaker and the sensor. If the phase shift of the signals A_{TF} and B_{TF} is additionally reduced digitally, the sum suppresses the common mode signal by 45 dB. Approximately the same suppression occurs for noise frequencies at 1000 Hz, 1500 Hz, 2500 Hz, and white noise. Without shielding, acoustical interference comes from all directions. If the loudspeaker is placed underneath the tuning fork for example, the cantilevers are reached at different times and the upper one is covered by the lower one. In the worst case, the differential signal can even increase the acoustical interference in this setup. An adaptive phase correction can reduce these orientation effects frequency-wise, if the signals are processed digitally. Common-mode noise is

obtained without further circuitry and can be processed subsequently. Operated as a three dimensional sensor, interference from all directions can be cancelled without additional reference sensors. The reference signal can already be obtained from $A_{\text{TF}} + B_{\text{TF}}$ according to Eq. (2.53) without further circuitry. If a reference signal is available, another approach for the suppression of acoustic interference is to use adaptive algorithms [Ree+15]. A reference can be obtained by e.g. a microphone or a vibration sensor. In [Ree+16b], reference sensors for noise cancellation of ME sensors are discussed.

The additional robustness and noise suppression is important for application, when measurements are conducted outside of shielded environments or when the sensor is operated in a mechanical scanning device. An example is the localisation of a brain-pacemaker. The fifth harmonic of a brain-pacemaker lies in the resonance frequency of the tuning fork and can thus be measured with the effect enhancement in the mechanical resonance. First investigations with head phantoms and a recycled brain-pacemaker yield localisation precision in the mm range with forward models based on the Biot-Savart law. Due to the vibration of the pneumatic head scanner the measurement is more robust with tuning forks. The tuning fork is also operated with MFC, which allows the measurement of almost arbitrary signal frequencies with decent LoDs (see Sec. 3.1.4).

3 | Frequency Conversion

For the measurement of biomagnetic signals, the LoD for direct detection is not sufficient (see Fig. 2.11). The main reasons are the missing resonance enhancement and the increase of the noise floor towards low frequencies mainly due to flicker noise. Therefore, it is advantageous to convert the desired signal frequency into the mechanical resonance frequency of the cantilever. The frequency conversion via the nonlinear characteristics of e.g. a magnetostrictive material or piezoelectric material of magnetoelectric thin-film sensors relocates a signal at some arbitrary frequency to other frequency ranges. In an exemplary physical system, an input spectrum consisting of the super-position $B_{1+2}(t) = B_1(t) + B_2(t)$ of two signals

$$B_1(t) = \hat{b}_1 \cos(2\pi f_1 t) \tag{3.1}$$

$$B_2(t) = \hat{b}_2 \cos(2\pi f_2 t), \tag{3.2}$$

with the time t, arbitrary amplitudes and frequencies $\hat{b}_1$, $\hat{b}_2$, f_1, f_2, is transferred to the output via a nonlinear function. The phase of the signals is neglected here for convenience. For example, a polynomial behaviour like $p(B(t)) = a_1 \cdot B(t) + a_2 \cdot B(t)^2$ with the coefficients a_1 for the linear term and a_2 for the quadratic term provides the required nonlinearity.

The achieved spectral components are

$$
\begin{aligned}
p(B_{1+2}(t)) =& a_1(B_1(t)+B_2(t)) + a_2\big(B_1(t)+B_2(t)\big)^2 \\
=& a_1\hat{b}_1\cos(\omega_1 t) + a_1\hat{b}_2\cos(\omega_2 t) \\
&+ a_2\left[\hat{b}_1^2\cos^2(\omega_1 t) + \hat{b}_2^2\cos^2(\omega_2 t) + 2\hat{b}_1\hat{b}_2\cos(\omega_1 t)\cos(\omega_2 t)\right] \\
=& \underbrace{a_1\hat{b}_1\cos(\omega_1 t)}_{1} + \underbrace{a_1\hat{b}_2\cos(\omega_2 t)}_{2} \\
&+ \frac{a_2\hat{b}_1^2}{2}\Big(\underbrace{1}_{3} + \underbrace{\cos(2\omega_1 t)}_{4}\Big) + \frac{a_2\hat{b}_2^2}{2}\Big(\underbrace{1}_{5} + \underbrace{\cos(2\omega_2 t)}_{6}\Big) \\
&+ a_2\hat{b}_1\hat{b}_2\Big(\underbrace{\cos\left[(\omega_2-\omega_1)t\right]}_{7} + \underbrace{\cos\left[(\omega_2+\omega_1)t\right]}_{8}\Big).
\end{aligned}
\tag{3.3}
$$

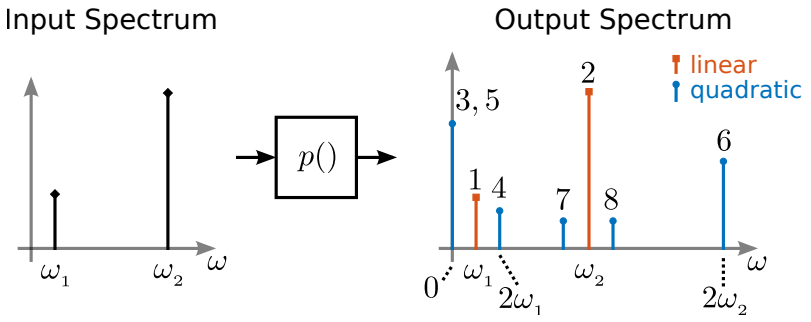

Figure 3.1: Frequency conversion process described by Eq. (3.3). On the left two input signals are shown vs. frequency. On the right the output spectrum is depicted, with component numbers according to Eq. (3.3). Linear components are marked with squares and quadratic components with circles. The amplitudes are not representative.

Fig. 3.1 illustrates the frequency conversion process described by Eq. (3.3) with the angular frequency $\omega = 2\pi f$. On the left, two input signals $B_1(t)$ and $B_2(t)$, located at frequencies f_1 and f_2, are converted into several different spectral components. The characteristic of the nonlinear function and the input frequencies determine which frequency components appear at the output. If the nonlinear function was purely quadratic, only the quadratic components (#3 to #8) would appear at the output [MG02]. Thus, the input signals would not be visible there. Frequency component #2 is the original pump frequency, also called *carrier* in the context of frequency conversion. Frequency components #7 and #8 are termed lower sideband (LSB) and upper sideband (USB), respectively. Unlike e.g. digital transfer functions, physical

nonlinear curves generally have non-zero higher order coefficients, which decrease towards higher orders. If one or more of the input frequencies can be chosen freely, the location of the components in the output spectrum can be designed according to Eq. (3.3). Typical components used for frequency conversion are for example diodes, Gilbert cells, or switches.
Frequency conversion makes it possible to detect frequency-relocated low-frequency magnetic signals, while making use of the effect enhancement of the mechanical resonance and thus lowering the LoD. Two methods for frequency conversion with magnetoelectric sensors are introduced in the following two sections.

3.1 Magnetic Frequency Conversion

If an additional magnetic signal, also called pump signal, is applied to the system and the nonlinearity of the magnetostriction curve is utilised for frequency conversion of the desired signal, the method is called *magnetic frequency conversion* (MFC). This method is patented in [JKQ11] and described in [Jah+12]. Similar approaches were used later in [Fet+13], [Gil+11] and [Pet+11], for bulk ME sensors. Instead of a bias field, as used for the direct detection (see Sec. 2.4), a magnetic pump signal (likewise carrier or modulation signal) is applied along the long axis of the investigated cantilevers. This periodic sinusoidal field alters the operating point, as it is seen by a small magnetic field to be measured, on the nonlinear magnetostriction curve and converts its frequency into the resonance frequency of the cantilever. Due to the resonance enhancement of the amplitude and less flicker noise at f_{res}, the LoD can be improved by several orders of magnitude [Jah+12]. Since the shape of the nonlinearity determines the output signals, magnetostriction curves of different magnetoelectric sensors are explained in the following. Some of the contents of this section have already been published in [Sal+17a; Sal+17b; Dur+17a].

3.1.1 Magnetic Behaviour

As was already stated, for MFC, the nonlinearity of the magnetostrictive material is utilised to convert the signal frequency into the resonance frequency of the cantilever. Shape, position, and scaling of the curve determine the output signals in both frequency and amplitude. Therefore, different magnetic materials or layer compositions may also require adapted signal processing for the best LoD.

The magnetic behaviour can be determined by measurement of the hysteresis curve of the material. When applying a magnetic field to a magnetic material, the change in magnetisation can be detected with e.g. an induction coil, while the exciting magnetic field is compensated by calibration.

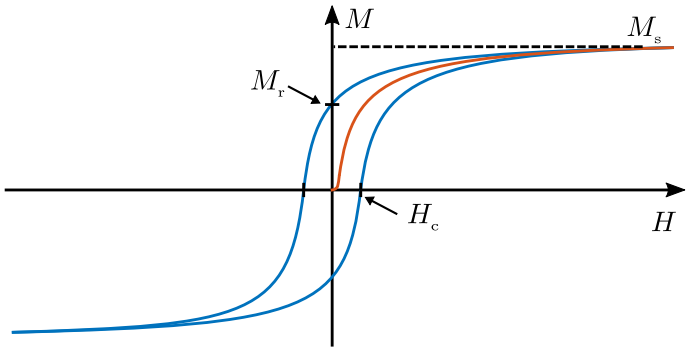

Figure 3.2: Schematic hysteresis curve of a ferromagnetic material with its characteristic parameters.

Fig. 3.2 shows a schematical hysteresis curve with its characteristic parameters saturation magnetisation M_s, remanence M_r, and coercive field H_c [CG09]. When measuring the hysteresis curve of a sample, a volume averaged information of only the magnetic behaviour is obtained. In order to resolve the local domain behaviour, other methods such as magneto-optical Kerr effect (MOKE) microscopy need to be applied [Ker77; CG09]. A magnetised material rotates the polarisation of incident plane polarised light. Inversely magnetised domains rotate the polarisation in opposite directions. The rotation is processed with an optical analyser filter and made visible by contrasts proportional to the rotation. This allows to investigate the domain wall formation and movement, e.g. at the edge of a sensor sample, with applied magnetic field.
Magnetostriction λ is proportional to the square of the magnetisation M [CG09]

$$\lambda \propto M^2. \tag{3.4}$$

This can also be seen from Fig. 3.2, if the hysteresis is neglected and the curve is squared because it then looks similar to a magnetostriction curve (cf. Fig. 2.5). Moreover, the ME coefficient α_{ME} is proportional to the derivative of the magnetostriction curve

$$\alpha_{ME} \propto \frac{\partial \lambda}{\partial H}. \tag{3.5}$$

Consequently, the ME coefficient is related to the magnetisation by

$$\alpha_{\mathrm{ME}} \propto \left| \frac{\partial (M)^2}{\partial H} \right| . \tag{3.6}$$

The ME coefficient additionally contains factors related to the piezoelectric layer, the stress, the transfer function, etc. Under small signal excitation and ferroelectric materials excluded, these factors are mainly linear. Therefore, information about the magnetic behaviour can be deduced from the characteristic and shape of α_{ME} or likewise the magnetic bias curve.

For the utilisation as a sensor, the magnetic material needs to be magnetically soft in order to react with a measurable change in magnetisation for small magnetic field changes. The sensors are sensitive along the long axis if the field induced anisotropy is aligned along the short axis of the sensor [Röb+15; Röb+17]. This anisotropy is imprinted after the deposition processes by application of a magnetic field oriented parallel to the short axis of the sensor at 250-300 ° Celsius for 30 min and subsequent cooling. This *annealing* leads to an alignment of the magnetic moments along the short axis. An applied field along the long axis then may rotate the magnetic moments to a maximum of 90 °, which then produces a maximum of magnetostriction. If present, other anisotropies such as shape anisotropy, crystalline anisotropy, stress anisotropy, etc. also influence the alignment of the magnetic moments. Stress anisotropy can occur because of different thermal expansion coefficients of the different sensor layers during the annealing, clamping, and ageing effects, amongst others.

Therefore, the measured bias curve allows to draw conclusions about the magnetic behaviour, as well as correct sensor orientation etc.

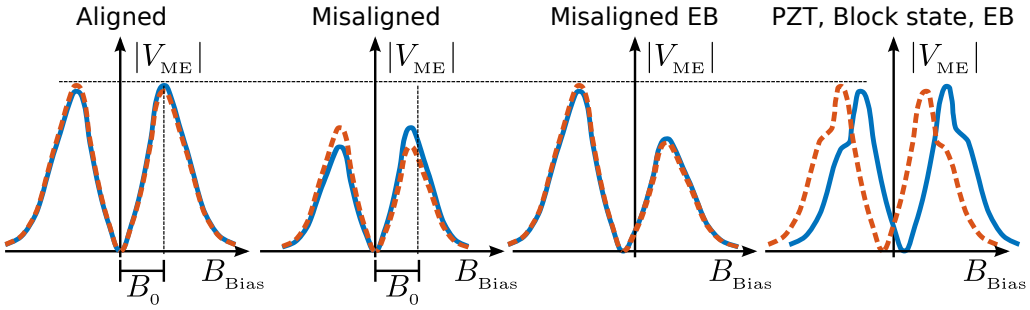

Figure 3.3: Schematic bias curves for several scenarios. B_0 is an arbitrary constant magnetic field. The solid line comes from negative and the dashed line from positive saturation.

Fig. 3.3 shows possible bias curves for a selection of scenarios without claim of completeness. To the left, the bias curve of a ME cantilever shaped sample with perfectly aligned 90° degree magnetic anisotropy (Aligned) is shown. It is perfectly symmetric and has low hysteresis. If the field induced magnetic anisotropy has a small angle deviation or if the sample is not clamped parallel to the exciting magnetic field, the curve may have less amplitude, less saturation field (see constant B_0), and more hysteresis (Misaligned). The third bias curve (Misaligned EB) is shifted towards negative fields and has asymmetrical amplitudes. The shift is due to the *exchange bias* (EB) of the magnetic layer [Lag+12; Lag14]: If a ferromagnet is directly mechanically coupled to an antiferromagnet such as manganese iridium (MnIr), the orientations of the magnetic moments of the ferromagnet are pinned by the antiferromagnet during an annealing.

An induced exchange bias anisotropy is unidirectional. The lower amplitudes towards positive saturation are due to less rotation of the magnetic moments in that direction because the magnetic anisotropy is slightly tilted away from the short axis of the cantilever. If the measured sample has a piezoelectric layer, it may also change the bias curve. Fig. 2.5 indicates that AlN behaves linearly, but PZT has a butterfly curve. Thus, PZT leads to a symmetrical shift of the zero crossings (PZT, Block state, EB). The trace also shows *shoulders* or small dips towards saturation, which are a result of block states [Urs+14]. Due to energetic reasons, the magnetic material forms a dense pattern of domains before transforming rapidly into a wide domain state.

Aside from a bias shift, exchange bias may also lead to a reduction of the number of domains in the magnetic material because the magnetic moments are aligned in the same direction. Moreover, domain nucleation (growing of domains) is strongly reduced during hysteresis loops and moments tend to rotate rather than jump. A multilayer of ferromagnets and antiferromagnets finally allows for smaller demagnetisation fields while increasing the EB coupling.

The shape of the magnetostriction curve, may thus be obtained from the bias curve by integration with regard to the magnetic field (cf. Eq. (3.5)). However, the actual change in length per applied field remains unknown.

Fig. 3.4 shows bias curves of a particular sensor measured over a time period of six months. During each measurement the sensor is magnetically saturated with $\pm 7\,\mathrm{mT}$ (not displayed). E.g. in the blue curve no. 1, pronounced dips or magnetic shoulders can be observed which increase the complexity of the nonlinear curve. The sensor

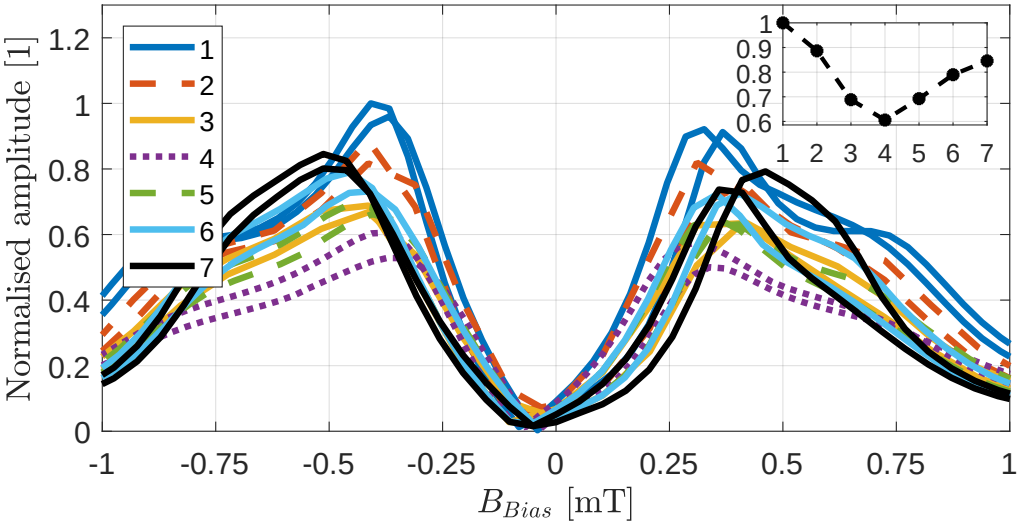

Figure 3.4: Bias curves of a multilayer sensor (see Subsec. 3.1.4 for sensor details) measured several times within a time interval of 6 months normalised to the maximum of curve number 1. The curve number (see legend) is temporally ordered. The inlay shows the maximum of each curve number.

has EB coupling, which is slightly misaligned. The curve changes significantly over time which changes its behaviour for MFC. The optimal bias field is shifted, the output amplitude initially decreases and later increases again (see inset of the Fig. 3.4). The shape of the curve is altered over time. Amongst others, possible reasons for the changes are temperature, humidity, and clamping effects. Electrical measurements of a representative sensor show that the resonance frequency increases with temperature by approximately 1 Hz/25° C measured from 5° C to 80° C. The loss tangent in resonance remains unaltered from room temperature to 80° C. Since the substrate material FR-4 on which the sensors are clamped is hygroscopic [XL16], humidity affects both the clamping and the damping factor of the fixation. Qualitative experiments with exposure of the sensor to humidity and distilled water reveals a significant influence on f_{res}, α_{ME}, and the shape of the bias curve. Resonance frequency shifts of up to 5 Hz are observed. In the worst case, the output amplitude breaks down completely. However, drying of the sensor after exposure can reset the sensor response back to 100 %. The used instant adhesive is also hygroscopic. Therefore, it is recommended to store the sensors with silica gel in constant humidity and temperature or in vacuum.

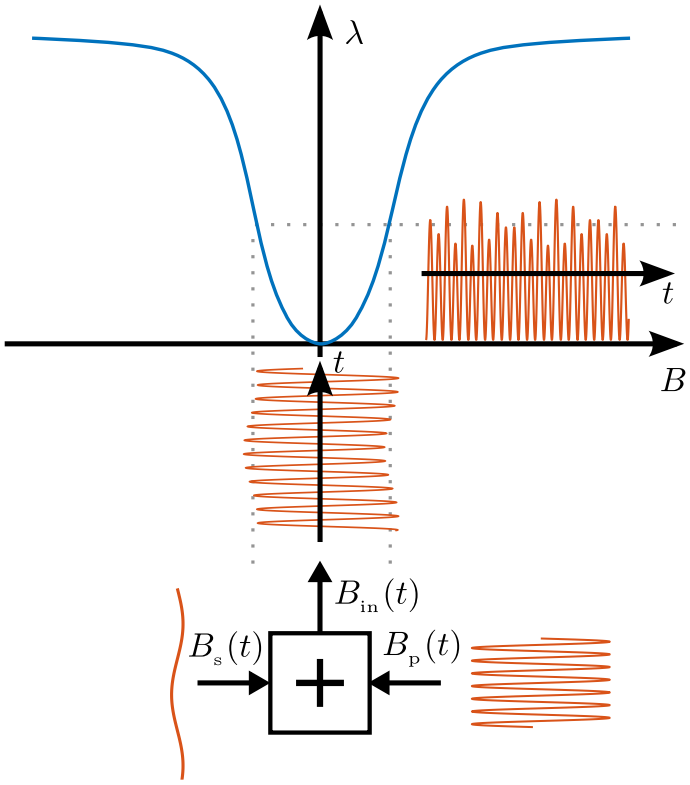

Figure 3.5: Schematic time domain representation of the MFC process. The superimposed excitation (see Eq. (3.9)) is drawn from below, and the output towards the right, both versus time t.

By defining a nonlinear curve which sufficiently matches the measured nonlinearity, a model of the MFC process can be formulated.

3.1.2 System Model of MFC

MFC is now mathematically described. The introduced model can be used to determine the behaviour of the measurement system under magnetic excitation. The nonlinear process has been basically described in [Jah+11]. In the following, the frequency conversion mechanism is reviewed, modified, and extended.
Fig. 3.5 illustrates the conversion process in time domain. The signal to be measured

$$B_{\mathrm{s}}(t) = \hat{b}_{\mathrm{s}} cos(2\pi f_{\mathrm{s}} t) \tag{3.7}$$

and an additional magnetic pump signal

$$B_{\mathrm{p}}(t) = \hat{b}_{\mathrm{p}} cos(2\pi f_{\mathrm{p}} t) \tag{3.8}$$

are superimposed in free space

$$B_{\mathrm{in}}(t) = B_{\mathrm{s}}(t) + B_{\mathrm{p}}(t). \tag{3.9}$$

The total magnetic field is then transferred into relative magnetostrictive length change via the nonlinear curve of the sensor's magnetostrictive material. For the following simulations, a hysteresis free magnetostriction curve across the long axis of the cantilever sensor is used for the mathematical model. The magnetostriction is a function of the applied magnetic field

$$\lambda\left(B_{\mathrm{in}}(t)\right). \tag{3.10}$$

The magnetostriction curve can be basically approximated by a quadratic function. Alternatively, the curve can be split up into several regions with different weighting functions that represent the nonlinearity more accurate or the curve can be developed into a Taylor series around the working point [Fet+13]. Due to the very specific characteristics, a polynomial λ_{app} of appropriate order $N_{\mathrm{n}} \in \mathbb{N}$

$$\lambda_{\mathrm{app}} = \sum_{n=0}^{N_{\mathrm{n}}} a_{\mathrm{n}} \cdot B_{\mathrm{in}}^{n} \tag{3.11}$$

is chosen to describe the nonlinearity of the magnetostriction curves (see Subsec. 3.1.1). A polynomial has the advantage of being versatile, such that the method can be applied to all magnetostriction curves without major adaptation. The coefficients a_{n} can be determined through a polynomial fit of measured data. The order of the polynomial depends on the complexity of the curve, where $N_{\mathrm{n}} = 6$ is generally sufficient for the investigated sensors. To simplify the model, the hysteresis of the magnetostriction is only taken into account by taking the mean value of the passage from negative saturation to positive saturation and vice versa. Using the polynomial approximation and defining the input signals, the output frequency components can be determined. A frequency component at $f_{\mathrm{p}} \pm f_{\mathrm{s}}$ for a polynomial with $N_{\mathrm{n}} = 6$ is given by

$$\begin{aligned}\lambda\big(B_{\mathrm{in}}(t)\big)\big|_{f_\mathrm{p}\pm f_\mathrm{s}} = &\left(\frac{15\,a_6\,\hat{b}_\mathrm{p}^5\,\hat{b}_\mathrm{s}}{8} + \frac{45\,a_6\,\hat{b}_\mathrm{p}^3\,\hat{b}_\mathrm{s}^3}{8} + \frac{3\,a_4\,\hat{b}_\mathrm{p}^3\,\hat{b}_\mathrm{s}}{2}\right.\\ &\left. + \frac{15\,a_6\,\hat{b}_\mathrm{p}\,\hat{b}_\mathrm{s}^5}{8} + \frac{3\,a_4\,\hat{b}_\mathrm{p}\,\hat{b}_\mathrm{s}^3}{2} + a_2\,\hat{b}_\mathrm{p}\,\hat{b}_\mathrm{s}\right)\\ &\cdot\left[\cos\big((f_\mathrm{p}+f_\mathrm{s})\,t\big) + \cos\big((f_\mathrm{p}-f_\mathrm{s})\,t\big)\right].\end{aligned} \tag{3.12}$$

If f_p is chosen such, that $f_\mathrm{p} \pm f_\mathrm{s} = f_\mathrm{res}$, the mechanical resonance of the cantilever can be exploited, because one of the sidebands is converted into f_res. Using this model, all frequency components at the output of the nonlinearity can be approximated.
If only the magnetic properties are taken into account, trends and relative changes can already be calculated. To calculate the resulting voltage from the sensor at a certain frequency, the mechanical coupling k and stress, the mechanical oscillator with its quality factor Q, and the piezoelectric phase with its piezoelectric coefficient, need to be taken into account [Nan+08].
This can also be seen in the block diagram in Fig. 3.6 describing MFC. The signal path is shown in solid boxes in black. Noise sources that are included in the noise model are indicated by dash-dotted boxes and are discussed later in Subsec. 3.1.7. External noise sources have dashed boxes.
Under the condition that $\hat{b}_\mathrm{s} \ll \hat{b}_\mathrm{p}$, $\Delta l/l$ can be considered as a linear function of the applied signal B_s because [SSR06]

$$\lambda(B_\mathrm{p}(t) + B_\mathrm{s}(t)) = \lambda(B_\mathrm{p}(t)) + \left.\frac{d\lambda}{dB}\right|_{B_\mathrm{p}(t)} \cdot B_\mathrm{s}(t). \tag{3.13}$$

This parametric approach shows that $B_\mathrm{p}(t)$ sets a dynamic working point and $B_\mathrm{s}(t)$ only conceives a small linear region. If the fitting factor k_MFC, the transfer function $G_\mathrm{mech}(f)$, the piezoelectric coefficient d_{31}, and the amplifier gain G_CA can also be considered to be linear, the system model is linearised for a frequency component f within the aforementioned boundaries. The magnetoelectric signal at the output of an amplifier with the gain G_CA is then given by

$$V_\mathrm{ME} \propto \lambda\big(B(t)\big) \cdot k_\mathrm{MFC} \cdot G_\mathrm{mech}(f) \cdot d_{31} \cdot G_\mathrm{CA}(f), \tag{3.14}$$

for a sensor with plate capacitor electrode layout.

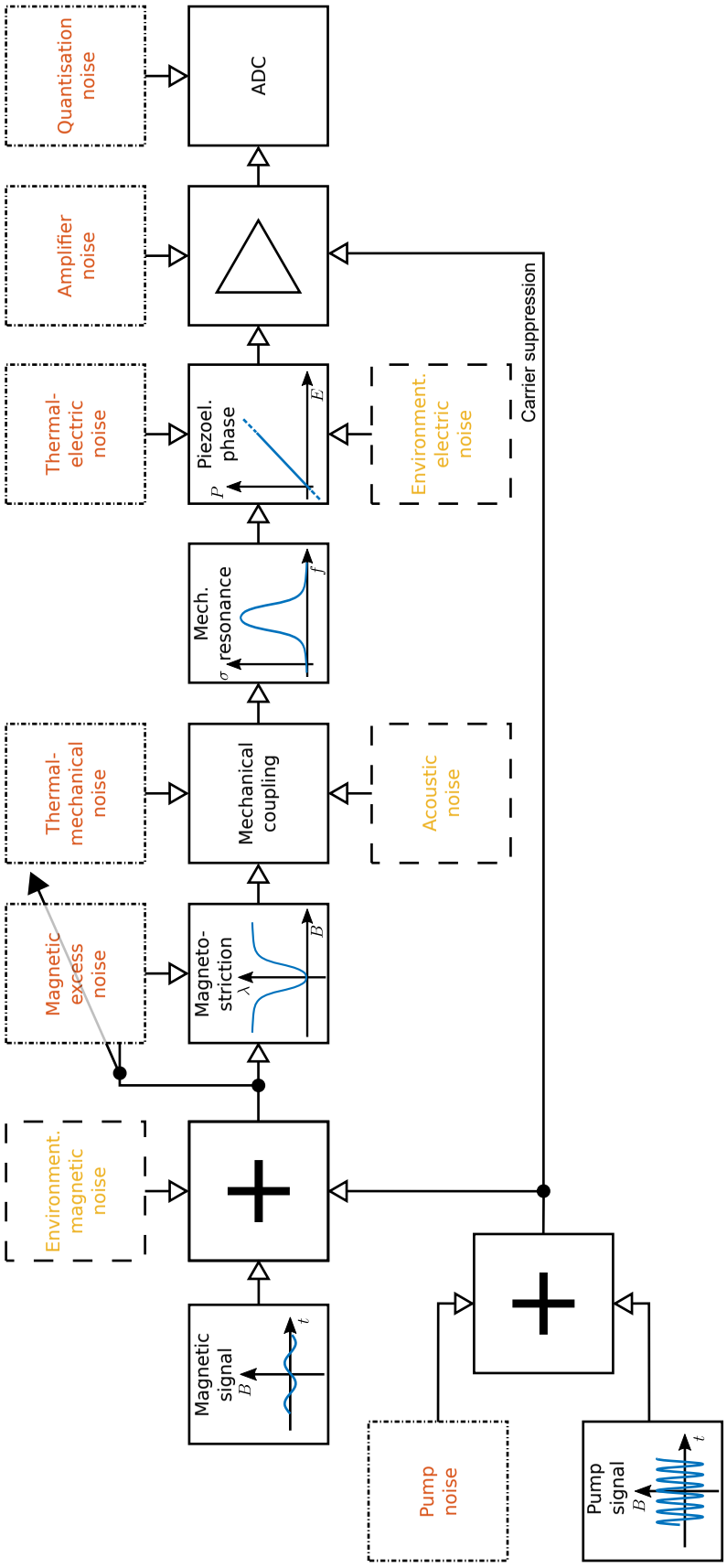

Figure 3.6: Block diagram for the description of MFC. Noise sources that are included in the noise model have dashed-dotted boxes. External noise sources have dashed boxes.

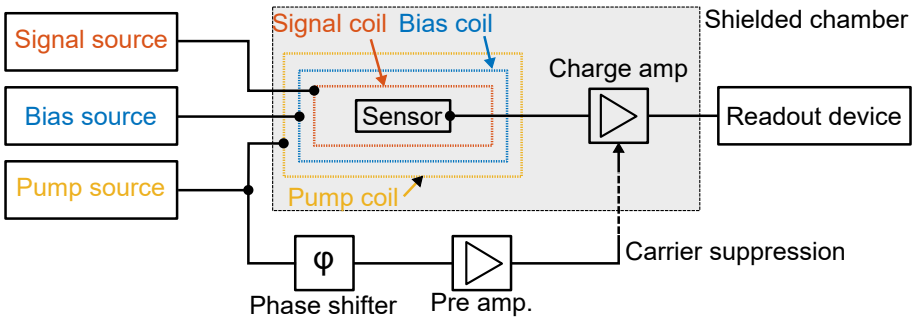

Figure 3.7: Standard measurement setup for MFC.

An important figure of merit for frequency conversion is the conversion loss (see e.g. [Poz12])

$$L_c = 10 \log \left(\frac{\text{available input power}}{\text{available output power at desired frequency}} \right). \tag{3.15}$$

which accounts for internal loss during the conversion process and conversion to undesired frequencies. Conversion loss depends on the pump or local oscillator level. For standard MFC, the minimum conversion loss is 3 dB since the desired signal frequency is upconverted into the USB and LSB.
Some parameters in the block diagram depend on the chosen measurement setup, which is explained in the next subsection.

3.1.3 Measurement Setup for MFC

In Fig. 3.7, a standard measurement setup for MFC is depicted. It is very similar to the setup used for direct detection (cf. Fig. 2.9). The basic system consists of a signal source to supply the signal to be measured, a pump source to excite the sensor with the pump signal, a DC bias source to supply a constant bias field to the sensor, three electrically shielded coils to transform the source currents into magnetic fields, a charge amplifier to convert the charge to a measurable voltage and a readout device to digitise the data. Optionally, a circuit for carrier suppression may be added.
The setup allows both a basic characterisation of the sensor and MFC without changing the measurement equipment. It allows independently controlled application of a signal, the pump, and a bias. Long cylindrical coils are utilised, designed to supply a sufficient flux density at their operating frequency while maintaining an impedance, which is low enough not to drive the sources into compliance. For most

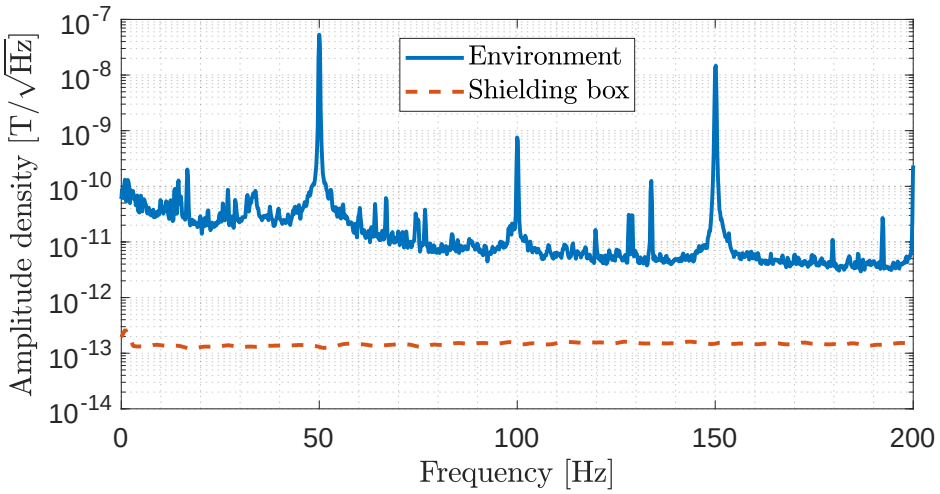

Figure 3.8: Noise floor of MFC measurement setup.

investigated magnetoelectric thin-film sensors bias fields for saturation are $\approx 7\,\mathrm{mT}$. Pump amplitudes up to $\approx 800\,\mu\mathrm{T}$ are necessary for optimal excitation. With the inductance L_{coil} of a long cylindrical coil

$$L_{\mathrm{coil}} = \mu_0\, N^2 \frac{A_{\mathrm{coil}}}{l_{\mathrm{coil}}}, \tag{3.16}$$

(vacuum permeability μ_0, number of windings N, cross-sectional area A_{coil}, length of the coil l_{coil}) and using data sheet parameters of e.g. copper wire, the flux density per current and the frequency dependent impedance can be calculated. The coil impedance is relevant for the excitation noise (see Sec. 3.1.7). Both the signal to be measured and the pump signal are generated by Keithley 6221 low noise current sources. Their current noise depends on the output amplitude and the set output range. Other available tested AC current sources produce more current noise than the chosen Keithley sources. The bias fields are generated with a Keysight B2962A power source with a low noise filter. The charge amplifier is home-made and consists of an AD745 operational amplifier, a feedback network (see Fig. 2.10), suppression inputs, and a 12 V supply battery to avoid additional noise from switching sources, supply grid, etc. For readout of measurements, several devices can be used: amongst others a SR785 spectrum analyser, or other ADCs. The shielding environment has already been explained in detail in Subsec. 2.5.1.

The magnetic noise floor of the µ-metal cylinders (*Aaronia Null-Gauss-Kammer ZG1*) is depicted with a dashed trace in Fig. 3.8 and is approximately 150 $\mathrm{fT}/\sqrt{\mathrm{Hz}}$.

Resonance frequency	851 Hz ±1 Hz
Quality factor	375
Sensor capacitance	640 pF
LoD @ f_{res}	$2\,\mathrm{pT}/\sqrt{\mathrm{Hz}}$
Cantilever width × height × length	2.2 mm×0.35 mm ×25.2 mm
Free-standing cantilever length	23 mm

Table 3.1: Properties of the investigated multilayer sensor.

Measured LoDs of magnetoelectric sensors with MFC generally have a noise floor at least 2 decades higher. In [Pet+12], $4\,\mathrm{pT}/\sqrt{\mathrm{Hz}}$ at 1 Hz are measured in an unshielded environment. Here, the environmental noise without shielding is depicted with a solid line and could be dominant without proper shielding. The DC offset inside the µ-metal cylinders is around 100 nT. This affects the optimal working point of the sensors, but can be neglected due to the much higher bias fields. The shielding can be degraded by the application of strong fields inside the boxes, mechanical stress, etc.
With the setup, measurements with MFC can be conducted.

3.1.4 Measurement with MFC

The measurement procedure is explained with a standard multilayer sensor already used in [Sal+17a]. The multilayer sensor differs slightly from the exemplary layer composition shown in 2.3. A 350 µm thick silicon substrate is covered by a plate capacitor piezoelectric layer with Ta (24 nm)/Pt (150 nm)/AlN (2000 nm)/Cr (5 nm)/Au (100 nm) on top (thickness in brackets). The AlN is deposited with a special low temperature method [Yar+16b].
On its bottom side, the magnetostrictive layer consists of a 20 times repeated sequence of Ta (5 nm)/Cu (3 nm)/MnIr (8 nm)/FeCoSiB (200 nm). The cantilever has the dimensions 25.2 mm×2.2 mm and the 1.4 mm×10 mm Cr/Au top electrode is flush with the clamping, i.e. it begins where the free standing part of the cantilever commences. An exchange bias is induced with magnetic field annealing (250° Celsius for 30 min with 100 mT). The field is oriented perpendicular to the long cantilever axis which in theory should not shift the bias curve for an excitation along the long cantilever axis. However, the anisotropy axis is not completely orthogonal to the excitation (see Fig. 3.4).
Tab. 3.1 summarises important properties of the investigated sensor.

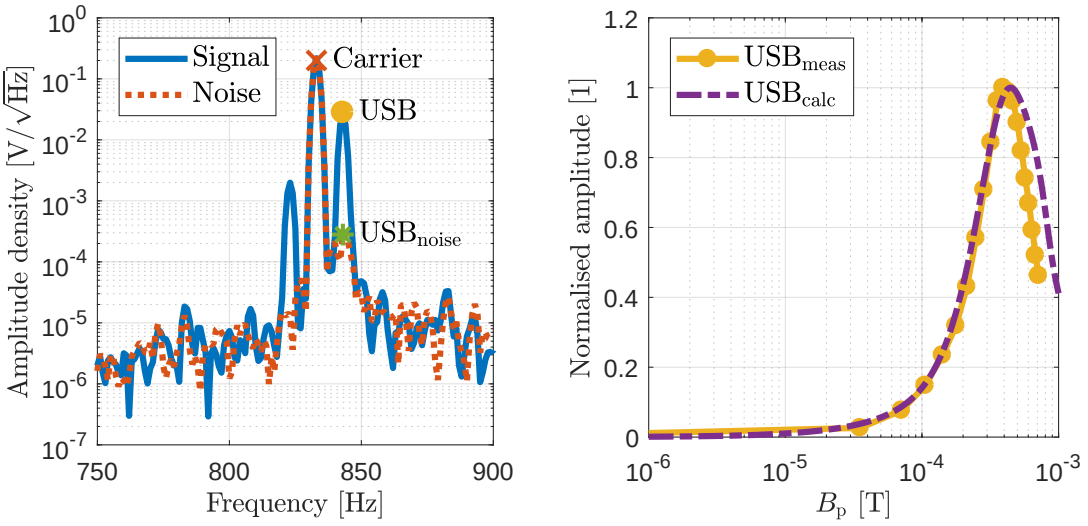

(a) (b)

Figure 3.9: (a) Measured signal and noise spectral densities for $B_\mathrm{p} = 420\,\mu\mathrm{T}$ and $B_\mathrm{s} = 100\,\mathrm{nT}$. The pump frequency is chosen such that the signal frequency is converted into an USB at the mechanical resonance of the sensor. (b) Measured and calculated normalised USB at resonance plotted over the pump amplitude. The sampling point for the USB is exemplarily indicated in (a) for $B_\mathrm{p} = 420\,\mu\mathrm{T}$ with a filled circle.

For standard MFC operation, the pump frequency is chosen such that the signal frequency is converted to the USB into the mechanical resonance frequency of the cantilever, requiring $f_\mathrm{p} = f_\mathrm{res} - f_\mathrm{s}$. Principally, it is also possible to utilise the LSB if $f_\mathrm{p} = f_\mathrm{res} + f_\mathrm{s}$ is chosen.

The resulting measured output signal and noise spectral density for $B_\mathrm{p} = 420\,\mu\mathrm{T}$ are depicted in Fig. 3.9a. The upconverted signal frequencies at $f_\mathrm{p} \pm f_\mathrm{s}$ are centred around the pump signal at f_p. Moreover, the noise floor is raised symmetrically to the resonance frequency. The USB is higher in amplitude than the LSB, due to resonance enhancement. Small remnants of upconverted mains frequency can be observed at $f_\mathrm{p} \pm n \cdot 50\,\mathrm{Hz}$ with $n \in \{\pm 1, \pm 3\}$. The cross, the dot and the asterisk indicate the sample points for the amplitude of the feedthrough of the pump signal (Carrier), the upper sideband (USB), and the noise level at resonance ($\mathrm{USB}_\mathrm{noise}$) measured with applied B_p but without an applied signal.

The optimum pump amplitude that upconverts the signal to be measured to yield the highest USB needs to be found. In order to obtain the latter, the magnetostriction curve is obtained by numerical integration of the bias curve. With Eq. (3.12) and

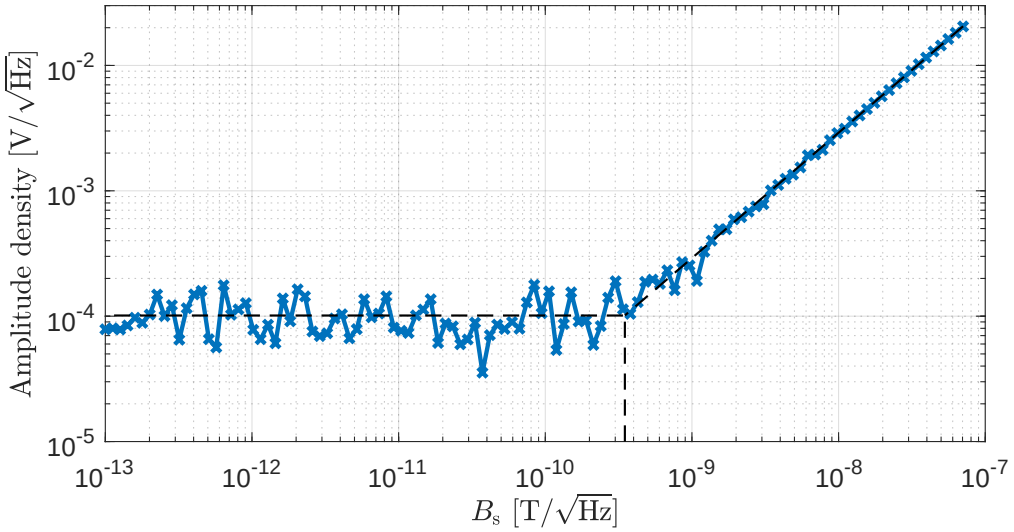

Figure 3.10: LoD measurement with MFC for $B_\mathrm{p} = 420\,\mu\mathrm{T}$ and $B_\mathrm{s} = 100\,\mathrm{nT}$ at the output of the charge amplifier. The linear signal regime, the average noise level, and the LoD are indicated with a dashed line. The measurement is averaged 50 times to reduce the variance.

the polynomial coefficients from the magnetostriction curve, the optimal amplitude can be estimated by sweeping the pump amplitude for a fixed signal $B_\mathrm{s} = 100\,\mathrm{nT}$ and $f_\mathrm{s} = 10\,\mathrm{Hz}$.

Fig. 3.9b shows the result of the calculation with a dash-dotted trace. The maximum normalised amplitude is obtained for $B_{\mathrm{p,opt,calc}} = 460\,\mu\mathrm{T}$. The measured USB for various B_p is depicted by a solid line. Its maximum differs slightly from the calculated value with an optimal pump of $B_{\mathrm{p,opt,meas}} = 420\,\mu\mathrm{T}$. This deviation can be explained by small errors in the coil calibration, neglected hysteresis of the magnetostriction curve in the model, and/or a polynomial fit error. The optimal pump amplitude somewhat matches the optimal bias of the sensor (cf. Fig. 3.4). This proves that the dynamic working point should be set in the vicinity of the optimal bias where the magnetostriction curve is steepest.

The excitation with $B_\mathrm{p} = 420\,\mu\mathrm{T}$ and $B_\mathrm{s} = 100\,\mathrm{nT}$ yields a $\mathrm{LoD}_\mathrm{MFC}$ of $350\,\mathrm{pT}/\sqrt{\mathrm{Hz}}$ as depicted in Fig. 3.10 with a dashed line. The signal decreases linearly until it reaches the noise level. Thus, a rough and fast estimation of the $\mathrm{LoD}_\mathrm{MFC}$ is possible by measuring the signal and the noise spectral density at the upconverted signal frequency for one signal amplitude as shown in Fig. 3.9a.

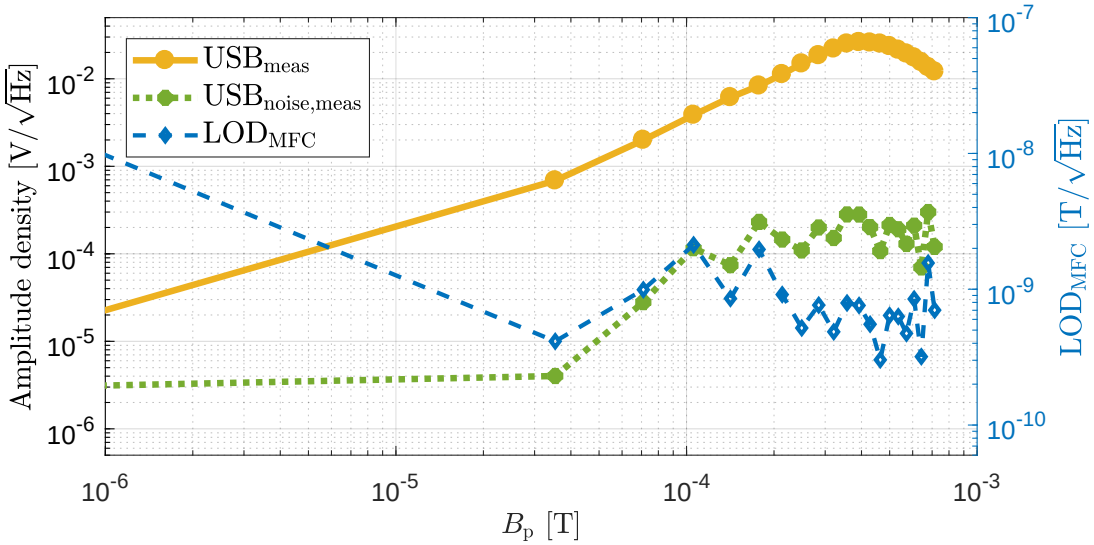

Figure 3.11: USB, $\mathrm{USB}_{\mathrm{noise}}$, and the $\mathrm{LoD}_{\mathrm{MFC}}$ as a function of the pump amplitude for $B_{\mathrm{s}} = 100\,\mathrm{nT}$. The measurements are not averaged.

The LoD can be calculated by

$$\mathrm{LoD}_{\mathrm{MFC}}(f_{\mathrm{res}}) = \frac{E_{\mathrm{o}}(f_{\mathrm{res}})}{S(f_{\mathrm{res}}) \cdot G_{\mathrm{CA}}(f_{\mathrm{res}})}. \tag{3.17}$$

The sensitivity is equivalent to the slope of the LoD plot in the linear part of the curve sufficiently above the noise level and is given by

$$S_{\mathrm{MFC}} = \frac{20.53\,\mathrm{mV}/\sqrt{\mathrm{Hz}}}{100\,\mathrm{nT}/\sqrt{\mathrm{Hz}} \cdot G_{\mathrm{CA}}} = 4534\,\mathrm{V/T}. \tag{3.18}$$

For the investigated sensor this yields a LoD of

$$\mathrm{LoD}_{\mathrm{MFC}}(f_{\mathrm{res}}) = \frac{0.10126\,\mathrm{mV}/\sqrt{\mathrm{Hz}}}{4534\,\mathrm{V/T} \cdot 64.1} = 348\,\mathrm{pT}/\sqrt{\mathrm{Hz}} \tag{3.19}$$

which complies with the measurement presented earlier.
The determination of the optimum pump amplitude for the best SNR solely by the USB amplitude is possible as long as the noise in the relevant region does not change, as it is the case for this sensor (see Fig. 3.11). The $\mathrm{LoD}_{\mathrm{MFC}}$ as a function of B_{p} is depicted with a dashed line. For this sensor, a small pump amplitude around 40 µT can be used as well to reach an only slightly degraded LoD. The advantage is significantly less power consumption and noise contribution of the pump source.

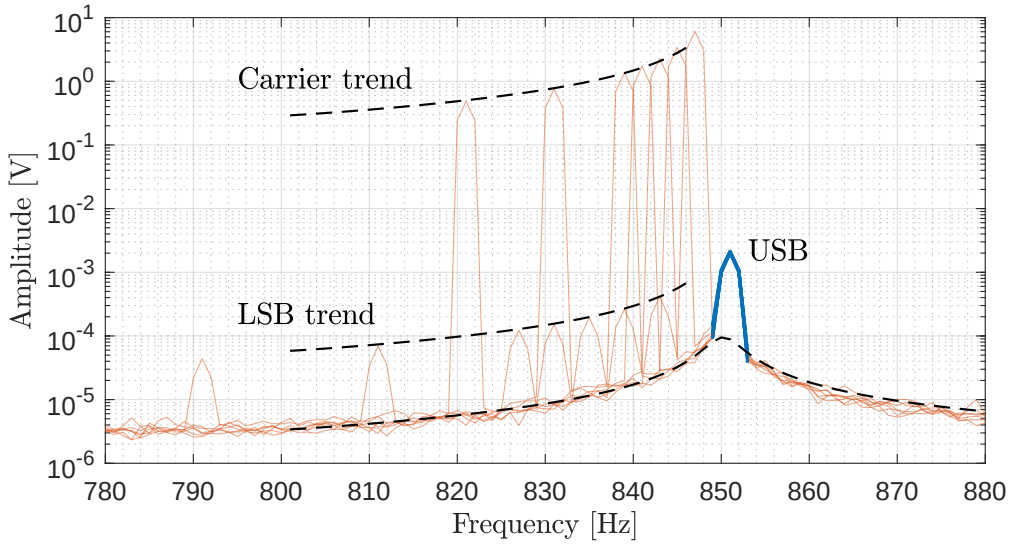

Figure 3.12: MFC Measurement with signal frequencies $f_s \in \{4,6,8,10,12,20,30\}$ Hz. The dashed lines indicate the progression of the resonance curve fitted to the noise, the carrier, and the lower sideband (LSB).

The block diagram in Fig. 3.6 suggests that the amplitude enhancement achieved by the resonator occurs after the conversion process. This can be proven by a MFC measurement with varying signal frequencies, e.g. $f_s \in \{4,6,8,10,12,20,30\}$ Hz. The pump frequency is chosen, such that $f_p - f_s = f_{res}$ is given and the USB stays at resonance.
Fig. 3.12 shows the measurements at various signal frequencies. The resonance curve is obtained by measurement and fitted to Eq. (2.3). The noise increase around the resonance and the progression of carriers and LSB fit well to the shape of the scaled resonance curve (dashed lines). An inverse resonance characteristic with the same parameters eliminates the influence of the resonator. The LSB amplitudes, the carrier amplitudes, and the noise floor are then constant and frequency independent. If the signals were amplitude enhanced by the resonator before the conversion process, the LSB amplitudes would vary due to the frequency conversion with an amplitude enhanced carrier. Thus, the noise, as well as the signals, are enhanced by the mechanical resonator after the frequency conversion process. Also, the dominant noise enters the system before the mechanical resonator.

Tuning Fork As mentioned before, a tuning fork setup may be used to suppress mechanical interferences. A tuning fork can likewise be operated with magnetic

frequency conversion. The individual sensors used for the investigations stem from the same batches with similar characteristics and are processed simultaneously, e.g. during annealing. The determination of the working point and the operation does not differ compared to single sensors because the coupling between the sensors synchronises their behaviour. Therefore, the methodology, results, and spectral outputs discussed above are also valid for the investigated tuning forks.

Higher Order Conversion The conversion process shifts the signal frequency not only to $f_\mathrm{p} \pm f_\mathrm{s}$, but also to $m_\mathrm{p} \cdot f_\mathrm{p}$, $m_\mathrm{s} \cdot f_\mathrm{s}$, and all combinations of $m_\mathrm{p} \cdot f_\mathrm{p} \pm m_\mathrm{s} \cdot f_\mathrm{s}$ with m_s,$m_\mathrm{p} \in \{1,2,\ldots,N_\mathrm{n}\}$. $N_\mathrm{n} \in \mathbb{N}$ is the order of the polynomial used for the approximation of the nonlinearity. In reality, N_n is of course infinity, but the converted signal amplitudes decrease for higher orders. With

$$f_\mathrm{p} = \frac{f_\mathrm{res} - f_\mathrm{s}}{n},\ n \in \{1,2,\ldots,N_\mathrm{n}\}, \tag{3.20}$$

the pump frequency can be chosen such that a higher order product is converted into the mechanical resonance frequency. For the sensor under investigation with $f_\mathrm{res} = 851\,\mathrm{Hz}$, the pump frequencies are then $f_\mathrm{p} \in \{841,420.5,280.\overline{3},210.25\}\,\mathrm{Hz}$. The USB, $\mathrm{USB}_\mathrm{noise}$, and the carrier are still processed at $f_\mathrm{res} = 851\,\mathrm{Hz}$ or $f = 841\,\mathrm{Hz}$ for the carrier, to exploit the resonance enhancement. For example, a pump with $f_\mathrm{p} = 210.25\,\mathrm{Hz}$ will convert a signal with $f_\mathrm{s} = 10\,\mathrm{Hz}$ with

$$\lambda\big(B_\mathrm{in}(t)\big)\big|_{4\cdot f_\mathrm{p} \pm f_\mathrm{s}} = \left(\frac{5\,a_5 \hat{b}_\mathrm{p}^4 \hat{b}_\mathrm{s}}{6}\right) \cdot \left[\cos\big((4 \cdot f_\mathrm{p} + f_\mathrm{s})\,t\big) + \cos\big((4 \cdot f_\mathrm{p} - f_\mathrm{s})\,t\big)\right] \tag{3.21}$$

into the mechanical resonance frequency because $4 \cdot f_\mathrm{p} + f_\mathrm{s} = f_\mathrm{res}$. With increasing order and for $B_\mathrm{p} = 420\,\mu\mathrm{T}$, simulations confirmed by measurements show that the USB decreases by more than a decade. The carrier increases slightly which worsens the ratio between the signal and the carrier. Finally, the measurements show no significant change in the noise level and increasing $\mathrm{LoD}(f = 851\,\mathrm{Hz})$. Consequently, the model allows the simulation of the sideband behaviour and it is not beneficial to use other modulation orders other than $n = 1$ for the investigated sensor.
The sensor's $\mathrm{LoD}_\mathrm{MFC}$ at 10 Hz is more than 2 decades worse than the LoD for direct detection at the resonance frequency. It can be either improved by increasing

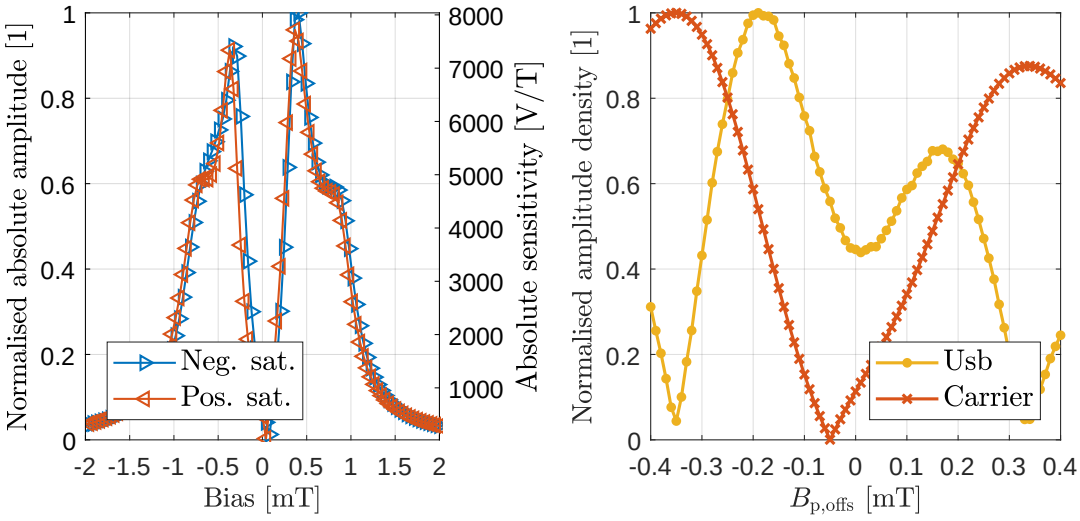

(a) (b)

Figure 3.13: (a) Bias curve of the investigated sensor that is used for the model to obtain the magnetostriction curve by integration. The sensor is saturated with ±7 mT during the measurement loop. (b) Normalised amplitudes of the USB and the carrier as a function of an applied offset $B_{p,offs}$, calculated by the model. The pump amplitude is $B_p = 100\,\mu T$.

the signal or by lowering the noise without affecting the other. In the following subsection, the LoD_{MFC} is lowered by increasing the USB amplitude.

3.1.5 Signal Enhancement of MFC

The amplitude of the desired signal upconverted into the mechanical resonance frequency can be influenced by means of further signal processing.

Offset Fig. 3.13a shows the bias curve of the investigated sensor used for the model. It is largely symmetrical around zero magnetic field, but shifted slightly towards positive values. In particular, the two peaks at around 0.4 mT have different heights. This implies that the steepness of the magnetostriction curve is different for positive and negative excitation.
Therefore, an offset $B_{p,offs}$ is superimposed to the pump signal to utilise a different section of the nonlinear magnetostriction curve

$$B_{p,offs}(t) = \hat{b}_p \cos(2\pi f_p t) + B_{p,offs}. \tag{3.22}$$

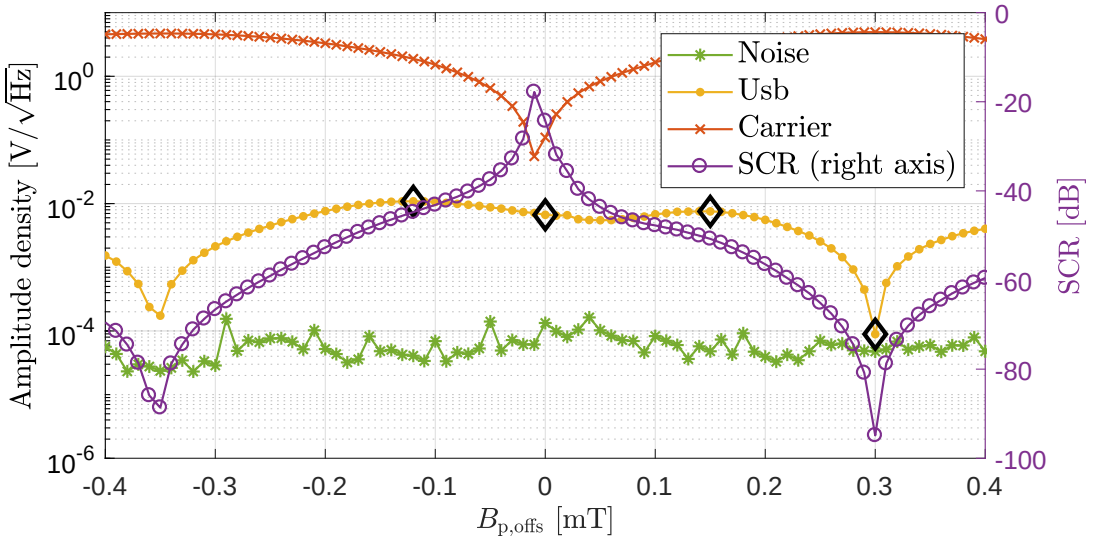

Figure 3.14: Measured sweep of the pump offset $B_{p,offs} = \pm 400\,\mu T$ for $B_p = 100\,\mu T$ and $B_s = 100\,nT$. The diamonds mark the offsets used for LoD measurements in Fig. 3.15.

With the model, the offset is swept roughly between the deflection points of the magnetostriction curve from $-0.4\,mT$ to $0.4\,mT$ for $B_p = 100\,\mu T$. The signal B_s is set to a fixed value for the simulations.

The results of the sweep are depicted in Fig. 3.13b. According to the model, the USB can be increased by more than 6 dB for an offset of $B_{p,offs} \approx -180\,\mu T$. For offsets in the vicinity of the bias curve peaks, the USB is reduced significantly. The carrier feedthrough in the output spectrum is minimised for an offset approximately equal to the shift of the minimum of the bias curve. To verify the calculations, a measurement with swept offset with $B_p = 100\,\mu T$ is performed.

The result is shown in Fig. 3.14. For an offset of $B_{p,offs} \approx -140\,\mu T$, the USB is increased from $6.5\,mV/\sqrt{Hz}$ to $12\,mV/\sqrt{Hz}$. The carrier shows a minimum for $B_{p,offs} \approx -18\,\mu T$ and thus can be decreased by the application of an offset. The signal-to-carrier ratio (SCR) is calculated by

$$SCR(B_{p,offs}) = 20 \cdot \log_{10}\left(\frac{USB(B_{p,offs})}{Carrier(B_{p,offs})}\right) \tag{3.23}$$

and indicates the carrier suppression. This will be further investigated in Subsec. 3.1.6. The noise, indicated with asterisks, is slightly decreased for increasing offsets.

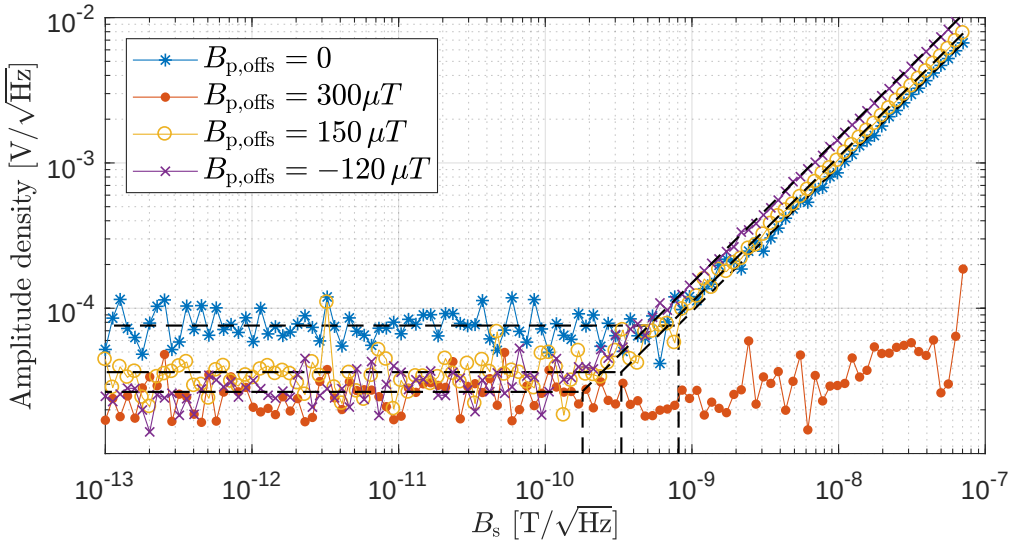

Figure 3.15: LoDs for four offsets indicated in the legend. The pump amplitude is $B_p = 100\,\mu T$. The linear signal regime, the average noise level, and the LoD are indicated with a dashed line. The measurement is averaged in order to reduce the variance.

Thus, the measured results fit the aforementioned calculations and a properly chosen offset should result in a better LoD.

The LoD is measured for four characteristic points: no offset, $B_{p,offs} = 300\,\mu T$, $B_{p,offs} = 150\,\mu T$, and $B_{p,offs} = -120\,\mu T$ as indicated in Fig. 3.14. The offsets are chosen because they are local maxima of the USB amplitude. The improvement of the LoD by a factor of approximately 5 can be seen in Fig. 3.15. This cannot be explained with a signal increase (factor 2.23), but is also due to decreased noise (factor 2.86). In Sec. 3.1.4, the pump amplitude for the highest USB is $B_p = 420\,\mu T$. Therefore, the calculations and measurements are also performed for this pump amplitude.

The calculation and measurement with offsets for $B_p = 420\,\mu T$ are depicted in Fig. 3.16. For this pump amplitude, an offset only reduces the USB amplitude.

The LoD plots are depicted in Fig. 3.17. Regardless of the offset, the LoD stays virtually unchanged. Thus, the noise and the signal decrease with the same ratio.

All resulting LoDs and sensitivities are summarised in Tab. 3.2. Both simulations and measurements show that the smaller the pump amplitude, the larger is the factor in amplitude (cf. Fig. 3.13b) that can be gained by an offset and the smaller is the absolute USB amplitude.

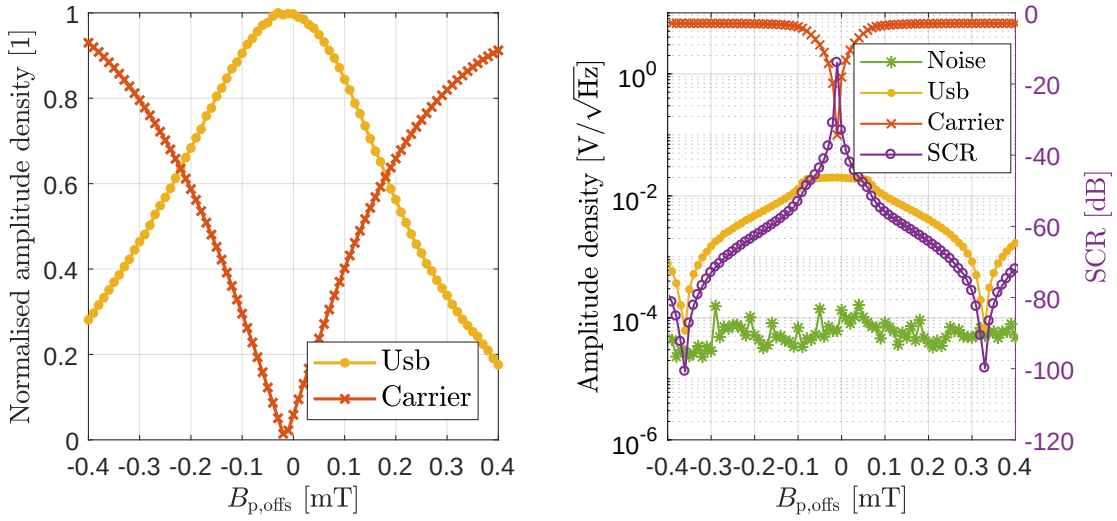

Figure 3.16: (a) Normalised amplitudes of the USB and the carrier as a function of an applied offset $B_{o,offs}$, calculated by the model. The pump amplitude is $B_p = 420\,\mu T$. (b) Measured sweep of the pump offset $B_{p,offs} = \pm 400\,\mu T$ for $B_p = 420\,\mu T$ and $B_p = 100\,nT$.

B_p [µT]	$B_{p,offs}$ [µT]	S_{MFC} [V/T]	LoD_{MFC} [pT/√Hz]
100	0	1479	800
	300	41	> 10000
	150	1727	320
	-120	2331	177
420	0	4517	349
	300	1484	386
	150	4214	341
	-120	2403	358

Table 3.2: Sensitivity and LoD results with MFC for a set of pump amplitudes and offsets.

The noise decreases for offsets as can be seen in the LoD plots above. This is further discussed in Sec. 3.1.7. The best LoD_{MFC} for this sensor does not occur for the aforementioned optimal pump amplitude $B_p = 420\,\mu T$. For all investigated pump amplitudes $B_p \in \{50,100,200,300,420,500\}\,\mu T$, a pump amplitude of $B_p = 100\,\mu T$ with an offset of $B_{p,offs} = -120\,\mu T$ yields the best LoD for this specific sensor.
Less sensitivity due to smaller pump amplitudes can be subsequently increased with an additional offset for ME sensors with certain characteristics. An excitation with

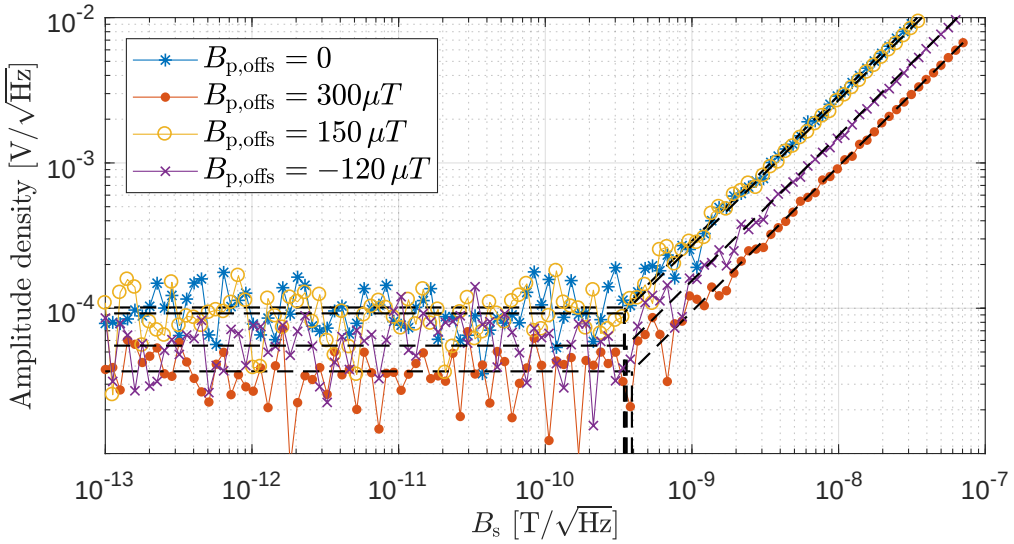

Figure 3.17: LoDs for four offsets indicated in the legend. The pump amplitude is $B_p = 420\,\mu T$. The linear signal regime, the average noise level, and the LoD are indicated with a dashed line. The measurement is averaged in order to reduce the variance.

a smaller pump amplitude and offset may even increase the LoD. Another idea to improve the signal behaviour is to apply non-sinusoidal pump signals.

Pump signal waveform Standard MFC uses a sinusoidal pump signal to excite the sensor. Slight improvements of the signal strength can be obtained by an offset. The pump signal sets a dynamic working point for the signal to be measured. Therefore, it should be advantageous to remain longer in the steepest points of the magnetostriction curve. A rectangular pump signal fulfils these requirements, and additionally passes the zero-crossing of the nonlinearity very fast. The pump coil acts as a low-pass filter, but rectangular signals with low frequencies such as $f_p = 850\,Hz$ are transformed into magnetic signals whose rectangular shape can still be measured with a magnetic sensor with enough bandwidth (see Figs. B.3 and B.4 in the appendix). In frequency domain, a rectangular signal consists of the fundamental frequency f_p and its odd harmonics with decreasing amplitude. Because the frequency response (2.3) of the sensor itself acts like a bandpass filter, only the conversion products of the fundamental frequency f_p are utilised in the resonance frequency. Therefore, a rectangular or similar signal waveforms such as a sinusoidal signal with fast zero transitions are not advantageous. There is also no

measurable advantage in terms of noise, which predominantly occurs in the zero-crossing of the nonlinearity. Domain wall movement excited by a weak alternating field can be described in analogy to a mass-spring system [CG09] with an oscillatory movement and damping mechanisms. With defects in the trajectory of the domain wall, they get stuck, and jump, regardless of the excitation frequency (see Subsec. 3.1.7). A theoretical rectangular excitation does not necessarily lead to a rectangular characteristic of the magnetisation due to the shape of the hysteresis curve. Therefore, no improvement in the noise behaviour is expected from a rectangular pump for this type of magnetic noise. In addition, for the investigated samples for MFC, the dominating mechanism is rotation instead of wall movement due to the multilayer structure of the magnetic layer. With a multi-mode excitation, single sinusoidal pumps can be generated such that they upconvert f_{s} into the mechanical resonance frequencies of the sensor, i.e. also into higher order resonance frequencies. For a multilayer sensor with 20 magnetic layers and EB very similar to the sensor investigated in [Röb+15], the first three bending modes are at 851 Hz with 2 Hz bandwidth, 5.287 kHz with 70 Hz bandwidth, and 14.9 kHz with 170 Hz bandwidth. According to [Ree+16a; Ree17], a readout scheme based on combination (*Maximum-Ratio Combination, MRC*) theoretically improves the SNR by

$$\Delta\mathrm{SNR} = 10\log_{10}\left(N_{\mathrm{s}}\right) \tag{3.24}$$

with the number N_{s} of available signals, if the individual noise sources are uncorrelated and equal in noise power. Therefore, the signals at several resonant modes of the sensor can be demodulated individually to obtain N_{s} signals. The combination is performed digitally after demodulation and equalisation, weighted with a linear factor according to SNR-based combination.

Fig. 3.18 shows the resulting spectral densities for multi-mode excitation at the first three resonant modes. The respective pump amplitudes are chosen in order to maximise the SNR of the single-mode excitations. The desired signal is converted into all three resonances. The difference in height between the side-bands corresponds to the bandwidth of the respective mode. All three signals contain the same signal information, yield comparable LoDs, and can therefore be used for combination.

Tab. 3.3 summarises the estimated LoDs for this sensor (results are also published in [Ree17]), whereas the noise floor is estimated from the measurements in the frequency range from 15 Hz to 25 Hz above the respective pump signal. For the

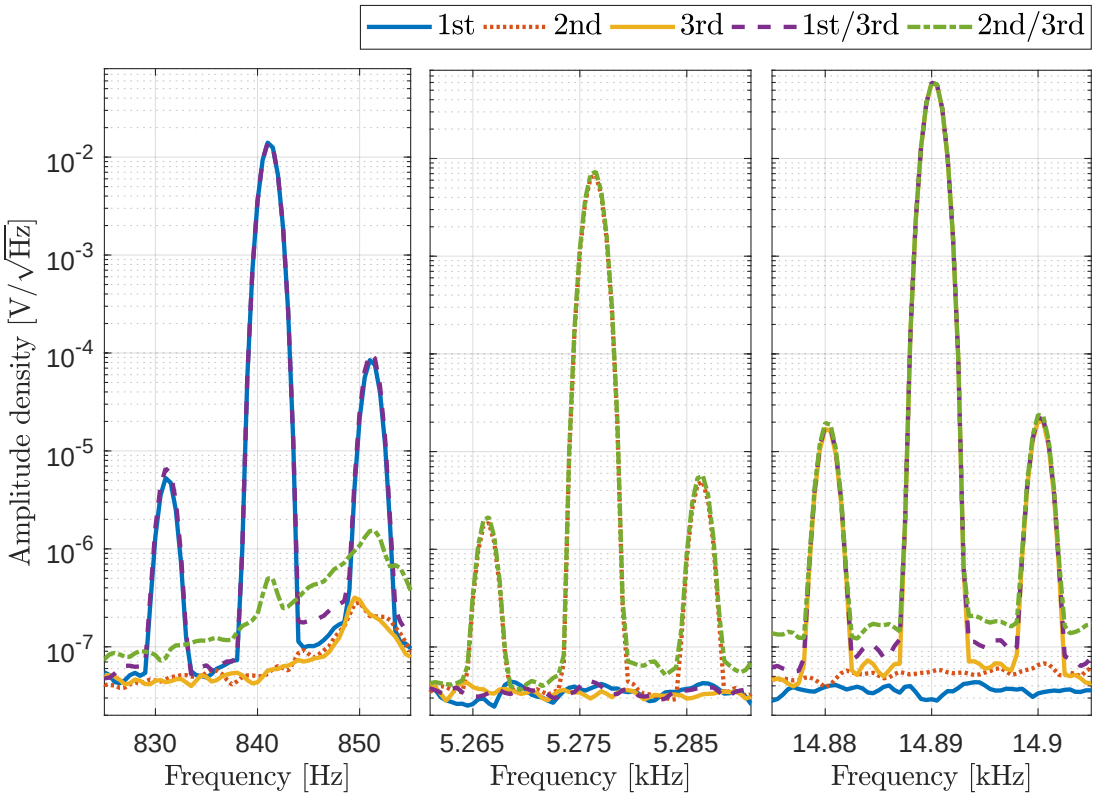

Figure 3.18: Excitation with three pumps signals B_1 at $f_{p1} = 841\,\text{Hz}$ with $B_{p1} = 43\,\mu\text{T}$, B_2 at $f_{p2} = 5.27\,\text{kHz}$ with $B_{p2} = 52.5\,\mu\text{T}$, and B_3 at $f_{p3} = 14.89\,\text{kHz}$ with $B_{p3} = 30\,\mu\text{T}$. The desired signal has a frequency of $f_s = 10\,\text{Hz}$ and an amplitude of $B_s = 100\,\text{nT}$.

single modes, the lowest estimated LoD is achieved for an excitation in the third mode for this sensor.

The combinations of mode 1st/3rd and mode 2nd/3rd are depicted with a dashed and a dash-dotted line in Fig. 3.18. The excitation of two modes simultaneously increases the noise level, as can be seen in 2nd/3rd, and also without applied signal B_s. It worsens also the LoDs at the resonance frequencies of the individual modes. This can be due to a higher total pump power in the system when two modes are excited simultaneously. If the second mode is excited, the noise increase is highest which may be due to the relatively high excitation amplitude of the second mode as compared to the other modes. Compared to the best single-mode excitation, the combination of the 1st/3rd mode slightly improves the LoD by 2.3 dB.

Excitation	Readout Frequency [Hz]	LoD [pT/$\sqrt{\text{Hz}}$]
B_1	851	285
B_2	5287	521
B_3	14900	166
B_1 & B_3	851	340
B_1 & B_3	14900	217
B_1 & B_3	851 & 14900	128
B_2 & B_3	5287	625
B_2 & B_3	14900	407
B_2 & B_3	5287 & 14900	253

Table 3.3: Estimated LoDs for MFC with excitation and readout at specific frequencies according to the signals of Fig. 3.18. The combined readout of mode 1st/3rd and mode 2nd/3rd are highlighted with a grey background.

In principle, a combination of several excited modes can improve the LoD for magnetic frequency conversion.
To exploit the stress concentrations of different modes, changes to the sensor layout are required, as is described in [Zab+16] for ΔE_{d}-sensors.
Additionally, the combination makes the readout more robust against acoustical noise due to an adaptive weighting of the modes mainly determined by their noise power [Ree+16a]. However, it is not possible to perform both SNR-based combination and noise reduction at the same time.
In summary, MFC with other signal waveforms than sinusoidal signals is not advantageous. A conversion to higher modes can lower the LoD while being more robust to low-frequency noise. In principle, a combination of several simultaneously excited modes can further lower the LoD and be used as a noise reduction technique.

3.1.6 Carrier Suppression for MFC

In previous measurements, the output spectra exhibit a carrier feedthrough at the frequency f_{p} which is sometimes three or four orders of magnitude higher in amplitude as compared to the sidebands. Depending on the noise level this can lead to problems with the DR of the signal processing electronics.

The necessary DR for the MFC is given by the coefficient of the largest and the smallest signal of interest in the output spectrum, i.e.

$$\mathrm{DR}_{\mathrm{ME}} = \frac{\text{Carrier amplitude}}{\text{USB amplitude}}. \tag{3.25}$$

For MFC the largest signal is, in most cases, the carrier at the output, whereas the smallest signal is either the sideband used for signal readout or the noise floor. All involved signals are boosted in amplitude by the mechanical resonator of the sensor according to the frequency dependent $G_{\mathrm{mech}}(f)$. Therefore, $G_{\mathrm{mech}}(f_{\mathrm{p}}) \neq G_{\mathrm{mech}}(f_{\mathrm{res}})$ and components at frequencies far outside resonance can be neglected.
Amongst others, possible undesired side-effects can be an overload of the analogue amplifier, which results in nonlinear behaviour in the signal path. On the other hand, or the ADC could run out of bits to adequately resolve the input noise, accompanied by an increase in quantisation noise. Both examples result in an increase in noise not caused by the sensor. The available DR of common readout electronics is around 120 dB to 140 dB.
The reason why the carrier appears as crosstalk at the output is the slight asymmetry of the nonlinear curve. As described by Eq. (3.3), a linear coefficient $a_1 \neq 0$ transforms the weighted input signals to the output. Considering a realistic nonlinear function there are higher order non-zero coefficients.
As an example, a polynomial with coefficients $a_i \neq 0, i \in \{0,\ldots,8\}$ is considered, for simplicity assuming that $a_i = 0$ for $i > 8$. The component at the pump frequency f_{p} is transformed to the output with the factor A_1

$$A_1 \cdot \cos\bigl(2\pi f_{\mathrm{p}} t\bigr) \tag{3.26}$$

with

$$\begin{aligned} A_1 = {} & \frac{35\,a_7\,\hat{b}_{\mathrm{p}}^7}{64} + \frac{105\,a_7\,\hat{b}_{\mathrm{p}}^5\,\hat{b}_{\mathrm{s}}^2}{16} + \frac{5\,a_5\,\hat{b}_{\mathrm{p}}^5}{8} + \frac{315\,a_7\,\hat{b}_{\mathrm{p}}^3\,\hat{b}_{\mathrm{s}}^4}{32} + \frac{15\,a_5\,\hat{b}_{\mathrm{p}}^3\,\hat{b}_{\mathrm{s}}^2}{4} \\ & + \frac{3\,a_3\,\hat{b}_{\mathrm{p}}^3}{4} + \frac{35\,a_7\,\hat{b}_{\mathrm{p}}\,\hat{b}_{\mathrm{s}}^6}{16} + \frac{15\,a_5\,\hat{b}_{\mathrm{p}}\,\hat{b}_{\mathrm{s}}^4}{8} + \frac{3\,a_3\,\hat{b}_{\mathrm{p}}\,\hat{b}_{\mathrm{s}}^2}{2} + a_1\,\hat{b}_{\mathrm{p}}. \end{aligned} \tag{3.27}$$

All non-zero odd coefficients contribute to the feedthrough of the pump signal. The level is then a function of the involved coefficients, the amplitude of the modulation

Resonance frequency	921 Hz ±1 Hz
Quality factor	131
Sensor capacitance	390 pF
Sensitivity	140 V/T
Cantilever width × height × length	2.2 mm×0.35 mm ×25.2 mm
Free standing cantilever length	22.9 mm

Table 3.4: Properties of the investigated multilayer sensor used for carrier suppression.

signal $\hat{b}_{\mathrm{p}}$ and the amplitude of the signal to be measured $\hat{b}_{\mathrm{s}}$. This proves that an asymmetry of a nonlinear curve is the origin of the feedthrough.
In the following, two methods to suppress this crosstalk are presented: Suppression by outphasing utilising an adaptive phase shifter (APS) and suppression of the phenomenon using an offset. The sensor used for this investigation is a standard multilayer sensor with the piezoelectric layer stack Ta (24 nm)/Pt (150 nm)/AlN (2000 nm)/Cr (5 nm)/Au (100 nm) forming a plate capacitor with a Cr/Au top electrode (thickness in brackets). It has the size of 1.2 mm × 5 mm and is located close to the clamping. On the reverse side of the 350 µm thick silicon substrate, the magnetostrictive layer stack with a 5 times repeated sequence of Ta (5 nm)/Cu (3 nm)/MnIr (8 nm)/FeCoSiB (200 nm) is deposited. An exchange bias anisotropy is applied via magnetic field annealing (250 °C, 30 min, 0.1 T) with 90 ° to the long axis of the cantilever.
Further sensor parameters are summarised in Tab. 3.4.

APS suppression In the spectrum the carrier appears, in good approximation, as a mono frequent peak (see Fig. 3.1), corresponding in time domain to a sinusoidal signal. Adding a second sinusoidal signal of equal frequency in antiphase with the same amplitude largely leads to extinction. In [Mal+13] a differential low-noise amplifier is inserted into the signal chain before the readout electronics. An amplitude and phase controlled signal, generated by a second independent generator, is applied to one input. By adjusting its amplitude and phase, the large carrier component in the output signal was reduced and the signal to noise ratio enhanced. The same approach was also applied in [ZSD12] and [Zhu+15b] for ME sensors.
From a signal processing point of view it makes sense to eliminate the carrier (carrier suppression, CS) before the signal is amplified by the charge amplifier (cf. [Ree+16a]), i.e. before the unwanted carrier is amplified even further and may

lead to overdrive. Therefore, the pump signal is added to the signal path, after its phase has been tuned to antiphase with respect to the original feedthrough. This does not necessarily mean that a phase shift of 180° degrees of the pump and adding it after the signal leads to desired destructive interference, because the sensor itself and other influences lead to an additional phase shift in the signal path. In practice, a sample of the pump signal is phase adjusted in an APS, amplitude adjusted, and subtracted from the sensor output.

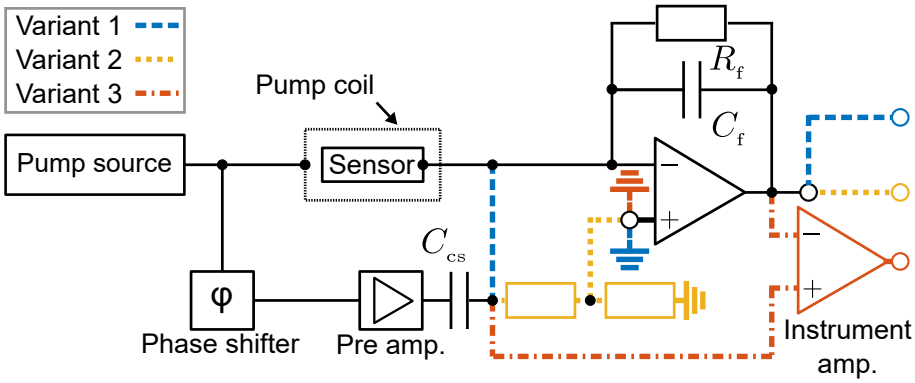

Figure 3.19: Coupling of the phase shifter signal into the signal path. The variants for three coupling alternatives are marked in different colours and line styles in the figure.

For the coupling, three variants are tested as depicted in Fig. 3.19. The output signal of the APS is coupled into the signal path via a coupling capacitor C_{cs}, either into the direct sensor path (variant 1, blue), the non-inverting input of the charge amplifier (variant 2, yellow), with a voltage divider to sustain a bias path to ground, or in the output path with an instrumentation amplifier (variant 3, red). Variant 2 is inspired by [Zhu+15b] where the non-inverting input is used to provide an excitation via a voltage divider. Variant 3 would eliminate the carrier after the amplification by the charge amplifier.

A possible solution to the phase shifter is depicted in Fig. 2.20. It basically consists of a microcontroller, and a concatenation of operational amplifiers and relays (see Sec. 2.4 for details). The phase shifter minimises the carrier amplitude in an automatic iteration. To determine the actual carrier amplitude, spectral information is processed. The phase shifter is then set by the microcontroller accordingly until a minimum is reached.

Fig. 3.20 shows the output signal of a MFC with CS applied or switched off using a coupling capacitor of $C_{cs} = 10\,\mathrm{pF}$ and the coupling variant 1 (cf. Fig. 3.19).

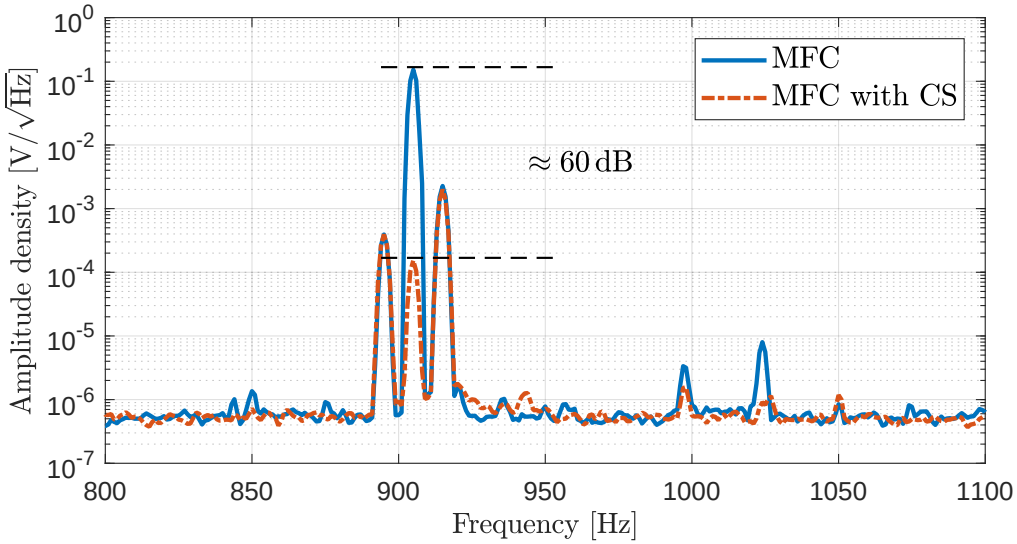

Figure 3.20: MFC measurement of the investigated sensor with and without CS. The signal to be measured is $B_s = 1\,\mu T$ and the carrier $B_p = 400\,\mu T$. The suppression of the carrier amplitude is approximately 60 dB.

The carrier feedthrough can be reduced by approximately 60 dB without affecting the sideband amplitude or increasing the noise floor. The other variants will be discussed later. Applying the suppression, the dynamic range is not degraded by a strong carrier, but is determined by the desired sideband amplitude for the given signal. If the signal B_s is lowered, the dynamic range of the applied amplifier or ADC will still be higher than the required dynamic range for the suppressed carrier, which is only about 50 dB.
The method can also be realised using a digitally generated signal that can be adjusted very precisely in amplitude and phase. In [Ree+16a] a carrier is suppressed by 50 dB by manually adjusting the amplitude and phase. The main difference is that the suppression signal is generated individually and needs to be frequency locked to the pump signal. In the aforementioned method the suppression signal is derived directly from the pump signal.
The APS suppression method should sufficiently suppress the carrier, if the phase could be set with enough precision.

Offset suppression Another method is to apply a very small suppressing offset to an unsymmetrical magnetostriction curve. In Subsec. 3.1.5, the offset applied in order to enhance the signal also affects the carrier and the SCR indicates the carrier

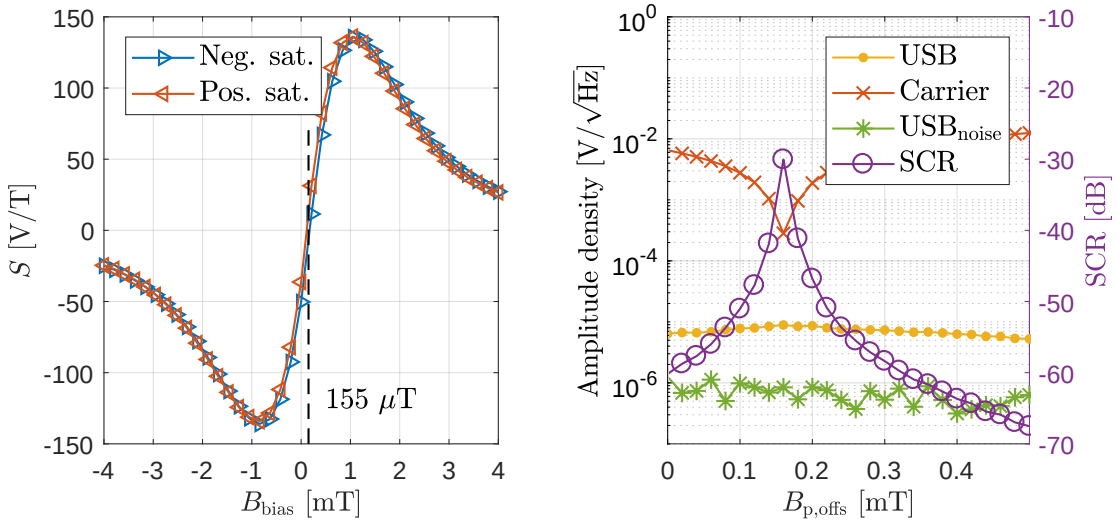

Figure 3.21: (a) Bias curve of the investigated sensor. The saturation direction is indicated with triangles. The offset from zero is $B_{\text{offs}} = 155\,\mu\text{T}$ (determined with interpolation). The sensor is saturated with $\pm 7\,\text{mT}$ during the measurement loop. (b) Measured USB, carrier, USB$_{\text{noise}}$, and SCR as a function of applied pump bias for $B_{\text{p}} = 10\,\mu\text{T}$ and $B_{\text{s}} = 100\,\text{nT}$. The sampling points are indicated in Fig. 3.9a.

suppression. A SCR of 0 dB ensures that the dynamic range is determined by the signal and not the carrier.

Fig. 3.21a shows the bias curve of the investigated sensor. The dashed line indicates the offset of the curve from zero, i.e. the asymmetry of the curve. In the introduction of this subsection, the origin of the feedthrough of the carrier is explained and it is indicated which coefficients are responsible. Reducing the asymmetry caused by a shift of the bias curve will thus reduce the carrier feedthrough. Centering the carrier B_{p} with an offset around the zero crossing of the bias curve decreases the aforementioned asymmetry.

Fig. 3.21b shows the USB, carrier, USB$_{\text{noise}}$, and the SCR for offsets ranging from 0 µT up to 500 µT. The best carrier suppression for the investigated sensor is achieved with an offset of $B_{\text{p,offs}} = 160 \pm 10\,\mu\text{T}$. That amount of field is similar to the offset of the bias curve. The pump signal alleviates the nonlinearity of its asymmetry and thus reduces the carrier amplitude. The carrier is suppressed by $\approx 27\,\text{dB}$ relative to an excitation without offset. As a side effect the sideband amplitude is also at its maximum at that offset for this pump amplitude and sensor. This is because the symmetry favours the quadratic mixing component (cf. Subsec. 3.1.2). Here

$B_{\mathrm{p,offs}}$ is supplied via an offset to the signal of the pump source, but it can also be installed by permanent magnets. The suppression depends on how precisely the offset is set, but also on the chosen pump amplitude. In Figs. 3.14 and 3.16b, the carrier suppressions by offset are 6 dB and 19 dB, respectively, for various pump amplitudes. In [Dur+17a], application of an offset suppresses the carrier by 57 dB resulting in a SCR of 0 dB. With this technique, tolerances and inaccuracies in the fabrication process of the sensor that lead to a shift of the magnetostriction curve can be alleviated without applying additional circuitry.

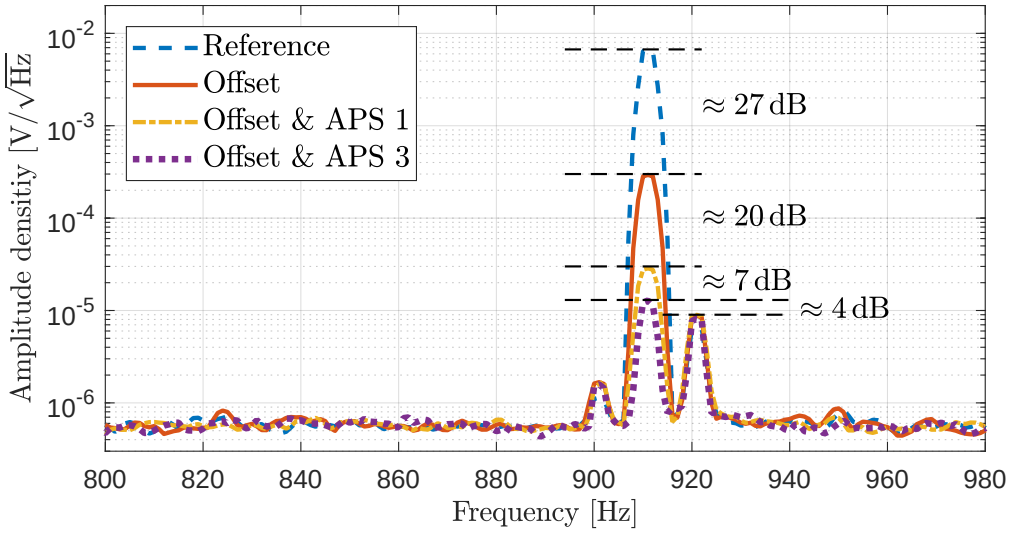

Figure 3.22: Spectra of the combinations of different carrier suppression approaches for $B_{\mathrm{s}} = 100\,\mathrm{nT}$ and $B_{\mathrm{p}} = 10\,\mu\mathrm{T}$

Combination The application of an offset is more practical than suppression with an APS, because less effort is required. However, for particular bias curves and pump amplitudes, the offset suppression cannot reach a SCR of 0 dB. The investigated sensor features not only asymmetry due to the shift of the zero-crossing, but also inherent asymmetry of the nonlinearity.

Fig. 3.23 shows the normalised magnetostriction curve. The trace for negative bias fields is mirrored at its deflection point for better comparison with the trace for positive fields. The magnetostriction curve is not mirror symmetrical. This is because there are more odd non-zero coefficients in the bias curve other than the DC offset. This inherent asymmetry is due to the offset. Every offset of the magnetostriction curve, e.g. caused by a tilt in the exchange bias anisotropy, also

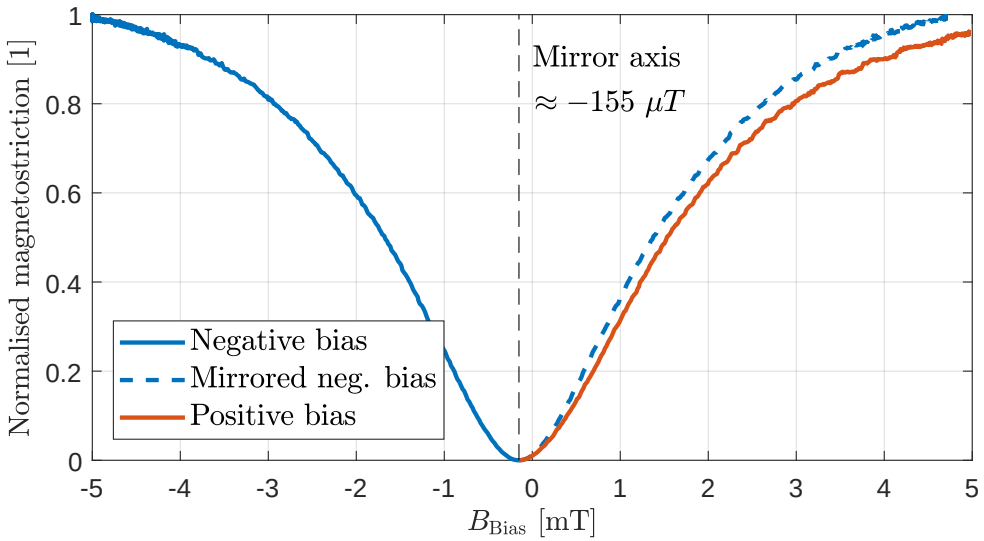

Figure 3.23: Magnetostriction curve of the investigated sensor, calculated from the bias curve in Fig. 3.21a. It is normalised to the maximum of the trace for the negative bias fields. The minimum of the curve is indicated by a dashed mirror axis.

causes an asymmetry proportional to the offset. The signal in the direction of the tilted exchange bias is increased (here the negative bias trace), whereas the signal in the opposite direction is decreased. The offset bias field or misaligned EB field can be seen as a scaling factor for the magnetostriction signal response with bias field. Thus, an offset cannot remove the curve's asymmetry and the carrier cannot be eliminated completely by the offset suppression.

However, the carrier suppression can be improved by combining the two above mentioned techniques. The result of the combination can be seen in Fig. 3.22. If the offset method is combined with APS suppression and coupling variant 1 with a coupling capacitor of $C_{\text{cs}} = 1\,\text{pF}$ and 1:10 voltage divider at the APS input, the suppression can be increased by another $\approx 20\,\text{dB}$. The variant 2 with different voltage dividers and coupling capacitors shows no improvement as compared to offset suppression and is thus not displayed or further discussed here. If variant 3, coupled with $C_{\text{cs}} = 100\,\text{pF}$, is used the additional yield is even $\approx 27\,\text{dB}$ resulting in a virtually complete carrier suppression of $\approx 54\,\text{dB}$, while the sideband stays unchanged. For this setup and these amplitudes, the combination yields the best result as compared to suppression exclusively with APS or offset.

In general, the method of applying additional offset is to be preferred, since it requires no additional coupling paths or electronics. The carrier cannot be suppressed

completely by any of the proposed methods because the precision of the phase setting for the APS is limited and due to the inherent asymmetry of the magnetostriction curve.
In principle, this asymmetry can be alleviated by pre-distortion of the carrier signal similar to pre-distortion for radio frequency power amplifiers [Cri02]. The main difference is that, in this case, the aim is not a linearisation but a *quadratisation*, to achieve maximum signal at the sideband and suppression of the carrier at the output. Investigations with asymmetric pumps resulted in outphasing of 70 dB suppression as a proof of concept, almost making the carrier disappear in the noise floor (see Fig. B.5 in the appendix).
With the discussed methods, even circuits with a relatively low dynamic range of $< 100\,\mathrm{dB}$ can be used for MFC measurements of any investigated sensors without obtaining noise caused by problems with the dynamic range. The noise of the MFC originates from other sources which will be discussed in the next subsection.

3.1.7 Noise in MFC

In Sec. 2.5, the noise sources for magnetoelectric thin-film sensors operated in direct detection were discussed. For MFC, there are two additional noise sources that become dominant during operation. They are magnetic excess noise originating from the magnetic material and pump noise introduced by the pump source that drives the sensor (cf. the block diagram in Fig. 3.6). However, MFC also reduces the influence of noise sources that might be dominant during direct detection. MFC converts a low frequency signal of interest into the mechanical resonance, i.e. to higher frequencies. Thus, flicker noise from the charge amplifier is avoided. External low frequency vibrational or acoustical noise is reduced at higher frequencies. Acoustical as well as amplifier noise enter the system after the upconversion process, as shown in the block diagram. In [Sal+17a; Dur+17c], it is discussed and confirmed by measurements that a magnetic pump signal does not convert low frequency acoustical noise into the USB (or LSB) of the carrier. Another noise source that needs to be considered for MFC is quantisation noise of the ADC which mainly depends on its pre-amplification and dynamic range. The devices used for readout in this investigation have a dynamic range of approximately $120 - 140\,\mathrm{dB}$. The SR785 spectrum analyser has a measured input noise floor of $16\,\mathrm{nV}/\sqrt{\mathrm{Hz}}$ up to $10\,\mu\mathrm{V}/\sqrt{\mathrm{Hz}}$ and depends on the input range of the adaptive internal pre-amplifier. Therefore,

the strong carrier in the output spectrum may lead to dominant quantisation noise. The suppression methods introduced in Subsec. 3.1.6 solve this problem.

Magnetic excess noise The sensor under investigation for the following investigations is explained in detail in Subsec. 3.1.4. In practice, it is experienced that the noise level at the mechanical resonance frequency increases drastically when a pump signal is applied to the sensor (see e.g. Fig. 3.12).

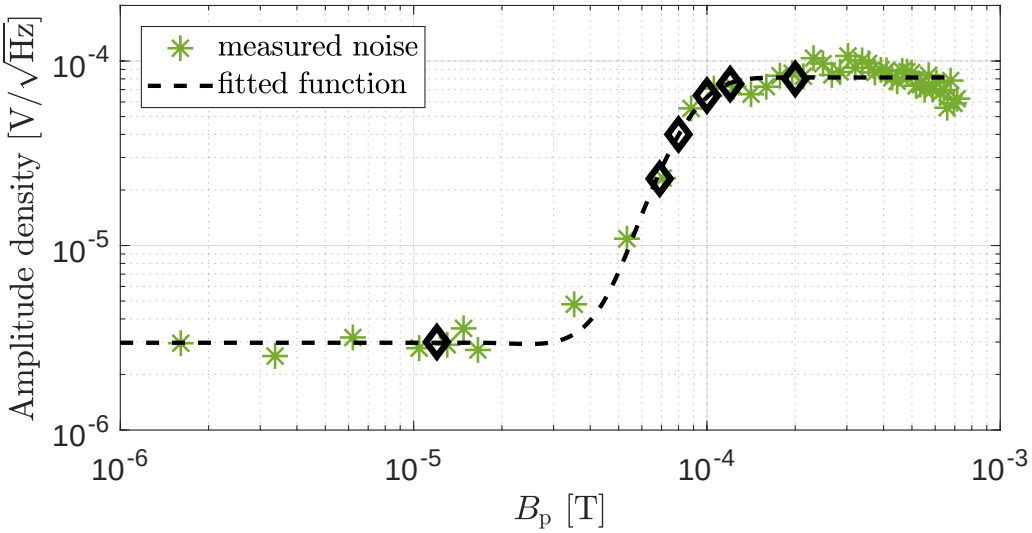

Figure 3.24: Increase of the noise at resonance ($\mathrm{USB}_{\mathrm{noise}}$) as a function of the applied pump amplitude. A fitting function is displayed with a dashed line. Sample points for MOKE images are indicated with diamond markers.

Fig. 3.24 depicts the noise at resonance $\mathrm{USB}_{\mathrm{noise}}$ as a function of the pump amplitude. The noise increase can be fitted with a Debye function (cf. [AS64]) as described in detail in [Sal+17a] and depicted in Fig. 3.24. All measured noise increases for various magnetoelectric thin-film sensors feature this Debye characteristic which enables a comparison by characteristic points. For low amplitudes $B_{\mathrm{p}} < 40\,\mu\mathrm{T}$, the noise level is constant. From $B_{\mathrm{p}} = 40\,\mu\mathrm{T}$ to $B_{\mathrm{p}} = 150\,\mu\mathrm{T}$, it rises significantly. For higher amplitudes, the noise stays at a constant high level approximately 2.5 decades higher than the constant lower level. The slight decrease towards $B_{\mathrm{p}} = 1\,\mathrm{mT}$ is due to the pump source not being able to supply enough power.
Respective time resolved MOKE images [Urs+16] for the pump amplitudes marked with diamond markers are depicted in Fig. 3.24. The sensor is excited with a pump-like signal and the magnetisation pattern is captured at specific sample points of the

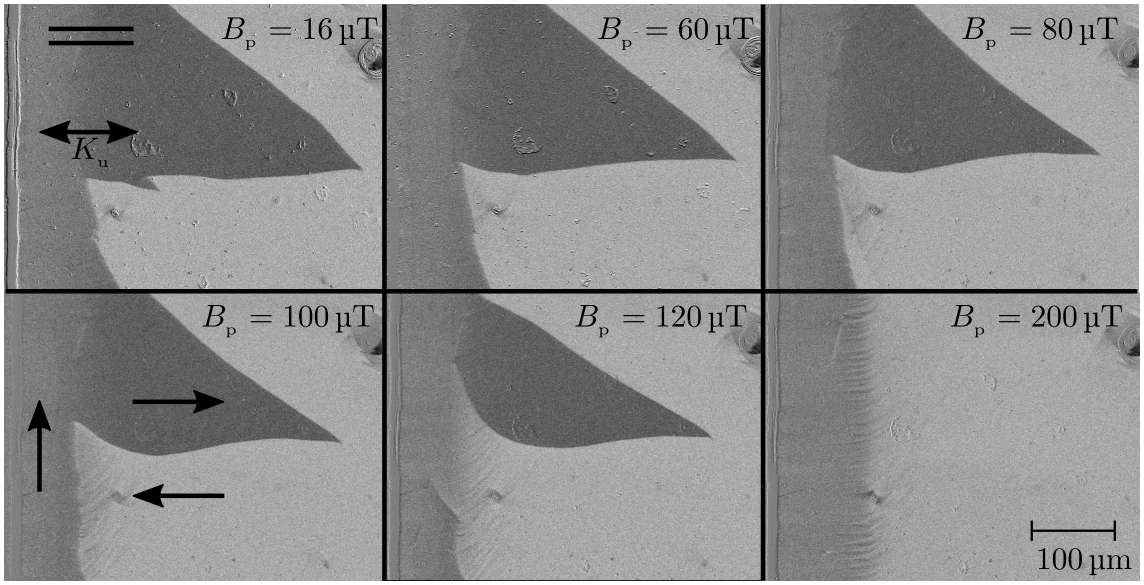

Figure 3.25: Dynamic MOKE images of the sensor at the edge of the long axis near the clamping measured in cooperation with the material science department. The pump amplitudes range from $B_p = 16\,\mu T$ up to $B_p = 200\,\mu T$ and is applied vertically. In the upper left picture the horizontal MOKE sensitivity direction is indicated by two parallel lines and the orientation of the induced magnetic anisotropy K_u is indicated by a double-headed arrow. The arrows in the lower left picture indicate conceivable magnetisation directions.

sinusoidal excitation, synchronised with a trigger line. This allows the visualisation of the domain structure at desired instants of the excitation period. The domain structure consists mainly of closure domains and qualitatively explains the noise function above. Closure domains occur due to a closure of the flux of stray fields and are likely located near the edges of a magnetic sample. The strongest magnetisation occurs between $B_p = 120\,\mu T$ and $B_p = 200\,\mu T$. A noise increase above $B_p = 200\,\mu T$ does not occur because the domain wall activity saturates.

In [Bar19], magnetic noise is detected via a pick-up coil setup with a high gain amplifier and a loudspeaker. The magnetisation of a magnetic core is steadily changed by the transversal movement of a permanent magnet. The change of magnetisation from the core is detected by the pick-up coil and converted to sound by the loudspeaker. Rapid changes of the magnetisation can be heard as sudden crackling sounds and cannot originate from steady field by the permanent magnet.

A setup inspired by that work is depicted and explained in Fig. 3.26.

Fig. 3.27 shows the results of the measurements with the setup. Without an offset, the detected voltage follows the excitation but features high frequency spikes on top

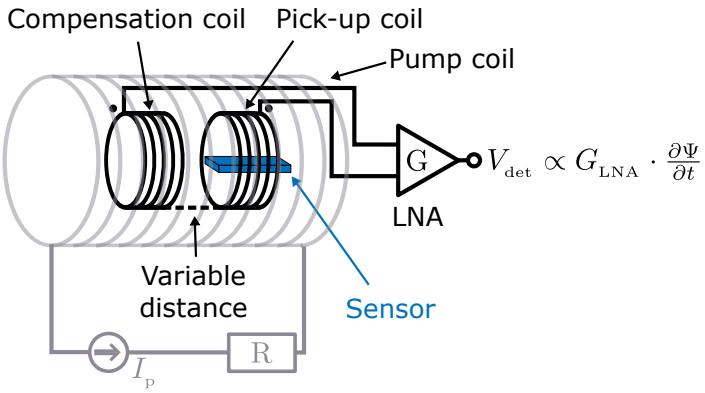

Figure 3.26: Measurement setup for magnetic excess noise measurement. The compensation coil is set to a specific distance relative to the reverse wound pick-up coil such that the resulting detection voltage V_{det} is zero without excitation. The pump current then I_{p} produces a pump signal via the pump coil. A low noise amplifier (LNA) with a gain of $G_{\mathrm{LNA}} = 500$ detects the differential detection voltage V_{det} which is proportional to the change in magnetic flux Ψ.

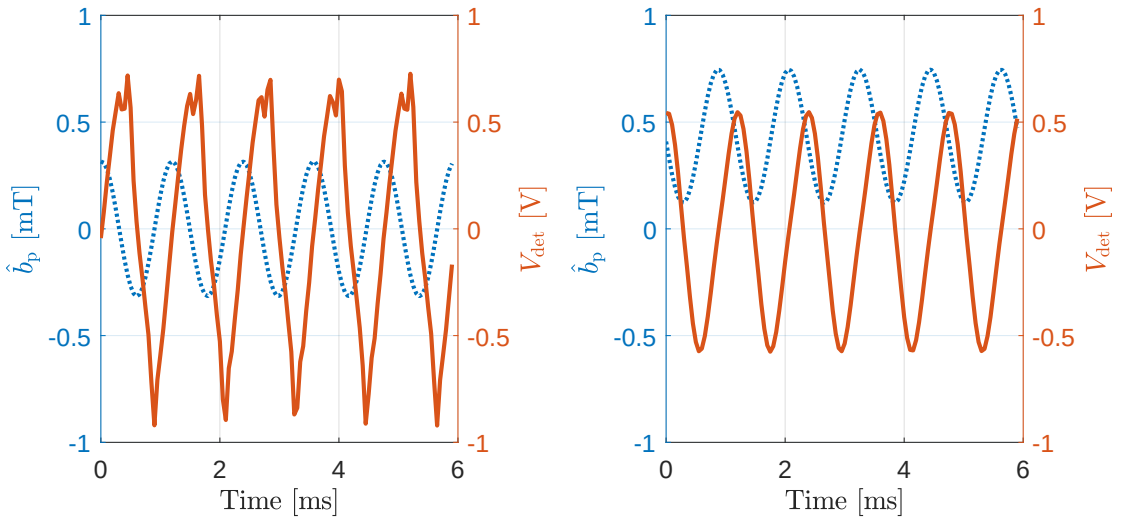

Figure 3.27: Magnetic excess noise measurements (a) without offset and (b) with $B_{\mathrm{p,offs}} = 400\,\mu\mathrm{T}$, conducted with the setup from Fig. 3.26. The dotted line represents the pump signal with $B_{\mathrm{p}} = 300\,\mu\mathrm{T}$ and $f_{\mathrm{p}} = 842\,\mathrm{Hz}$ used for excitation (left axes). The solid line shows the detected voltage (right axes).

of the triangular shaped signal. In the frequency regime, the spikes result in white noise. They are the result of an unsteady change in magnetisation although the applied pump signal is sinusoidal. The magnetic noise occurs mainly in the zero-crossings of the magnetostriction curve as can be seen in Fig. 3.27a. In Subsec. 3.1.5,

the noise decreased for offsets. Therefore, an offset is chosen such that the pump does not go through the zero-crossing of the magnetostriction curve ($B_{\mathrm{p,offs}} > B_{\mathrm{p}}$). The application of an offset eliminates the spikes at the maxima of the detected voltage (see Fig. 3.27b). In the spectral domain, the wideband noise decreases more than 20 dB for the application of an offset. This is due to less domain activity because rearrangement and nucleation of domains that predominantly occur in the zero-crossing can be avoided by the offset.
In the following, a discourse about the relationship between magnetic domains and noise and the development of magnetoelectric thin-film sensors regarding magnetic noise is provided.
Magnetic excess noise is mainly due to domain wall motion and nucleation in the material [Jil00]. Therefore, hysteresis is an indicator for magnetic noise and goes hand in hand with energy loss. Especially when domain walls collapse during a magnetisation cycle, the rearrangement and reorientation causes significant domain wall activity. Local magnetoelastic effects strongly influence the overall noise behaviour of a cantilever. More details can be read in [Urs+14].
The conclusion for the sensor fabrication is to reduce the domain wall movement. This is done by designing single domain magnetostrictive layers. A design with exchange bias lowers the noise by preventing domain nucleation (growing of domains), and allows only rotational movement of the magnetic moments at the cost of less signal [Lag+14; Röb+15]. Sensors with more multilayers can have more magnetostrictive material and feature increased magnetostriction, i.e. signal, as compared to a small number of multilayers while maintaining, to some extent, the aforementioned noise advantages.
With multilayer sensors, there is no visible noise in the magnetic excess noise measurement. Still, the measurement of the noise function shows increased noise at the resonance frequency for increasing pump amplitude.
According to the block diagram, another possible noise source is the noise of the pump source.

Phase noise The noise of an excitation source, like the one used for pumping the magnetostrictive layer, can be categorised into amplitude noise and phase noise. The latter is distributed in noise sidebands around the excitation frequency, mainly with an $1/f$ characteristic [Bel85]. Typically, phase noise of a source decreases for lower oscillation frequencies. For standard MFC, the pump signal in the output

spectrum is f_s Hz away from f_{res} where the increase by G_{mech} reaches its maximum. A superposition with an $1/f^q$ characteristic would result in an asymmetric shape of the noise increase. Moreover, the noise would decrease for growing offset $f_{res} - f_p$.

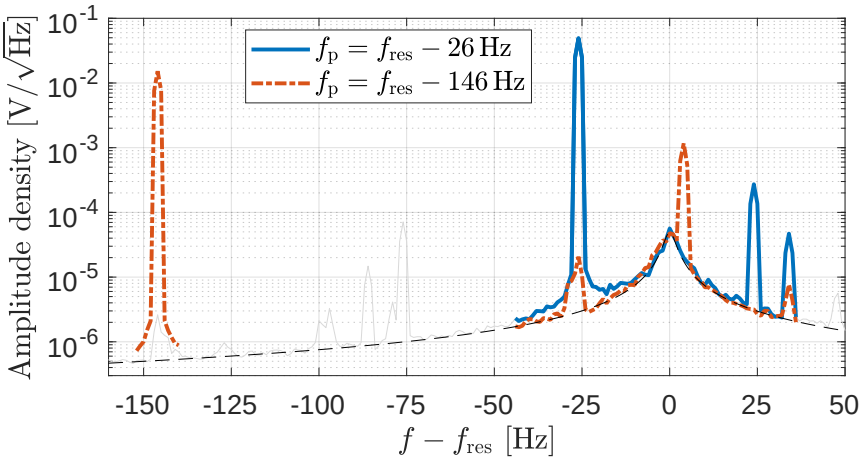

Figure 3.28: Measurement of the noise increase at the resonance frequency in dependency of the pump signals with equal amplitude and with 26 Hz and 146 Hz offset to f_{res}. The frequency axis is normalised to f_{res}. For better visibility, the relevant frequencies are highlighted. The complete spectral density for the pump signal with $f_p - f_{res} = 26$ Hz is depicted in light grey for reference. A fitted resonance curve is indicated with a dashed line.

Fig. 3.28 shows the result of a measurement with two pump signals of equal amplitude at two offset frequencies from the resonance frequency. The increase of noise around f_{res} is symmetrically distributed around f_{res}, equal for both excitations, and it fits the shape of the resonance curve. Consequently, the noise has a white frequency behaviour, is enhanced by G_{mech}, and its source is not the phase noise of the pump source.
In order to arrive at a better understanding of the noise behaviour of MFC, the noise model for the direct detection is extended for the sources discussed above. The wideband noise of the source is of particular interest.

MFC noise model The noise model for MFC includes all noise sources from Sec. 2.5.5. Additionally, the magnetic excess noise $\tilde{E}_{mag}$ and the wideband noise of the pump converted into magnetic noise $\tilde{E}_{mp}$ are considered in the form of equivalent voltage noise sources.

For modulated laminated magnetoelectric sensors, the noise from the measurement system is found to be the dominant component [Zhu+15a] without going into detail. Other publications on magnetoelectric sensors with MFC do not consider the noise of the excitation source at all.

The pump source used in the present investigation is a voltage controlled low noise current source. It supplies the pump coil with the current required to excite the desired pump amplitude B_p. The current noise of the source is thus also converted into a magnetic field.

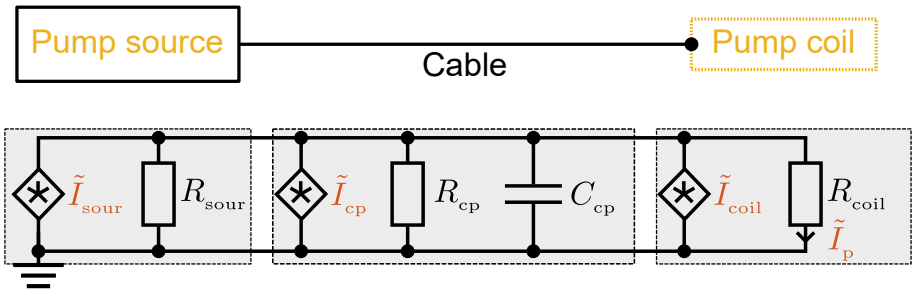

Figure 3.29: Noise equivalent circuit of the excitation network. The respective elements are indicated above the ECD. The source current $\tilde{I}_\mathrm{sour} = (\tilde{I}^2_{R_\mathrm{sour}} + \tilde{I}^2_\mathrm{DA})^{1/2}$ consists of the noise current spectral density (NCSD) from the output resistance R_sour and the noise of the digital to analogue converter (DAC) $\tilde{I}^2_\mathrm{DA}$. $\tilde{I}_\mathrm{cp}$ is thermal noise from the cable between the pump source and the coil, with its resistance R_cp and capacitance C_cp. The pump coil contributes the current noise $\tilde{I}_\mathrm{coil}$ due to its loss represented by R_coil. Its inductance and the source capacitance are neglected for the noise calculation. The total noise current through the pump coil is $\tilde{I}_\mathrm{p}$.

It can be calculated with the following equations and the noise equivalent circuit depicted in Fig. 3.29.

The resistance and impedance of the cable are given by

$$R_\mathrm{cp} = \frac{1}{\omega C_\mathrm{cp} \tan\delta_\mathrm{cp}} \tag{3.28}$$

and

$$Z_\mathrm{cp} = \frac{1}{\frac{1}{R_\mathrm{cp}} + j\omega C_\mathrm{cp}}. \tag{3.29}$$

The total impedance of the excitation network is

$$Z_\mathrm{p} = R_\mathrm{sour} \parallel Z_\mathrm{cp} \parallel R_\mathrm{coil} = \frac{R_\mathrm{sour} Z_\mathrm{cp} R_\mathrm{coil}}{R_\mathrm{sour} Z_\mathrm{cp} + R_\mathrm{sour} R_\mathrm{coil} + Z_\mathrm{cp} R_\mathrm{coil}}. \tag{3.30}$$

The individual components at the pump coil can then be determined to be

$$\tilde{I}_{\mathrm{p,i}} = \frac{|Z_{\mathrm{p}}|}{R_{\mathrm{coil}}} \cdot \tilde{I}_{\mathrm{i}}, \quad i \in \{\mathrm{sour,cp,coil}\}. \tag{3.31}$$

The total noise current spectral density to be converted into a magnetic field is

$$\tilde{I}_{\mathrm{p}} = \sqrt{\tilde{I}^2_{\mathrm{p,sour}} + \tilde{I}^2_{\mathrm{p,cp}} + \tilde{I}^2_{\mathrm{p,coil}}}. \tag{3.32}$$

For the Keithley 6221, the amplitude of the output current determines the internal output range. The current noise $\tilde{I}_{\mathrm{sour}}$ depends on the output range [KE08]. In the highest range, the current noise is $\tilde{I}_{\mathrm{sour}} = 20\,\mathrm{nA}/\sqrt{\mathrm{Hz}}$ for frequencies between 800 Hz and 900 Hz measured at the terminals of the pump coil. For the required high currents up to 100 mA at pump frequencies around $f_{\mathrm{p}} \approx 850\,\mathrm{Hz}$, the Keithley 6221 yields the lowest current noise of the available equipment.
The calculated current noise can be converted into a magnetic field using a long cylindrical coil [Tum11] and amounts to

$$\tilde{B}_{\mathrm{p}} = \mu_0 \cdot \frac{N}{l_{\mathrm{coil}}} \cdot \tilde{I}_{\mathrm{p}}, \tag{3.33}$$

with the vacuum permeability μ_0, the number of windings N and the length of the coil l_{coil}. In order to determine the transfer via the nonlinear characteristics of the magnetostrictive material using the system model, the magnetic noise is converted into time domain. The auto-correlation function of $\tilde{B}_{\mathrm{p}}(f)$ is calculated with an inverse fast Fourier transformation. With the Levinson-Durban algorithm (see e.g. [Hay14]) the characteristics of this auto-correlation function are predicted. The resulting filter coefficients are then used to filter a white noise signal while preserving the statistical properties of the auto-correlation function above. The obtained time-domain noise is then converted into a noise voltage density $\tilde{E}_{\mathrm{mp}}$ with the system model and can be added to the noise ECD of MFC.

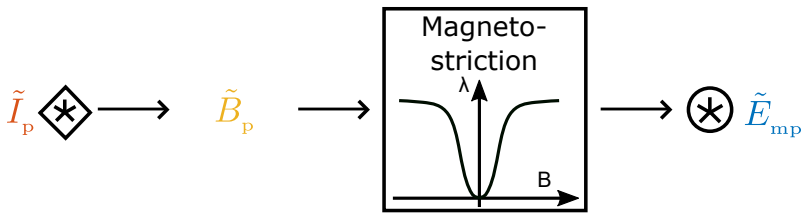

Figure 3.30: Conversion process from current noise of the excitation network $\tilde{I}_{\mathrm{p}}$ to voltage noise at the output of the nonlinearity $\tilde{E}_{\mathrm{mp}}$.

The conversion process from $\tilde{I}_\mathrm{p}$ to $\tilde{E}_\mathrm{mp}$ is schematically depicted in Fig. 3.30. With the new noise source $\tilde{E}_\mathrm{mp}$, the ECD can be extended.

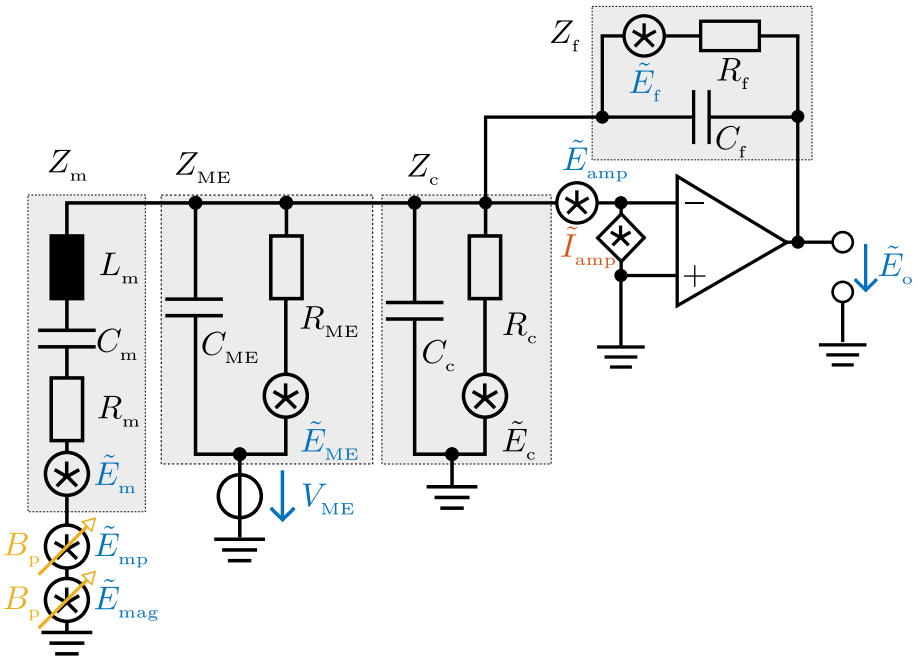

Figure 3.31: Equivalent noise circuit for MFC. Both equivalent noise sources $\tilde{E}_\mathrm{mp}$ and $\tilde{E}_\mathrm{mag}$ depend on the pump amplitude and are marked with control arrows.

The final equivalent noise circuit for MFC is depicted in Fig. 3.31. The sensor signal V_ME is placed in series with the sensor to comply with previous models [Jah+11] that include the resonance enhancement within the ME coefficient (cf. Eq. (2.12)). Alternatively, the signal can be placed in series with the resonant branch and be subject to the resonance enhancement in the same way as the noise from the mechanical resistance $\tilde{E}_\mathrm{m}$, the pump $\tilde{E}_\mathrm{mp}$, and the magnetic layer $\tilde{E}_\mathrm{mag}$.
The two additional noise sources $\tilde{E}_\mathrm{mag}$ and $\tilde{E}_\mathrm{mp}$ can be transferred to the output by

$$\tilde{E}_\mathrm{omag} = \frac{|Z_\mathrm{f}|}{|Z_\mathrm{m}|} \cdot \tilde{E}_\mathrm{mag} \tag{3.34}$$

and

$$\tilde{E}_\mathrm{omp} = \frac{|Z_\mathrm{f}|}{|Z_\mathrm{m}|} \cdot \tilde{E}_\mathrm{mp}. \tag{3.35}$$

Resonance frequency	828 Hz
Quality factor	1062
Sensor capacitance	549 pF
LoD @ f_{res}	$13\,\mathrm{pT}/\sqrt{\mathrm{Hz}}$
Cantilever width × height × length	2.2 mm×0.35 mm ×25.2 mm
Free-standing cantilever length	≈23 mm

Table 3.5: Properties of the investigated multilayer sensor for the MFC noise model.

With the unchanged equations for the other noise sources in Subsec. 2.5.5, the total output noise is then given by

$$\tilde{E}_{\mathrm{o}} = \sqrt{\tilde{E}^2_{\mathrm{oampV}} + \tilde{E}^2_{\mathrm{oampI}} + \tilde{E}^2_{\mathrm{of}} + \tilde{E}^2_{\mathrm{oME}} + \tilde{E}^2_{\mathrm{oc}} + \tilde{E}^2_{\mathrm{oQuant}} + \tilde{E}^2_{\mathrm{om}} + \tilde{E}^2_{\mathrm{omag}} + \tilde{E}^2_{\mathrm{omp}}}. \quad (3.36)$$

The derivation of the formulas can be found in Sec. A in the appendix. With the noise model, the impact of the pump source can be investigated.

Pump source noise As mentioned before, the magnetic excess noise for the multilayer sensors can be measured with the pick-up coil setup and is expected to be dominant. A recent type of multilayer sensor with a modified magnetic stack exhibits much less magnetic noise which is not measurable with the pick-up coil setup.
The sensor used for this investigation has a 350 µm double-side polished silicon substrate and is covered by a piezoelectric layer stack consisting of Ta (24 nm)/Pt (150 nm)/AlN (2000 nm)/Cr (5 nm)/Au (100 nm) with a top gold electrode with rectangular dimensions of 7.5×1.4 mm. The AlN is deposited with a low temperature process [Yar+16a]. The reverse side consists of a twenty times repeated stack of Ta (5 nm)/Cu (3 nm)/MnIr (8 nm)/FeCoSiB (90 nm)/Ta (5 nm)/Cu (3 nm)/MnIr (8 nm)/FeCoSiB (110 nm) with Ta (10 nm) on top to prevent oxidation. The sensors are designed to feature an anti-parallel alignment of EB in subsequent layers which make them align in a low energy state in pairs of two. The resulting flux closure structure reduces the formation of magnetic closure domains [Que+06], resulting in less magnetic noise.
Further sensor parameters are summarised in Tab. 3.5.
The Keithley 6221 has an output resistance $R_{\mathrm{sour}} = 10^{14}\ \Omega$ and capacitance of $C_{\mathrm{sour}} = 10\,\mathrm{pF}$. The pump coil has a resistance $R_{\mathrm{coil}} = 88\ \Omega$, length $l_{\mathrm{coil}} = 29\,\mathrm{cm}$, inductance $L_{\mathrm{coil}} = 57.7\,\mathrm{mH}$, and $N \approx 3000$ windings. The cable of the excitation network has an isolation resistance $R_{\mathrm{cp}} = 147\,\mathrm{M\Omega}$ and capacitance $C_{\mathrm{cp}} = 208\,\mathrm{pF}$.

The parameters from the charge amplifier and the cable between the sensor and the charge amplifier are the same as for direct detection: $\tilde{E}_{\mathrm{amp}} = 3\,\mathrm{nV}/\sqrt{\mathrm{Hz}}$, $\tilde{I}_{\mathrm{amp}} = 6.5\,\mathrm{fA}/\sqrt{\mathrm{Hz}}$, $R_{\mathrm{f}} = 5\,\mathrm{G\Omega}$, $C_{\mathrm{f}} = 10\,\mathrm{pF}$, $R_{\mathrm{C}} = 184\,\mathrm{M\Omega}$, and $C_{\mathrm{C}} = 36\,\mathrm{pF}$. The sensor has the mechanical resistance $R_{\mathrm{m}} = 358\,\mathrm{k\Omega}$, $L_{\mathrm{m}} = 8.1\,\mathrm{kH}$, and $C_{\mathrm{m}} = 56\,\mathrm{fF}$. With [Jah13]

$$Q = \frac{1}{R_{\mathrm{m}}}\sqrt{\frac{L_{\mathrm{m}}}{C_{\mathrm{m}}}} \tag{3.37}$$

the quality factor of the sensor is $Q = 1062$. With these parameters, the noise behaviour of the system with the investigated sensor can be calculated.

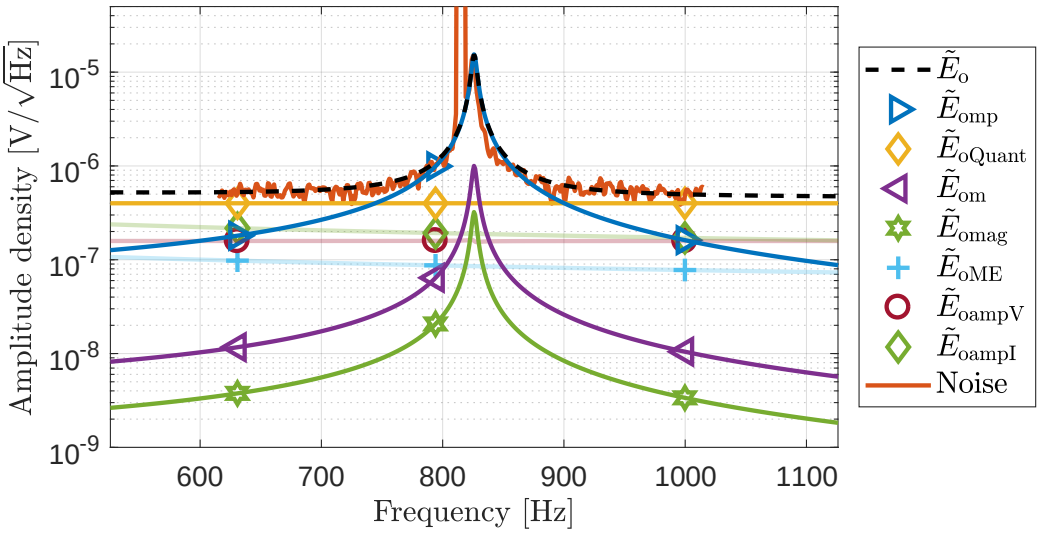

Figure 3.32: Noise calculation for the investigation sensor with MFC. The pump amplitude is $B_{\mathrm{p}} = 800\,\mu\mathrm{T}$ and appears in the output with an amplitude of approximately 1 $\mathrm{V}/\sqrt{\mathrm{Hz}}$. The magnetic excess noise $\tilde{E}_{\mathrm{mag}}$ is qualitatively included such that it is not dominant.

The result for $B_{\mathrm{p}} = 800\,\mu\mathrm{T}$ is depicted in Fig. 3.32 with $f_{\mathrm{p}} = f_{\mathrm{res}} - 10\,\mathrm{Hz}$. The total output noise $\tilde{E}_{\mathrm{o}}$ depicted with a dashed line fits the reference measurement. At the resonance frequency, it is solely determined by the noise from the pump $\tilde{E}_{\mathrm{omp}}$. All three noise sources in the resonant branch are affected by the resonance enhancement with the peak at the resonance frequency. Due to the high carrier in the output, the quantisation noise of the SR785 spectrum analyser is dominant outside of f_{res}. With the carrier suppression techniques presented in Subsec. 3.1.6, the carrier and the quantisation noise can be reduced until the current noise of the amplifier is

dominant in that region. The current noise of the amplifier can be reduced with a less noisy amplifier, e.g. with a low noise field effect transistor pre-stage [Dur+17b]. However, this does not lower the LoD since the sensor is read out at f_{res}. The noise contributions from the feedback resistance and the cable are neglected because they are less than the sensor noise. For the calculation, their elements are part of the transfer functions and cannot be left aside.

For the investigated sensors with parallel EB or without EB, the magnetic noise is presumably dominant. The total output noise in resonance of this sensor is equal to the calculated noise from the excitation network. Thus, the dominant noise component for the chosen parameters in this measurement system is the noise from the pump source. The magnetic noise is reduced by the multilayer design of the sensor.

For $B_{\mathrm{p}} < 100\,\mu\mathrm{T}$, the dominant noise component in the system is the thermal-mechanical noise $\tilde{E}_{\mathrm{om}}$ [Dur+17c]. It is not affected by the MFC and limits the LoD in the same way as for direct detection. For the investigated sensor, this ultimate LoD is approximately $30\,\mathrm{pT}/\sqrt{\mathrm{Hz}}$.

To investigate whether the noise at the resonance frequency f_{res} or the noise near the signal frequency f_{s} leads to the dominant $\tilde{E}_{\mathrm{omp}}$, the individual components need to be isolated. In order to do so, either a low-pass filter (LPF) or a high-pass filter (HPF) is applied to the pump noise before addition with the pump amplitude in the block diagram in a simulation. The LPF allows the passage of noise near f_{s} that can then be upconverted while eliminating any noise near f_{res}. On the other hand, the HPF grants passage to noise near f_{res} and blocks low frequency noise.

The influence of the filters is depicted in Fig. 3.33. With the LPF, the noise from the pump at the output of the system is similar to the noise without any filtering (cf. Fig. 3.32). The HPF has a significant effect: the noise is lowered such that the thermal-mechanical noise is dominant in resonance. The upconverted low frequency wideband noise formed by the mechanical resonator leads to the noise increase in resonance. Thus, it is to be expected that the application of an HPF lowers the LoD and the dominant noise component at the resonance frequency is then either magnetic excess noise or even thermal-mechanical noise.

As mentioned before, the noise from the pump source for this setup depends on the output range of the Keithley 6221. The higher the necessary output current, the higher is the output range. Depending on the impedance of the coil, the source switches to its highest output range at about $B_{\mathrm{p}} = 100\,\mu\mathrm{T}$. To lower the noise from

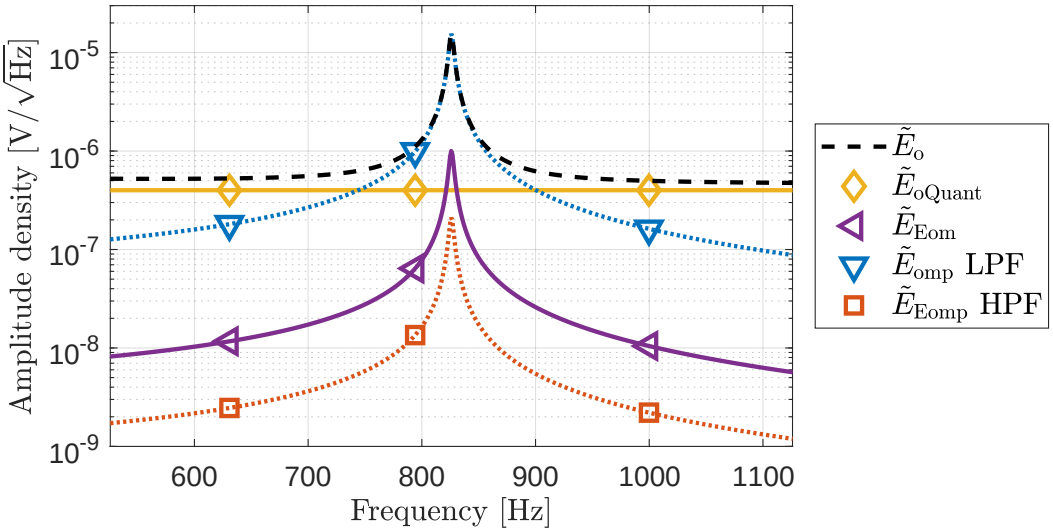

Figure 3.33: Noise calculation for the investigation sensor with MFC with filtered pump noise. The pump amplitude is $B_\mathrm{p} = 800\,\mu\mathrm{T}$. The low-pass filter (LPF) and the high-pass filter (HPF) are applied in the time domain before the pump noise is added to the pump signal.

the pump, a passive HPF is set in between the pump source and the pump coil. Active components cannot be used because they introduce additional noise sources into the system. The components of the filter need to sustain the voltage and current from the Keithley 6221, therefore power metal film capacitors and inductors for high currents are used.

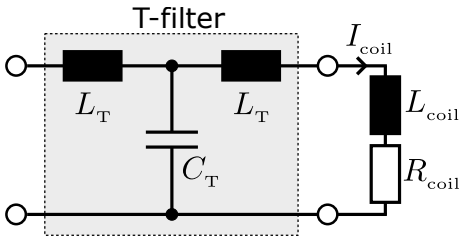

Figure 3.34: T-filter network.

The filter is designed as a T-network as depicted in Fig. 3.34. The current through the coil can be calculated with

$$I_\mathrm{coil}(\omega) = I_\mathrm{sour}\frac{j\omega L_\mathrm{T} + \frac{1}{j\omega C_\mathrm{T}} \parallel (j\omega L_\mathrm{T} + j\omega L_\mathrm{coil} + R_\mathrm{coil})}{j\omega L_\mathrm{T} + j\omega L_\mathrm{coil} + R_\mathrm{coil}}, \tag{3.38}$$

with the angular frequency $\omega = 2\pi f$.

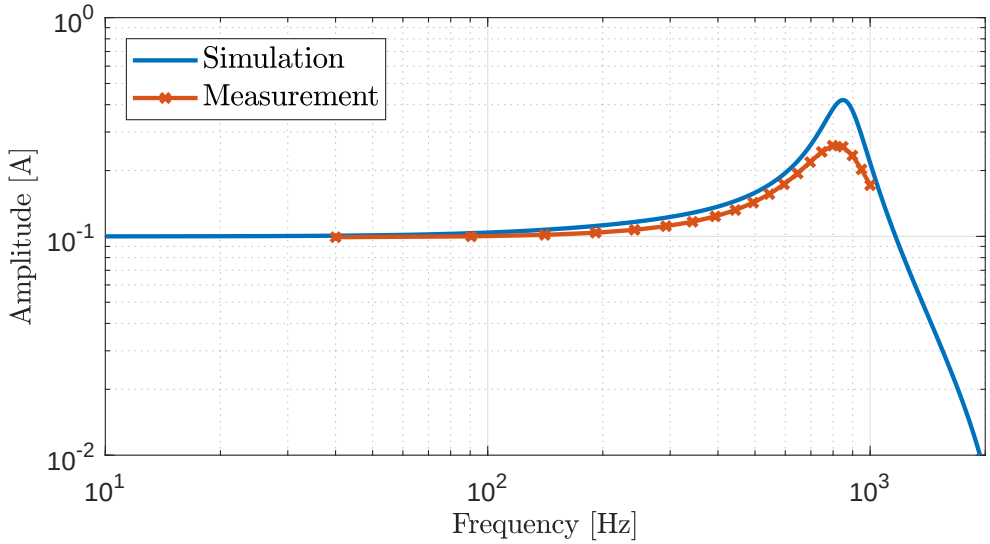

Figure 3.35: Simulation and measurement of the transfer characteristic of the T-filter for $I_{\mathrm{sour}} = 100\,\mathrm{mA}$. The inductance and capacitance of the filter are $L_{\mathrm{T}} = 10\,\mathrm{mH}$ and $C_{\mathrm{T}} = 500\,\mathrm{nF}$.

Fig. 3.35 shows the simulated and measured transfer characteristic of the realised filter. The parameters are chosen such that the resonance frequency of the filter fits the pump frequency f_{p}. At its resonance frequency, the filter increases the current by a factor of about 4 according to the simulation. The measurement shows good agreement with the shape of the filter transfer function and the parameters to tune the resonance frequency. The current is enhanced by a factor of 2.6 which is lower than in the simulation. This is presumably due to loss in the filter structure and in particular explained by the non-zero resistances of the filter inductances that have been neglected so far. The increased current is sustained by a higher output voltage of the Keithley 6221, maintaining the energy balance sheet. The switching of the output range of the device is coupled to the current. The *current amplification* factor can be increased by increasing the inductances L_{T}. However, higher currents require higher voltages from the source. The Keithley 6221 has a maximum voltage compliance of 105 V. Alternatively, the filter can also be designed with other passive networks, for example a simple capacitor with $C_{\mathrm{c2g}} = 0.63\,\mu\mathrm{F}$ in parallel which results in slightly lower measured factors.

With applied filter, the noise starts to increase at higher pump amplitudes B_{p}.

Fig. 3.36 shows the measured noise curves for the investigated sensor and for the sensor investigated in Subsec. 3.1.4 as reference. The reference sensor still has

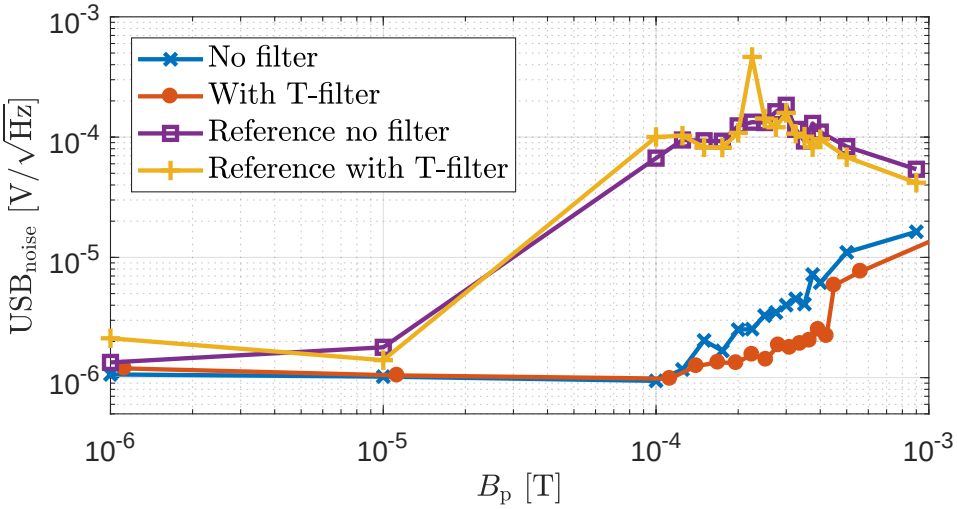

Figure 3.36: Measurements of $\mathrm{USB}_{\mathrm{noise}}$ (i.e. at f_{res}) of the investigated sensor and of the sensor investigated in Subsec. 3.1.4 as a reference with and without application of the T-filter.

dominant magnetic excess noise. Therefore, the filter does not change the noise behaviour in the measured region because the filter only affects the noise from the pump source. For the sensor investigated in this subsection however, the magnetic noise is not dominant. At pump amplitudes below 100 µT, the thermal-mechanical noise contributes most of the noise. For higher amplitudes, the noise of the pump source becomes dominant. However, with the T-filter in between the pump source and the pump coil, the noise increases at higher pump amplitudes. This behaviour is also seen with other measured sensors. Since the USB increases with and without the filter in the same manner up to approximately $B_{\mathrm{p}} = 800\,\mu\mathrm{T}$, the LoD is lowered by the filter.

In Fig. 3.37, the improvement of the LoD down to $50\,\mathrm{pT}/\sqrt{\mathrm{Hz}}$ is depicted (cf. also Fig. 3.40). The optimal pump amplitude for this sensor is between $B_{\mathrm{p}} = 300\,\mu\mathrm{T}$ and $B_{\mathrm{p}} = 400\,\mu\mathrm{T}$. The USB is still increasing for these pump amplitudes and has not yet reached its maximum. This proves again that the method of determining the optimal pump amplitude solely by the USB amplitude is not favourable. The noise presumably decreases even more, if the current amplification factor is increased. For the used setup, this is not possible because the voltage compliance of the pump source limits the factor.

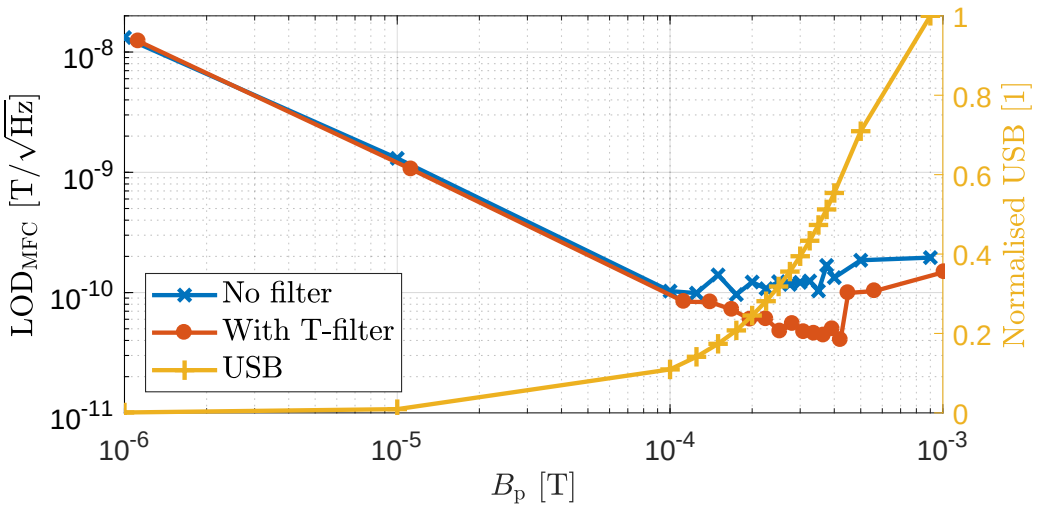

Figure 3.37: Measurements of the LoD of the investigated sensor with and without application of the T-filter. On the right axis, the normalised USB amplitude is depicted.

The new multilayer design lowers the magnetic excess noise such that the increase in noise as a function of the pump amplitude is only about one decade. With a time-domain model of the noise behaviour of MFC, the wideband noise of the pump source is found to be the dominant noise component. With a filtered pump signal, the LoD of a magnetoelectric thin-film multilayer sensor can be reduced to $50\,\mathrm{pT}/\sqrt{\mathrm{Hz}}$.

3.1.8 Optimal Magnetostriction Curve for MFC

The nonlinear curve results from the magnetic properties of the magnetostrictive materials. It can be deliberately designed to a certain extent, as can be deduced from Subsec. 3.1.1. For example, the minimum of the magnetostriction curve can be shifted along the field axis if the field-induced anisotropy is applied with a tilt. The overall output signal can be increased by enlarging the magnetic volume, which deteriorates the noise behaviour. Due to the shape anisotropy, the magnetic behaviour may also be engineered by altering the cantilever dimensions, which changes also the mechanical behaviour. Moreover, the characteristic is very susceptible to the manufacturing, storage, and external influences such as humidity (see for example

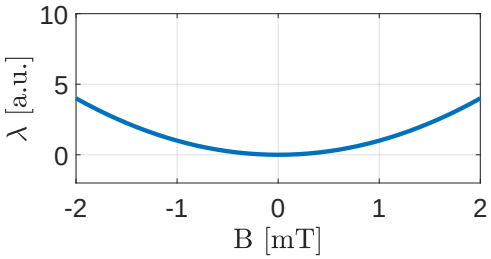

(a) $f_1 = B^2(t)$.

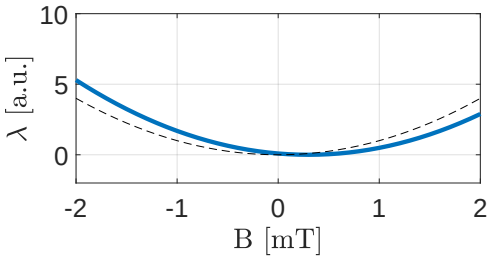

(b) $f_2 = \big(B(t) - 0.3\big)^2$

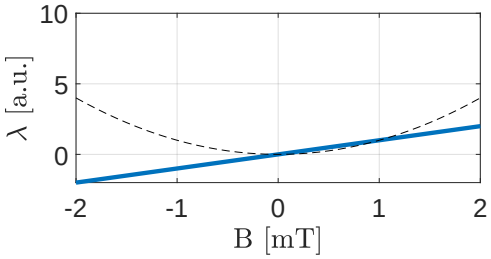

(c) $f_3 = B(t)$

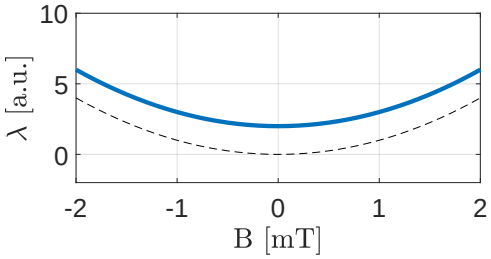

(d) $f_4 = B^2(t) + 2$

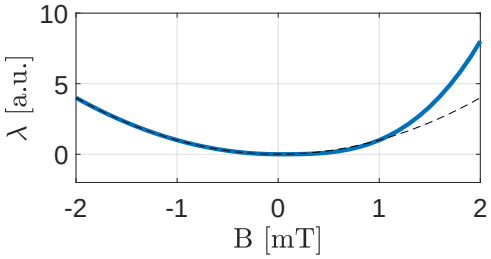

(e) f_5: Eq. (3.39)

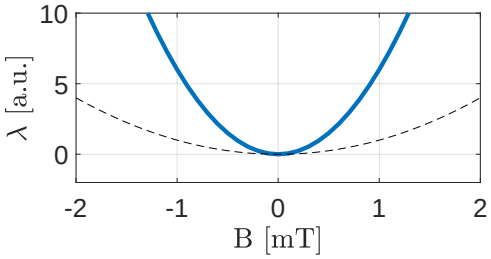

(f) $f_6 = \big(B(t) \cdot \sqrt{6}\big)^2$

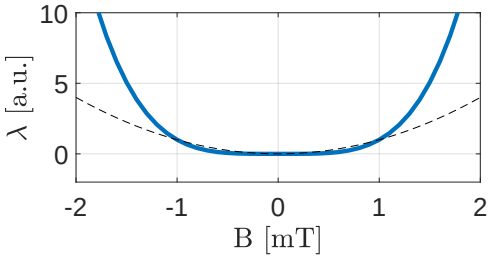

(g) $f_7 = B^4(t)$

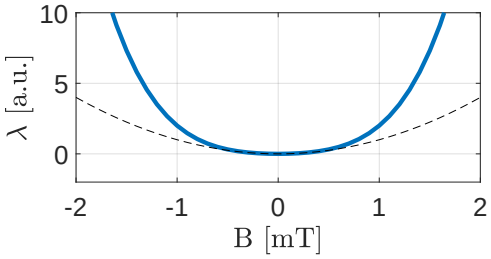

(h) $f_8 = B^2(t) + B^4(t)$

Figure 3.38: Selection of nonlinear function types for the determination of the optimal magnetostriction curve. For reference, a quadratic curve is additionally depicted in every plot with a dashed line to emphasise the differences.

the change in the bias curve over time in Fig. 3.4). Nevertheless, for signal level, dynamic range, and processing there is an optimal curve shape.

To determine the optimal curve characteristic the polynomial approach is evaluated for a set of basic functions ($f_1 - f_8$) displayed in Fig. 3.38. The functions serve to consolidate the understanding of the relationship between the magnetostriction curve and the coefficients although this may seem trivial at a first glance. The associated coefficients for the depicted curves can be found in Tab. B.2 in the appendix. Fig. 3.38b shows that a shift along the abscissa is due to non-zero a_0 and a_1 coefficients. The latter, as well as all odd coefficients, lead to an asymmetry of the nonlinearity, Figs. 3.38c, 3.38d, 3.38e. Fig. 3.38d shows a shift on the ordinate which may result from remanence. Function f_5 is given by

$$f_5\big(B(t)\big) = \begin{cases} B^2(t) & \text{if } B < 0 \\ B^3(t) & \text{if } x \geq 0, \end{cases} \tag{3.39}$$

and represents a more complex asymmetrical curve. Its quadratic coefficient is dominant, thus it can be used for standard MFC. The last three functions show how the slope depends on the coefficients and that a mix of even coefficients with high values is not preferable. For example, Fig. 3.38h has a shallow slope at the beginning. Operated with MFC, very high pump amplitudes would be required to obtain a decent slope and thus sensitivity.

In Subsec. 3.1.6 measurements show that real magnetostriction curves of course contain characteristics from all functions. With Eq. (3.11) the coefficients components can be obtained by a fit of the measured magnetostriction curve. According to Eq. (3.12) and if the signal is to be converted into $f_{\mathrm{res}} = f_{\mathrm{p}} \pm f_{\mathrm{s}}$, only the even coefficients

$$\begin{aligned} \Bigg(& \frac{15\,a_6 \boxed{\hat{b}_{\mathrm{p}}^5\,\hat{b}_{\mathrm{s}}}}{8} + \frac{45\,a_6 \boxed{\hat{b}_{\mathrm{p}}^3\,\hat{b}_{\mathrm{s}}^3}}{8} + \frac{3\,a_4 \boxed{\hat{b}_{\mathrm{p}}^3\,\hat{b}_{\mathrm{s}}}}{2} \\ & + \frac{15\,a_6 \boxed{\hat{b}_{\mathrm{p}}\,\hat{b}_{\mathrm{s}}^5}}{8} + \frac{3\,a_4 \boxed{\hat{b}_{\mathrm{p}}\,\hat{b}_{\mathrm{s}}^3}}{2} + a_2 \boxed{\hat{b}_{\mathrm{p}}\,\hat{b}_{\mathrm{s}}} \Bigg) \end{aligned} \tag{3.40}$$

contribute to the desired frequency component. Thus, the curve should not be shifted along the abscissa or be asymmetrical. The a_2 coefficient is dominant because the product $\hat{b}_{\mathrm{p}} \cdot \hat{b}_{\mathrm{s}}$ is several decades larger than the products of the other boxed

terms in Eq. (3.40). For standard MFC operation and an optimal signal, the desired nonlinearity λ_{des} should be a quadratic function similar to

$$\lambda_{\mathrm{des}} = a_2 \cdot B^2(t), \tag{3.41}$$

with a_2 as high as possible. This nonlinearity would feature no carrier at the output and maximise the signal, because the higher a_2 is, the steeper is the slope and the greater is the sensitivity. Also, the quadratic component rises linearly with the excitation amplitude $\hat{b}_{\mathrm{p}}$.
As long as the limiting noise components are thermal-mechanical noise or magnetic excess noise, the shape of the nonlinear characteristic is not relevant with respect to the noise except for a shifted pump signal as explained in Subsec. 3.1.7. Upconverted noise from the pump source depends on the steepness of the nonlinearity just as the signal does.
For the excitation source, it is advantageous to have the peaks of the bias curve at small fields, or likewise a very steep nonlinearity, to limit the necessary current for optimal excitation.

3.1.9 Evaluation of MFC

MFC allows the measurement of low frequency signals with LoDs below $100\,\mathrm{pT}/\sqrt{\mathrm{Hz}}$ by converting the signal frequency into the mechanical resonance frequency of the cantilever. The conversion process occurs in the nonlinear magnetostrictive material and signal amplitude is enhanced by the mechanical resonator. It therefore strongly depends on the magnetic behaviour of the magnetic layer. A mathematical model allows the prediction of the relative output amplitudes which can be used to determine an advantageous mode of operation in terms of signal processing and SNR. The absolute output level cannot be estimated without calibration because the model does not include material specific parameters such as mechanical coupling, piezoelectric coefficients, etc. For a low LoD, the SNR is to be maximised. By DC offsets of the exciting pump the signal amplitude can be increased for certain sensors. While some waveforms such as a rectangular pump are not advantageous, an excitation of higher order resonant modes or combinations can lower the LoD.
The noise that occurs during MFC is investigated. In particular, noise sources that do not occur with direct detection are taken into account. While for sensors with a single layer magnetostrictive material and no exchange bias, the magnetic excess

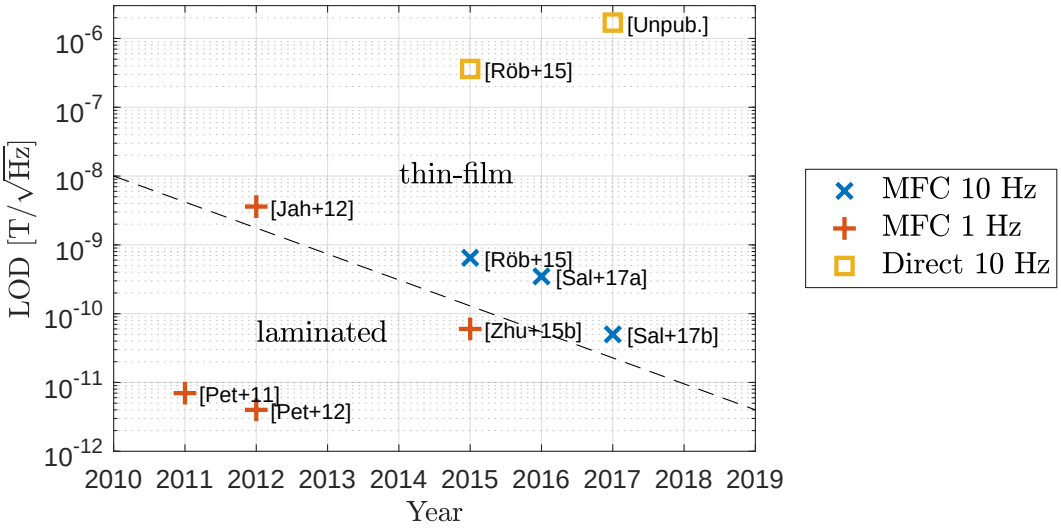

Figure 3.39: Reported LoDs for 10 Hz and 1 Hz for magnetoelectric sensors with direct detection and MFC. The dashed line additionally divides results from thin-film and laminated magnetoelectric sensors, respectively.

noise is dominant [Jah+12], amongst others, multilayer sensors with exchange bias show less magnetic noise. By extending the noise model for MFC, the noise of the excitation source is found to be dominant for these sensors, which is then proven by measurements. While the phase noise and the direct wideband noise around the mechanical resonance frequency are not relevant, the low frequency upconverted noise formed by the mechanical resonator is dominant and limits the LoD. By inserting a filter between the pump source and the pump coil, the pump noise can be reduced and the LoD lowered. The available factor in current is limited by the voltage compliance of the excitation source. The excitation with high currents at frequencies of several hundred Hertz, in particular with low current noise, can only be supplied by very specific devices. In consequence, the sensors should be designed to have a narrow, steep, quadratic, and hysteresis free magnetostriction curve.
The chronological development of the LoDs for signals at 1 Hz and 10 Hz is depicted in Fig. 3.39. It is evident that MFC reduces the LoD at 10 Hz considerably as compared to direct detection.
For a low-noise multilayer sensor with 20 repeated layers, the LoD for various signal frequencies using direct detection and MFC is depicted in Fig. 3.40. For the detection of a 10 Hz signal, MFC can improve the LoD by 3 decades and more [Röb+15],

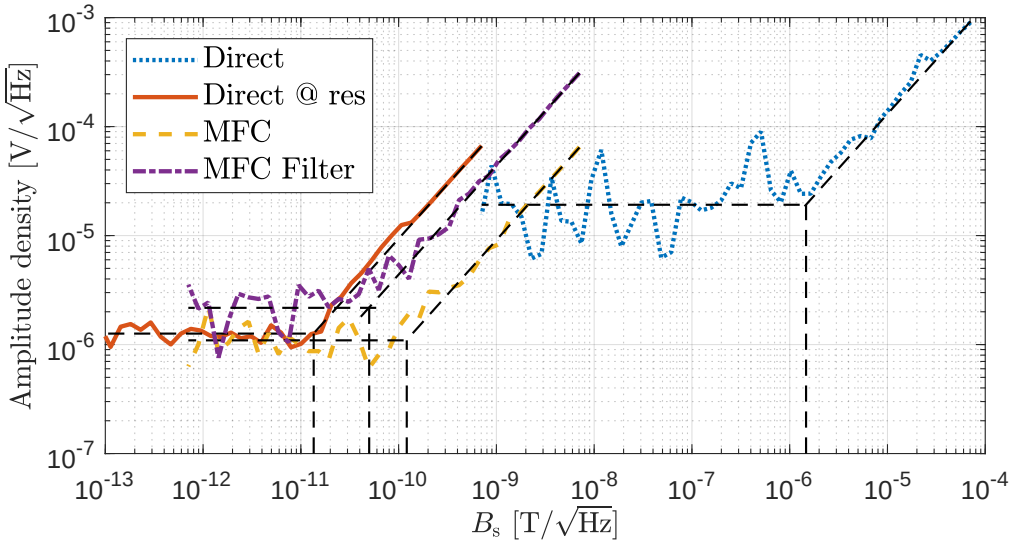

Figure 3.40: LoDs for a multilayer sensor with 20 repeated layers with direct detection of $f_s = 10\,\text{Hz}$, direct detection of a signal in resonance at 828 Hz, MFC of $f_s = 10\,\text{Hz}$ with $B_p = 100\,\mu\text{T}$, and MFC with additional filter of $f_s = 10\,\text{Hz}$ with $B_p = 300\,\mu\text{T}$.

as compared to a direct detection scheme at 10 Hz. In Fig. 3.40, the improvement is more than 4 decades (see Fig. 3.39, year 2017).

The method has certain drawbacks such as the additionally required pump coil. Also, the excitation with high AC currents requires additional energy and makes small size integration difficult. The pump excitation also inherently puts a limit to the possible resonance frequencies because the necessary current increases with the frequency of the excitation of the coil. Multiple sensors can be used in arrays in principle, if the resonance frequencies are chosen such that the magnetic components of nearby sensors do not interfere with each other.

The challenge with the development of low-noise magnetic layers is to keep the signal output amplitude reasonably high for a good SNR. Designing a magnetic layer with very low magnetic noise itself is almost a trivial task. The best compromise between signal and noise is, however, a challenging scientific task and yet has to be found.

Fig. 3.40 shows a conversion loss for MFC of approximately 3.2 dB. The noise limit with the filter is very close to the thermal-mechanical noise limit. This is considered the ultimate noise limit and discussed in Subsec. 2.5.5. If the noise contributions can be lowered to the level of the amplifier noise, the LoD would be below $10\,\text{pT}/\sqrt{\text{Hz}}$ enabling it to measure certain biomagnetic signals without massive averaging.

To avoid the additional pump coil and the high currents, the frequency conversion can also be performed electrically as it is explained in the next section.

3.2 Electric Frequency Conversion

MFC yields low LoDs in the range of some ten pico-Tesla, but its practicability is limited due to the additional coil and energy consumption for excitation of the magnetic pump field. The aforementioned drawbacks can be avoided by replacing the magnetic pump signal with an electric excitation. An electric pump can be applied directly to a sensor with two piezoelectric layers without the need for additional circuitry. The method is then called *electric frequency conversion* (EFC).
A similar method is used in [ZSD12; Zhu+15b; Zhu+15a] for bulk ME sensors with resonances in the range between ten and hundred kilohertz, where the carrier is placed directly into the mechanical resonance frequency. Another related readout method is used for ΔE_{d}-sensors, where the sensor is also excited with a small AC voltage [Jah+14]. The change in the elastic modulus of the sensor, caused by an applied magnetic field, can be measured as a change in the impedance at the sensor terminals which results in a change of measured current at its output.
This chapter introduces the concept of EFC, presents a proof of concept, discusses an assumption on the physical background from a system point of view, and applies first improvements to the method. Some of the contents of this section have already been published in [Sal+15; Hay+16].

3.2.1 Setup and Sensor for EFC

The EFC measurement setup contains three sources which are for the test signal, bias field, and pump signal, respectively, and the respective signal and bias coils. The test signal is generated with a Keithley 6221, the bias with a Keysight B2962A power source, and the pump either with a *RME Fireface UCX* sound card or the signal output of the SR785 spectrum analyser. The spectrum analyser has the advantage of being able to output DC voltages. An AD745 charge amplifier is used for readout with a feedback resistance of $R_{\mathrm{f}} = 5\,\mathrm{G\Omega}$ and capacitance $C_{\mathrm{f}} = 10\,\mathrm{pF}$. Both the sensor and the amplifier are encased in the shielding box explained in Subsec. 2.5.1. The output data is processed either with the RME sound card or a SR785 spectrum analyser.

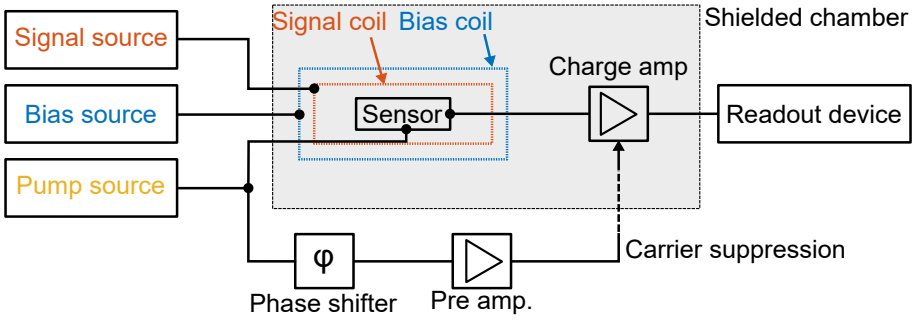

Figure 3.41: Measurement setup for EFC.

Resonance frequency	782 Hz
Quality factor	258
PZT capacitance	338 nF
AlN capacitance	527 pF
Cantilever width × height × length	2.2 mm×0.35 mm ×25.2 mm
Free-standing cantilever length	23 mm

Table 3.6: Properties of the investigated EFC sensor.

The measurement setup is depicted in Fig. 3.41.

The core of the investigated sensor comprises a 300 µm double side polished silicon substrate. On one side, it is covered by a 100 nm platinum seed layer, 2 µm PZT deposited with chemical solution deposition [Pio+13], and a Cr/Au electrode with 24.4 µm length. In contrast to the aforementioned report, no poling is applied to the PZT for the investigated sensor. On the reverse side, the magnetostrictive layer as well as a second piezoelectric layer used for readout are deposited. The magnetostrictive layer consists of a 10 times repeated 200 nm exchange biased FeCoSiB layer stack explained in detail in [Röb+15]. On top, a 2 µm AlN layer and a Cr/Au electrode of the dimensions 7.5 mm×1.2 mm are deposited. The AlN is structured by wet etching in order to be able to electrically contact the FeCoSiB layer which acts as the ground potential of the sensor. The field annealing is conducted with a 45° in-plane anisotropy with respect to the long axis of the cantilever (100 mT, 250° C, 30 min).

Important sensor parameters are summarised in Tabl. 3.6. More details on the sensor fabrication of a similar cantilever are given in [Hay+16].

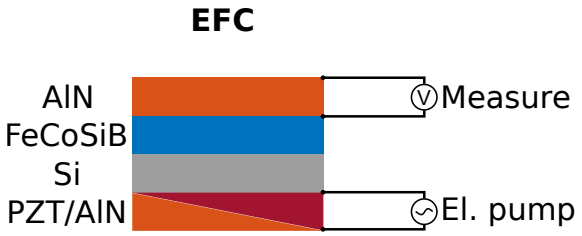

Figure 3.42: Schematic of the EFC sensor and its active layers. The divided layer indicates that both PZT and AlN can be used interchangeably.

3.2.2 Excitation and Noise of MFC

The principle of EFC is very similar to MFC. However, the sensors used for EFC have a different layer structure including two piezoelectric layers. One piezoelectric layer is used to apply the pump signal, the other for readout via a charge amplifier. Using two individual layers provides electrical isolation between the excitation and the readout.

Fig. 3.42 shows a schematic of the active layers of the EFC sensor. For the excitation, both AlN and PZT can be used. Fig. 2.5 depicts the transfer functions of AlN and non-polarised PZT. Poled PZT is somehow linear and therefore used for readout e.g. for the IDT sensors. Since the transfer function of AlN is linear, it is suitable for readout. The PZT introduces a second nonlinearity into the system, if the electric fields leave the quasi linear regime of the butterfly curve. In fact, the excitation with small amplitudes up to $\approx 5\,\mathrm{V}$ with an offset to either positive or negative side of the butterfly curve is not entirely linear. The excitation follows a slight opening of the quasi linear trace due to ferroelectric hysteresis. However, the effect is small and can be neglected for EFC.

The mechanical bending of the cantilever induced by an excitation via PZT is more than a decade higher as compared to AlN for similar 2 µm thick piezoelectric layers (see Fig. 3.43). This is in accordance with the piezoelectric coefficients of AlN and PZT (cf. [TM04]). Therefore, it is favourable to apply the pump via a PZT layer.

The effect on the bending can be investigated by applying a voltage without offset to the PZT layer and processing the output signals with the setup described in Subsec. 3.2.1. In order to exclude the nonlinearity from the magnetostrictive layer, the sample can be held magnetically saturated with a bias field of 10 mT. The output spectrum includes peaks at the pump frequency $f_\mathrm{p} = 772\,\mathrm{Hz}$ and harmonics at $n \cdot f_\mathrm{p}$, $n \in \{\mathbb{N} > 1\}$. They remain unaltered for the magnetic saturation which indicates

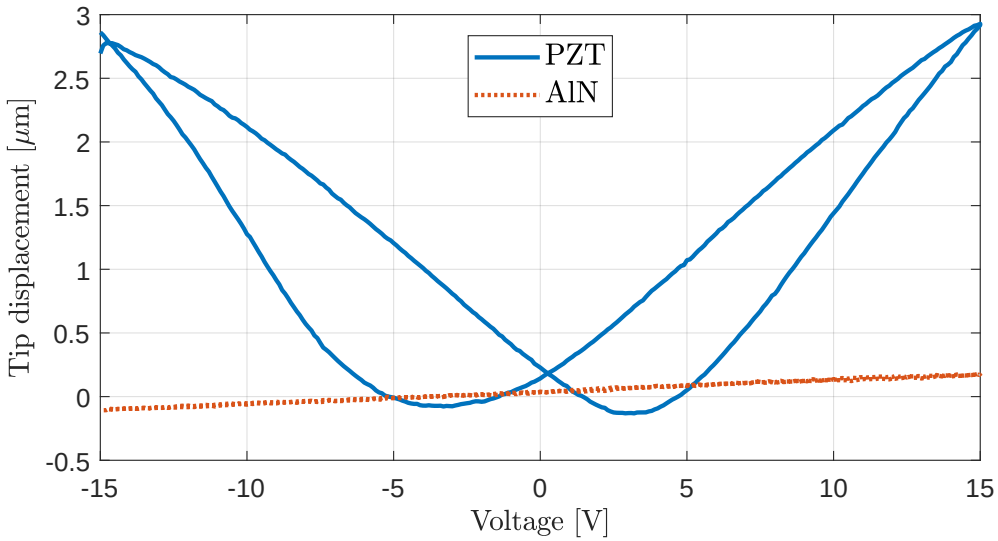

Figure 3.43: Measured tip displacements for a ME sensor under application of a DC electric field to a 2 µm PZT or AlN piezoelectric layer [Hay+16].

that they are not of magnetic origin. Because the PZT is nonlinear as well, the harmonics can be attributed to the PZT. A voltage DC offset of the pump reduces the peak amplitudes. The measured spectra have a distinct increase of noise at the resonance frequency of the cantilever which depends on the amplitude of the pump applied via the PZT. It is higher than the thermal-mechanical noise and would thus be dominant in case of EFC. A sensor with two AlN layers shows the same peaks at harmonics of the excitation. For AlN, offsets to the pump have no influence on the peak amplitude. To determine the origin of the peaks, the same experiment is also conducted in an optical setup, as well as with cantilevers that only have a substrate and one piezoelectric layer made of either AlN (only AlN) or PZT (only PZT). In the optical setup, a laser is pointed at the tip of the cantilever at a specific angle and the reflection as a function of the cantilever bending is processed by a one-dimensional position sensitive device (PSD) from *SiTek*. Magnetic fields are induced by Helmholtz coils without core and the currents are generated by a standard signal generator *Keysight 33500B* and a Kepco power source utilised as a voltage controlled current source. The setup is not shielded against electric, acoustic, or magnetic interferences. The PSD signal is processed by a SR785 spectrum analyser after being processed with a *Laser Components LC-301* PSD amplifier. A similar setup is used in [Dur+17c]. Even for the only AlN-sensor, the peaks still appear and are a function of the applied pump voltage V_{p}. For both PZT and AlN, the peaks also appear for

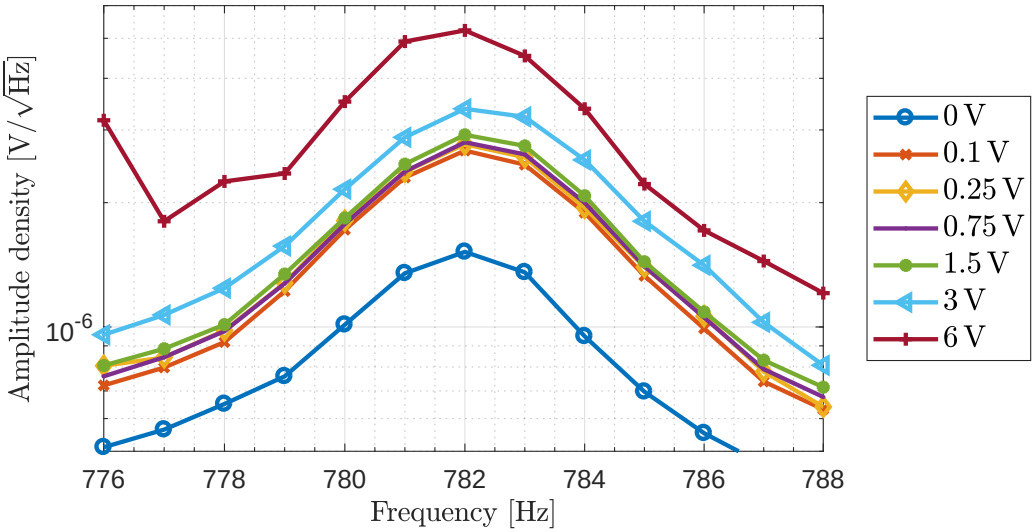

Figure 3.44: Measured spectral densities around $f_{res} = 782\,\text{Hz}$ for various pump amplitudes (see legend) at $f_p = 772\,\text{Hz}$ generated with a RME Fireface UCX soundcard. The sample is additionally magnetically saturated with 10 mT. No signal B_s is applied to the cantilever. The pump signals are suppressed as explained in Subsec. 3.2.4 to avoid problems with the dynamic range of the readout device.

an acoustical excitation via a piezo-loudspeaker, but with smaller amplitude. The peaks cannot originate from the magnetic layer, because it is saturated for these experiments. Since the acoustic excitation of a cantilever consisting only of the substrate material shows no harmonic peaks. They must be due to the piezoelectric layer. For EFC, the additional peaks can be neglected because they do not interfere with the conversion products and are not investigated further.

Fig. 3.44 shows measured spectral densities that show the increase in noise. For $V_p = 6\,\text{V}$, the noise without magnetic saturation is approximately a factor of 3 higher which indicates that magnetic excess noise also needs to be considered. To investigate contributions prior to the magnetic layer, a magnetic saturation excludes magnetic noise as a reason for the noise increase. Since ferroelectric materials also have domains it is assumed that the noise is due to ferroelectric domain wall movement. In analogy to ferromagnetic materials, ferroelectric materials also feature noise due to the nucleation and movement of domain walls, and pinning [Shu+01]. The fabrication process for the PZT is explained in detail in [Pio+13]. However, no measures to suppress ferroelectric noise are taken during sensor fabrication up to now. The noise from the ferroelectric layer cannot be excluded because an elec-

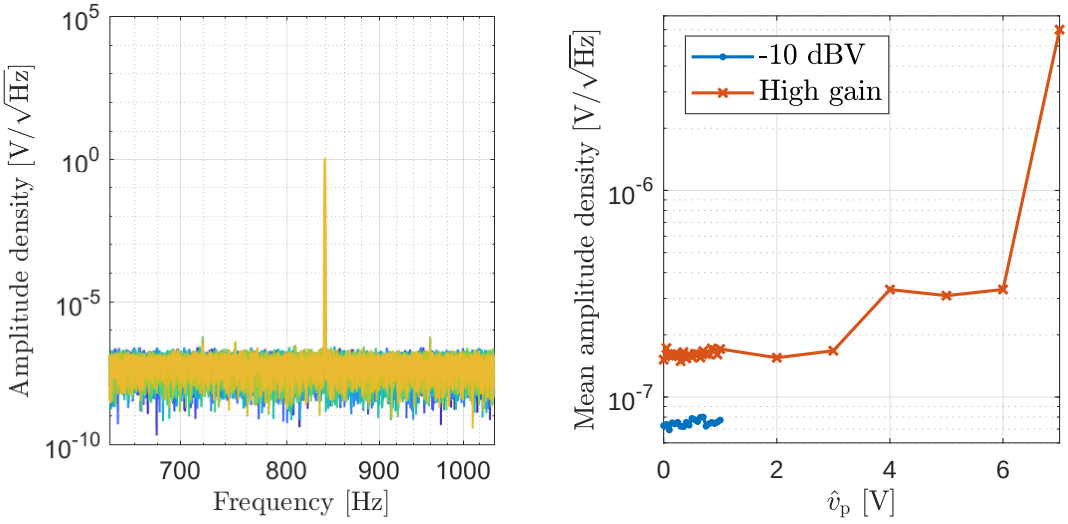

(a) (b)

Figure 3.45: Noise behaviour of Fireface UCX soundcard. (a) NVSDs for pump amplitudes up to $V_p = 1\,\mathrm{V}$ in the lowest output gain range of a Fireface UCX soundcard used for excitation. (b) Mean value of the noise floor of Fig. 3.45a for various pump amplitudes and gain settings.

trical saturation with a high DC voltage is not possible. DC voltages high enough to saturate the PZT either destroy the bond-wires or short-circuit the piezoelectric layer.

Another possible explanation is noise from the pump source. The noise from the RME Fireface UCX soundcard depends both on its set output gain and output level. The noise floor of the D/A converter of the soundcard is measured to be constant at about $75\,\mathrm{nV}/\sqrt{\mathrm{Hz}}$ up to amplitudes of $V_p \approx 1\,\mathrm{V}$ at the lowest output gain named *-10 dBV* (see Fig. 3.45). At *High gain*, the noise density is approximately a factor of 2 higher and rises further for pump amplitudes above $V_p = 3\,\mathrm{V}$. The noise from the source is transferred via the nonlinear piezoelectric layer and additionally via the nonlinear magnetostrictive layer. Therefore, standard noise correlation analyses does not help in order to determine the dominant noise contribution at the output. In order to determine the influence of the pump noise, the pump is superimposed with known artificial noise. An increase at f_{res} becomes visible at the output of the sensor starting from additional white noise densities above $1\,\mu\mathrm{V}/\sqrt{\mathrm{Hz}}$. This indicates that the noise of the source without additional noise is not dominant. Measured noise floors from the soundcard without additional noise exceed $1\,\mu\mathrm{V}/\sqrt{\mathrm{Hz}}$ only for

amplitudes above 6 V in the highest output gain setting. Therefore, pump noise cannot be responsible for the noise increase and can be neglected for this scenario.

3.2.3 System Model for EFC

Fig. 3.47 shows a block diagram for EFC with two piezoelectric layers. Via the piezoelectric effect, an applied voltage V_p leads to a mechanical stress which is transferred to the cantilever via the mechanical coupling with the other layers. A magnetic signal of interest B_s is converted into the mechanical resonance frequency in a similar way as explained for MFC in Subsec. 3.1.2 If the pump frequency f_p is chosen according to $f_\mathrm{p} = f_\mathrm{res} - f_\mathrm{s}$, the resulting spectral density is comparable to MFC, e.g. in Fig. 3.20.

Two paths need to be considered for the exciting pump for EFC: Firstly, a direct path from the exciting piezoelectric layer to the ADC which leads to a high carrier amplitude in the output spectrum. This path is mainly due to direct elastic coupling. Secondly, an indirect path that leads to the ADC after a detour through the magnetostrictive layer, as indicated by arrows in Fig. 3.47. Using this inverse magnetostrictive effect, the magnetisation is subject to a dynamical change which leads to a frequency conversion with an applied magnetic signal B_s. The indirect path has to be taken into consideration because an excitation with the linear AlN also leads to a frequency conversion of the desired magnetic signal with a frequency spectrum similar to Fig. 3.48a. A frequency conversion in the nonlinear PZT via magnetoelastic coupling of the desired signal B_s cannot be entirely precluded. However, without a bias field the induced bending by a small desired signal can be neglected which makes the aforementioned indirect path more likely.

A first EFC signal model is very similar to the MFC model. The electrically induced mechanical movement causes indirectly a magnetic pump signal B_p which is utilised to imitate the conversion process. It is a function of the pump voltage V_p applied to the piezoelectric layer. In analogy to MFC, the addition of the desired signal B_s and the magnetic pump signal $B_\mathrm{p}(V_\mathrm{p})$ is then transferred via the nonlinear magnetostrictive curve and weighted with the transfer function of the mechanical resonator. V_p is additionally transferred to the output with a direct conversion factor. To evaluate the model, a sensor with two AlN piezoelectric layers is measured in an optical setup as explained in Subsec. 3.2.2. Since the inner material parameters such as the absolute magnetostriction are not known, the simulation contains a

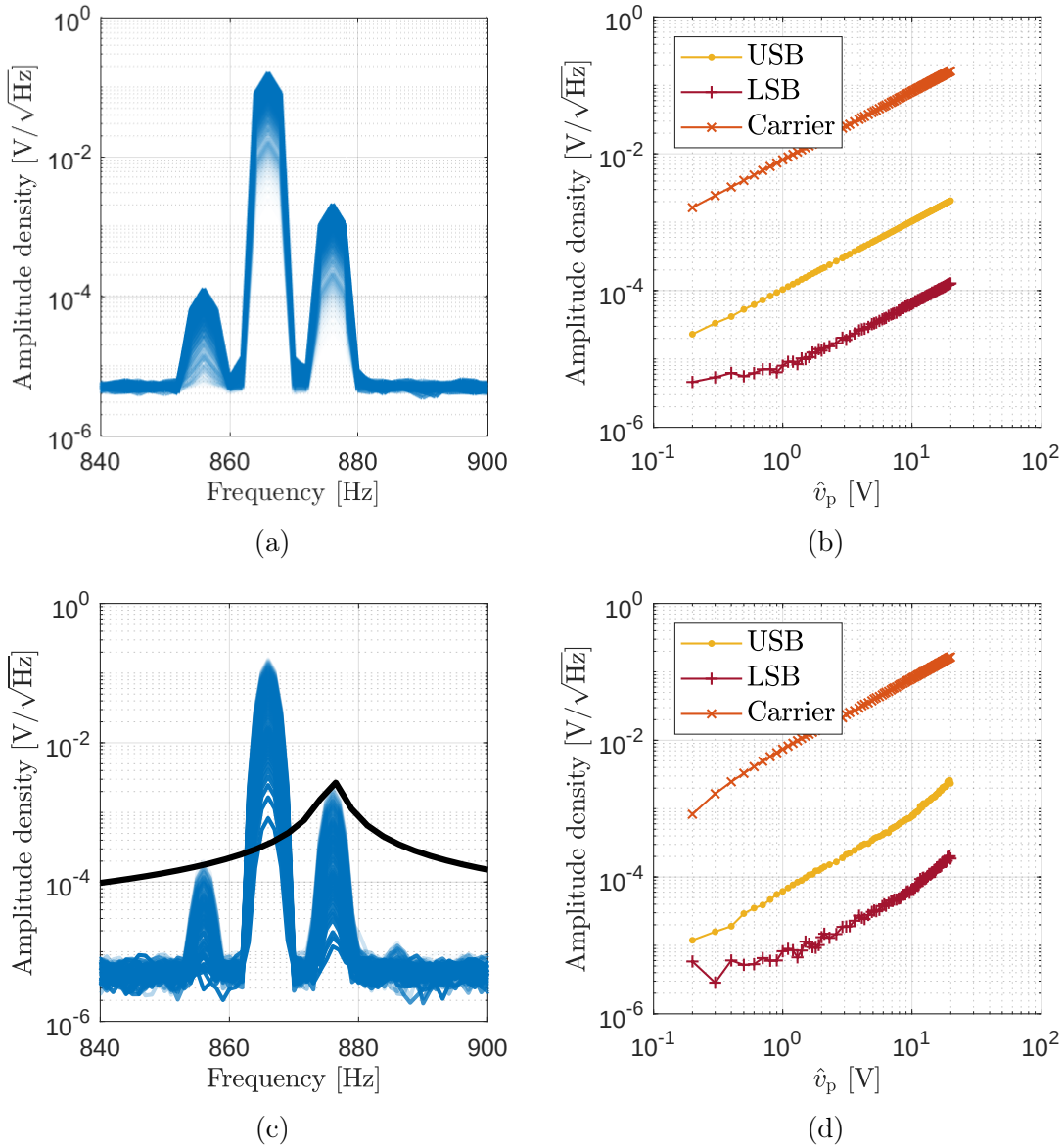

Figure 3.46: Comparison of simulated and measured EFC results. The measurements are conducted in the optical measurement setup. (a) Simulated spectral densities of the proposed EFC signal model for various pump amplitudes V_p applied at $f_{res} - f_s$ Hz. The desired signal has $B_s = 10\,\mu T$ at $f_s = 10\,Hz$. (b) Simulated trends of the USB, LSB, and the carrier as a function of the applied pump amplitude. (c) Measured spectral densities of the proposed EFC signal model for various pump amplitudes V_p applied at $f_{res} - f_s$ Hz. The desired signal has $B_s = 10\,\mu T$ at $f_s = 10\,Hz$. A solid black line indicates a scaled version of the measured resonance curve. (d) Measured trends of the USB, LSB, and the carrier as a function of the applied pump amplitude.

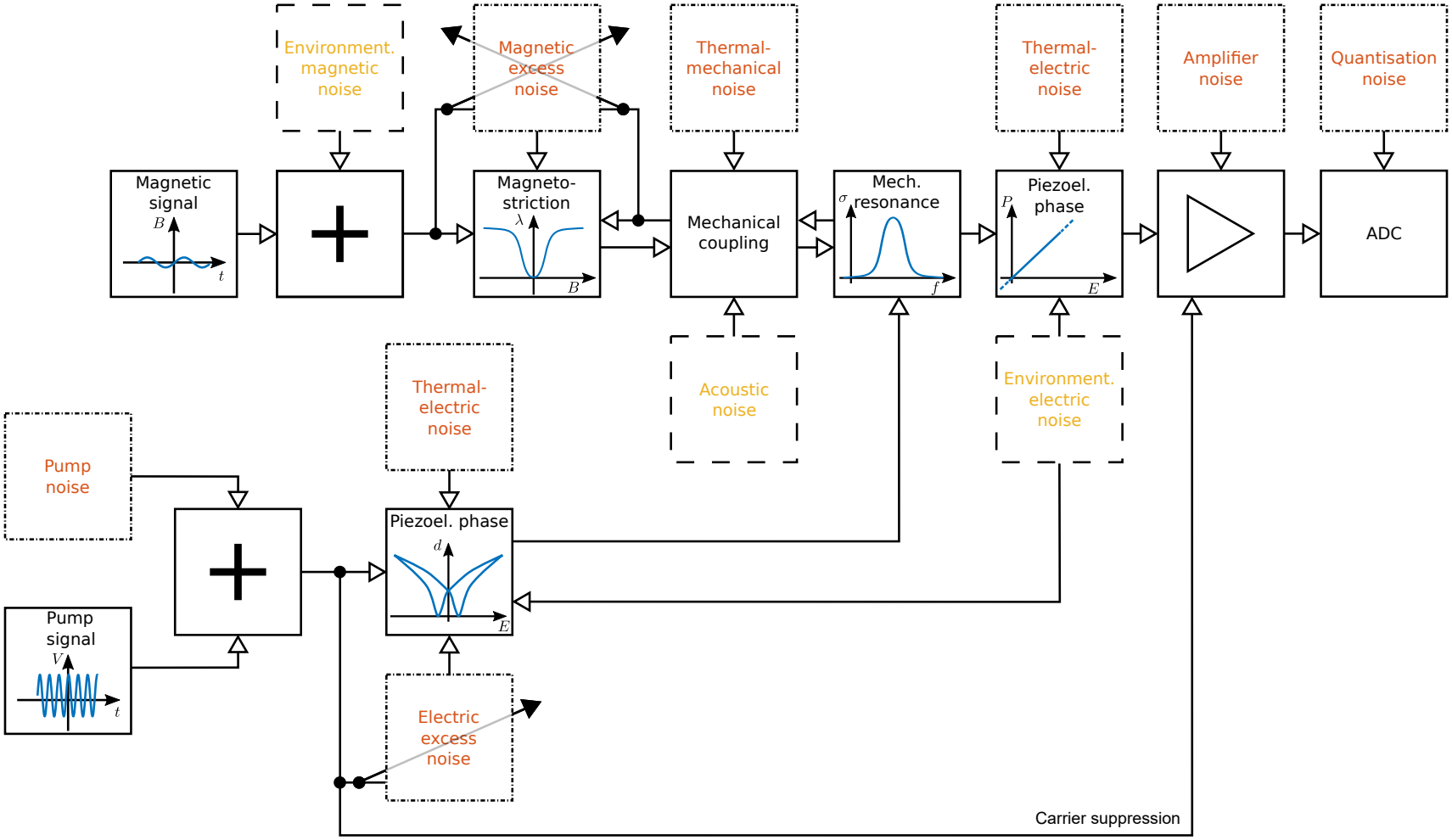

Figure 3.47: Block diagram of the EFC. Noise sources that are included in the noise model have dashed-dotted boxes. External noise sources have dashed boxes. The control arrows indicate that the noise sources depend on an input signal.

number of factors that are matched to fit the measured amplitudes. The comparison of simulated spectral densities correspond to measurements very well (see Fig. 3.46 for $B_{\mathrm{s}} = 10\,\mu\mathrm{T}$) and is plausible for various amplitudes of the desired signal.
In the signal model, noise is not considered. A major difference compared to MFC is the entry of thermal-electric noise and electric excess noise before the conversion process. They are therefore subject to the mechanical resonator and multiplied with the transfer function G_{mech} in Eq. (2.3).
However, the block diagram in Fig. 3.47 indicates that the electric pump invokes an inverse magnetostrictive effect. The inverse magnetostriction curve with λ over stress looks different from the curves depicted in Fig. 2.5. In [WRC06], an inverse magnetostriction curve for an galfenol alloy is depicted. Therefore, the signal model needs to be modified accordingly for future investigations.

3.2.4 Measurement with EFC

To characterise the sensor with EFC, a test signal B_{s} with $f_{\mathrm{s}} = 10\,\mathrm{Hz}$ is applied via the signal coil. The test signal is converted into the mechanical resonance frequency by an electric pump signal with $f_{\mathrm{p}} = f_{\mathrm{res}} - f_{\mathrm{s}}$. For all EFC measurements, an optimal bias field of $B_{\mathrm{opt}} = -120\,\mu\mathrm{T}$ is applied via a bias coil.
In [ZSD12; Zhu+15b; Zhu+15a], the pump signal is applied via the positive input of the readout amplifier. The pump signal can only be very small because it is fed directly into the amplifier, driving it rapidly into saturation which limits the LoD due to the limited dynamic range. The strong carrier is suppressed in a subsequent filter stage because the excitation directly at the positive input of the readout amplifier prevents a suppression before the amplification.
The sensor layout with two piezoelectric layers and application of the pump via one of these layers allows the application of the carrier suppression technique explained in Subsec. 3.1.6 for MFC. For the investigated sensor, the carrier suppression is conducted digitally with a second pump signal. It is applied via a coupling capacitor C_{cs} according to variant 1 (see Fig. 3.19).
Fig. 3.48a shows the resulting 50 dB carrier suppression. The wideband noise floor is decreased due to the dynamic range of the readout device while the USB stays constant. In the inset of Fig. 3.48a, the noise in resonance is depicted. The dotted line represents the contribution from the thermal-mechanical noise measured without the application of a pump. When a pump is applied, the noise level rises. However,

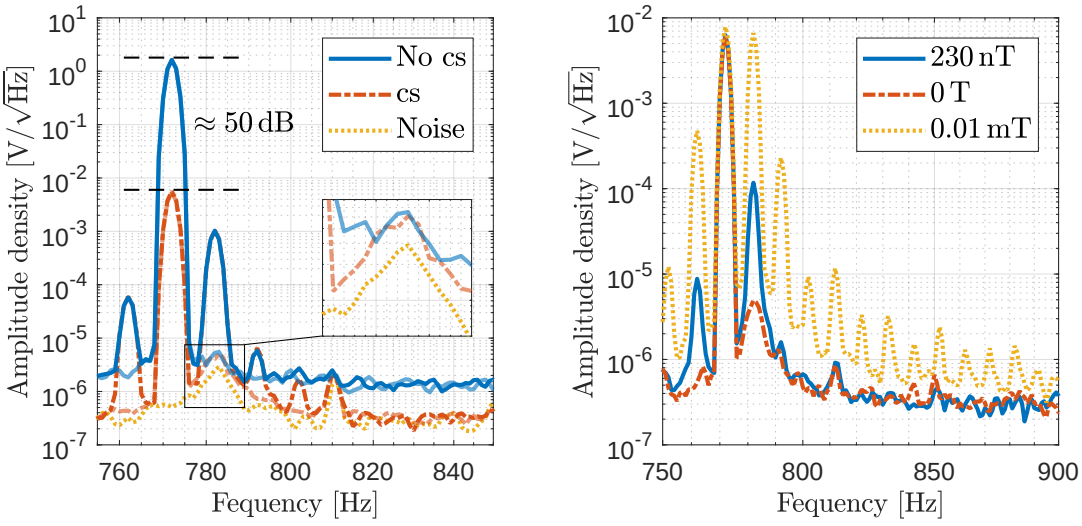

(a) (b)

Figure 3.48: (a) Spectral densities of EFC with and without carrier suppression (cs). The pump is applied at $f_p = 772\,\text{Hz}$ with $V_p = 1.5\,\text{V}$. The suppression signal with $V_{p,cs} = 3.8\,\text{V}$ and $f_{p,cs} = 772\,\text{Hz}$ has a phase offset of $\Delta\phi = 165.6°$ relative to the exciting pump. The desired signal has $B_s = 1\,\mu\text{T}$ and the frequency $f_s = 10\,\text{Hz}$. The respective spectra without applied B_s are slightly opaque. The inset zooms into the noise floors around f_{res}. (b) Measured EFC spectral densities for $V_p = 1.5\,\text{V}$ and $f_p = 10\,\text{Hz}$. The signal B_s is indicated in the legend. The dotted line shows the spectral density for a desired signal of $B_s = 10\,\mu\text{T}$ with several peaks with a spacing of $f_s = 10\,\text{Hz}$.

it is not affected by carrier suppression because the dynamic range only affects the wideband noise level.

Consequently, the carrier suppression does not lower the LoD for EFC, but it is essential to prevent nonlinear effects due to overload of the charge amplifier or the readout device.

To determine the optimal pump amplitude, V_p is applied in a range from 0 V to 3 V, both with and without an applied signal B_s while tracking the carrier, the USB, and the noise at the USB.

The best SNR for the investigated sensor results for pump amplitudes around $V_p = 1.5\,\text{V}$ (see Fig. 3.49). A DC offset to the pump decreases the SNR for this sensor and should not be applied.

The resulting measured spectral densities are depicted in Fig. 3.48b. By linearly decreasing the signal until it reaches the noise floor, the measured LoD of the sensor is $9\,\text{nT}/\sqrt{\text{Hz}}$.

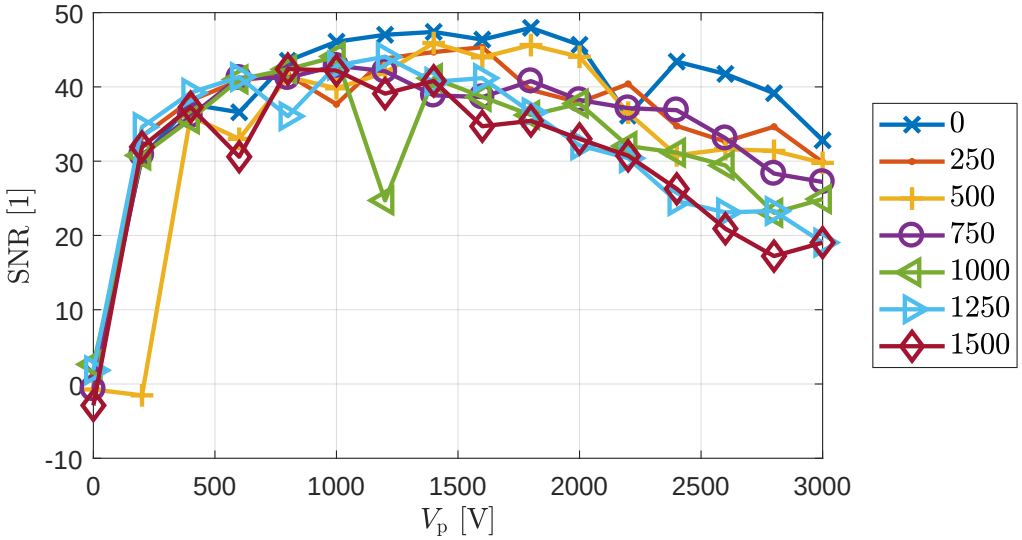

Figure 3.49: EFC analysis and sweep of an additional DC offset to the pump signal (see legend). The sweep is conducted with and without application of a desired signal with $B_s = 1\,\mu T$ and $f_s = 10\,Hz$. An optimal bias field of $B_{opt} = -120\,\mu T$ is additionally applied. The recorded spectral densities are averaged 30 times to reduce the variance.

By applying a stronger signal, the modulation index is increased and higher mixing products rise above the noise floor, as discussed in Sec. 3.2.3.
Similar to MFC, the detection limit is determined by the noise increase around f_{res} (cf. Fig. 3.48a or the thermal mechanical noise). The available sensor has no exchange bias, magnetic multilayer, or other features to reduce magnetic domain wall movement. Because the sensor has the same layout as standard ME sensors, it is also subject to the thermal-mechanical noise, as can be seen in Fig. 3.48a with a dotted line.

3.2.5 Evaluation of EFC

EFC converts desired signals into the mechanical resonance frequency. In analogy to MFC, the LoD for low-frequency signals can be lowered with this method. By altering the sensor structure to two piezoelectric layers, it is possible to apply an electric pump signal with low power instead of an energy consuming magnetic pump. The additional pump coil is not required for this detection scheme.
First investigations on the physical background of the conversion process for EFC are conducted. A direct and an indirect path for the pump voltage are found. The

LoD in resonance	$10\,\mathrm{pT}/\sqrt{\mathrm{Hz}}$
$\mathrm{LoD}_{\mathrm{MFC}}$	$7\,\mathrm{nT}/\sqrt{\mathrm{Hz}}$
$\mathrm{LoD}_{\mathrm{EFC}}$	$9\,\mathrm{nT}/\sqrt{\mathrm{Hz}}$

Table 3.7: Measured LoDs for the investigated sensor.

frequency conversion takes place in the magnetostrictive layer since it works as well for applying the pump signal through the linear AlN. A preliminary signal model is in good agreement with measurements.

Tab. 3.7 summarises LoDs for different detection schemes. The LoDs for MFC and EFC are nearly equal for the investigated sensor. A strong noise increase at the resonance frequency dependent upon the pump amplitude raises the LoD for the investigated sensors. Thus, EFC may potentially be a candidate to replace MFC in order to progress towards application. However, until now only a small number of less than 10 sensor prototypes with very different parameters and layer compositions have been investigated with EFC and are still far from optimum.

The magnetic layers investigated with MFC should be integrated into EFC sensors to lower the noise around resonance. Then, the influence of the additional noise sources from the second piezoelectric layer and the pump can be further investigated. Both contributions are enhanced by the mechanical resonator.

An advantage of EFC is that voltage sources for the pump signal are less noisy than comparable current sources because less power is required for a voltage pump. The excitation with a voltage is not limited by the impedance of a pump coil and therefore also higher excitation frequencies can be chosen. In Sec. 2.5, the advantages in terms of thermal-mechanical noise and bandwidth of higher bending modes are discussed.

To reduce the complexity of the sensor, the readout can also be performed with an induction coil as reported in [FPS07; ZSD12]. However, inductive readout requires an additional induction coil and is also prone to further coupling of interferences. First measurements with EFC, one piezoelectric layer, and inductive readout via an induction coil are conducted and prove its applicability for thin-film magnetoelectric sensors.

4 | Magnetoelectric Microwave Resonator

Magnetic and also magnetoelectric components historically have found various applications in microwave technology. For example, magnetoelectric thin-films are used as microwave filers based on yttrium iron garnet (YIG) [TS99]. A microwave (µw) applied in the proximity of the ferromagnetic resonance is coupled to a YIG cylinder causing a filter effect. With a magnetic bias, the ferromagnetic resonance can be tuned resulting in a tuneable filter. Via an additional piezoelectric layer, the tuning can be achieved with an applied voltage [SZT06]. Other applications include the tuning of antennas by exploiting their µw resonance [Yan+08] or the measurement of small magnetic fields with nano-electromechanical (NEMS) resonators [Nan+13]. In these NEMS sensors, the impedance of the resonator varies both in amplitude and phase as a function of the applied magnetic DC field. The electromechanical resonance frequency of the resonator can be used to enhance the output signal.

A cantilever, covered with a magnetostrictive layer, can, however, also be used as a microwave resonator and thus act as a magnetic field sensor. The sensor's microwave resonator is monitored by a readout signal in the GHz range. The µw resonance $f_{\mathrm{res,\mu w}}$ can be tuned by a magnetic signal that induces a bending of the cantilever. Because the readout is conducted via the processing of a shift in the µw resonance, a piezoelectric layer can be omitted at the cantilever sensors used for this method. By exploiting both the mechanical resonance and the µw resonance, an improvement of the SNR may be expected for this readout scheme. The concept of a magnetostrictively detuned microwave resonator operated as a magnetic field sensor is entirely new.

In this chapter, the working principle, a model for the operation, the sensor, measurements, and the performance of the resonator readout method are discussed. A patent application for the method has been handed in [Sal+18].

4.1 Principle of Magnetoelectric Microwave Resonator

In this readout method, the sensor is utilised as a magneto-mechanical transducer. The basic principle is the same as for a conventional ME sensor (see Sec. 2), except for the missing piezoelectric layer. A magnetic signal induces a bending in the sensor via mechanical coupling of the length change $\Delta l/l$ of the magnetostrictive layer. An optimal bias field B_{opt} or a specifically applied EB maximises $\Delta l/l$. The bending amplitude reaches local maxima at the mechanical resonant frequencies of the cantilever due to Eq. (2.3).
In order to incorporate a µw resonator with the cantilever, it may be integrated into a transmission line structure.

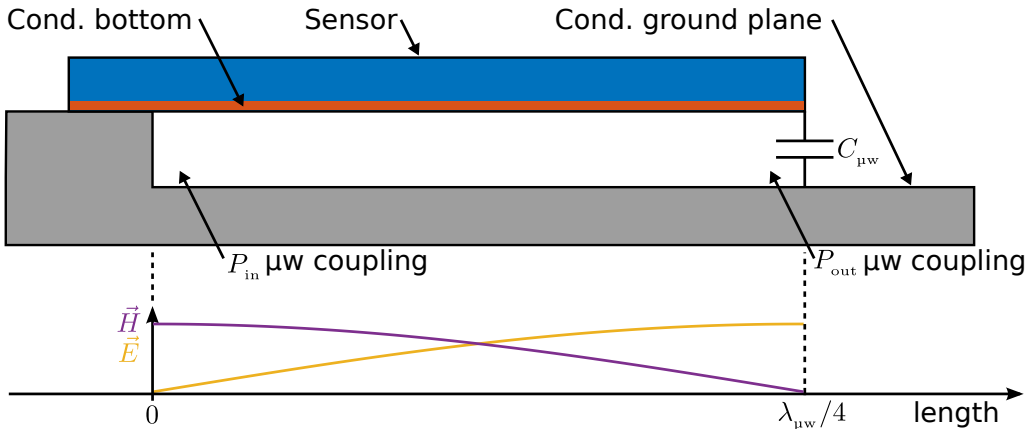

Figure 4.1: Schematic of a possible realisation of the magnetoelectric µw resonator. The position of the µw coupling is arbitrarily chosen. The lower diagram depicts the electric and magnetic field strengths as a function of the free-standing cantilever length.

Fig. 4.1 depicts a possible realisation that is used in the following to explain the principle. The cantilever is attached on one side on a conductive ledge over a ground plane. Its surface or at least its bottom side needs to be highly conductive at microwave frequencies in order to allow a resonating mode. If the resonator is excited with a microwave power P_{in} at $f_{\mathrm{res,\mu w}}$, e.g. via capacitive or inductive coupling, it can act as a $\lambda_{\mu w}/4$ or $\lambda_{\mu w}/2$ µw resonator, with the microwave wavelength $\lambda_{\mu w}$. Its length thus determines the associated resonance frequency $f_{\mathrm{res,\mu w}}$. The transmitted microwave power P_{out} contains information about changes to the signal such as a phase shift. It can be coupled at another suitably chosen point or, if the resonator

is operated as a reflection resonator, at the same port where P_{in} is supplied. In the exemplary structure of Fig. 4.1, the electric field $\vec{E}$ reaches its maximum at the tip of the cantilever, whereas the magnetic field reaches its maximum at the clamping point. The tip of the cantilever and the ground plane form a distributed capacitance $C_{\mu\text{w}}$, which is part of the ECD for the resonator.
A bending of the sensor changes $C_{\mu\text{w}}$ and leads to a shift of $f_{\text{res},\mu\text{w}}$. This shift can then be detected by appropriate signal processing.

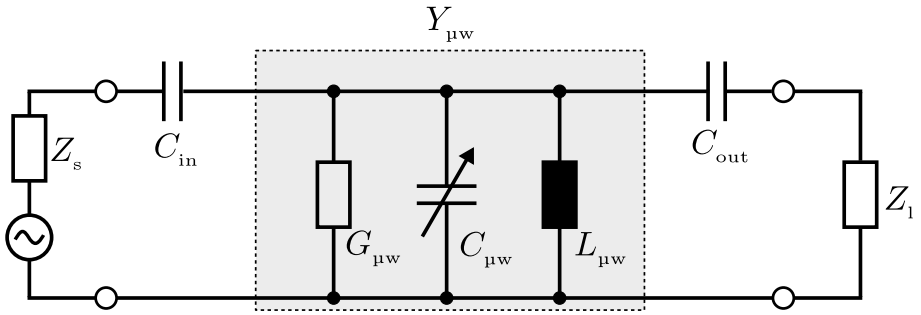

Figure 4.2: Equivalent circuit diagram for a two-port resonator driven by a source with impedance Z_{s} and a load impedance Z_{l}. C_{in} and C_{out} are coupling capacitors. The control arrow indicates a change of capacitance due to a tuning screw.

The ECD for a transmission resonator and its coupling is depicted in Fig. 4.2. If the resonator is excited in resonance, the transmitted power reaches its maximum and acts like a band-pass filter. The admittance of the resonant circuit is given by (see e.g. [Poz12])

$$Y_{\mu\text{w}} = G_{\mu\text{w}} + j\left(\omega\, C_{\mu\text{w}} - \frac{1}{\omega\, L_{\mu\text{w}}}\right) \tag{4.1}$$

and its unloaded quality factor by

$$Q_{\mu\text{w},0} = \frac{\omega_{\text{res},\mu\text{w}} C_{\mu\text{w}}}{G_{\mu\text{w}}}. \tag{4.2}$$

The unloaded quality factor cannot be seen directly because the resonator is loaded by the source and load impedances which can be mathematically transformed to the reference planes of the internal resonator. The scattering (S)-parameters of the resonator can be obtained by measurements with a vector network analyser. The loaded quality factor can be calculated from the 3 dB bandwidth of the transmission coefficient S_{21} with Eq. (2.5).

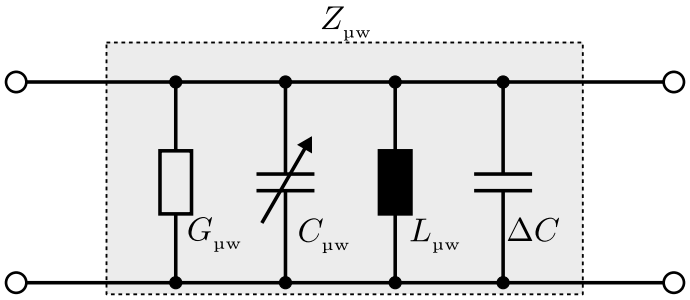

Figure 4.3: ECD of the unloaded resonator with a varying capacitor ΔC that represents the change of capacitance induced by the cantilever bending. The control arrow indicates a change of capacitance due to a tuning screw.

The loaded Q-factor can also be calculated by

$$Q_{\mu w} = \frac{Q_{\mu w,0}}{1 + \beta_{in} + \beta_{out}}, \tag{4.3}$$

with the coupling factors

$$\beta_{in} = \frac{1 - |S_{11}(\omega_{res,\mu w})|}{|S_{11}(\omega_{res,\mu w})| + |S_{22}(\omega_{res,\mu w})|} \tag{4.4}$$

and

$$\beta_{out} = \frac{1 - |S_{22}(\omega_{res,\mu w})|}{|S_{11}(\omega_{res,\mu w})| + |S_{22}(\omega_{res,\mu w})|}, \tag{4.5}$$

where S_{11} and S_{22} are the reflection coefficients from the measured S-parameter matrix of the system. In the ECD in Fig. 4.2, the coupling factors represent the actual capacitive or inductive coupling. With Eq. (4.3), the unloaded Q-factor can then be determined. In practice, the coupling should be sufficiently small for a given $Q_{\mu w,0}$ in order to achieve a high $Q_{\mu w}$.
The sensitivity of the microwave resonator to cantilever motion is essential for the readout method. Due to a mechanical bending of the cantilever, e.g. induced by an applied magnetic field, a small change of the resonator's capacitance occurs.
Fig. 4.3 illustrates an ECD of the unloaded resonator including an additional varying ΔC. It is expected to be small with respect to $C_{\mu w}$. In analogy to Eq. (4.1), the resonator's impedance is

$$Z_{\mu w} = \left(G_{\mu w} + \frac{1}{j\omega L_{\mu w}} + j\omega \Big(C_{\mu w} + \Delta C \Big) \right)^{-1}, \tag{4.6}$$

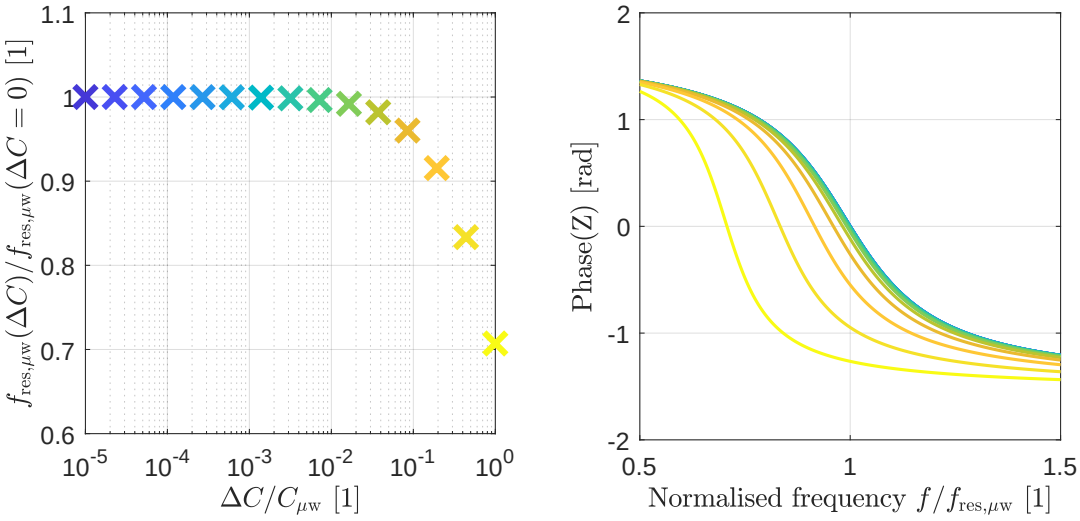

(a) (b)

Figure 4.4: (a) Change of resonance frequency normalised to $f_{\mathrm{res},\mu w}(\Delta C = 0)$ versus ΔC normalised to $C_{\mu w}$. The used values for ΔC on the abscissa range from $C_{\mu w} \cdot 10^{-5}$ (blue) up to $C_{\mu w}$ (yellow). Values in between are drawn with a colour gradient from blue to yellow. (b) Shift of the phase of the resonator's input impedance versus frequency normalised to the static resonance frequency $f_{\mathrm{res},\mu w}$ for various values of ΔC depicted with the same colour gradient as in (a).

with the conductance $G_{\mu w} = 1/R_{\mu w}$.
The resonance frequency of the resonator is then

$$\omega_{\mathrm{res},\mu w} = \frac{1}{\sqrt{L_{\mu w}(C_{\mu w} + \Delta C)}} \tag{4.7}$$

and its unloaded quality factor is

$$Q_{\mu w,0} = \omega_{\mathrm{res},\mu w} \frac{1}{G_{\mu w}} \Big(C_{\mu w} + \Delta C \Big). \tag{4.8}$$

To determine the influence of ΔC on the change of resonance frequency Δf, Eq. (4.6) is evaluated for fixed and arbitrarily chosen loss and inductance.
Fig. 4.4a illustrates the change of resonance frequency normalised to $f_{\mathrm{res},\mu w}(\Delta C = 0)$ versus ΔC normalised to $C_{\mu w}$ in order to clearly display the change Δf and the ratio between the two capacitors, respectively. A higher loss affects the unloaded Q-factor while a different inductance alters the resonance frequency. However, neither one of them change the characteristic of the curve in Fig. 4.4a.

If the change of capacitance is too small with respect to $C_{\mu w}$, Δf is negligible. Only just starting from approximately a factor of $\Delta C/C_{\mu w} = 10^{-3}$, a significant Δf is visible in Fig. 4.4a, although the curve constantly decreases. In consequence, the ratio between the capacitance at the tip of the cantilever $C_{\mu w}$ and ΔC must not be too small. To further illustrate the change of resonance frequency, Fig. 4.4b depicts the phase of the resonator's impedance for various values of ΔC. In practice, ΔC predominantly depends on the surface area on the top of the tuning screw, its distance to the cantilever tip, and the bending amplitude of the cantilever under excitation. It is assumed that a thicker tuning screw or a planar ledge with a larger cross-sectional area parallel to the cantilever increases the sensor's sensitivity. Also, the distance between the cantilever at maximum deflection and the tuning screw or ledge should be as small as possible.
Another consequence of the presented curves is that linearity can only be assumed for small ΔC. This implies that, for a desired sensitivity and tolerance in linearity, an optimum capacitance ratio exists which can be determined from Fig. 4.4a.
As mentioned in Sec. 2.2, the quality factor is inversely proportional to the loss in the resonator. The loaded Q-factor divides into the individual quality factors according to the loss contributions in the system and is calculated by Eq. (4.9). It is proportional to the amplitude enhancement, as well as the phase slope, at $f_{res,\mu w}$. Consequently, if it is desired to detect small changes of the resonance frequency, it is advantageous to have a resonator with a high Q-factor.

4.2 Loss Mechanisms, Sensor, and Setup of Magnetoelectric Microwave Resonator

The main aim for the sensor design is a sensitive readout to measure the low-frequency magnetic field. The loaded Q-factor $Q_{\mu w}$ determines the sensitivity of the resonator or equally the slope of the phase curve at $f_{res,\mu w}$. In order to increase $Q_{\mu w}$, the loss mechanisms in the system have to be identified and, if possible, lowered.

Total loss The loaded Q-factor can be written as

$$\frac{1}{Q_{\mu w}} = \frac{1}{Q_{\mu w,0}} + \frac{1}{Q_{ext,in}} + \frac{1}{Q_{ext,out}}, \tag{4.9}$$

where $Q_{ext,in}$ and $Q_{ext,out}$ consider the loading through the external circuit.

The unloaded $Q_{\mu w,0}$ itself depends in internal loss mechanisms and can be written as

$$\frac{1}{Q_{\mu w,0}} = \frac{1}{Q_{\text{surface}}} + \frac{1}{Q_{\text{radiation}}}, \tag{4.10}$$

with loss contributions from the surface including the conductivity of the resonator materials and from radiation. Loss from hysteresis and eddy currents are neglected here. The individual Q-factors divide into several contributors such as the surfaces from the ground plane, the sensor, a tuning screw, etc.

Clamping Because there is a current maximum and the surface currents flow from the ground plane via the clamping to the sensor surface, the conductivity and connection at the clamping point is important.
The cantilevers need to be clamped conductively. That precludes instant adhesive which is used for the standard magnetoelectric cantilevers. Instead, conductive glue or low-temperature solder is required. The clamping is investigated with standard conductive silver adhesive from *Plano GmbH*, conductive one-component adhesive *Elecolit 3653* from *Panacol*, and by a mechanical fixation with specified torque.
For the investigation, the resonator depicted in Fig. 4.9 with a cantilever of the dimensions 25 mm × 1.9 mm × 0.5 mm made of copper is used to exclude other influences.
The measured quality factors with conductive silver adhesive and the Elecolit 3653 eventually yield comparable results with a loaded Q-factor of 112. For adhesive clamping, the drying time, temperature and amount of glue is critical for both the µw resonance and the mechanical resonance of the cantilever. For example, the conductive silver adhesive requires > 40 min at room temperature drying time until the relative change of the quality factor goes below 2 % for consecutive measurements with an amount of one wire tip glue. A clamping with a mechanical fixation and specifically set torques has the same Q-factor of approximately 112. Therefore, the clamping method can be neglected if sufficient drying time is provided. The clamping behaviour may differ for various cantilever materials due to adhesion properties.

Coupling The coupling strength expressed with β_{in} and β_{out} is given in Eqs. (4.4) and (4.5). The relation between the coupling and the loaded Q-factor is given by Eq. (4.3). As mentioned before, the measured or likewise loaded Q-factor is inversely proportional to the coupling. For capacitive coupling, simulation and measurements

Material	κ [MS/m]	μ_r [Vs/Am]
Copper	56	0.99999
Brass (91 %)	27	≈ 1
Brass (65 %)	11-14	≈ 1
Aluminium	35	1.000024
Gold	43	0.99993
Titanium	2.5	≈ 1
Stainless steel 1010	7	-
Stainless steel 1.4305	1.37	-

Table 4.1: Specific conductivity κ and relative permeability μ_r of selected materials [Sti15].

confirm that the coupling increases the more the inner conductor protrudes above the ground plane. The closer the coaxial connections are to the maxima of the electric field, the stronger is the coupling. Fig. 4.1 depicts the field strengths as a function of the cantilever length. Another option to increase the coupling is to solder round copper plates on top of the inner conductor which increases the capacitance. Coupling factors ranging from $3 \cdot 10^{-4}$ up to 0.2 are measured with variations of the above parameters, showing the potential for adjustability. Inductive coupling yields comparable measured results. It is implemented by bent metallic wires that continue the inner conductors of the coaxial connectors towards ground. In order to vary the inductive coupling, the cross sectional area of the conductor loop as well as the position of the loop can be varied. Bigger cross sectional areas, orthogonal direction with respect to the magnetic field lines, and placement near magnetic field maxima increase the inductive coupling. Because the signal strength decreases for lower coupling factors, the coupling needs to be set such that the output signal is still processable with sufficient SNR by subsequent stages.

Conductivity and material The finite conductivity of the used materials decreases Q_{surface}. Effects such as oxidation on the surface may reduce the conductivity further.
The conductivities of a number of selected materials are given in Tab. 4.1. Moreover, used materials are required to be non-magnetic (except the magnetic layer) with a $\mu_r \approx 1$, somehow processable and durable, and thicker than the skin depth. The skin depth δ is given by [Sti15]

Material	$Q_{\mu w}$	$Q_{\mu w,0}$	β_{in}	β_{out}
Copper	177	180	$4.75 \cdot 10^{-4}$	$1.95 \cdot 10^{-2}$
Brass (91 %)	155	158	$4.43 \cdot 10^{-4}$	$1.71 \cdot 10^{-2}$
Brass (65 %)	139	141	$4.17 \cdot 10^{-4}$	$1.5 \cdot 10^{-2}$
Gold	170	173	$4.6 \cdot 10^{-4}$	$1.88 \cdot 10^{-2}$
Stainless steel 1010	115	116	$3.81 \cdot 10^{-4}$	$1.26 \cdot 10^{-2}$
Stainless steel 1.4305	71	72	$3.17 \cdot 10^{-4}$	$0.79 \cdot 10^{-2}$

Table 4.2: Simulation results for the ME sensor for a variation of the cantilever bulk material. The ground plane is copper. Simulations are conducted with *CST Microwave Studio* 2014. The parameters are extracted from the S-parameter curves as described above.

$$\delta = \frac{1}{\sqrt{\pi \kappa \mu f}}, \tag{4.11}$$

with the permeability $\mu = \mu_0 \mu_r$, and the frequency f. According to [MG86], conductive layers on isolating substrates should be at least five times as thick as the skin depth because the resistance rises with decreasing conductive cross-section through which current flows.

To determine the influence of individual loss sources is not trivial because changes to the model often alter multiple loss contributions. The loss due to the materials can be estimated with simulations. For a given model, the material can be varied while keeping all other parameters constant.

Changes to the Q-factors due to the material and the specific conductivity of the cantilever are listed in Tab. 4.2 for the model of the investigated magnetoelectric µw resonator.

The relationship between the Q-factors and the conductivity is depicted in Fig. 4.5. The curve has a logarithmic or a square root characteristic and can be fitted with a function of the form

$$\text{factor} \cdot \sqrt{\text{conductivity}}. \tag{4.12}$$

For the material of the ground plane a similar relation is deduced by simulation. In analogy, the quality factor of a cavity resonator is proportional to the square root of the conductivity [Kar17]

$$Q \propto \sqrt{\kappa}. \tag{4.13}$$

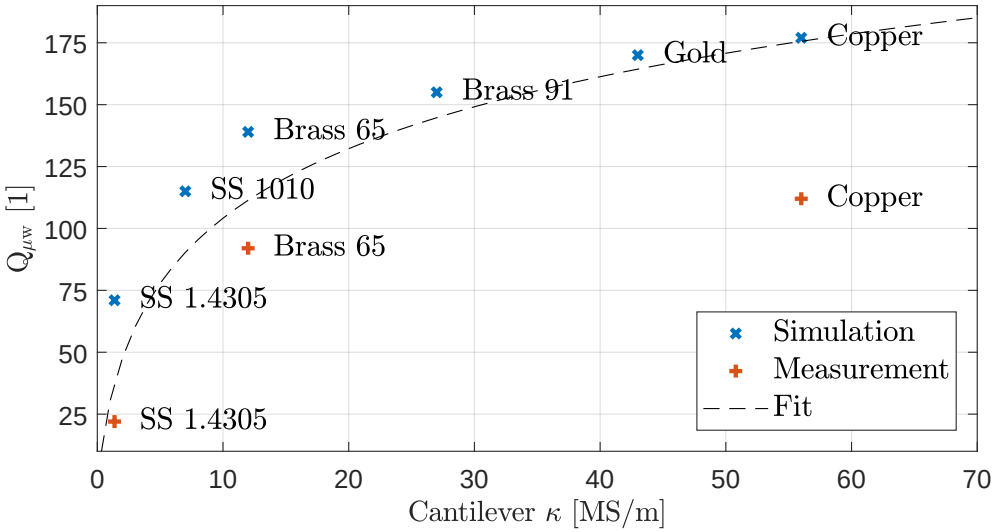

Figure 4.5: Measured and simulated Q-factors for the conductivities from Tab. 4.2.

Measured results with a limited number of cantilever materials show a similar characteristic, but a lower Q-factor due to the non-ideal surface roughness, clamping, etc (cf. Fig. 4.5).

Surface roughness The surface roughness is measured with a *VK-X 260k* laser scanning microscope from Keyence. Reflections at surface irregularities increase the loss summarised with $1/Q_{\text{surface}}$. According to [Mor49], grooves in metallic surfaces induce dissipation due to eddy currents. Since Morgan obtains approximately the same results for different simple shapes, their exact form is negligible. E.g. the milling head leaves scratches and gaps on the surface depending on the milling direction, speed, size of the milling head, etc.
Fig. 4.6 shows coloured images and roughness profiles two exemplary very rough surfaces of manufactured copper and brass ground planes. The rotation and linear movement of the milling head can be seen in both pictures. Because the copper is harder to process due to its cutting properties, the mean roughness is worse for copper by a factor of more than 4 as compared to brass. According to [HK00], the dissipation due to roughness needs to be taken into consideration because the skin depths can be in the order of magnitude of the surface roughness. A common way to evaluate the roughness is to express the average roughness R_{a} normalised to the skin depth for the given material. Further roughness measurements showed a R_{a}/δ of of approximately 0.5 and 0.1 for copper and brass, respectively. For stainless steel,

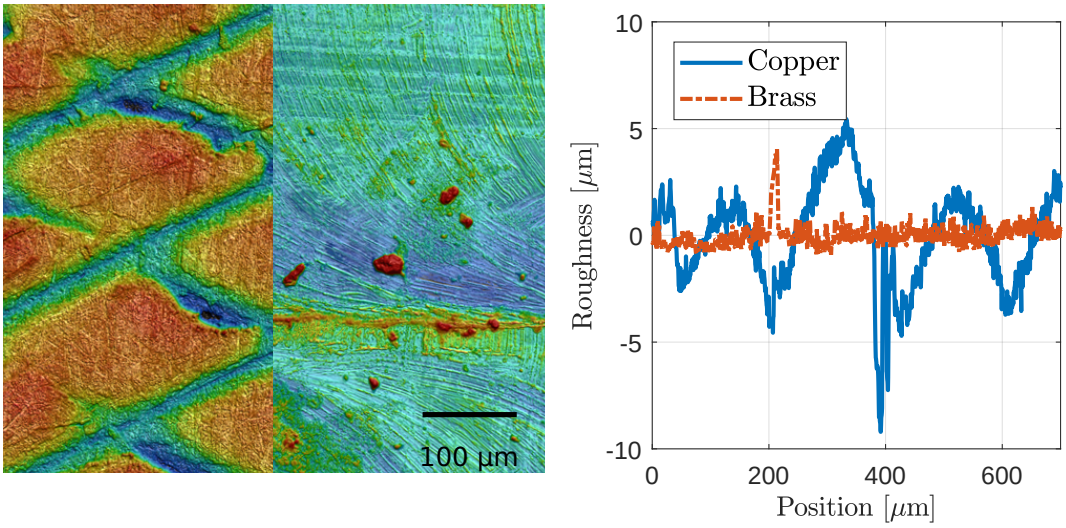

(a) (b)

Figure 4.6: (a) Surface roughness's of a copper (left) and a brass (right) surface manufactured with a milling machine with exemplary high roughness. The measurement is conducted with a Keyence VK-X 260k. The higher the elevation, the warmer the colour. (b) Respective measured roughness profiles of copper and brass ground planes.

it is a decade smaller and for gold even two decades smaller than for brass. The gold surface of the sensor has a very low average roughness due to the fabrication process with sputtering. According to [Mor49], the relative power dissipation due to surface roughness is then negligible for brass, stainless steel, and gold, and small for copper. The available fabrication processes responsible for the sensor and ground plane roughness's are not discussed in detail here.
From the available materials, copper is chosen for the ground plane due to its higher conductivity. The elastic modulus of a material determines its resistance against a elastic deformation. For the sensor material, gold is chosen because its elastic modulus is a factor of approximately 1.42 smaller than for copper which should allow better cantilever bending.

Radiation According to [Hof83], discontinuities such as a short-circuit and an open-circuit of a microstrip are subject to radiation loss. Because the ME µw resonator is similar to a microstrip without substrate, the radiation is a volume radiation whose radiated power scales with the square of the frequency and therefore

increases with frequency. The radiation Q-factor of a microstrip with an open-circuit discontinuity is given by

$$Q_{\text{rad,open-circuit}} = \frac{Z_{\text{ms}}}{120\pi \left(\frac{h}{c_0/f_{\text{res,µw}}}\right)^2 \frac{8}{3}}, \tag{4.14}$$

with the characteristic impedance Z_{ms} of the microstrip, the height of the conductor above the ground plane h, and the speed of light c_0. With the insertion loss for the investigated sensors being around 40 dB and the resonance frequency $f_{\text{res,µw}} \approx 3$ GHz, the radiation loss for the open-circuit as well as the short-circuit can thus be neglected.

Investigated sensor and resonator The utilised cantilever sensor has the dimensions 24.9 mm×1.9 mm. Its core consists of a single-side polished silicon 300 µm substrate. On the upper polished side, 4 µm FeCoSiB with the usual adhesion layers of 10 nm Ta on both sides is deposited. Magnetic anisotropy is induced during the sputter process along the short cantilever axis. To increase the conductivity, the top side is additionally covered with Au on top of 5 nm Cr, with the sputter process parameters set for a thickness of 1.3 µm. The customary thin cover of Ta that prevents oxidation is not applied due to its conductivity of $\kappa \approx 7$ MS/m and possible refraction effects. On the reverse side, rough silicon substrate is the outer layer.

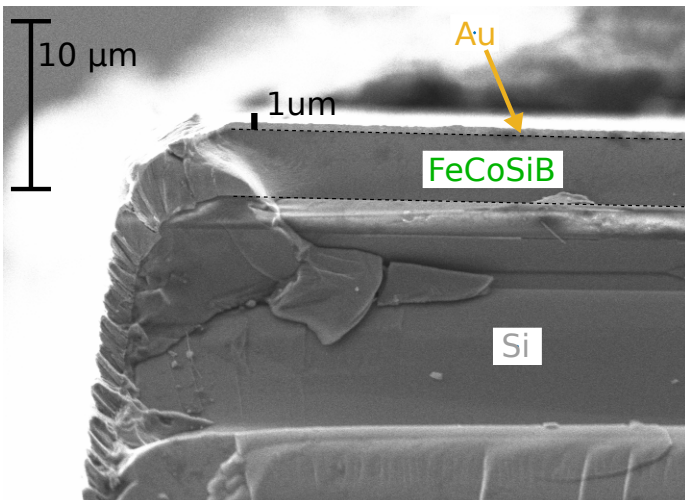

Figure 4.7: Scanning electron microscope (SEM) picture of a break-off edge of a similar sensor. The distinct grey contrasts indicate different materials. A dashed line emphasises the borders of the FeCoSiB.

Fig. 4.7 shows a scanning electron microscope (SEM) picture of a comparable sensor to determine whether the layers, and in particular the Au layer, have sufficient thickness in terms of skin depth. For gold and the resonance frequency of about 3.16 GHz, the skin depth is 1.37 µm according to Eq. (4.11). The SEM image proves that the intended thickness from the fabrication process of 1.3 µm is not reached. Instead, the thickness is only ≈ 500 nm. In consequence, fields penetrate the gold layer and reach the layer below the gold, experiencing refraction effects and a different conductivity. The surface roughness is lower than 200 nm. Measured S-parameters of the resonator yield a loaded Q-factor of 43 and $f_{\mathrm{res,\mu w}} = 3.14$ GHz, and coupling factors of $\beta_{\mathrm{in}} = 0.059$ and $\beta_{\mathrm{out}} = 0.087$. A cantilever without Au and with Ta on top of the FeCoSiB only has a Q-factor of 16, and a cantilever made of solid copper in the same dimensions has a Q-factor of 112. As assumed from previous sections, the cantilever material has a significant impact on the measured Q-factor. All measured Q-factors are significantly lower than the simulated values. According to [GH12], this is mainly due to the surface roughness and skin effect that becomes more important the higher the operation frequency. The accordance of measured and simulated results is better for brass than for copper which may be due to the higher surface roughness of copper (cf. Fig. 4.6). Since the cantilever is only covered with gold on one side, the conductivity on the reverse side is determined by the silicon and $\kappa_{\mathrm{Si}} \approx \kappa_{\mathrm{Cu}}/(10^{10})$. The measured Q-factor compared to a later available cantilever with gold on both sides is roughly 50 %.

Fig. 4.8 shows the measured relation between the Q-factor and the thickness of the outer conductive layer. The sensor used for this measurement is a 2 mm × 25 mm × 350 µm Si cantilever completely coated with 18 nm Ta and different thicknesses of Au. After reaching the skin depth thickness, the quality factor does not increase further for thicker gold layers. The measured value fits well into the expected quality factor for a solid gold cantilever, estimated with a fit of the measured values in Fig. 4.5. Therefore, the cantilever should be completely covered by a conductive material such as gold with a thickness greater than the skin depth.

The resonator used for the following measurements is depicted in Fig. 4.9 and reassembles the schematic of Fig. 4.1. Because the dimensions are thumb nail sized, the SMA connectors are especially small with an inner conductor diameter of 0.3 mm. The dielectric insulator made of Teflon has a diameter of 2.2 mm. Both the inner conductor and the insulator are level with the surface of the ground plane in order to obtain a weak coupling. To obtain a maximal effect, a tuning screw

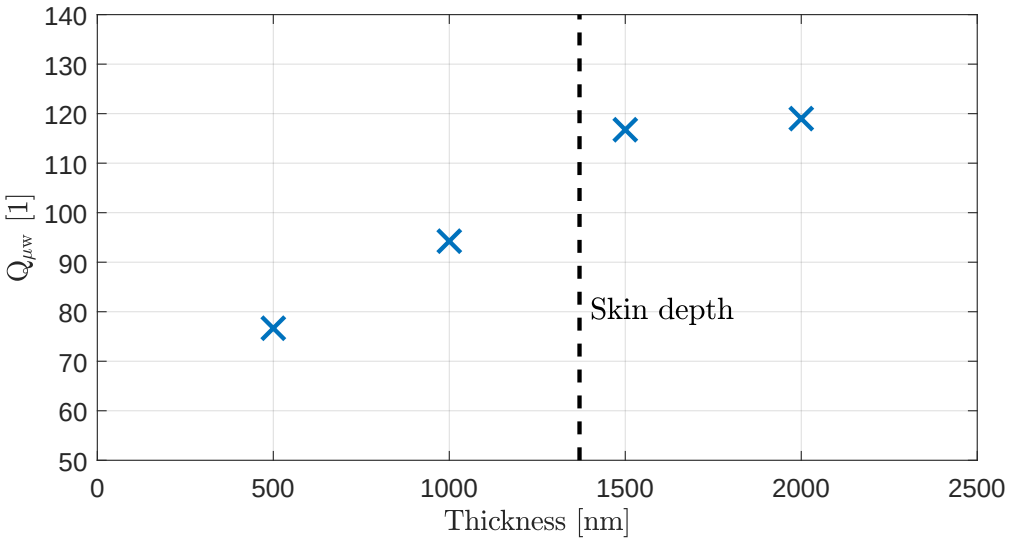

Figure 4.8: Measured Q-factor as a function of gold layer thickness. The gold layer completely encloses the cantilever. All measurement points are averages of three available samples per thickness, each measured four times.

is positioned near the maximum electric field of the resonator. The smaller the distance between the tip of the tuning screw and the sensor, the lower the resonance frequency of the resonator and the higher the measured Q-factor. For the following measurements, the tuning screw is manually set at the closest distance to the sensor without shorting the circuit. The copper surface roughness measurement in Fig. 4.6 stems from this resonator.
In conclusion, the most expedient measure to reduce the total loss is to enclose the whole cantilever with a gold layer sufficiently thicker than the skin depth. The second dominant loss contribution according to the discrepancy between measurement and simulation stems from the clamping and the roughness at the transition between ground plane and the cantilever.

Test setup The test signals are generated by a Keithley 6221 current source and transformed into magnetic fields via a signal coil. A Keysight B2962A low noise power source [KS16a] supplies the bias field via bias coil. The resonator and the coils are inside a shielding box as explained in Subsec. 2.5.1. Because the sensor is most sensitive along its long axis, the resonator is fixed with a holder that ensures axial alignment of the sensor. For excitation with a µw measurement signal, a *SMBV100A* signal source from *Rohde & Schwarz* [RS17a] is utilised. The device

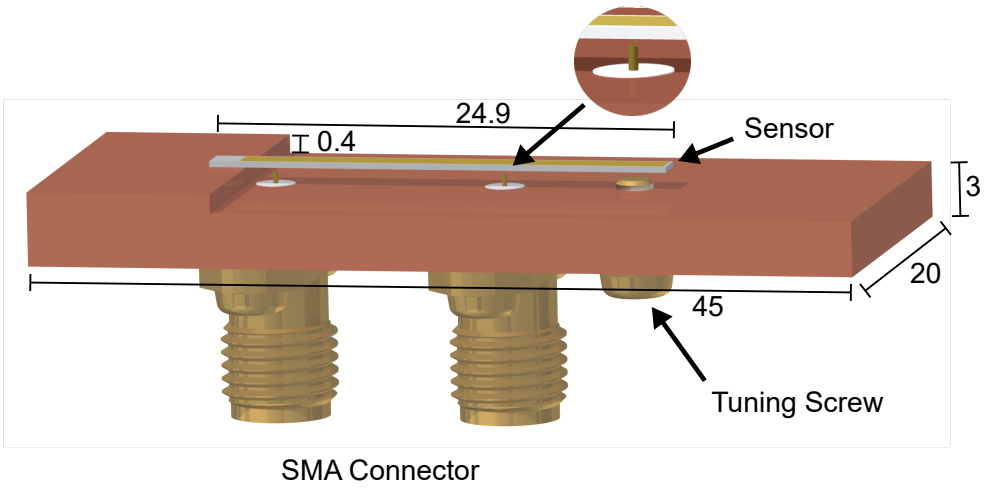

Figure 4.9: Model of the plane magnetoelectric µw resonator. The sensor is attached to the copper base with conductive adhesive. The microwave resonance can be varied with a fine tread tuning screw. The microwave signal is capacitively coupled with standard flange SMA connectors. The inner conductor protrudes above the plane copper surface. The dimensions are given in mm.

is chosen because it features the lowest phase noise at 3 GHz from the available tuneable laboratory sources. Phase noise is measured with an *FSWP-26* phase noise analyser [RS16] and will be discussed further in following sections. Readout is performed either with a SR785 spectrum analyser or a *FSV* spectrum analyser from *Rohde & Schwarz* [RS17b] with a bandwidth of 1 Hz unless otherwise noted. External noise is shielded as described in Subsec. 2.5.1.
In order to conduct measurements with the direct detection, a system model on the basis of the sensor principle and loss mechanisms is introduced in the next section that explains the signal behaviour.

4.3 System Model for Magnetoelectric Microwave Resonator

The system model serves to predict and verify the output of the sensor.
Fig. 4.10 shows a block diagram of the system. The sensor part of the block diagram remains unchanged as compared to direct detection, except that the piezoelectric layer is omitted. Instead, the sensor signal modulates the µw resonance of the resonator, indicated by the control arrow. Depending on the set µw measurement frequency, the phase and amplitude of the µw signal is modulated which can be seen

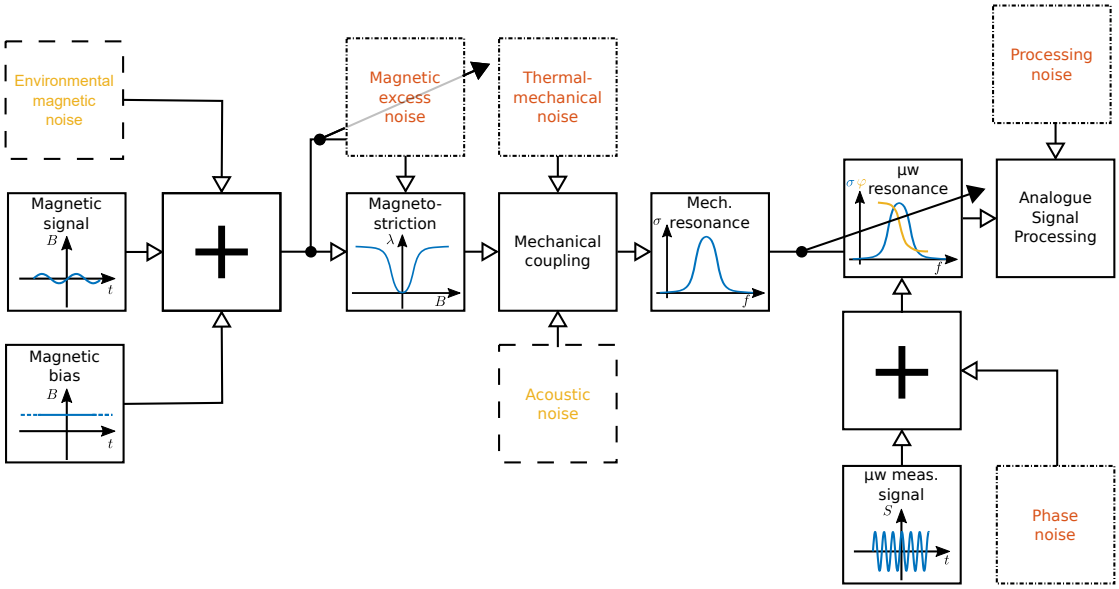

Figure 4.10: Block diagram of the magnetoelectric µw resonator system. System noise sources are depicted with dashed-dotted boxes. Environmental noise sources are indicated with dashed boxes.

as sidebands in the output spectrum. For a phase modulation, the measurement signal can be described as

$$S_{\mathrm{p,\mu w}} = P_{\mu w} \cdot \cos\left(\omega_{\mathrm{res,\mu w}} t + \eta \, \cos(\omega_{\mathrm{s}} t)\right), \tag{4.15}$$

with the signal power $P_{\mu w}$ and the modulation index η. For small modulation indices, Eq. 4.15 can be expanded to [HM07]

$$\begin{aligned} S_{\mathrm{p,\mu w}} \approx\ & P_{\mu w} \cdot \cos\left(\omega_{\mathrm{res,\mu w}} t\right) \\ & - \frac{P_{\mu w}\eta}{2}\Big[\sin\left((\omega_{\mathrm{res,\mu w}} + \omega_{\mathrm{s}})t\right) + \sin\left((\omega_{\mathrm{res,\mu w}} - \omega_{\mathrm{s}} t)\right)\Big]. \end{aligned} \tag{4.16}$$

A detailed derivation is given in Sec. A in the appendix. In the output spectrum, the carrier and two sidebands that contain the sensor information can be seen.
Fig. 4.11 depicts a schematic spectrum with a noisy microwave signal and two sidebands. Without phase information, the output spectrum cannot be distinguished from an amplitude modulation. A more general solution of Eq. (4.15) is given by Bessel functions producing several peaks around the carrier with a distance of ω_{s}. The sideband amplitudes do not comply with Bessel functions as would be the case

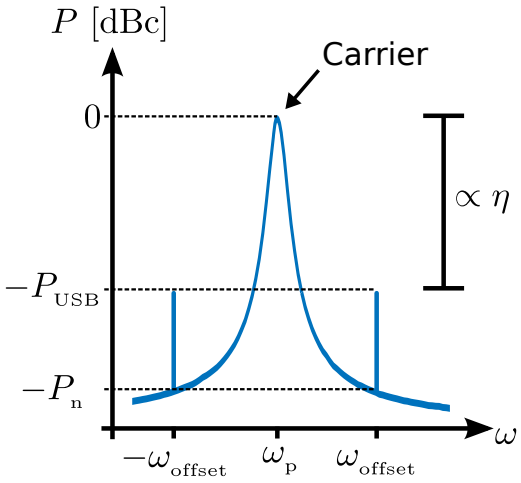

Figure 4.11: Typical spectrum of a noisy measurement signal with two sidebands resulting from a phase modulation. The modulation index η is proportional to the ratio of the sideband to the carrier.

for a pure phase modulation. A mix of phase and amplitude modulation is assumed. Since the modulation index is small for weak desired signals B_s, the narrowband approximation is valid here.
The modulation index η is given by

$$\eta = 2 \cdot 10^{\frac{P_\mathrm{USB}}{20}} \tag{4.17}$$

with the USB ratio with respect to the carrier P_USB. It allows to calculate the sensitivity of the phase modulation for applied magnetic fields η_s with

$$\eta_\mathrm{s} = \frac{\eta}{B_\mathrm{s}}. \tag{4.18}$$

With a known noise floor ratio with respect to the carrier P_n, the LoD can be calculated by

$$\mathrm{LoD} = \frac{2}{\eta_\mathrm{s}} \cdot 10^{\frac{P_\mathrm{n}}{20}}. \tag{4.19}$$

For an exemplary sideband amplitude of $P_\mathrm{USB} = -70\,\mathrm{dBc}$ for $B = 1.5\,\mu\mathrm{T}$ at 132 Hz, this yields a $\eta_\mathrm{s}(132\ \mathrm{Hz}) = 421\,\mathrm{rad/T}$. With Eq. (4.19) and $P_\mathrm{n} \approx -85.4\,\mathrm{dBc/Hz}$ from Fig. 4.12, the calculated LoD is $254\,\mathrm{nT}/\sqrt{\mathrm{Hz}}$ which is a resolution of approximately 299 nT with the chosen settings.

The used signal sources have phase and amplitude noise, whereas the amplitude noise of the system components is often much smaller and negligible [TWK98]. Phase noise originates from several noise sources within the generator such as its white noise floor and its flicker noise with $1/f$ characteristic.

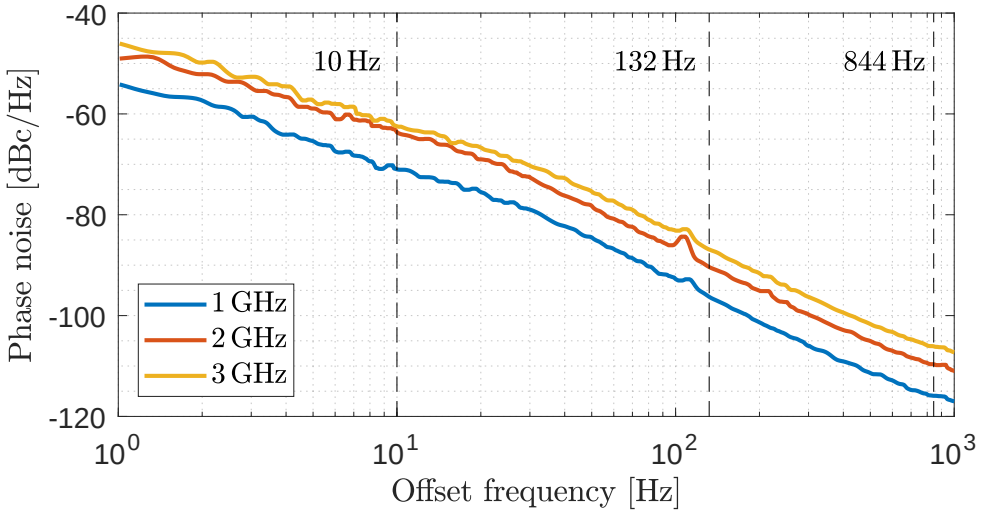

Figure 4.12: Phase noise measurement of the SMBV100A signal sources conducted with a FSWP-26 phase noise analyser. The test signal frequencies are indicated with dashed lines.

Fig. 4.12 shows the phase noise of the utilised signal source SMBV100A. It is measured with a FSWP-26 phase noise analyser. The phase noise of other available and measured signal sources such as a *HP83650A* from *Hewlett-Packard*, a *HP83752B* from *Hewlett-Packard*, or a *Marconi 2032* from *Marconi Instruments* is higher. Phase noise generally increases for higher frequencies and decreases for higher offset frequencies.

The phase noise is assumed to deteriorate the detection limit for direct detection, as can be seen from measurements in Fig. 4.13. The noise floors of the readout devices are negligible for the magnetoelectric µw resonator.

Thus, the SNR for direct detection is determined by η_s and the phase noise of the microwave signal.

In the next section, the model is verified by measurements with direct detection.

4.4 Direct Detection with Magnetoelectric Microwave Resonator

For direct detection via the magnetoelectric µw resonator, three test signals are chosen to characterise the system. Low-frequency biomagnetic measurements are represented by a 10 Hz signal.
The block diagram for the direct detection scheme of the µw resonator is included in the system block diagram in Fig. 4.10. 132 Hz is an arbitrarily chosen frequency without a relation to any grid or signal frequencies and 844 Hz is the mechanical resonance frequency of the cantilever. In order to achieve the highest output amplitudes, the bias fields are set to their optimal values of -0.8 mT, -0.8 mT, and -0.2 mT, respectively. The output signal is processed with an FSV spectrum analyser.

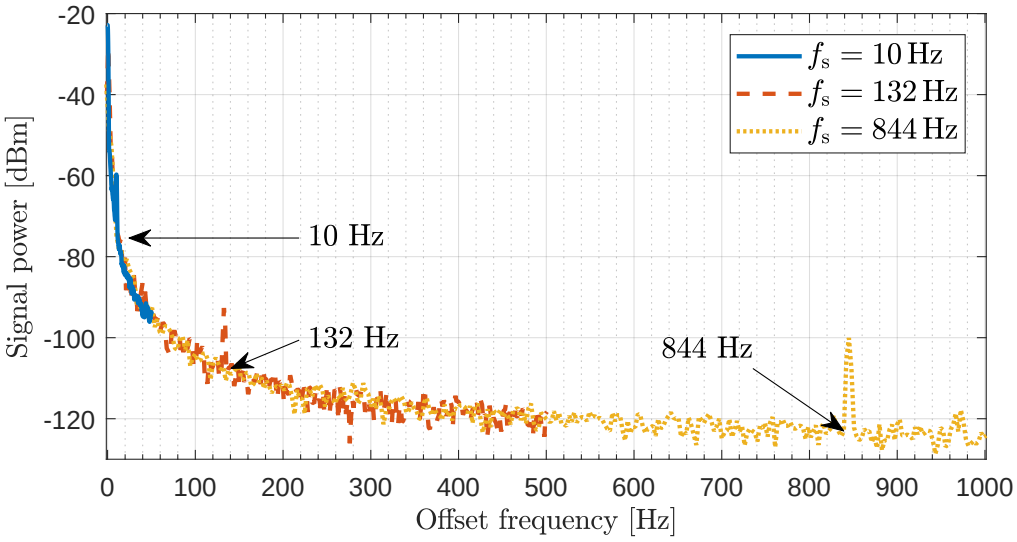

Figure 4.13: Spectra for direct detection of the magnetoelectric µw resonator for three signal frequencies at 10 Hz, 132 Hz, and 844 Hz. Arrows point at the respective noise floors at the signal frequencies. The µw signal is applied at $f_{\mathrm{res,\mu w}} = 3.16$ GHz with 25 dBm. The signal amplitudes are chosen such that the signals are visible in the spectrum and are 40 µT, 1.5 µT, and 18 nT, respectively.

Fig. 4.13 shows the positive spectrum of offset frequencies from the µw signal at $f_{\mathrm{res,\mu w}} = 3.16$ GHz for a direct detection. Signals at 10 Hz, 132 Hz and 844 Hz can be differentiated from the noise floor as peaks. The noise floor stems from the phase noise of the µw signal which decreases with frequency [TWK98]. Therefore, the signal at 844 Hz experiences the lowest noise floor of the three signals.

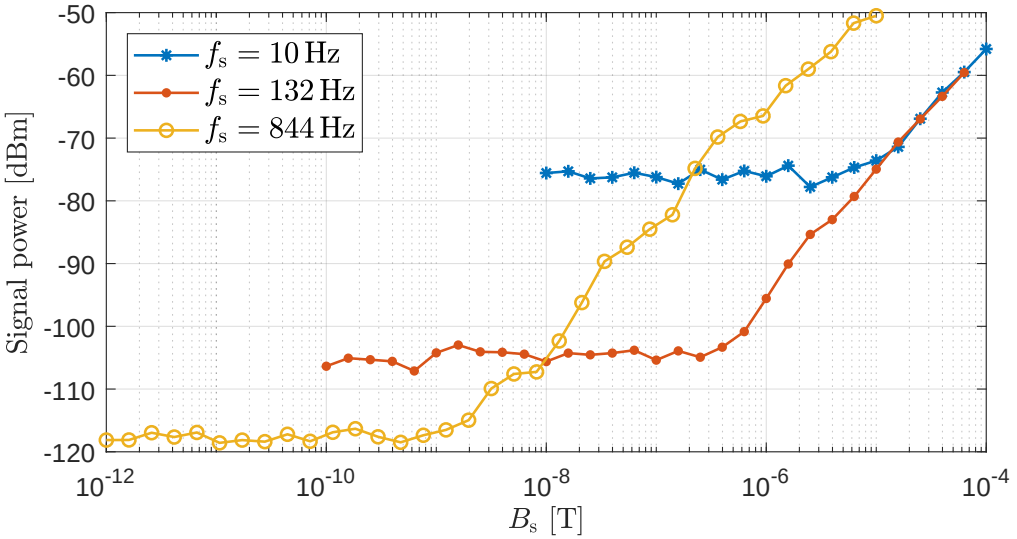

Figure 4.14: Resolution measurements for the three test signals with $f_{\mathrm{res,\mu w}} = 3.16\,\mathrm{GHz}$ and $P_{\mu w} = 25\,\mathrm{dBm}$.

Fig. 4.14 shows the respective output signals with respect to their magnetic amplitude. Until the signals reach the noise floor, they show linear behaviour. The sensitivity of the signals at 10 Hz and 132 Hz are comparable and the difference in resolution is solely due to the deviant noise floor. The 844 Hz signal additionally benefits from the enhanced amplitude at f_{res} and thus features the best resolution. All results correspond to calculated values with Eq. 4.19.
However, the detection limits are constrained by the phase noise of the system (cf. Fig. 4.12). Sources with better phase noise characteristics are commercially available, but often operate only at fixed frequencies, e.g. crystal oscillators. Moreover, the µw frequency $f_{\mu w}$ is subject to a drift which impedes demodulation and readout because no fixed reference frequency is available.
A solution to these problems is a readout scheme with a matched phase discriminator as explained in the next section.

4.5 Frequency Discriminator with Magnetoelectric Microwave Resonator

The readout via direct detection is mainly limited by the phase noise of the µw signal. In order to reduce the phase noise, a detection scheme with a frequency discriminator (FD) can be used.

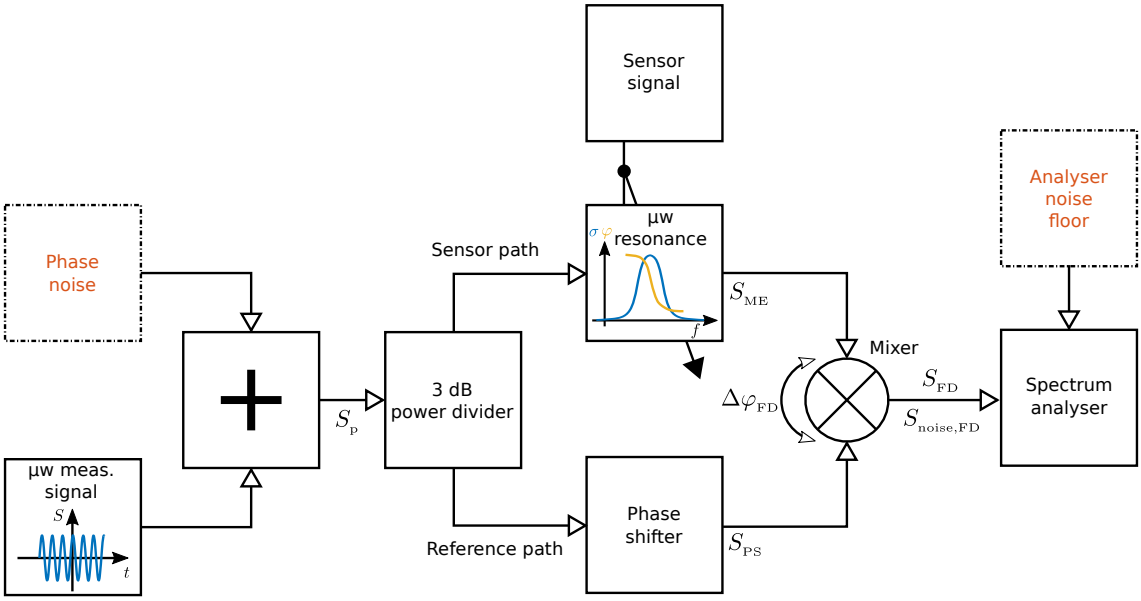

Figure 4.15: Block diagram of the frequency discriminator (FD) detection scheme for the magnetoelectric µw resonator. Noise sources are depicted with dash-dotted boxes. The phase difference between the sensor path and the reference path is indicated with a double arrow and $\Delta\varphi_{FD}$.

The block diagram for the FD detection scheme is depicted in Fig. 4.15. For this detection scheme, the µw measurement signal is divided into a sensor and a reference path by a 3 dB power divider. The sensor path functions similar to the direct detection in the last section. It introduces a static phase shift φ_{ME} without applied signal B_s. In the reference path, a phase shifter inserted in the signal path adds a set phase φ_{PS}. It enables to set the relative phase difference $\Delta\varphi_{FD} = \varphi_{ME} - \varphi_{PS}$ at the phase discriminator (without an applied magnetic signal B_s).
Assuming a microwave signal with the phase noise $\Delta\varphi_p$

$$S_{p,\mu w} = P_{\mu w} \cdot \cos(\omega_{res,\mu w} t + \Delta\varphi_p), \tag{4.20}$$

the signals after the phase shifter and the sensor are given by

$$S_{\mathrm{PS}} = \frac{P_{\mu\mathrm{w}}}{2} \cdot \cos(\omega_{\mathrm{res},\mu\mathrm{w}} t + \Delta\varphi_{\mathrm{FD}} + \Delta\varphi_{\mathrm{p}}) \tag{4.21}$$

and

$$S_{\mathrm{ME}} = \frac{P_{\mu\mathrm{w}}}{2} \cdot \cos(\omega_{\mathrm{res},\mu\mathrm{w}} t + \eta\, \cos(\omega_{\mathrm{s}} t) + \Delta\varphi_{\mathrm{p}}), \tag{4.22}$$

now assuming a phase modulation induced by a sensor signal with ω_{s} and a modulation index η. Additional amplitude noise is neglected here. The output of the phase discriminator can be calculated by

$$\begin{aligned} S_{\mathrm{FD}} &= S_{\mathrm{PS}} \cdot S_{\mathrm{ME}} \\ &= \frac{P_{\mu\mathrm{w}}^2}{4} \cdot \cos(\omega_{\mathrm{res},\mu\mathrm{w}} t + \eta\, \cos(\omega_{\mathrm{s}} t) + \Delta\varphi_{\mathrm{p}}) \cdot \cos(\omega_{\mathrm{res},\mu\mathrm{w}} t + \Delta\varphi_{\mathrm{FD}} + \Delta\varphi_{\mathrm{p}}), \end{aligned} \tag{4.23}$$

which can be rewritten as

$$\begin{aligned} S_{\mathrm{FD}} &= \frac{P_{\mu\mathrm{w}}^2}{8} \cdot \left\{ \cos\left[\eta \cos(\omega_{\mathrm{s}} t) - \Delta\varphi_{\mathrm{FD}}\right] + \cos\left[2\omega_{\mathrm{res},\mu\mathrm{w}} t + \Delta\varphi_{\mathrm{FD}} + \eta \cos(\omega_{\mathrm{s}} t) + 2\Delta\varphi_{\mathrm{p}}\right] \right\} \\ &\overset{\mathrm{LPF}}{=} \frac{P_{\mu\mathrm{w}}^2}{8} \cdot \cos\left[\eta \cos(\omega_{\mathrm{s}} t) - \Delta\varphi_{\mathrm{FD}}\right], \end{aligned} \tag{4.24}$$

if only the low-frequency part passes through a low-pass filter (LPF). The residual phase noise in the baseband is neglected here and explained later. The slope of the cosine is maximum in its deflection points or equally for

$$\Delta\varphi_{\mathrm{FD}} = \varphi_{\mathrm{ME}} - \varphi_{\mathrm{PS}} = (2i-1)\frac{\pi}{2}, \tag{4.25}$$

with $i \in \mathbb{N}$. The amplitude modulated sidebands cancel for $i \in \mathbb{N}$ and the mixer operates as a phase discriminator. For the following measurements, the FD is set to the largest slope according to Eq. (4.25) with the phase shifter. With $\Delta\varphi_{\mathrm{FD}} = 90°$, Eq. (4.24) simplifies to

$$\begin{aligned} S_{\mathrm{FD}} &= \frac{P_{\mu\mathrm{w}}^2}{8} \cdot \sin\left[\eta \cos(\omega_{\mathrm{s}} t)\right] \\ &\approx \frac{P_{\mu\mathrm{w}}^2}{8} \cdot \eta \cos(\omega_{\mathrm{s}} t) \end{aligned} \tag{4.26}$$

which is a sideband at ω_{s} in the frequency domain that contains information about the desired signal. The more incident power $P_{\mu\mathrm{w}}$ is applied via the microwave source, the larger are the sideband and the phase noise. However, the FD method has the same phase noise in both branches, as can be seen in Eqs. (4.21) and (4.22).
In the low-frequency part of Eq. (4.24), the phase noise $\Delta\varphi_{\mathrm{p}}$ is somehow suppressed because the phase noises in both paths stem from the same source. The quantitative phase noise suppression depends on the delay time between the two paths. If the noise is modelled as a phase modulation with $\eta \cos(\omega_{\mathrm{offset}} t)$, then the demodulated noise sideband $S_{\mathrm{noise,FD}}$ is given as

$$S_{\mathrm{FD,n}} \approx \frac{\eta P_{\mu\mathrm{w}}^2}{8} \left[\cos\left(\omega_{\mathrm{p}} + \omega_{\mathrm{offset}} \left(t - \frac{\tau_{\mu\mathrm{w}}}{2}\right)\right) \cdot \sin\left(\frac{\omega_{\mathrm{offset}} \tau_{\mu\mathrm{w}}}{2}\right)\right]. \tag{4.27}$$

Derivations of Eqs. (4.27). (4.28), and (4.29) are provided in Sec. A in the appendix.
On the input of the FD, the noise sideband level normalised to the carrier level $P_{\mathrm{in,n}}$ is given by

$$P_{\mathrm{in,n}} = \frac{P_{\mu\mathrm{w}} \cdot \frac{\eta}{2}}{P_{\mu\mathrm{w}}} = \frac{\eta}{2}. \tag{4.28}$$

The noise sideband normalised to the signal level at its output $P_{\mathrm{out,n}}$ is given by

$$P_{\mathrm{out,n}} = \frac{\frac{P_{\mu\mathrm{w}}^2 \eta}{8} \cdot \sin\left(\frac{\omega_{\mathrm{offset}} \tau_{\mu\mathrm{w}}}{2}\right)}{\frac{P_{\mu\mathrm{w}}^2}{8}} = \eta \sin\left(\frac{\omega_{\mathrm{offset}} \tau_{\mu\mathrm{w}}}{2}\right). \tag{4.29}$$

The phase noise suppression is then given by the ratio of Eqs. (4.28) and (4.29)

$$\frac{P_{\mathrm{out,n}}}{P_{\mathrm{in,n}}} = \frac{20 \cdot \lg\left[\eta \cdot \sin\left(\frac{\omega_{\mathrm{offset}} \tau_{\mu\mathrm{w}}}{2}\right)\right]}{20 \cdot \lg\left(\frac{\eta}{2}\right)} = 6 + 20 \cdot \lg\left[\sin\left(\frac{\omega_{\mathrm{offset}} \tau_{\mu\mathrm{w}}}{2}\right)\right]. \tag{4.30}$$

Fig. 4.16 depicts the reduction of phase noise as a function of the relative delay time between the two paths. The phase noise suppression decreases for rising delay time and offset frequency with 20 dB/decade. The delay time of the investigated

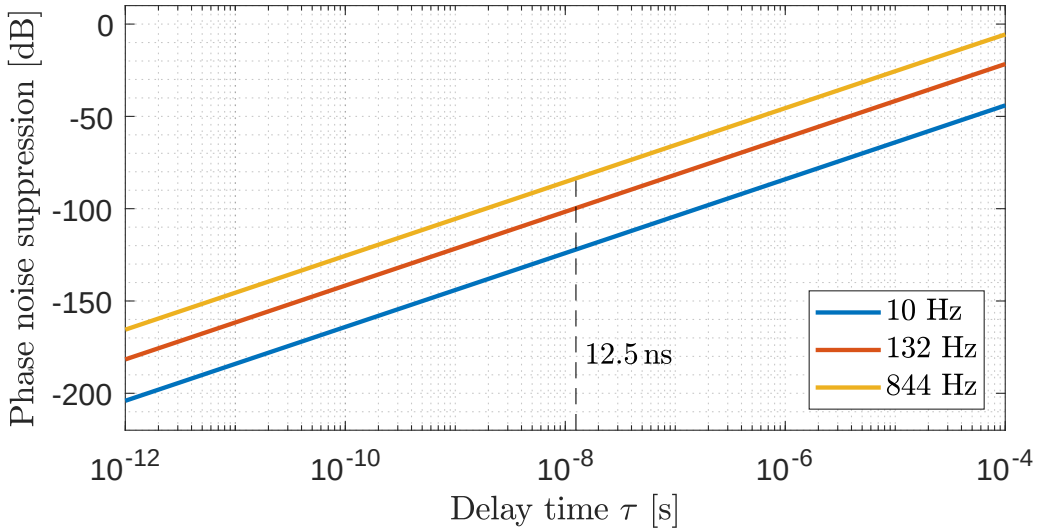

Figure 4.16: Reduction of the phase noise of a FD as a function of the delay time $\tau_{\mu w}$ according to Eq. (4.30).

setup is 12.5 ns which yields a phase noise reduction of -121 dB, -98 dB, and -80 dB for 10 Hz, 132 Hz, and 844 Hz, respectively.
The 3 dB divider is a home-made 50 Ω microstrip divider with SMA connectors. A *ZAM-42* mixer from Mini-Circuits is used as a phase discriminator. For the reference path, the phase is matched manually with a digital counting phase shifter from *ATM* according to Eq. (4.25) using a standard oscilloscope. A SR785 spectrum analyser is used to process S_{FD}.
To test the detection scheme, the same test signals as in Sec. 4.4 are applied to the sensor.
Fig. 4.17 shows the obtained LoDs. The 10 Hz and the 132 Hz signal have the same sensitivity, but different LoDs of 20 nT/$\sqrt{\mathrm{Hz}}$ and 7 nT/$\sqrt{\mathrm{Hz}}$, respectively. This is due to a $1/f$ component of the noise. At f_{res}, the sensitivity of the sensor is strongly enhanced resulting in an LoD of 25 pT/$\sqrt{\mathrm{Hz}}$.

Frequency discriminator with MFC To lower the LoD for the detection of the 10 Hz signal, the sensor is driven with MFC as explained in Sec. 3.1. A MFC analysis as performed in Subsec. 3.1.4 yields an optimal pump amplitude of $B_{\mathrm{p}} = 100\,\mu\mathrm{T}$ for a pump frequency of $f_{\mathrm{p}} = f_{\mathrm{res}} - 10\,\mathrm{Hz}$ and readout of the upper sideband. The resulting LoD for a 10 Hz signal is 650 pT/$\sqrt{\mathrm{Hz}}$. This is due to the increased noise at the resonance frequency as discussed in Sec. 3.1.7 and the chosen pump

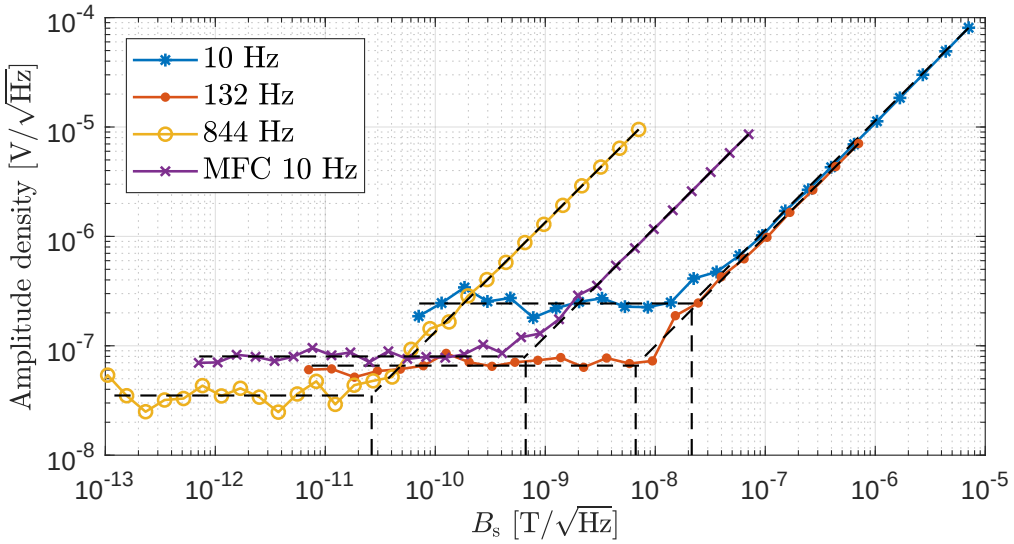

Figure 4.17: LoD measurement for the magnetoelectric µw resonator operated in a FD setup. The bias fields are -0.8 mT, -0.8 mT, and -0.2 mT, respectively. The linear signal regime, the average noise level, and the LoD are indicated with a dashed line. The measurements are averaged 10 times to reduce the variance. A measurement of a 10 Hz signal with MFC of the µw resonator is depicted with crosses. The pump amplitude is $B_p = 100\,\mu T$.

amplitude for optimal SNR. With a different pump amplitude, the sensitivity can be increased but the SNR would decrease due to the increased noise. The investigated sensor features no layer design that reduces magnetic noise such as the previously discussed multilayer sensors. Since the sensor phase φ_{ME} is now a function of the MFC signal, the whole spectrum including the carrier and the two sidebands can be seen in S_{FD}. The increase in LoD as compared to the detection of the 844 Hz signal depicted in Fig. 4.17 is due to increased noise at the upper sideband or likewise f_{res}. The origin of the noise is either magnetic excess noise or noise of the pump source and discussed in Subsec. 3.1.7. Because these noise sources enter the system before the mechanical resonator, they are the same as for standard MFC.

Limiting noise contribution Two noise sources are possibly dominant for the detection of the desired signals with the FD method: the phase noise induced by the sensor itself and the flicker noise of the phase discriminator. Magnetic noise from the µw measurement signal is neglected because according to [Urs+16] the domain wall motion cannot follow fields with frequencies in the GHz range. The flicker noise can be eliminated by introducing a second mixer into the sensor path

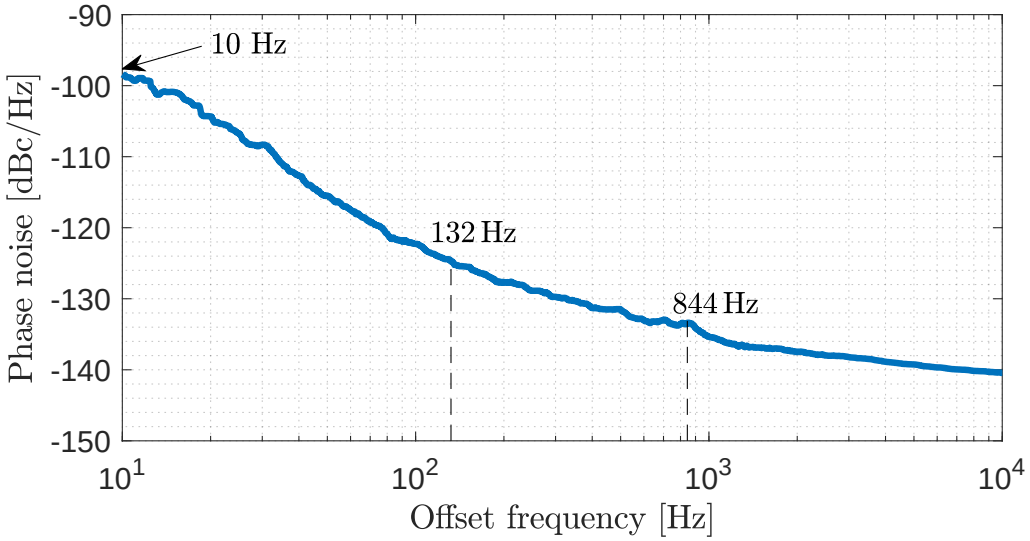

Figure 4.18: Additive phase noise measurement of the magnetoelectric µw resonator measured with an FSWP-26 phase noise analyser and a excitation signal of 10 dBm at $f_{\mathrm{res,\mu w}}$. The frequencies of precious measurements are marked with dashed lines.

right before the phase discriminator (heterodyne principle). If the second mixer has non-dominant noise and its LO source has negligible phase noise, the overall noise floor will be lowered. Nevertheless, the ultimate noise floor stems from the phase noise originating from the ME sensor because its thermal-mechanical noise is part of the signal that modulates the sensor phase φ_{ME}.

To determine which noise source is dominant, the additive phase noise of the magnetoelectric µw resonator is measured with an FSWP phase noise analyser. Fig. 4.18 shows the measured phase noise. For the measurement, the shielding of the sensor is very important because external interferences naturally raise the noise floor. Therefore, the measurement is conducted in the shielding box. In comparison with the phase noise from the microwave signal (cf. Fig. 4.12), it is significantly reduced. With Eq. (4.19), the LoD can be calculated.

	10 Hz	132 Hz	844 Hz
Signal [dBc]	-37	-70	-78
Phase noise [dBc]	-52	-85.5	-102
Sensor noise [dBc]	-99	-125	-135
Resolution direct [T]	8 µ/7.98 µ	300 n/299 n	1 n/1.27 n
LoD FD [T/$\sqrt{\text{Hz}}$]	20 n/31 n	7 n/2.6 n	25 p/25 p

Table 4.3: Calculated and measured values of resolution/LoD for the magnetoelectric µw resonator (measured/calculated).

Tab. 4.3 shows the measured and calculated resolutions and relevant parameters. The measured and calculated values match well. Therefore, it is concluded that the sensor noise is the dominant noise contribution in the system.

4.6 Evaluation of Magnetoelectric Microwave Resonator

In this chapter, a completely novel resonator based readout method for magnetoelectric sensors is introduced. A ME cantilever is integrated into a microwave resonator which is excited with a GHz signal. The detuning of the resonator is proportional to a desired magnetic signal and is read out with appropriate signal processing.
After a description of the resonator principle and the system, the loss contributions of the microwave resonator are discussed. To increase the Q-factor, the cantilever should be completely enclosed with a highly conductive material of sufficient thickness relative to the skin depth at microwave frequencies. The sensitivity for the measurement of desired magnetic fields strongly depends on the induced change in capacitance due to the cantilever bending. First measurements with direct detection and calculations with a new system model identify the phase noise of the source as the dominant noise contribution. The phase noise is suppressed with a FD setup which is verified and quantified with a detailed mathematical derivation. As a result, the LoD is significantly lowered by more than two decades down to 25 pT/$\sqrt{\text{Hz}}$ at the mechanical resonance of the cantilever.
The main advantage of this readout scheme is that the piezoelectric layer can be omitted. This lowers the technological complexity and avoids the thermal-electrical noise from the layer. Also, no charge amplifier is necessary whose amplification is dependent on the sensor capacitance and whose feedback network needs to be

adapted accordingly. Whether in order to miniaturise or to introduce a remote access, the layout of the resonator can easily be altered. The devices required for readout are standard microwave equipment. Another advantage is the usage of two separated resonance frequencies. Both frequencies can be set individually which allows for new tuning possibilities. For example, the Q-factor of the resonator can be set by the µw resonance e.g. by adjusting the tuning screw or varying the coupling. This allows a tuning of the signal strength. Because the sensor can be enclosed in a cavity, external acoustical or electrical interferences may already be shielded by the layout. As compared to other sensor concepts, the measurement frequency in the GHz range has the benefit that it induces virtually no domain wall movement and magnetic noise [Urs+16]. Since the sensor itself works in the same way than for standard readout, many of the investigations and results can be adopted. Unfortunately, this also implies that the ultimate noise limit by the thermal-mechanical noise confines the LoD for this concept as well. In this readout scheme, it enters the system as additional phase noise and is the dominant noise contribution. However, a vacuum encapsulation does not require major changes in a cavity layout and may increase the SNR as discussed in Sec. 2.5.5.

5 | Summary

This chapter concludes the investigations on readout methods for thin-film magnetoelectric sensors. In the following two sections, the findings and results of the investigations are summarised and an outlook for future research is provided.

5.1 Summary

The focus of this dissertation is the increase of the signal-to-noise ratio to lower the LoD of ME sensors in order to eventually allow the measurement of weak biomagnetic signals in medical applications.
In the introductory part, the magnetoelectric effect and thin-film magnetoelectric sensors are reviewed. Due to the affiliation to the multi-disciplinary research projects CRC 855, grant PAK 902, and the CRC 1261, certain topics are discussed in more detail because the contents appeal to readers from different scientific background. The existing noise model for the sensors operated with direct detection, mostly at their mechanical resonance frequency, is extended on the basis of earlier publications. A noise contribution in the mechanical resonance is proven to be due to thermal-mechanical noise as opposed to acoustical noise. The simulation results of this and following models are verified with measurements that prove their validity. In order to reduce this noise contribution, the loss mechanisms of the sensor need to be decreased. In a closed loop setup, the mechanical quality factor at the resonance can be increased, but the SNR stays constant for the investigated setup. In order to transfer measurements into a realistic unshielded environment, a noise suppression technique with ME sensors in tuning fork setup is investigated further. In practice, the location of the source has a significant effect on the suppression which motivates advanced designs that take the directionality into consideration.
With knowledge of the basic sensor characteristics and parameters, readout methods for the detection of low-frequency signals are introduced. Extensive measurements

have been conducted and routines for characterisation standardisation have been established in cooperation with the sensor producers. In order to understand the noise contributions during MFC, the magnetic behaviour is reviewed from a system point of view. This helps to extend an existing signal model to predict signal behaviour and enhance the SNR by raising the signal strength by means of signal processing. It also explains, why the carrier feedthrough occurs and what can be done to suppress it. Several ways to perform carrier suppression are discussed, reducing it to an extent where it does not degrade the output signals. Earlier, MFC was conducted with an optimum pump level only with respect to the USB output amplitude. To increase the SNR of MFC, the optimum pump level is now determined by additionally taking into consideration the noise in resonance which significantly improves the LoD. The model is extended for a system noise description that supports the development of new sensor layouts to reduce magnetic noise. Since the magnetic noise was lowered significantly, a new dominant noise source, the noise of the exciting source, was identified and its noise contribution lowered by the application of filter stages. It is confirmed that, with all the above measures, the noise that occurs during MFC nearly reaches the ultimate noise limit determined by the thermal-mechanical noise. In order to further improve the readout method, desirable sensor characteristics are proposed for the fabrication process. Also, MFC is successfully applied to tuning forks. The LoD with MFC was lowered to $50\,\mathrm{pT}/\sqrt{\mathrm{Hz}}$ at 10 Hz.

For better practicability, the frequency conversion can also be performed with electrical excitation requiring only minor changes to the sensor layout. EFC is investigated on the basis of a limited number of available sensors. Different combinations of piezoelectric layers were tested and basic measurements conducted in order to evaluate the method in comparison with the magnetic counterpart. First findings on the physical background helped to introduce a first signal model that is able to predict the relative sensor output and aids to further understand the signal propagations and transformations inside the sensor.

A novel approach for the readout integrates magnetoelectric sensors and a µw resonator which detects magnetic signals by a shift in its µw resonance. No piezoelectric layer is required for this method. It is shown that the system sensitivity depends on the quality factor of the µw resonator. The individual loss contributions are discriminated and the sensor and resonator layout modified according to the results. In order to increase the signal-to-noise ratio, a system model is developed. Following a detailed mathematical derivation of phase noise suppression, the LoD from first

measurements is significantly lowered by application of a FD. The ultimate noise contribution is found to be the thermal-mechanical noise of the cantilever. For detection in resonance, this approach reached the same LoD as the standard readout with conventional magnetoelectric sensors.

5.2 Conclusion and Outlook

In the course of this dissertation, the signal-to-noise ratio has been lowered to $50\,\mathrm{pT}/\sqrt{\mathrm{Hz}}$ at 10 Hz with MFC which currently is the lowest LoD for thin-film magnetoelectric sensors at 10 Hz. More important is that the signal and noise limits of the individual readout methods are identified and understood which is essential for further developments. Setting the working point under consideration of the arising magnetic noise may also increase the SNR for other readout methods.
As an alternative to magnetic excitation, EFC is proven to perform equally well compared to MFC for the investigated sensor. However, without new sensors with more advanced magnetic layers it cannot be determined whether EFC can reach LoDs as low as MFC because additional noise sources are introduced into the system.
With an entirely new µw resonance based readout method, the sensor and system can get rid of a number of noise sources and its piezoelectric layer. This simplifies the fabrication process while achieving comparable results with respect to standard detection. For the readout, other effects such as for example ΔE_d could be utilised as well. In order to increase the impact of the varying capacitance on the change of the resonance frequency and thus to improve the µw sensitivity, a redesign of the resonator's geometry and tuning elements is required. By altering the design of the resonator e.g. to a passive microstrip ring resonator, contactless readout could be implemented utilising antennas to couple the µw signal. This would allow a broad range of applications e.g. its use in inhospitable environments with complete non-magnetic casing or the wireless mounting of the sensor to moving parts of a head scanner for the measurement of brain-pacemaker signals.
The close cooperation with groups working in magnetics and sensor fabrication was indispensable for the investigations.
Unfortunately, the measured LoDs are still not low enough to measure biomagnetic signals without averaging. It is expected that further reduction of the LoD by a factor of 5 at 10 Hz may enable to measure R-waves of the cardiogram. This may be achieved by enhancing the signal strength of the magnetic layers while

keeping the magnetic noise reasonably small. First approaches have been undertaken with novel multilayer sensors with thicker exchange bias stacks. An increase of the piezoelectric coefficient e.g. by the incorporation of new piezoelectric materials such as aluminium scandium nitride (AlScN) will not increase the SNR due to dominance of the thermal-mechanical noise. If the magnetostriction curve can be engineered steeper, the required current of the pump could be smaller resulting in less noise. Generally, it is anticipated that specifically adapted sensor dimensions, thickness, and electrode design for the utilised resonance boosts the signal strength. With sensors reaching LoDs around $1\,\mathrm{pT}\sqrt{\mathrm{Hz}}$ in resonance, the thermal-mechanical noise can principally be low enough to let LoDs around $10\,\mathrm{pT}\sqrt{\mathrm{Hz}}$ at 10 Hz seem possible with MFC.

With ongoing changes and developments of the sensors, the signal processing is required to be adapted continuously. Whenever a noise source of the signal processing becomes dominant, as may be the case e.g. for EFC with improved magnetic layers, the models need to be refined and the noise lowered until it is not dominant. For the measurements and evaluation in this discourse, sinusoidal test signals have been utilised. Realistic measurements are better represented by e.g. artificial heart signals which may require changes to the readout, in particular concerning bandwidth. The synchronisation of the tuning fork needs to be investigated for non-sinusoidal signals with more frequency components. The carrier suppression has already been conducted by an automatic algorithm that adapts online to changes in the signal chain. Measurements outside the mechanical resonance frequency are not promising because the Fano resonator characteristic indicates that the signal decreases by more than Q outside of the resonance and other noise contributions such as the amplifier noise are dominant there. For further practicability, the working points, parameters for carrier suppression, etc. should be determined adaptively as well and in real-time. An important foundation for adaptive signal processing is provided in [Ree17]. Especially working points can be set with closed loops for example if the sensor is operated in the feedback of an oscillator loop.

The results for the magnetic layers should be transferred to smaller integrated sensors with higher mechanical resonance frequencies and bandwidth. Loss by clamping and viscous damping can be lowered by integrating the sensors in a frame with vacuum encapsulation [Kir17].

In [Ale+15], optical pumped magnetometers (OPM) are already used in clinical environments to measure weak biomagnetic signals such as fetal magnetocardiograms.

OPMs are small, can be integrated in arrays, are multi-directional, do not need to be cooled, and reach very low noise floors down to $15\,\mathrm{fT}\sqrt{\mathrm{Hz}}$ between 1 to 100 Hz (see Sec. B). They are expected to replace superconducting quantum interference device (SQUID) sensors for clinical application.
Finally, thin-film magnetoelectric sensors have the potential to measure biomagnetic signals while being low-cost, small, and easily integrable sensors.

List of Abbreviations, Notations, and Symbols

Abbreviations

µw	Microwave
AC	Alternating current
AD745	Ultralow noise, high speed, BiFET operational amplifier AD745 [AD02]
ADC	Analogue to digital converter
AlN	Aluminium nitride
AlScN	Aluminium scandium nitride
APS	Adaptive phase shifter
Au	Gold
CMMR	Common-mode-rejection-ratio
Cr	Chromium
CS	Carrier suppression
DAC	Digital to analogue converter
DC	Direct current
DFG	German Research Foundation (Deutsche Forschungsgesellschaft)
DR	Dynamic range
EB	Exchange bias
ECD	Equivalent circuit diagram
ECG	Electrocardiogram
EFC	Electric frequency conversion
ENBW	Equivalent noise bandwidth
FD	Frequency discriminator
FeCoSiB	Iron cobalt silicon boron

FR-4 ..... PCB board material, flame retardant, glass-reinforced epoxy laminate
HPF ..... High-pass filter
ICD ..... Implantable cardioverter-defibrillator
icEEF ..... Intercranial electroencephalography
JFET ..... Junction gate field-effect transistor (JFET)
Keithley 6221 .... Keithley 6221 low noise current source [KE08]
Kepco ..... Kepco BOP 20-10ML power source [KE11]
LNA ..... Low noise amplifier
LoD ..... Limit of detection
LPF ..... Low-pass filter
LS ..... Linear spectrum
LSB ..... Signal in the lower sideband for frequency conversion.
LSD ..... Linear spectral density
MCG ..... Magnetocardiography
ME ..... Magnetoelectric
MEG ..... Magnetoencephalography
MEMS ..... Mircoelectromechanical system
MFC ..... Magnetic frequency conversion
MnIr ..... Manganese iridium
MOKE ..... Magneto-optical Kerr effect
MRC ..... Maximum-Ratio Combination
NCSD ..... Noise current spectral density
NEMS ..... Nano-electromechanical system
NVSD ..... Noise voltage spectral density
OPM ..... Optical-pumped magnetometer
PCB ..... Printed circuit board
PSD ..... Position sensitive device
Pt ..... Platinum
PVC ..... Polyvinyl chloride
PZT ..... Lead zirconate titanate
RMS ..... Root mean square
SCR ..... Signal-to-carrier ratio
SEM ..... Scanning electron microscope
Si ..... Silicon

SMA ..... SubMiniature version A RF coaxial connectors
SNR ..... Signal-to-noise ratio
SQUID ..... Superconducting quantum interference device
SR830 ..... Stanford Research lock-in amplifier SR830 [SR11]
Ta ..... Tantalum
USB ..... Signal in the upper sideband for frequency conversion.
$\mathrm{USB}_{\mathrm{noise}}$ ..... Noise at the resonance frequency for MFC.
YIG ..... Yittrium iron garnet

Notation

$< x >$ ..... Mean value of x
$\hat{x}$ ..... Amplitude of x or offset
$\tilde{X}$ ..... Spectral density of X
$x \parallel y$ ..... x parallel to y

Symbols

α_{ME} ..... Magnetoelectric coefficient [kV/cmOe]
β_{in} ..... Input coupling factor of µw resonator [1]
β_{out} ..... Output coupling factor of µw resonator [1]
β_ν ..... Factor for ν-th mode calculation
ΔC ..... Change of capacitance induced by the cantilever bending [F]
Δf ..... Bandwidth [Hz]
Δl ..... Change in length [m]
η ..... Modulation index [rad]
η_{s} ..... Phase sensitivity [rad/T]
$\gamma(s)$ ..... Feedback factor [1]
κ ..... Electric conductivity [S/m]
λ ..... Magnetostriction [ppm]
$\lambda_{\mu\mathrm{w}}$ ..... Microwave wavelength [m]
λ_{app} ..... Approximated polynomial of magnetostriction curve [1]
$\tan\delta$ ..... Loss tangent [1]
$\tan\delta_{\mathrm{cp}}$ ..... Loss tangent pump source cable [1]
$\tan\delta_{\mathrm{meas}}$ ..... Measured loss tangent [1]
$\tan\delta_{\mathrm{meas}}$ ..... Measured loss tangent [1]
$\tan\delta_{\mathrm{ME}}$ ..... Loss tangent of the piezoelectric layer [1]
$\tan\delta_{\mathrm{m}}$ ..... Loss tangent of the mechanical resonator (equivalent) [1]

μ_0 ..... Vacuum permeability $\approx 4\pi \cdot 10^{-7}$ [H/m]
μ_r ..... Relative permeability
ν ..... Index of resonant mode
ω ..... Angular frequency $\omega = 2\pi f$ [rad/s]
ω_{offset} ..... Angular frequency signal offset frequency [rad]
ω_{p} ..... Angular frequency of µw signal [rad]
$\omega_{\text{res,µw}}$ ..... Angular µw resonance frequency [rad]
ω_{s} ..... Angular frequency of the signal to be measured [Hz]
Ψ ..... Magnetic flux [WB]
ρ_{cant} ..... Material density of a cantilever [kg/m^3]
ρ_{Si} ..... Material density of silicon [kg/m^3]
σ ..... Mechanical stress [N/m^2]
τ ..... Time constant [s]
τ_{D} ..... Dielectric relaxation time [s]
τ_{ME} ..... Time constant of the ME sensor [s]
$\tilde{D}$ ..... Deflection noise density [m/$\sqrt{\text{Hz}}$]
$\tilde{E}_{\text{amp}}$ ..... NVSD amplifier [V/$\sqrt{\text{Hz}}$]
$\tilde{E}_{\text{c}}$ ..... NVSD connector cable [V/$\sqrt{\text{Hz}}$]
$\tilde{E}_{\text{f}}$ ..... NVSD feedback resistance [V/$\sqrt{\text{Hz}}$]
$\tilde{E}_{\text{mag}}$ ..... Equivalent NVSD of magnetic excess noise [V/$\sqrt{\text{Hz}}$]
$\tilde{E}_{\text{ME}}$ ..... NVSD piezoelectric losses [V/$\sqrt{\text{Hz}}$]
$\tilde{E}_{\text{mp}}$ ..... Equivalent NVSD of pump source [V/$\sqrt{\text{Hz}}$]
$\tilde{E}_{\text{m}}$ ..... NVSD mechanical resistance [V/$\sqrt{\text{Hz}}$]
$\tilde{E}_{\text{oampI}}$ ..... Equivalent NVSD amplifier current noise at output [V/$\sqrt{\text{Hz}}$]
$\tilde{E}_{\text{oampV}}$ ..... NVSD amplifier voltage noise at output [V/$\sqrt{\text{Hz}}$]
$\tilde{E}_{\text{oCA}}$ ..... Total NVSD from charge amplifier at output [V/$\sqrt{\text{Hz}}$]
$\tilde{E}_{\text{oc}}$ ..... NVSD connector cable at output [V/$\sqrt{\text{Hz}}$]
$\tilde{E}_{\text{of}}$ ..... NVSD feedback network at output [V/$\sqrt{\text{Hz}}$]
$\tilde{E}_{\text{omag}}$ ..... NVSD magnetic excess noise at output [V/$\sqrt{\text{Hz}}$]
$\tilde{E}_{\text{oME}}$ ..... NVSD piezoelectric layer at output [V/$\sqrt{\text{Hz}}$]
$\tilde{E}_{\text{omp}}$ ..... NVSD pump source at output [V/$\sqrt{\text{Hz}}$]
$\tilde{E}_{\text{om}}$ ..... NVSD resonant branch at output [V/$\sqrt{\text{Hz}}$]
$\tilde{E}_{\text{oQuant}}$ ..... Quantisation NVSD readout device [V/$\sqrt{\text{Hz}}$]
$\tilde{E}_{\text{o}}$ ..... Total NVSD at output [V/$\sqrt{\text{Hz}}$]
$\tilde{E}_{\text{total}}$ ..... Total system NVSD [V/$\sqrt{\text{Hz}}$]

$\tilde{F}$ ..... Fluctuating force density [N/$\sqrt{\text{Hz}}$]
$\tilde{I}_{\text{amp}}$ ..... Current noise LSD amplifier [A/$\sqrt{\text{Hz}}$]
$\tilde{I}_{\text{coil}}$ ..... NCSD pump coil [A/$\sqrt{\text{Hz}}$]
$\tilde{I}_{\text{cp}}$ ..... NCSD pump source cable [A/$\sqrt{\text{Hz}}$]
$\tilde{I}_{\text{cp}}$ ..... NCSD pump source cable at pump coil [A/$\sqrt{\text{Hz}}$]
$\tilde{I}_{\text{DA}}$ ..... NCSD pump source quantisation noise [A/$\sqrt{\text{Hz}}$]
$\tilde{I}_{\text{p}}$ ..... NCSD pump source at pump coil [A/$\sqrt{\text{Hz}}$]
$\tilde{I}_{\text{sour}}$ ..... NCSD pump source [A/$\sqrt{\text{Hz}}$]
$\tilde{I}_{R_{\text{sour}}}$ ..... NCSD pump source resistance [A/$\sqrt{\text{Hz}}$]
$\tilde{S}_{\text{R}}$ ..... NVSD resistor [V/$\sqrt{\text{Hz}}$]
ε ..... Permittivity [F/m]
ε_0 ..... Vacuum permittivity $\varepsilon_0 \approx 8.854 \cdot 10^{-12}$ [F/m]
ε_{r} ..... Relative permittivity [F/m]
$\vec{B}$ ..... Magnetic flux density [T]
$\vec{E}$ ..... Electric field [V/m]
$\vec{H}$ ..... Magnetic field [A/m]
$\vec{P}$ ..... Polarisation [C/m^2]
$A(s)$ ..... Two port gain [1]
A_{coil} ..... Cross-sectional area of a cylindrical coil [m^2]
A_{elec} ..... Cross-sectional area of electrode [m^2]
$A_{\text{f}}(s)$ ..... Feedback gain [1]
a_{n} ..... Coefficients of a polynomial [various]
A_{TF} ..... Positive filtered output of tuning fork amplifier [V]
B_0 ..... Arbitrary constant magnetic field [T]
B_{bias} ..... Magnetic bias field [T]
B_{in} ..... Superimposed input signal [T]
B_{opt} ..... Optimal magnetic bias field [T]
$B_{\text{p,offs}}$ ..... Offset of the pump signal [T]
B_{p} ..... Pump signal [T]
B_{s} ..... Magnetic signal to be measured [T]
B_{s} ..... Signal to be measured [T]
B_{TF} ..... Negative filtered output of tuning fork amplifier [V]
C ..... Capacitance [F]
c_0 ..... Speed of light $\approx 3 \cdot 10^8$ [m/s^2]
$C_{\mu\text{w}}$ ..... Capacitance of the µw resonator [F]

C_{cs} ..... Coupling capacitance for CS
C_{c} ..... Capacitance of a connector cable [F]
C_{in} ..... Input coupling capacitance [F]
C_{meas} ..... Measured capacitance [F]
C_{ME} ..... Capacitance of the piezoelectric layer [F]
C_{m} ..... Capacitance of the mechanical resonator (equivalent) [F]
C_{out} ..... Output coupling capacitance [F]
C_{p} ..... Parallel capacitance [F]
C_{T} ..... Capacitance of the T-filter [F]
d ..... Displacement [m]
d_{31} ..... Piezoelectric coefficient in 31 direction [C/N]
d_{33} ..... Piezoelectric coefficient in 33 direction [C/N]
$E_{\mathrm{d,cant}}$ ..... Elastic modulus of a cantilever [N/m^2]
$E_{\mathrm{d,Si}}$ ..... Elastic modulus of silicon [N/m^2]
E_{d} ..... Elastic modulus [N/m^2]
f ..... Frequency [Hz]
f_{f} ..... Fluctuating force [N]
$f_{\mathrm{res,1}}$ ..... First mechanical resonance frequency [Hz]
$f_{\mathrm{res,2}}$ ..... Second mechanical resonance frequency [Hz]
$f_{\mathrm{res,\mu w}}$ ..... µw resonance frequency [Hz]
f_{res} ..... Resonance frequency [Hz]
f_{s} ..... Frequency of the signal to be measured [Hz]
F_{up} ..... Frequency of the upper extreme value of C_{meas} [Hz]
f_{up} ..... Frequency of upper extreme value of C_{meas} [Hz]
f_{ν} ..... Frequency of the ν-th resonance [Hz]
$G_{\mu\mathrm{w}}$ ..... Conductance of the µw resonator [1/Ω]
G_{CA} ..... *Voltage* gain of the charge amplifier [1]
G_{comm} ..... Common-mode gain of a differential operational amplifier [1]
G_{diff} ..... Differential gain of a differential operational amplifier [1]
G_{LNA} ..... LNA gain for magnetic excess noise setup [1]
G_{mech} ..... Transfer function of a mechanical resonator [1]
h ..... Height of a cantilever above a ground plane [m]
H_{c} ..... Coercive field [T]
i ..... Running index (multiple usages)
I_{coil} ..... Current through the pump coil [A]

I_{ind} ..... Induction current to produce induction field [A]
I_{p} ..... Pump current [A]
k ..... Spring constant [N/m]
k_{B} ..... Boltzmann constant ($1.3806488 \cdot 10^{-23}$) [J/K]
k_{MFC} ..... Fitting factor of MFC model [1]
K_{u} ..... Magnetic anisotropy [J/m^3]
l ..... Length [m]
$L_{\mu\mathrm{w}}$ ..... Inductance of the µw resonator [H]
l_{cant} ..... Length of a cantilever [m]
L_{coil} ..... Inductance of a cylindrical coil [H]
L_{coil} ..... Pump coil inductance [H]
l_{coil} ..... Length of a cylindrical coil [m]
L_{c} ..... Conversion loss
L_{ME} ..... Inductance of the piezoelectric layer [H]
L_{m} ..... Inductance of the mechanical resonator (equivalent) [H]
L_{T} ..... Inductance of the T-filter [H]
M ..... Magnetisation [A/m]
m ..... Mass [kg]
M_{r} ..... Remanence magnetisation [A/m]
M_{s} ..... Saturation magnetisation [A/m]
N ..... Number of windings of a cylindrical coil [1]
N_{n} ..... Order of a polynomial [1]
N_{s} ..... Number of signals with similar SNR for combination [1]
$P_{\mu\mathrm{w}}$ ..... Power of µw signal [dBm]
$P_{\mathrm{FD,n}}$ ..... Demodulated noise sideband [dBm/Hz]
P_{in} ..... Input power [dBm]
P_{n} ..... Noise floor ratio [dBc]
P_{USB} ..... Upper sideband ratio [dBc]
Q ..... Quality factor [1]
$Q_{\mu\mathrm{w},0}$ ..... µw Quality factor [1]
R ..... Resistance [Ω]
$R_{\mu\mathrm{w}}$ ..... Resistance of the µw resonator [Ω]
R_{A} ..... Average roughness [m]
R_{C1} ..... Pump source cable resistance [Ω]
R_{coil} ..... Pump coil resistance [Ω]

R_{c} ..... Resistance of a connector cable [Ω]
R_{f} ..... Resistance of the feedback network [Ω]
R_{meas} ..... Measured resistance [Ω]
R_{mech} ..... Mechanical resistance [Ns/m]
R_{ME} ..... Resistance of the piezoelectric layer [Ω]
R_{m} ..... Resistance of the mechanical resonator (equivalent) [Ω]
R_{sour} ..... Pump source resistance [Ω]
R_{var} ..... Variable resistance of phase shifter [Ω]
S ..... Sensitivity [V/T]
$S_{\mathrm{p,\mu w}}$ ..... Phase modulated pump signal [dBm]
S_{xx} ..... $_{\mathrm{xx}} \in \{11,12,21,22\}$ S-parameters [1]
T ..... Temperature [K]
t ..... Time [s]
t_{cant} ..... Thickness of a cantilever [m]
t_{piezo} ..... Thickness the piezoelectric layer [m]
V_{det} ..... Detection voltage of pick-up coil [V]
V_{ME} ..... Magnetoelectric voltage [V]
V_{o} ..... System voltage output [V]
V_{p} ..... Pump voltage for EFC [V]
W ..... Spectral linear density [V/$\sqrt{\mathrm{Hz}}$]
w_{cant} ..... Width of a cantilever [m]
X ..... Reactance [Ω]
X_{meas} ..... Measured reactance [Ω]
Y ..... Output of a differential operational amplifier [V]
Z ..... Impedance [Ω]
z ..... Displacement [m]
Z_{cp} ..... Pump source cable impedance [Ω]
Z_{c} ..... Characteristic impedance [Ω]
Z_{c} ..... Impedance of the connector cable [Ω]
Z_{f} ..... Impedance of the feedback network [Ω]
Z_{l} ..... Load impedance of µw resonator [Ω]
Z_{meas} ..... Measured impedance [Ω]
Z_{ME} ..... Impedance of the piezoelectric layer [Ω]
Z_{mMEc} ..... Parallel circuit of formed by $Z_{\mathrm{m}} \parallel Z_{\mathrm{ME}} \parallel Z_{\mathrm{c}}$ [Ω]
Z_{m} ..... Impedance of the mechanical resonator (equivalent) [Ω]

Z_{p} ..... Excitation network impedance [Ω]
Z_{s} ..... Source impedance of µw source [Ω]

List of Figures

Bibliography

General Bibliography

[ABG06] M. Abel, S. Bergweiler, and R. Gerhard-Multhaupt. "Synchronization of organ pipes: experimental observations and modeling". In: *J. Acoust. Soc. Am.* 105.4 (2006).

[AD02] *Ultralow noise, high speed, BiFET operational amplifier AD745*. Rev. D. Analog Devices, Inc. 2002.

[Ale+15] O. Alem et al. "Fetal magnetocardiography measurements with an array of microfabricated optically pumped magnetometers". In: *Physics in medicine and biology* 60.12 (2015), pp. 4797–4811.

[AN07] W. Andrä and H. Nowak. *Magnetism in Medicine*. Vol. 2. Wiley-VCH, 2007.

[Arm15] E. H. Armstrong. "Some Recent Developments in the Audion Receiver". In: *Proceedings of the IRE* 3.3 (1915), pp. 215–238.

[Arm22] E. H. Armstrong. "Some recent developments of regenerative circuits". In: *Proceedings of the Institute of Radio Engineers* 10.4 (Aug. 1922), pp. 244–260.

[AS64] M. Abramowitz and I. Stegun. *Handbook of Mathematical Functions with Formulas*. Applied Mathematical Series 55. Washington, DC: NBS, 1964, p. 998.

[Bal07] R. Ballas. *Piezoelectric Multilayer Beam-Bending Actuators (Microtechnology and MEMS)*. Springer, 2007.

[Bar19] H. Barkhausen. "Zwei mit Hilfe der neuen Verstärker entdeckte Erscheinungen". In: *Physikalische Zeitschrift* 20 (1919), pp. 401–403.

[Bel85] D. A. Bell. *Noise and the Solid State*. Pentech Press, 1985.

[Ben+02] M. Bennett et al. "Huygens's clocks". In: *Proceedings of the Royal Society A: Mathematical, Physical and Engineering Sciences* 458.2019 (2002), pp. 563–579.

[BEO10] E. Böhmer, D. Ehrhardt, and W. Obersch. *Elemente der angewandten Elektronik*. 16th ed. Vieweg+Teubner, 2010.

[Bir56] T. Birch. *The history of The Royal Society of London for improving of natural knowledge, in which the most considerable of those papers communicated to the Society, which have hitherto not been published, are inserted in their proper order, as a supplement to the Philosophical Transactions*. Vol. 2. London: Johnson. (Reprint 1968), 1756, pp. 19, 21, 23–24.

[BML01] S. Baillet, J. C. Mosher, and R. M. Leahy. "Electromagnetic brain mapping". In: *IEEE Signal Processing Magazine* 18.6 (Nov. 2001), pp. 14–30.

[CB06] J. Clarke and A. I. Braginski. *The SQUID Handbook. Vol. 1, Fundamentals and Technology of SQUIDS and SQUID Systems*. Vol. 2. Wiley-VCH, 2006.

[CC82] J. Curie and P. Curie. "Phénomènes électriques des cristaux hémièdres à faces inclinées". In: *Journal de Physique Théorique et Appliquée* 1.1 (1882), pp. 245–251.

[CG09] B.D. Cullity and C.D. Graham. *Magnetic Materials*. 2nd. Wiley, 2009.

[Cri02] S. C. Cripps. *Advanced Techniques in RF Power Amplifier Design*. Artech House, 2002.

[CW51] H. B. Callen and T. A. Welton. "Irreversibility and Generalized Noise". In: *Journal of Applied Physics* 83 (1951).

[Dju00] Z. Djuric. "Noise sources in microelectromechanical systems". In: *2000 22nd International Conference on Microelectronics. Proceedings (Cat. No.00TH8400)*. Vol. 1. 2000, 85–96 vol.1.

[Dur+17b] P. Durdaut et al. "Noise of a JFET Charge Amplifier for Piezoelectric Sensors". In: *IEEE Sensors Journal* 17.22 (2017), pp. 7364–7371.

[Ede07] A. Edelstein. "Advances in magnetometry". In: *Journal of Physics: Condensed Matter* 19.16 (2007), p. 165217.

[FCD09] C. Furse, D. A. Christensen, and C. H. Durney. *Basic introduction to bioelectromagnetics*. 2nd ed. CRC Press, 2009.

[Fet+13] L. Y. Fetisov et al. "Nonlinear resonant magnetoelectric interactions and efficient frequency doubling in a ferromagnetic-ferroelectric layered structure". In: *Journal of Applied Physics* 113.11 (2013), p. 116101.

[Fie05] M. Fiebig. "Revival of the magnetoelectric effect". In: *Journal of Physics D: Applied Physics* 38.8 (2005), R123–R152.

[FPS07] Y. K. Fetisov, V. M. Petrov, and G. Srinivasan. "Inverse magnetoelectric effects in a ferromagnetic–piezoelectric layered structure". In: *Journal of Materials Research* 22.08 (2007), pp. 2074–2080.

[Fra04] J. Fraden. *Handbook of Modern Sensors*. 3rd. Springer, 2004.

[Gab93] T. B. Gabrielson. "Mechanical-thermal noise in micromachined acoustic and vibration sensors". In: *IEEE Transactions on Electron Devices* 40.5 (May 1993), pp. 903–909.

[Ger13] M. Gerken. "Resonance line shape, strain and electric potential distributions of composite magnetoelectric sensors". In: *AIP Advances* 3.6 (2013), p. 062115.

[GH12] G. Gold and K. Helmreich. *7th European Microwave Integrated Circuits Conference (EuMIC), 2012: 29 - 30 Oct. 2012, Amsterdam, The Netherlands; 15th European Microwave Week (EuMW 2012)*. Piscataway, NJ: IEEE, 2012.

[GHM17] A. Grosz, M.J. Haji-Sheikh, and S.C. Mukhopadhyay. *High Sensitivity Magnetometer*. Vol. 19. Springer, 2017.

[Gil+11] S. M. Gillette et al. "Improved Sensitivity and Noise in Magneto-Electric Magnetic Field Sensors by Use of Modulated AC Magnetostriction". In: *IEEE Magnetics Letters* 2 (2011), p. 2500104.

[Goj+11] B. Gojdka et al. "Fully integrable magnetic field sensor based on delta-E effect". In: *Applied Physics Letters* 99.22 (2011), p. 223502.

[Gre+10] H. Greve et al. “Giant magnetoelectric coefficients in $(Fe_{90}Co_{10})_{78}Si_{12}B_{10}$-AlN thin film composites”. In: *Applied Physics Letters* 96.18 (2010), p. 182501.

[Gro+16] A. Grosz et al. “A High-Resolution Planar Hall Effect Magnetometer for Ultra-Low Frequencies”. In: *IEEE Sensors Journal* 16.9 (2016), pp. 3224–3230.

[Hay14] S. Haykin. *Adaptive Filter Theory*. 5th. Upper Saddle River New Jersey: Pearson, 2014.

[HEA03] Z. Hao, A. Erbil, and F. Ayazi. “An analytical model for support loss in micromachined beam resonators with in-plane flexural vibrations”. In: *Sensors and Actuators A: Physical* 109.1-2 (2003), pp. 156–164.

[HK00] C. L. Holloway and E. F. Kuester. “Power loss associated with conducting and superconducting rough interfaces”. In: *IEEE Transactions on Microwave Theory and Techniques* 48.10 (2000), pp. 1601–1610.

[HM07] S. Haykin and M. Moher. *An Introduction to Analog and Digital Communications*. Vol. 2. John Wiley and Sons, 2007.

[Hof83] R. K. Hoffmann. *Integrierte Mikrowellenschaltungen*. Springer, 1983.

[IE88] Standards Committee of the IEEE Ultrasonics IEEE, Ferroelectrics, and and Frequency Control Society. “Standard on Piezoelectricity”. In: *SMPTE Journal* 97.6 (1988), pp. 516–517.

[Jah+11] R. Jahns et al. “Noise Performance of Magnetometers With Resonant Thin-Film Magnetoelectric Sensors”. In: *IEEE Transactions on Instrumentation and Measurement* 60.8 (2011), pp. 2995–3001.

[Jah+12] R. Jahns et al. “Sensitivity enhancement of magnetoelectric sensors through frequency-conversion”. In: *Sensors and Actuators A: Physical* 183 (2012), pp. 16–21.

[Jah+13] R. Jahns et al. “Giant Magnetoelectric Effect in Thin-Film Composites”. In: *Journal of the American Ceramic Society* 96.6 (2013), pp. 1673–1681.

[Jah+14] R. Jahns et al. “Microelectromechanical magnetic field sensor based on ΔE effect”. In: *Applied Physics Letters* 105.5 (2014), p. 052414.

[Jah11] R. Jahns. *Magnetoelectric Sensors for Biomagnetic Measurements: IEEE International Workshop on Medical Measurements and Applications*. Piscataway, N.J.: IEEE, 2011.

[Jah13] R. Jahns. "Untersuchung und Optimierung von Empfindlichkeit und Rauschverhalten magnetoelektrischer Sensoren". PhD thesis. Technische Fakultät der Christian-Albrechts-Universtät zu Kiel, 2013.

[Jia+12] J. Jiao et al. "An improved magnetic field detection unit based on length-magnetized Terfenol-D and width-polarized ternary $0.35Pb(In_{1/2}Nb_{1/2})O_3$-$0.35Pb(Mg_{1/3}Nb_{2/3})O_3$-$0.30PbTiO_3$". In: *Applied Physics Letters* 101.23 (2012), p. 232906.

[Jil00] D.C. Jiles. "Dynamics of Domain Magnetization and the Barkhausen Effect". In: *Czechoslovak Journal of Physics* 50.8 (2000), pp. 893–988.

[JKQ11] R. Jahns, R. Knöchel, and E. Quandt. "Verfahren zur Magnetfeldmessung mit Magnetoelektrischen Sensoren". 10 2011 008 866 A1. DE patent. Jan. 2011.

[JKQ12] R. Jahns, R. Knöchel, and E. Quandt. "Method for measuring a magnetic field using magnetoelectric sensors". 9 383 417 B2. US patent. Jan. 2012.

[Joh28] J. B. Johnson. "Thermal Agitation of Electricity in Conductors". In: *Physical Review* 32 (1928).

[JRK13] R. Jahns, H. Runkowske, and R. Knöchel. "Magnetic Field Measuring Device with Vibration Compensation, EP 2811314 B1". 2013.

[Kar17] K. W. Kark. *Antennen und Strahlungsfelder*. Vol. 6. Springer Vieweg, 2017, p. 208.

[KE08] *6221 AC and DC current source*. Rev. C. Kepco, Inc. 2008.

[KE11] *Bop 20-10ML power supply*. Rev. 2. Kepco, Inc. 2011.

[Ker77] J. Kerr. "XLII. On rotation of the plane of polarization by reflection from the pole of a magnet". In: *The London, Edinburgh, and Dublin Philosophical Magazine and Journal of Science* 3.19 (1877), pp. 321–343.

[Kir+13] C. Kirchhof et al. "Giant magnetoelectric effect in vacuum". In: *Applied Physics Letters* 102.23 (2013), p. 232905.

[Kir17] C. Kirchhof. “Resonante magnetoelektrische Sensoren zur Detektion niederfrequenter Magnetfelder”. PhD thesis. Technische Fakultät der Christian-Albrechts-Universtät zu Kiel, 2017.

[Kom+03] I. K. Kominis et al. “A subfemtotesla multichannel atomic magnetometer”. In: *Nature* 422.6932 (2003), pp. 596–599.

[KS15] H. Karo and I. Sasada. “Magnetocardiogram measured by fundamental mode orthogonal fluxgate array”. In: *Journal of Applied Physics* 117.17 (2015), 17B322.

[KS16a] *B2961A/B2962A Low Noise Power Source*. Keysight. 2016.

[KS16b] Y. J. Kim and I. Savukov. “Ultra-sensitive Magnetic Microscopy with an Optically Pumped Magnetometer”. In: *Scientific reports* 6 (2016), p. 24773.

[Lag+12] E. Lage et al. “Exchange biasing of magnetoelectric composites”. In: *Nature materials* 11.6 (2012), pp. 523–529.

[Lag+14] E. Lage et al. “Magnetic domain control and voltage response of exchange biased magnetoelectric composites”. In: *Applied Physics Letters* 104.13 (2014), p. 132405.

[Lag14] E. Lage. “Magnetoelektrische Dünnschichtkomposite mit integriertem Exchange Bias”. PhD thesis. Technische Fakultät der Christian-Albrechts-Universtät zu Kiel, 2014.

[LE06] J. Lenz and S. Edelstein. “Magnetic sensors and their applications”. In: *IEEE Sensors Journal* 6.3 (2006), pp. 631–649.

[Lev08] F. A. Levinzon. “Ultra-Low-Noise High-Input Impedance Amplifier for Low-Frequency Measurement Applications”. In: *IEEE Transactions on Circuits and Systems I: Regular Papers* 55.7 (2008), pp. 1815–1822.

[LL03] P. Lu and K. H. Lee. “An alternative derivation of dynamic admittance matrix of piezoelectric cantilever bimorph”. In: *Journal of Sound and Vibration* 266.4 (2003), pp. 723–735.

[LLB92] J. Lepaisant, M. Lam Chok Sing, and D. Bloyet. “Low–noise preamplifier with input and feedback transformers for low source resistance sensors”. In: *Review of Scientific Instruments* 63.3 (1992), pp. 2089–2094.

[Lüb+11] J. Lübbe et al. “Measurement and modelling of non-contact atomic force microscope cantilever properties”. In: *Measurement Science and Technology* 22 (2011), p. 055501.

[Ma+11] J. Ma et al. “Recent progress in multiferroic magnetoelectric composites: from bulk to thin films”. In: *Advanced materials (Deerfield Beach, Fla.)* 23.9 (2011), pp. 1062–1087.

[Mal+13] M. Malatek et al. “Improvement of the off-diagonal magnetoimpedance sensor white noise”. In: *Sensors and Actuators A: Physical* 204 (2013), pp. 20–24.

[MC93] C. D. Motchenbacher and J. A. Conelly. *Low-Noise Electronic System Design*. Wiley, 1993.

[MG02] R. Mäusl and J. Göbel. *Analoge und digitale Modulationsverfahren*. Hüthig GmbH, 2002.

[MG86] H. Meinke and F. W. Gundlach. *Taschenbuch der Hochfrequenztechnik*. Vol. 4. Springer, 1986.

[MH03] A. J. Moulsen and J. M. Herbert. *Electroceramics*. 2nd. Wiley, 2003.

[Mic14] Microelectromechanical Systems Standards Development Committee of the IEEE Electron Devices Society. “IEEE Standard for Sensor Performance Parameter Definitions”. In: *IEEE Std 2700-2014* (2014), pp. 1–69.

[Mir85] M. Mirowski. “The automatic implantable cardioverter-defibrillator: An Overview”. In: *Journal of the American COllege of Cardiology* 6.2 (1985), pp. 461–466.

[MNK10] F. Mohd-Yasin, D. J. Nagel, and C. E. Korman. “Noise in MEMS”. In: *Measurement Science and Technology* 21.1 (2010), p. 012001.

[Moh+17] I. S. Mohamed et al. “The clinical impact of integration of magnetoencephalography in the presurgical workup for refractory nonlesional epilepsy”. In: *Epilepsy & Behavior : E & B* 79 (2017), pp. 34–41.

[Mor49] S. P. Morgan. “Effect of Surface Roughness on Eddy Current Losses at Microwave Frequencies”. In: *Journal of Applied Physics* 20.4 (1949), pp. 352–362.

[Nan+08] C. Nan et al. “Multiferroic magnetoelectric composites: Historical perspective, status, and future directions”. In: *Journal of Applied Physics* 103.3 (2008), p. 031101.

[Nan+13] T. Nan et al. “Self-biased 215 MHz magnetoelectric NEMS resonator for ultra-sensitive DC magnetic field detection”. In: *Scientific reports* 3 (2013), p. 1985.

[NPS91] B. Neri, B. Pellegrini, and R. Saletti. “Ultra low-noise preamplifier for low-frequency noise measurements in electron devices”. In: *IEEE Transactions on Instrumentation and Measurement* 40.1 (1991), pp. 2–6.

[NU15] S. Nakayama and T. Uchiyama. “Real-time measurement of biomagnetic vector fields in functional syncytium using amorphous metal”. In: *Scientific reports* 5 (2015), p. 8837.

[Nyq28] H. Nyquist. “Thermal Agitation of Electric Charge in Conductors”. In: *Physical Review* 32 (1928).

[Pet+11] Jonathan Petrie et al. “Enhancing the sensitivity of magnetoelectric sensors by increasing the operating frequency”. In: *Journal of Applied Physics* 110.12 (2011), p. 124506.

[Pet+12] J. Petrie et al. “Shifting the operating frequency of magnetoelectric sensors”. In: *Journal of Applied Physics* 111.7 (2012), p. 07C714.

[Pio+13] A. Piorra et al. “Magnetoelectric thin film composites with interdigital electrodes”. In: *Applied Physics Letters* 103.3 (2013), p. 032902.

[Pio14] A. Piorra. “Ferroelektrische Schichten für magnetoelektrische Komposite”. PhD thesis. Technische Fakultät der Christian-Albrechts-Universtät zu Kiel, 2014.

[Pop04] R. S. Popovic. *Hall Effect Devices*. 2nd ed. IOP, 2004.

[Poz12] D. M. Pozar. *Microwave Engineering*. Vol. 4. John Wiley and Sons, 2012.

[Que+06] U. Queitsch et al. “Domain wall induced modes of high-frequency response in ferromagnetic elements”. In: *Journal of Applied Physics* 100.9 (2006), p. 093911.

[Ree+16a] J. Reermann et al. “Adaptive Readout Schemes for Thin-Film Magnetoelectric Sensors Based on the delta-E Effect”. In: *IEEE Sensors Journal* (2016), pp. 4891–4900.

[Ree17] J. Reermann. “Signalverarbeitung für magnetoelektrische Sensorsysteme”. PhD thesis. Technische Fakultät der Christian-Albrechts-Universtät zu Kiel, 2017.

[Rie+97] R. P. Ried et al. “6-MHz 2-N/m piezoresistive atomic-force microscope cantilevers with INCISIVE tips”. In: *Journal of Microelectromechanical Systems* 6.4 (1997), pp. 294–302.

[Röb+15] V. Röbisch et al. “Exchange biased magnetoelectric composites for magnetic field sensor application by frequency conversion”. In: *Journal of Applied Physics* 117.17 (2015), 17B513.

[RS16] *R & S FSWP Phase Noise Analyzer*. Rohde & Schwarz. 2016.

[RS17a] *R & S FSVA/FSV Signal and Spectrum Analyzer*. Rohde & Schwarz. 2017.

[RS17b] *R & S SMBV100A Vector Signal Generator*. Rohde & Schwarz. 2017.

[SB06] K. Sternickel and A. I. Braginski. “Biomagnetism using SQUIDs: Status and perspectives”. In: *Superconductor Science and Technology* 19.3 (2006), S160–S171.

[Sch+17] V. Schultze et al. “An Optically Pumped Magnetometer Working in the Light-Shift Dispersed Mz Mode”. In: *Sensors (Basel, Switzerland)* 17.3 (2017).

[SF05] N. A. Spaldin and M. Fiebig. “The renaissance of magnetoelectric multiferroics”. In: *Science (New York, N.Y.)* 309.5733 (2005), pp. 391–392.

[Shu+01] V. Ya. Shur et al. “Barkhausen jumps in the motion of a single ferroelectric domain wall”. In: *Physics of the Solid State* 43.6 (2001), pp. 1128–1131.

[SR11] *DSP Lock-In Amplifier SR830*. Rev. 2.5. Stanford Research Systems. 2011.

[SS04] A.S. Sedra and K.C. Smith. *Microelectronic circuits*. Vol. 5. Oxford University Press, 2004.

[SSR06] B Schiek, H-J. Siweries, and I Rolfes. *Noise in High-Frequency Circuits and Oscillators*. Wiley, 2006.

[Sti15] L. Stiny. *Passive elektronische Bauelemente: Aufbau, Funktion, Eigenschaften, Dimensionierung und Anwendung*. 2nd. Springer Vieweg, 2015.

[SZT06] G. Srinivasan, I. V. Zavislyak, and A. S. Tatarenko. "Millimeter-wave magnetoelectric effects in bilayers of barium hexaferrite and lead zirconate titanate". In: *Applied Physics Letters* 89.15 (2006), p. 152508.

[TM04] S. Trolier-McKinstry and P. Muralt. "Thin Film Piezoelectrics for MEMS". In: *Journal of Electroceramics* 12.1/2 (2004), pp. 7–17.

[TS99] C. S. Tsai and J. Su. "A wideband electronically tunable microwave notch filter in yttrium iron garnet–gallium arsenide material structure". In: *Applied Physics Letters* 74.14 (1999), pp. 2079–2080.

[Tum11] S. Tumanski. *Handbook of Magnetic Measurements*. 1st. CRC Press, 2011.

[TWK98] M. Thumm, W. Wiesbeck, and S. Kern. *Hochfrequenzmesstechnik, Verfahren und Meßsysteme*. Vol. 2. B.G. Teuber Stuttgart, 1998.

[Urs+14] N. O. Urs et al. "Origin of hysteretic magnetoelastic behavior in magnetoelectric 2-2 composites". In: *Applied Physics Letters* 105.20 (2014), p. 202406.

[Urs+16] N. O. Urs et al. "Advanced magneto-optical microscopy: Imaging from picoseconds to centimeters - imaging spin waves and temperature distributions (invited)". In: *AIP Advances* 6.5 (2016), p. 055605.

[Wal+96] D. A. Walters et al. "Short cantilevers for atomic force microscopy". In: *Review of Scientific Instruments* 67.10 (1996), pp. 3583–3590.

[Wan+11] Y. Wang et al. "An extremely low equivalent magnetic noise magnetoelectric sensor". In: *Advanced materials (Deerfield Beach, Fla.)* 23.35 (2011), pp. 4111–4114.

[WRC06] M. Wun-Fogle, J. B. Restorff, and A. E. Clark. "Magnetomechanical Coupling in Stress-Annealed Fe–Ga (Galfenol) Alloys". In: *IEEE Transactions on Magnetics* 42.10 (2006), pp. 3120–3122.

[XL16] C. Xie and S. Lu. “Performance degradation analysis and reliability statistical inference of PCB”. In: *2016 IEEE Chinese Guidance, Navigation and Control Conference (CGNCC)*. Aug. 2016, pp. 2215–2218.

[Yan+08] G. Yang et al. “Electronically Tunable Miniaturized Antennas on Magnetoelectric Substrates With Enhanced Performance”. In: *IEEE Transactions on Magnetics* 44.11 (2008), pp. 3091–3094.

[Yar+16b] E. Yarar et al. “Low temperature aluminum nitride thin films for sensory applications”. In: *AIP Advances* 6.7 (2016), p. 075115.

[Yas+00] K. Y. Yasumura et al. “Quality factors in micron- and submicron-thick cantilevers”. In: *Journal of Microelectromechanical Systems* 9.1 (2000), pp. 117–125.

[Zab+16] S. Zabel et al. “Multimode delta-E effect magnetic field sensors with adapted electrodes”. In: *Applied Physics Letters* 108.22 (2016), p. 222401.

[Zha+09] P. Zhao et al. “Fabrication and characterization of all-thin-film magnetoelectric sensors”. In: *Applied Physics Letters* 94.24 (2009), p. 243507.

[Zhu+15a] X. Zhuang et al. “Mechanical Noise Limit of a Strain-Coupled Magneto(Elasto)electric Sensor Operating Under a Magnetic or an Electric Field Modulation”. In: *IEEE Sensors Journal* 15.3 (2015), pp. 1575–1587.

[Zhu+15b] X. Zhuang et al. “Sensitivity and Noise Evaluation of a Bonded Magneto(elasto) Electric Laminated Sensor Based on In-Plane Magnetocapacitance Effect for Quasi-Static Magnetic Field Sensing”. In: *IEEE Transactions on Magnetics* 51.1 (2015), pp. 1–4.

[ZSD12] X. Zhuang, M. L. C. Sing, and C. Dolabdjian. “Investigation of the near-carrier noise for strain-driven ME laminates by using cross-correlation techniques”. In: *IEEE Transactions on Magnetics* 49.1 (2012), pp. 120–123.

Publications with own Involvement

[Dur+17a] Durdaut, P. and Salzer, S et al. “Improved Magnetic Frequency Conversion Approach for Magnetoelectric Sensors”. In: *IEEE Sensors Letters* (2017), p. 1.

[Dur+17c] P. Durdaut et al. “Thermal-Mechanical Noise in Resonant Thin-Film Magnetoelectric Sensors”. In: *IEEE Sensors Journal* (2017), p. 1.

[Hay+16] P. Hayes et al. “Electrically modulated magnetoelectric sensors”. In: *Applied Physics Letters* 108.18 (2016), p. 182902.

[Ree+15] J. Reermann et al. “Adaptive Acoustic Noise Cancellation for Magnetoelectric Sensors”. In: *IEEE Sensors Journal* 15.10 (2015), pp. 5804–5812.

[Ree+16b] J. Reermann et al. “Comparison of Reference Sensors for Noise Cancellation of Magnetoelectric Sensors”. In: *2016 IEEE Sensors*. Orlando, USA, Nov. 2016.

[Ree+17] J. Reermann et al. “Evaluation of Magnetoelectric Sensor Systems for Cardiological Applications”. In: *Measurement* 116 (2017), pp. 230–238.

[Röb+17] V. Röbisch et al. “Pushing the detection limit of thin film magnetoelectric heterostructures”. In: *Journal of Materials Research* 32.06 (2017), pp. 1009–1019.

[Sal+15] S. Salzer et al. “Comparison of Frequency Conversion Techniques for Magnetoelectric Sensors”. In: *Procedia Engineering* 120 (2015), pp. 940–943.

[Sal+16] S. Salzer et al. “Tuning fork for noise suppression in magnetoelectric sensors”. In: *Sensors and Actuators A: Physical* 237 (2016), pp. 91–95.

[Sal+17a] S. Salzer et al. “Generalized Magnetic Frequency Conversion for Thin-Film Laminate Magnetoelectric Sensors”. In: *IEEE Sensors Journal* 17.5 (2017), pp. 1373–1383.

[Sal+17b] S. Salzer et al. “Noise limits in thin-film magnetoelectric sensors with magnetic frequency conversion”. In: *IEEE Sensors Journal* 18.2 (2017), pp. 596–604.

[Sal+18] S. Salzer et al. “Mikrowellenresonator-Magnetfeldmessvorrichtung sowie Magnetfeldmessverfahren”. 10 2018 110 511. DE patent application. May 2, 2018.

[Yar+16a] E. Yarar et al. “Inverse bilayer magnetoelectric thin film sensor”. In: *Applied Physics Letters* 109.2 (2016), p. 022901.

A | Derivations

$\mathbf{SNR_{tm}}$ Calculation

The SNR for dominant thermal-mechanical noise in resonance is given by

$$\mathrm{SNR}_{\mathrm{tm}}(f_{\mathrm{res}}) \overset{(2.50)}{=} \frac{S(f \ll f_{\mathrm{res}}) \cdot G_{\mathrm{mech}}(f_{\mathrm{res}}) \cdot B_{\mathrm{s}} \cdot G_{\mathrm{CA}}(f_{\mathrm{res}})}{\tilde{E}_{\mathrm{om}}(f_{\mathrm{res}})\sqrt{\Delta f}} \tag{A.1}$$

with

$$G_{\mathrm{mech}}(f_{\mathrm{res}}) \overset{(2.3)}{=} Q \overset{(3.37)}{=} \frac{1}{R_{\mathrm{m}}}\sqrt{\frac{L_{\mathrm{m}}}{C_{\mathrm{m}}}}. \tag{A.2}$$

The gain in resonance can be calculated with

$$G_{\mathrm{CA}}(f_{\mathrm{res}}) = \frac{|Z_{\mathrm{f}}|(f_{\mathrm{res}})}{|Z_{\mathrm{ME}}(f_{\mathrm{res}})|}, \tag{A.3}$$

whereas the impedance of the sensor can be written as

$$\begin{aligned} |Z_{\mathrm{ME}}(f_{\mathrm{res}})| &= \frac{1}{\sqrt{\frac{1}{R_{\mathrm{ME}}^2} + (2\,\pi\,f_{\mathrm{res}}\,C_{\mathrm{ME}})^2}} \\ &\overset{(2.10)}{=} \frac{1}{\sqrt{(2\,\pi\,f_{\mathrm{res}}\,C_{\mathrm{ME}})^2 \cdot (1 + \tan\delta_{\mathrm{ME}}^2)}}. \end{aligned} \tag{A.4}$$

The thermal-mechanical noise at resonance at the output is given by

$$\tilde{E}_{\mathrm{om}}(f_{\mathrm{res}}) \overset{(2.49)}{=} \frac{|Z_{\mathrm{f}}(f_{\mathrm{res}})|}{\sqrt{R_{\mathrm{m}}}} \cdot \sqrt{4k_{\mathrm{B}}T}. \tag{A.5}$$

With the above equations, the $\mathrm{SNR}_{\mathrm{tm}}$ simplifies to

$$\mathrm{SNR}_{\mathrm{tm}}(f_{\mathrm{res}}) = \frac{S(f \ll f_{\mathrm{res}}) \cdot B_{\mathrm{s}}}{\sqrt{4k_{\mathrm{B}}T}\sqrt{\Delta f}} \cdot \sqrt{\frac{L_{\mathrm{m}}}{C_{\mathrm{m}} \cdot R_{\mathrm{m}}}} \cdot \sqrt{(2\pi\, f_{\mathrm{res}}\, C_{\mathrm{ME}})^2 \cdot (1 + \tan\delta^2_{\mathrm{ME}})} \quad \text{(A.6)}$$

With Eqs. (2.33), (2.34), and (2.35) the SNR in resonance is finally given by

$$\mathrm{SNR}_{\mathrm{tm}}(f_{\mathrm{res}}) = \frac{S(f \ll f_{\mathrm{res}}) \cdot B_{\mathrm{s}}}{\sqrt{4k_{\mathrm{B}}T}\sqrt{\Delta f}} \sqrt{\frac{2\pi\, f_{\mathrm{res}}^5\, C_{\mathrm{ME}}(1 + \tan\delta^2_{\mathrm{ME}})}{\tan\delta_{\mathrm{meas}}(f_{\mathrm{res}}) \left[f_{\mathrm{up}}^2 - f_{\mathrm{res}}^2\right]^2}}. \quad \text{(A.7)}$$

MFC Noise Calculation

A large part of this derivation originates from [Jah13]. The equivalent circuit model for MFC is depicted in Fig. 3.31 and repeated here:

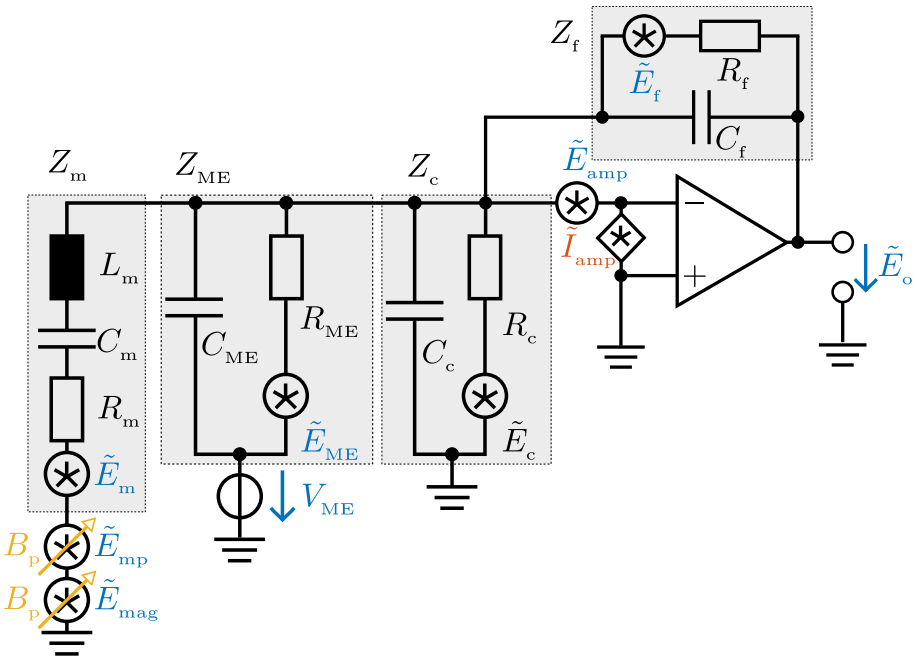

Figure A.1: Equivalent noise circuit for MFC. Both equivalent noise sources $\tilde{E}_{\mathrm{mp}}$ and $\tilde{E}_{\mathrm{mag}}$ depend on the pump amplitude and are marked with control arrows. For signals, the output voltage is V_{o} parallel to $\tilde{E}_{\mathrm{o}}$.

In the following, the calculation of the individual noise components at the output of the charge amplifier is derived.

Gain G_{CA} For the calculation of the gain of this model, the resonant branch and the cable are short-circuited by the charge amplifier. The voltage gain is then calculated by

$$G_{\mathrm{CA}} = \frac{V_{\mathrm{o}}}{V_{\mathrm{ME}}} = \frac{I\,|Z_{\mathrm{f}}|}{I\,|Z_{\mathrm{ME}}|} = \left|\frac{Z_{\mathrm{f}}}{Z_{\mathrm{ME}}}\right| \tag{A.8}$$

since the current through both circuits is the same. For individual noise sources, the gain may be different as can be seen in the following paragraphs.

Thermal mechanical noise $\tilde{E}_{\mathrm{om}}$ Z_{ME} and Z_{c} are short-circuited by the virtual mass at the input of the charge amplifier.

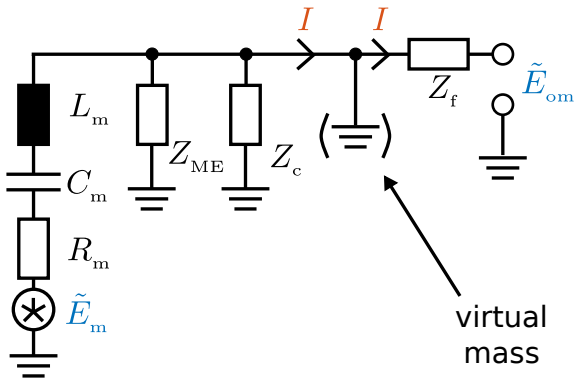

Figure A.2: Thermal mechanical noise $\tilde{E}_{\mathrm{om}}$. The virtual mass is indicated by brackets.

$$I^2 = \frac{\tilde{E}_{\mathrm{m}}^2}{|Z_{\mathrm{m}}|^2} \tag{A.9}$$

$$\tilde{E}_{\mathrm{om}}^2 = I^2 \cdot |Z_{\mathrm{f}}|^2 = \tilde{E}_{\mathrm{m}}^2 \cdot \frac{|Z_{\mathrm{f}}|^2}{|Z_{\mathrm{m}}|^2} \tag{A.10}$$

ME noise $\tilde{E}_{\mathbf{oME}}$ Z_{m}, C_{ME} and Z_{c} are short-circuited by the virtual mass of the charge amplifier.

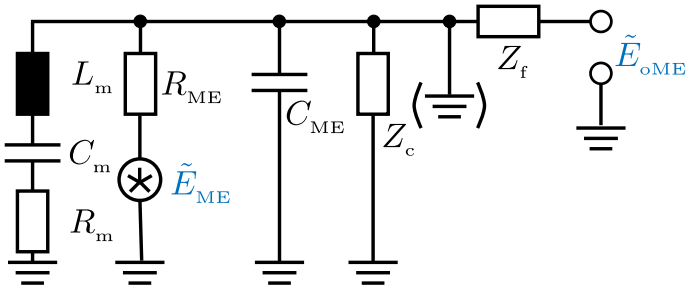

Figure A.3: ME noise $\tilde{E}_{\mathrm{ME}}$.

$$\begin{aligned}\tilde{E}_{\mathrm{oME}}^2 &= \tilde{E}_{\mathrm{ME}}^2 \cdot \frac{|Z_{\mathrm{f}}|^2}{R_{\mathrm{ME}}^2} \\ &= \tilde{E}_{\mathrm{ME}}^2 \cdot \frac{|Z_{\mathrm{f}}|^2}{R_{\mathrm{ME}}^2} \cdot \frac{|Z_{\mathrm{ME}}|^2}{|Z_{\mathrm{ME}}|^2} \\ &= \tilde{E}_{\mathrm{ME}}^2 \cdot G_{\mathrm{CA}}^2 \frac{|Z_{\mathrm{ME}}|^2}{R_{\mathrm{ME}}^2}\end{aligned} \tag{A.11}$$

Cable noise $\tilde{E}_{\mathbf{oc}}$ Z_{ME}, Z_{m} and C_{c} are short-circuited by the virtual mass at the input of the charge amplifier.

$$\begin{aligned}\tilde{E}_{\mathrm{oc}} &= \tilde{E}_{\mathrm{c}}^2 \cdot \frac{|Z_{\mathrm{f}}|^2}{R_{\mathrm{c}}^2} \\ &= \tilde{E}_{\mathrm{c}}^2 \cdot \frac{|Z_{\mathrm{f}}|^2}{R_{\mathrm{c}}^2} \cdot \frac{|Z_{\mathrm{ME}}|^2}{|Z_{\mathrm{ME}}|^2} \\ &= \tilde{E}_{\mathrm{c}}^2 \cdot G_{\mathrm{c}}^2 \frac{|Z_{\mathrm{ME}}|^2}{R_{\mathrm{c}}^2}\end{aligned} \tag{A.12}$$

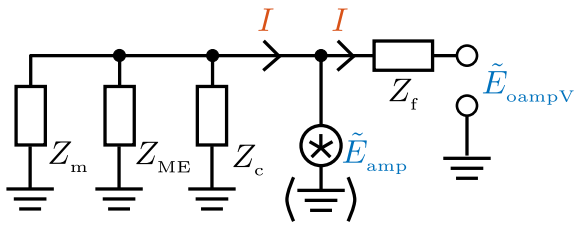

Figure A.4: Voltage noise of the amplifier $\tilde{E}_{amp}$.

Voltage noise of the amplifier $\tilde{E}_{oampV}$

$$Z_{mMEC} = Z_m || Z_{ME} || Z_c \tag{A.13}$$

$$I^2 = \frac{\tilde{E}^2_{amp}}{|Z_{mMEc}|^2} \tag{A.14}$$

$$\tilde{E}^2_{oampV} = \tilde{E}^2_{amp} + \tilde{E}^2_{amp} \cdot \frac{|Z_f|^2}{|Z_{mMEc}|^2} = \tilde{E}^2_{amp} \cdot \left| 1 + \frac{Z_f}{Z_{mMEc}} \right|^2 \tag{A.15}$$

Consequently, the following is incorrect because the noise transfers with the squared absolute

$$\tilde{E}^2_{oampV} = \tilde{E}^2_{amp} + \tilde{E}^2_{amp} \cdot \frac{|Z_f|^2}{|Z_{mMEc}|^2} = \tilde{E}^2_{amp} \cdot \left(1 + \frac{|Z_f|^2}{|Z_{mMEc}|^2} \right). \tag{A.16}$$

Current noise of the amplifier $\tilde{E}_{oampI}$ Z_{ME}, Z_m and Z_c are short-circuited by the virtual mass at the input of the charge amplifier.

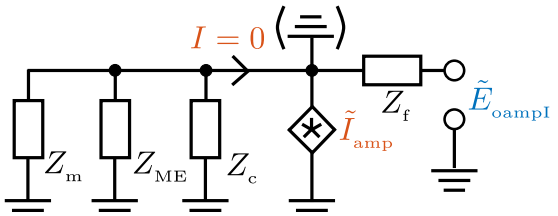

Figure A.5: Current noise of the amplifier $\tilde{I}_{amp}$.

$$Z_{mMEC} = Z_m || Z_{ME} || Z_c \tag{A.17}$$

$$\tilde{E}^2_{oampI} = \tilde{I}^2_{amp} \cdot |Z_f|^2 \tag{A.18}$$

Noise of the feedback resistance $\tilde{E}_{\mathrm{of}}$ Z_{ME}, Z_{m} and Z_{c} are short-circuited by the virtual mass at the input of the charge amplifier.

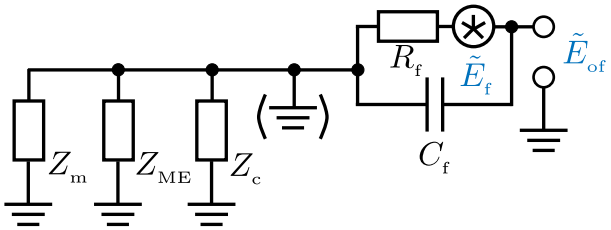

Figure A.6: Noise of the feedback resistance $\tilde{E}_{\mathrm{f}}$.

$$\frac{\tilde{E}_{\mathrm{of}}^2}{\tilde{E}_{\mathrm{f}}^2} = \frac{|\frac{1}{j\omega C_{\mathrm{f}}}|^2}{|R_{\mathrm{f}} + \frac{1}{j\omega C_{\mathrm{f}}}|^2} \tag{A.19}$$

$$\tilde{E}_{\mathrm{of}}^2 = \tilde{E}_{\mathrm{f}}^2 \cdot \frac{1}{|1 + j\omega C_{\mathrm{f}} R_{\mathrm{f}}|^2} \tag{A.20}$$

Excitation noise $\tilde{E}_{\mathrm{omp}}$ Z_{c} and Z_{ME} are short-circuited by the virtual mass at the input of the charge amplifier.

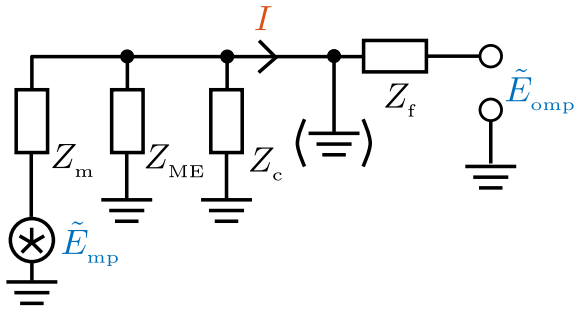

Figure A.7: Excitation noise $\tilde{E}_{\mathrm{omp}}$.

$$I^2 = \frac{\tilde{E}_{\mathrm{mp}}^2}{|Z_{\mathrm{m}}|^2} \tag{A.21}$$

$$\tilde{E}_{\mathrm{omp}}^2 = I^2 \cdot |Z_{\mathrm{f}}|^2 = E_{\mathrm{mp}}^2 \cdot \frac{|Z_{\mathrm{f}}|^2}{|Z_{\mathrm{m}}|^2} \tag{A.22}$$

Magnetic noise $\tilde{E}_{\mathbf{omag}}$ Z_{c} and Z_{ME} are short-circuited by the virtual mass at the input of the charge amplifier.

$$I^2 = \frac{\tilde{E}^2_{\mathrm{mag}}}{|Z_{\mathrm{m}}|^2} \tag{A.23}$$

$$\tilde{E}^2_{\mathrm{omag}} = I^2 \cdot |Z_{\mathrm{f}}|^2 = \tilde{E}^2_{\mathrm{mag}} \cdot \frac{|Z_{\mathrm{f}}|^2}{|Z_{\mathrm{m}}|^2} \tag{A.24}$$

Direct Detection of magnetoelectric µw-Resonator

The µw measurement signal is given by

$$S_{\mathrm{p,\mu w}} = P_{\mu \mathrm{w}} \cdot \cos(\omega_{\mathrm{res,\mu w}} t). \tag{A.25}$$

The desired magnetic signal can be expressed as

$$B_{\mathrm{s}} = \hat{b}_{\mathrm{s}} \cdot \cos(\omega_{\mathrm{s}} t). \tag{A.26}$$

The phase modulated signal can then be described with

$$S_{\mathrm{p,\mu w}} = P_{\mu \mathrm{w}} \cdot \cos(\omega_{\mathrm{res,\mu w}} t + \eta \, \cos(\omega_{\mathrm{s}} t)), \tag{A.27}$$

with the modulation index η. With the trigonometric identities

$$\cos(x \pm y) = \cos(x)\cos(y) \mp \sin(x)\sin(y) \tag{A.28}$$

$$\sin(x)\cos(y) = \frac{1}{2}\left[\sin(x-y) + \sin(x+y)\right] \tag{A.29}$$

$$\cos(\eta \cos(\omega_{\mathrm{s}} t)) \approx 1, \text{ for } \eta \ll 1 \tag{A.30}$$

$$\sin(\eta \cos(\omega_{\mathrm{s}} t)) \approx \eta \cos(\omega_{\mathrm{s}} t), \text{ for } \eta \ll 1 \tag{A.31}$$

Eq. (A.27) can be rewritten as

$$\begin{aligned} S_{\mathrm{p,\mu w}} &= P_{\mu \mathrm{w}} \cdot \cos(\omega_{\mathrm{res,\mu w}} t + \eta \, \cos(\omega_{\mathrm{s}} t)) \\ &= P_{\mu \mathrm{w}} \left[\cos(\omega_{\mathrm{res,\mu w}} t)\cos(\eta \cos(\omega_{\mathrm{s}} t)) - \sin(\omega_{\mathrm{res,\mu w}} t)\sin(\eta \cos(\omega_{\mathrm{s}} t))\right] \\ &= P_{\mu \mathrm{w}} \left[\cos(\omega_{\mathrm{res,\mu w}} t) - \sin(\omega_{\mathrm{res,\mu w}} t)\eta \cos(\omega_{\mathrm{s}} t)\right] \\ &= P_{\mu \mathrm{w}} \left\{\cos(\omega_{\mathrm{res,\mu w}} t) - \frac{\eta}{2}\left[\sin((\omega_{\mathrm{res,\mu w}} - \omega_{\mathrm{s}})t + \sin((\omega_{\mathrm{res,\mu w}} + \omega_{\mathrm{s}})t))\right]\right\}. \end{aligned} \tag{A.32}$$

Phase Noise Reduction

The pump signal with a noise sideband at ω_{offset} that represents the phase noise is given as

$$S_{\text{p,n}} = P_{\mu\text{w}} \cdot \cos\left[\omega_c t + \eta \cos\left(\omega_{\text{offset}} t\right)\right]. \tag{A.33}$$

With

$$\cos\left[a + b\cos\left(c\right)\right] = \cos\left(a\right) \cdot \cos\left[b\cos\left(c\right)\right] - \sin\left(a\right) \cdot \sin\left[b\cos\left(c\right)\right] \tag{A.34}$$

Eq. (A.33) can be rewritten as

$$S_{\text{p,n}} = P_{\mu\text{w}} \cdot \cos\left(\omega_{\text{p}} t\right) \cdot \cos\left[\eta \cos\left(\omega_{\text{offset}} t\right)\right] - P_{\mu\text{w}} \cdot \sin\left(\omega_{\text{p}} t\right) \cdot \sin\left[\eta \cos\left(\omega_{\text{offset}} t\right)\right]. \tag{A.35}$$

For small modulation indices $\eta \ll 1$ the following two simplifications can be made:

$$\cos\left[\eta \cos\left(\omega_{\text{offset}} t\right)\right] \approx 1 \tag{A.36}$$

and

$$\sin\left[\eta \cos\left(\omega_{\text{offset}} t\right)\right] \approx \eta \cos\left(\omega_{\text{offset}} t\right). \tag{A.37}$$

With Eqs. (A.36) and (A.37), Eq. (A.35) can be rewritten as

$$S_{\text{p,n}} \approx P_{\mu\text{w}} \cos\left(\omega_{\text{p}} t\right) + P_{\mu\text{w}} \eta \sin\left(\omega_{\text{p}} t\right) \cos\left(\omega_{\text{offset}} t\right). \tag{A.38}$$

With

$$\sin\left(a\right)\cos\left(b\right) = \frac{1}{2}\Big[\sin\left(a-b\right) + \sin\left(a+b\right)\Big], \tag{A.39}$$

Eq. (A.38) can be further simplified to

$$S_{\text{p,n}} \approx P_{\mu\text{w}} \cos(\omega_{\text{p}} t) + \frac{P_{\mu\text{w}}}{2}\eta \sin\Big[(\omega_{\text{p}} + \omega_{\text{offset}})t\Big] + \frac{P_{\mu\text{w}}}{2}\eta \sin\Big[(\omega_{\text{p}} - \omega_{\text{offset}})t\Big]. \tag{A.40}$$

Eq. (A.40) represents a microwave signal with noise sidebands. In the frequency discriminator, the noisy reference signal is divided into two paths by a 3 dB coupler. The path via the phase shifter is given by

$$S_{\mathrm{PS,n}} \approx \frac{P_{\mu\mathrm{w}}}{2}\cos(\omega_{\mathrm{p}}t) + \frac{P_{\mu\mathrm{w}}}{4}\eta\sin\Big[(\omega_{\mathrm{p}}+\omega_{\mathrm{offset}})t\Big] + \frac{P_{\mu\mathrm{w}}}{4}\eta\sin\Big[(\omega_{\mathrm{p}}-\omega_{\mathrm{offset}})t\Big]. \quad \text{(A.41)}$$

The phase shift φ_{PS} is included in the relative time delay $\tau_{\mu\mathrm{w}}$ of the second path via the ME resonator given by

$$\begin{aligned} S_{\mathrm{ME,n}} \approx{}& \frac{P_{\mu\mathrm{w}}}{2}\cos(\omega_{\mathrm{p}}(t-\tau_{\mu\mathrm{w}}) \\ &+ \frac{P_{\mu\mathrm{w}}}{4}\eta\sin\Big[(\omega_{\mathrm{p}}+\omega_{\mathrm{offset}})(t-\tau_{\mu\mathrm{w}})\Big] + \frac{P_{\mu\mathrm{w}}}{4}\eta\sin\Big[(\omega_{\mathrm{p}}-\omega_{\mathrm{offset}})(t-\tau_{\mu\mathrm{w}})\Big]. \end{aligned} \quad \text{(A.42)}$$

Here, it is assumed that the sensor contributes no additional phase noise into the signal path. The time delay $\tau_{\mu\mathrm{w}}$ is given by

$$\tau_{\mu\mathrm{w}} = \frac{(\varphi_{\mathrm{PS}} - \varphi_{\mathrm{ME}})}{360^\circ \cdot f} \quad \text{(A.43)}$$

and incorporates the phase difference between the two paths for a set phase shift φ_{PS}. The time delay can also be expressed as the number of periods n that fit on the branch with

$$\tau_{\mu\mathrm{w}} = \frac{n}{f}. \quad \text{(A.44)}$$

On a branch with the length $l_{\mu\mathrm{w}}$ fit n full wavelengths of a frequency f_1

$$l_{\mu\mathrm{w}} = n \cdot \lambda_1 \quad \text{(A.45)}$$

and $(n+1)$ full wavelengths of a frequency f_2

$$l_{\mu\mathrm{w}} = (n+1) \cdot \lambda_2. \quad \text{(A.46)}$$

From Eqs. (A.45) and (A.46), n is given by

$$n = \frac{f_1}{f_2 - f_1}. \quad \text{(A.47)}$$

With an oscilloscope at the output of the FD, the delay time can then be determined by

$$\tau_{\mu w} = \frac{1}{f_2 - f_1}. \tag{A.48}$$

The expanded output of the phase discriminator yields 19 summands of which the ones with positive ω_{offset} are of interest:

$$\frac{\eta {P_{\mu w}}^2 \sin\left(\omega_{offset} t + \omega_p \tau_{\mu w}\right)}{16} - \frac{\eta {P_{\mu w}}^2 \sin\left(\omega_{offset} t - \omega_{offset} \tau_{\mu w} + \omega_p \tau_{\mu w}\right)}{16}. \tag{A.49}$$

With

$$\sin(x) - \sin(y) = 2 \sin\left(\frac{x-y}{2}\right) \cos\left(\frac{x+y}{2}\right) \tag{A.50}$$

Eq. (A.49) can be rearranged to

$$S_{FD,n} \approx \frac{\eta P_{\mu w}^2}{8} \left[\cos\left(\omega_p + \omega_{offset}\left(t - \frac{\tau_{\mu w}}{2}\right)\right) \cdot \sin\left(\frac{\omega_{offset} \tau_{\mu w}}{2}\right)\right]. \tag{A.51}$$

$S_{FD,n}$ represents the baseband component of the phase noise at the output of the FD. The noise depends on the time delay $\tau_{\mu w}$ between the two paths.

B | Additional Material, Figures and Pictures

Magnetic field sensing

Magnetic fields can be measured with various magnetic field sensors. In the following, an overview of used (reference) sensors is provided. General reviews are given in [LE06; Ede07] or more recently in [GHM17]. The *gold standard* for ultra sensitive, and also biomagnetic, measurements in research are superconducting quantum interference device (SQUID) sensors at helium temperatures. SQUID sensors for biomagnetic sensing mainly consist of a superconductive ring (e.g. made of Niob) with a Josephson contact (weak link) and an inductively coupled tank circuit. An external AC magnetic field changes the tank circuit's inductance and can thus be measured. Depending on the used superconducting material, SQUID sensors either need to be cooled with liquid helium to 4 K or with liquid nitrogen to 77 K (high-temperature SQUID, less sensitive). Size, cooling, and high operational cost prevent a widespread diagnostic application of this sensor type. Recent developments in atomic magnetometers show even lower LoDs than SQUID sensors, but are not yet in operational use [Kom+03].
Optical-pumped magnetometers (OPM) exploit the magnetic field induced change in optical behaviour of a vapor cell (e.g. rubidium), which is targeted with a laser. The transmission is captured with a photodetector. Because OPMs are zero-field magnetometers they are sensitive to bias fields, which drives them into saturation. For operation, mostly a bias compensation is applied. In this work, the measurement with an optical-pumped magnetometer is conducted with a QuSpin Zero-Field Magnetometer from QuSpin [KS16b]. It is supposed to have a field sensitivity of less than $15\,\mathrm{fT}/\sqrt{\mathrm{Hz}}$ between 1 and 100 Hz, which is proven by the measurement in the

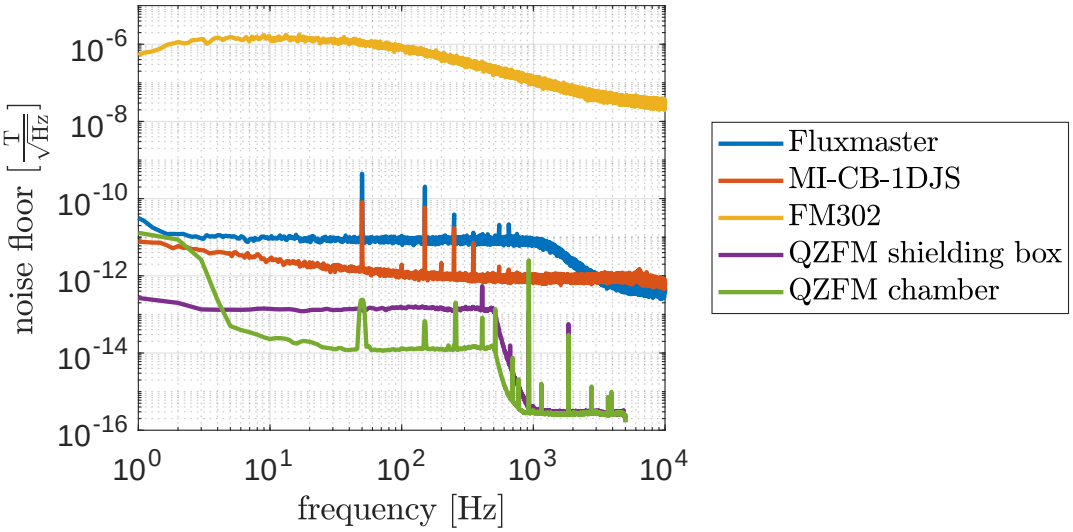

Figure B.1: Magnetic noise floors of a fluxgate sensosr *Fluxmaster* from *Stefan Meyer Instruments*, a magnetoimpedance sensor *MI-CB-1DJS* from *Aichi Micro Intelligent Corporation*, a Hall-effect sensor *Teslameter FM302* from *Projekt Elektronik*, and an OPM sensor *QZFM* from *QUSPIN*.

shielding chamber (see green trace in Fig. B.1) (see Subsec. 2.5.1 for a description of the shielding chamber). While almost being comparable to SQUIDs in sensitivity, the sensor can be operated at ambient temperatures and can measure in two axes simultaneously. Because they do not need to be cooled they may be placed closer to the signal source than SQUIDs which makes their capability to detect biomagnetic signals comparable.

For the calibration of the coils a hall-effect sensor is utilised. Hall effect sensors are low cost, temperature robust and easy to use sensors with a LoD in the range from 30 nT up to 1 T [Pop04]. The detectable deflection of currents through a metal or a semiconductor caused by magnetic fields is called the hall-effect. The hall effect sensor *Teslameter FM-302* from *Projekt Elektronik* has a measurement range from µT to mT in frequencies from DC to 100 kHz. An advantage of this sensor is its robustness against DC fields, making unshielded measurements possible. Fluxgate sensors can be used as a sensitive reference sensor for the development of signal processing schemes. Their principle is based on a dynamic magnetisation of a core inside an excitation and a detection coil. Via the induced current in the detection coil, changes in the magnetisation of the core can be detected. Magnetoimpedance

Sensor	Advantages	Disadvantages	LoD [fT/$\sqrt{\text{Hz}}$] at 10 Hz
SQUID [SB06]	LoD	cooling, price, size	1
OPM [Sch+17]	LoD	size	10
Bulk ME [Wan+11]	cheap	size	1000
MI [KS15]			5000
Fluxgate [NU15]			10000
thin-film ME [Röb+15]	size	LoD	100000
Hall-effect [Gro+16]	size, electrical	LoD	200000

Table B.1: Representative parameters of the noise equivalent circuit around the resonance frequency for a selection of magnetic field sensors.

sensors change their impedance depending on the applied magnetic field which can be measured with an applied detection voltage.
Tab. B.1 compares a selection of magnetic field sensors in terms of their advantages, disadvantages, and LoD.

Additional figures and tables

This section contains supplementary material about the measurement at the second mechanical mode of thin-film ME sensors from Subsec. 2.5.5, the transfer characteristics of a Hall sensor and a Fluxgate sensor both utilised to measure rectangular waveforms from Subsec. 3.1.5, the spectral density output of that Hall sensor, output spectral densities for asymmetric offset suppression, and the coefficients for the presented basic functions in Subsec. 3.1.8.

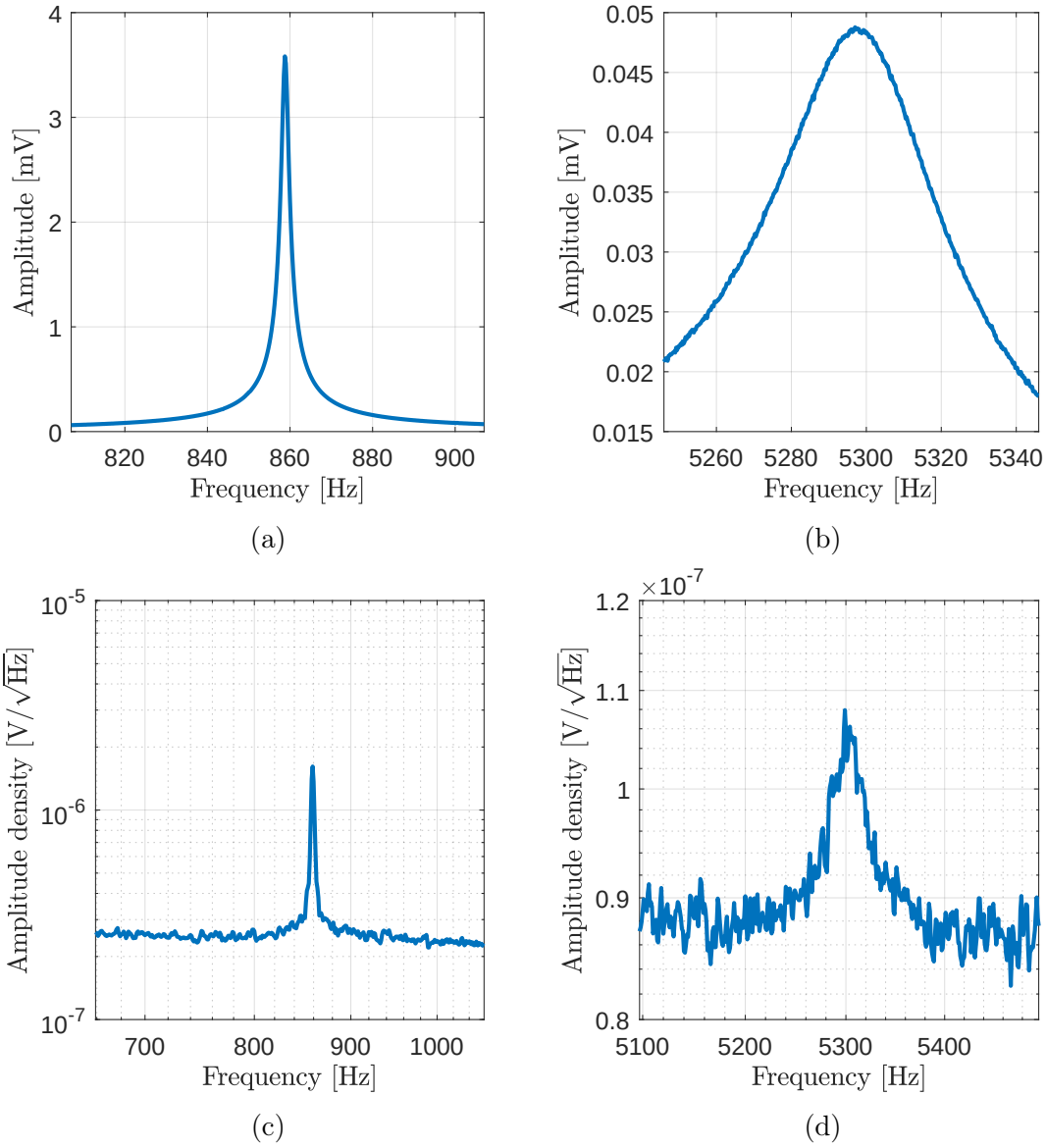

Figure B.2: Measurements of the first and second mechanical resonances of a standard multilayer sensor. (a) Resonance curve of the first mechanical resonance of a standard multilayer sensor. A magnetic bias $B_{\text{opt}} = 0.88\,\text{mT}$ is applied via bias coil. (b) Resonance curve of the second mechanical resonance of a standard multilayer sensor. A magnetic bias $B_{\text{opt}} = 0.86\,\text{mT}$ is applied via bias coil. (c) Noise measurement of the first mechanical resonance of a standard multilayer sensor. (d) Noise measurement of the second mechanical resonance of a standard multilayer sensor. The measurement is conducted with a special charge amplifier with a JFET prestage to lower the amplifier noise [Dur+17b].

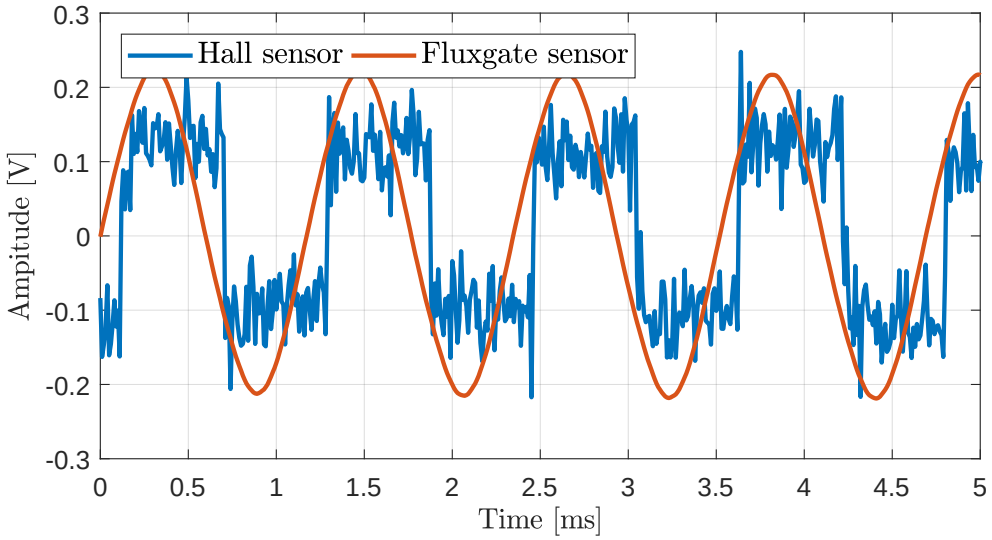

Figure B.3: Measured magnetic field with a rectangular excitation. The Hall-sensor measures a noisy rectangular signal, whereas, the Fluxgate sensor measures a distorted sinusoidal signal due to its limited bandwidth of only 1 kHz.

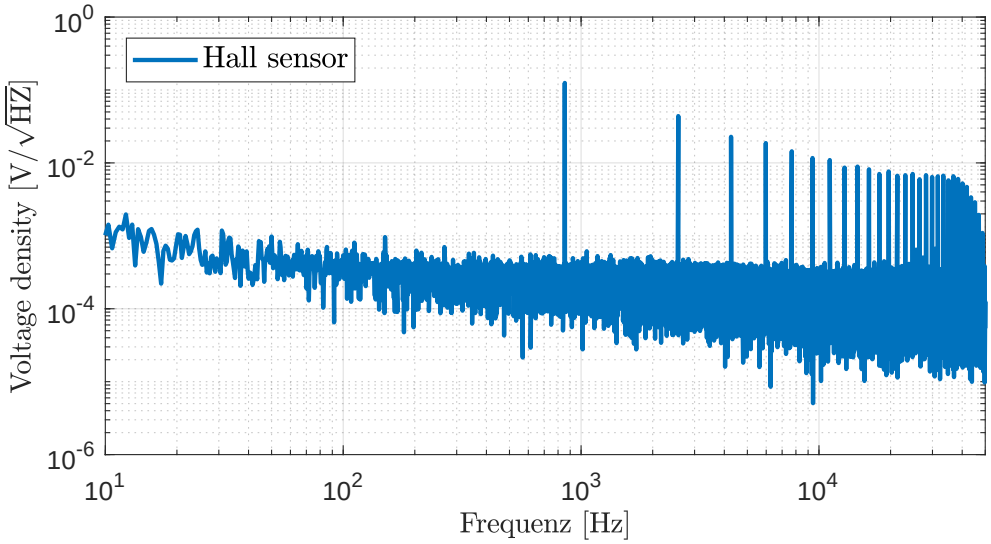

Figure B.4: Spectral density of measured magnetic field of a rectangular excitation, measured with a Hall sensor.

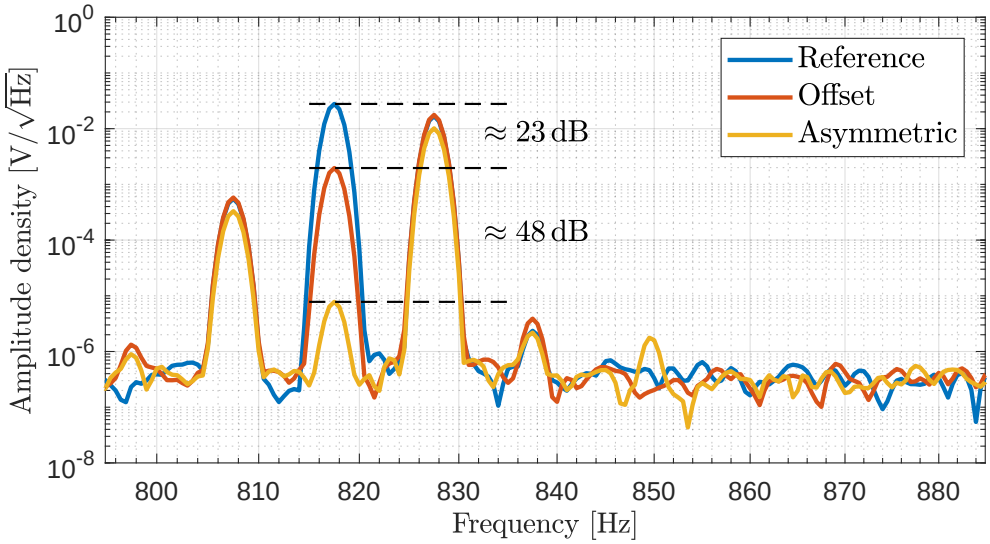

Figure B.5: Spectral densities of a sensor with asymmetric and offset magnetostriction curve. The desired signal has $B_\mathrm{s} = 10\,\mu\mathrm{T}$ at 10 Hz, and the pump level is only $B_\mathrm{p} = 30\,\mu\mathrm{T}$. An offset with $B_\mathrm{offset} = 63.1\,\mu\mathrm{T}$ is applied for offset suppression. The asymmetric pump has a higher positive sinusoidal flank by a factor of five. For the asymmetric pump, the sideband amplitude also decreases slightly.

Table B.2: Coefficients of the polynomial approximation of the functions in Tab. 3.38.

Coefficient	$f_1(B) = B^2$	$f_2(B) = (B - 0.3)^2$	$f_3(B) = B$	$f_4(B) = B^2 + 2$
$a_0\,[\mathrm{mT}]$	0	0.09	0	2
$a_0\,[\frac{1}{\mathrm{mT}}]$	0	−0.6	1	0
$a_2\,[\frac{1}{(\mathrm{mT})^2}]$	1	1	0	1
$a_3\,[\frac{1}{(\mathrm{mT})^3}]$	0	0	0	0
$a_4\,[\frac{1}{(\mathrm{mT})^4}]$	0	0	0	0
$a_5\,[\frac{1}{(\mathrm{mT})^5}]$	0	0	0	0
$a_6\,[\frac{1}{(\mathrm{mT})^6}]$	0	0	0	0
Coefficient	f_5	$f_6(B) = (B \cdot \sqrt{6})^2$	$f_7(B) = B^4$	$f_8(B) = B^2 + B^4$
$a_0\,[\mathrm{mT}]$	−0.0463	0	0	0
$a_0\,[\frac{1}{\mathrm{mT}}]$	−0.3081	0	0	0
$a_2\,[\frac{1}{(\mathrm{mT})^2}]$	0.9159	6	0	1
$a_3\,[\frac{1}{(\mathrm{mT})^3}]$	0.2952	0	0	0
$a_4\,[\frac{1}{(\mathrm{mT})^4}]$	0.1689	0	1	1
$a_5\,[\frac{1}{(\mathrm{mT})^5}]$	0.0083	0	0	0
$a_6\,[\frac{1}{(\mathrm{mT})^6}]$	−0.0054	0	0	0